Towards Sustainable Construction: Innovations in Hemp-Lime Composite Production for Carbon-Negative Building Materials

By

Osamah Mahmood

Under the Supervision of

Dr. Miroslava Kavgic and Dr. Martin Noël

Thesis submitted to the University of Ottawa in partial fulfillment of the requirements of the degree of Doctor of Philosophy in Civil Engineering

Department of Civil Engineering

Faculty of Engineering

University of Ottawa

Ottawa

February 2026

Abstract

Hemp-lime composites (HLC) have captured significant attention in the construction industry due to their sustainability, availability, and excellent hygrothermal performance. These bio-based insulating materials are produced by mixing a lime-based binder with hemp shivs and water. Despite their positive attributes, the properties and performance of the resulting composite depend on various parameters such as the ratio of constituent materials, manufacturing method, binder type, and shiv characteristics (e.g., particle size and purity). Therefore, its widespread adoption has been impeded by the notable variation in hemp-lime formulation and manufacturing methods, leading to inconsistent performance. In this research, new methods are proposed to enhance the homogeneity and uniformity of hemp-lime composites while minimizing their environmental impact to produce a carbon-negative insulating material with predictable and reproducible properties. The main objectives of this research are: 1) to improve the consistency and repeatability of hemp lime composites performance by reducing the hemp shiv particle size and introducing vibration as a compaction method; 2) to investigate the effect of impurities (e.g., hemp fibres) on the mechanical and hygrothermal properties of hemp lime composites; and 3) to investigate the effectiveness of producing hydrated lime from different $CaCO_3$ sources, including organic waste, using an electrochemical decarbonation process to formulate carbon-negative hemp lime composites for sustainable construction.

In accordance with the above objectives, modifications are proposed to the hemp shiv particle size, binder source, and placement method used to make hemp-lime composites. The experimental results demonstrate a marked improvement in hygrothermal properties compared to values reported in available literature, with thermal conductivity in the range of 0.053-0.060 W/m K and moisture buffering values between 2.21 to 2.53 g/m² RH, as well as a very low coefficient of variation of dry density between 0.37-0.73%. The results also demonstrate a noteworthy reduction in the directional difference of thermal conductivity,

reduced to less than 3% when employing fine hemp fragments. Furthermore, using finer particles reduces the amount of binder needed which significantly lowers the carbon footprint when using conventional hydrated lime produced through calcination. An alternative process is also introduced in which hydrated lime is produced through electrolysis, which facilitates direct carbon capture. This process is evaluated using three different limestone sources and two organic sources (mussel and eggshells) as feedstock. The precipitated materials are mainly comprised of $Ca(OH)_2$ with a suitable chemical composition and particle size distribution required for Type N hydrated lime. The environmental assessment of wall assemblies revealed that hemp–lime composites incorporating electrochemically decarbonated hydrated lime (ED-HLC) offer comparable thermal and moisture performance to conventional binders while achieving superior mechanical strength. Life-cycle analysis demonstrated a markedly lower embodied footprint and a carbon-negative balance, reaching –23.1 kg CO_2 eq. when carbon sequestration was included. Compared to conventional lime-based hemp–lime composites and glass wool insulation, the ED-HLC wall showed 15.7% and 457% lower global warming potentials, respectively, confirming its strong potential as a carbon-conscious insulation solution.

Acknowledgment

First and foremost, I would like to express my deepest gratitude to my supervisors, Dr. Miroslava Kavgic and Dr. Martin Noël, for their invaluable guidance, continuous support, and unwavering patience throughout the course of my PhD journey. Their insightful feedback, constructive criticism, and encouragement pushed me to sharpen my thinking and brought my work to a higher level. Chapter six of this thesis is based on a publication co-authored with (Darío Ramírez-Amaya, Natalia P. Martinez, Felipe Troncoso P., Valeria Gazzano, and Roberto Canales). While I am not the first author of the paper, my main contributions included conducting experiments, analyzing results, performing data interpretation and visualization, and contributing to discussion and validation of results. I gratefully acknowledge their valuable input while emphasizing that the central elements of this research form part of my doctoral work.

To my family, I owe more than words can express. Thank you for your love, understanding, and sacrifices. Your belief in me kept me grounded and motivated through the toughest times.

This thesis is dedicated to all those who walked this path with me, in spirit or in presence.
Thank you.

Table of Contents

List of Figures

List of Tables

Nomenclature and Symbols

K_1	slope of the absorption curve
W_t	water absorption (%)
f_c	fibre content (%)
m_0	initial mass (gm)
m_d	dry mass (gm)
m_f	dry mass of the fibres
B/H	binder to hemp ratio
CA	conventional approach
CO_2e	carbon dioxide equivalent
Cp	specific heat capacity (J/kg K)
CV	coefficient of variation
DM	deposited material
DTGA	differential thermogravimetric analysis
ED	electrochemical decarbonation
ED-HLC	hemp-lime composite with ED hydrated lime
EDX	energy dispersive X-Ray spectroscopy
ES	eggshells
FE-SEM	field emission scanning electron microscopy
FU	functional unit
GHG	greenhouse gas
GWP	global warming potential
HLC	hemp-lime composite
IRA	initial rate of absorption
k	thermal conductivity (W/m K)
LCA	life cycle assessment
LCI	life cycle inventory

LOI	loss on ignition
MBV	moisture buffer value (g/m²·RH)
MS	mussel shells
R	thermal resistance (m²·K/W)
RH	relative humidity
SSABET	specific surface area Brunauer, Emmett and Teller method
TGA	thermogravimetric analysis
XRD	X-Ray diffraction
XRF	X-Ray fluorescence
ρ	density (kg/m^3)
M	mass (kg)
V	Volume (m^3)
W	initial water content (%)
t	time (seconds)
α	thermal diffusivity (m^2/s) x10^{-6}

Chapter 1 : Introduction

1.1. Background and Rationale

Compared to other major sectors of human activity, the building and construction sector has a significant impact on the environment through depletion of natural resources and energy consumption. This sector is also a substantial contributor of greenhouse gas (GHG) emissions, responsible for 40% of those gases globally [Lawrence, 2015], and it is expected to rapidly increase due to population growth and globalization. Opposing global warming has been a priority of lawmakers and organizations in the form of laws and regulations to push for sustainable solutions to enhance life quality and combat climate change [Hussain et al., 2019]. Canada has committed to decreasing GHG emissions by 40-45% from 2005 levels by 2030 and achieving net-zero emissions by 2050 [Government of Canada, 2020]. As the sector transitions toward more sustainable alternatives, there is growing interest in bio-based and carbon-negative materials, particularly those that integrate renewable resources, industrial symbiosis, and circular economy principles.

One such material gaining attention is hemp-lime composite (HLC)—a bio-aggregate construction material composed primarily of hemp shiv (the woody inner core of the hemp stalk) and a lime-based binder. Hemp offers significant advantages over other biomass types (i.e. wood) in the production of lime-based composites due to its rapid renewability, high carbon sequestration potential, and superior hygrothermal properties. Unlike wood, which requires decades to mature, hemp grows within 3–4 months while capturing 10–15 tons of CO_2 per hectare during its growth cycle, which is subsequently locked into the composite [Amaducci et al., 2015; Ip & Miller, 2012]. Hemp-lime utilizes the woody core (shiv), an agricultural byproduct of the fibre industry, thereby supporting circular economy principles and minimizing waste [Stevulova et al., 2014].

Additionally, hemp-lime composites demonstrate favourable thermal insulation and moisture regulation compared to denser wood-based products, alongside lower embodied energy requirements [Walker & Pavía, 2014; Pretot et al., 2014]. These attributes position hemp as a more sustainable and environmentally effective alternative to wood for non-structural building composites.

HLC is valued not only for its environmental credentials but also for its desirable thermal and moisture-regulating properties. Due to the carbon sequestration during hemp growth and the carbonation of lime binders over time, HLCs can potentially function as carbon-negative construction materials, locking away more CO_2 than is emitted during their production and use [Hirst, 2013]. In general, carbon emissions reduction could be achieved either through reducing the operational energy consumption or using low-carbon materials that have low embodied energy. HLCs possess both attributes as hemp stores carbon during its growth and has the ability to control the humidity and thermal climate in buildings to healthy levels using minimal energy demands [Elfordy et al., 2008]. Consequently, the carbon footprint of buildings using HLC in their envelope is reduced. However, further research into natural materials and new technologies is needed to address remaining challenges and form a solid foundation for future development.

While HLCs hold significant promise, their mechanical, thermal, and environmental performance depends heavily on the physical characteristics of the hemp shiv, particularly its particle size [Bourdot et al., 2017]. Hemp shiv is a porous, lightweight, and irregular bio-aggregate, and its properties can vary considerably depending on processing methods and particle grading [Hussain et al., 2019]. The size of the shiv particles influences binder adhesion, compaction behaviour, moisture transport, and composite porosity—all of which in turn affect the composite's strength, thermal conductivity, hygric balance, and long-term durability [Brzyski et al., 2020; Niyigena et

al., 2018]. Despite its importance, the role of hemp shiv particle size in determining HLC performance remains underexplored in academic and industrial literature. Finer particles may increase the reactive surface area, improving binder interaction and mechanical integrity, but could also reduce porosity and insulation value. Coarser shiv may enhance thermal insulation and reduce material density but may also compromise structural consistency and result in uneven compaction [Bourdot et al., 2017]. Therefore, a systematic evaluation of different shiv gradations is necessary to identify optimal particle size ranges for specific applications—whether for insulating infill panels, structural walls, or prefabricated elements.

In addition to material composition, manufacturing is another crucial factor affecting hemp-lime performance due to the material's anisotropic behaviour, which may yield different mechanical and thermal properties based on the direction in which the material is tested [Brzyski et al., 2021]. In real-world applications, hemp-lime composites are applied via spraying, casting on-site, or installing precast products (e.g., panels, blocks) [Williams et al., 2017]. Regardless of the method, the compaction level, the depth of the layer, and the direction of compaction can significantly affect the distribution of density, thermal conductivity, compressive and tensile strength, and capillary rise [Niyigena et al., 2018; Brzyski et al., 2021; Williams et al., 2017; Williams et al., 2017]. To overcome these limitations, it is necessary to implement alternative production methods, such as vibration-assisted molds and semi-automated formwork systems, which offer improved compaction uniformity, reduced human error, and the potential for prefabrication and modular construction. These technologies also enable more controlled experiments to isolate the effects of material variables on final composite performance.

The hemp plant stem is made of two main components: the outer layer representing the hemp fibres (commonly used for textiles and other applications) and the inner woody part representing the

hemp shivs (generally viewed as a low-value waste material). Due to their high porosity and low density, hemp fibres have been used as an insulation material with a range of thermal conductivity between 0.040-0.076 W/m K [Chen et al., 2014]. However, the process of separating the hemp fibres from the shivs is complicated, expensive, energy-demanding, and highly variable depending on the type of equipment and methods used in the decortication facilities [Tronet et al., 2016]. It also requires a viable market to ensure its success and profitability. However, due to a lack of standard specifications and test methods to determine hemp shiv purity and fibre content, limited research has been conducted to evaluate the effect of the fibre content ratio in the shiv on the produced HLC properties.

In order to achieve truly carbon-negative HLCs, innovations in casting and aggregate design must be matched by low-emission binder alternatives. Hydrated lime production is carbon-intensive primarily due to the high energy requirements and associated carbon dioxide (CO_2) emissions involved in the process. The production of 1 ton of hydrated lime generates around 1.2 tons of CO_2 [Simoni et al., 2022; Gutiérrez et al., 2012]. Hydrated lime production begins with the calcination of limestone, primarily composed of calcium carbonate ($CaCO_3$). This limestone is heated in a kiln at temperatures around 900–1000 °C to undergo calcination [Simoni et al., 2022], which decomposes the calcium carbonate into calcium oxide and carbon dioxide. The resulting calcium oxide is then subjected to a process known as slaking, where it is mixed with water to produce calcium hydroxide, commonly referred to as hydrated lime [Laveglia et al., 2022]. Another significant challenge facing conventional hydrated lime production is the depletion of natural resources. Extracting limestone, a non-renewable resource, through extensive quarrying leads to numerous environmental and ecological issues [Saleem & Ayalew, 2025]. These include the degradation of land and destruction of natural habitats, as quarrying removes vegetation and

topsoil, disrupting ecosystems and threatening biodiversity [Simoni et al., 2022; Saleem & Ayalew, 2025]. Additionally, mining activities generate substantial dust and noise, negatively impacting air quality and local communities. Quarrying can also interfere with groundwater systems, either by lowering the water table or introducing contaminants [Saleem & Ayalew, 2025; Cîrţînă & Tudorache, 2019]. Despite its abundance, the growing demand for lime in construction and industry places increasing pressure on limestone reserves, raising concerns about the long-term sustainability of this resource. Moreover, while the carbonation of lime in service can eventually reabsorb some of this CO_2, the net carbon balance of the binder remains a critical challenge for sustainability claims.

By integrating these areas, this research seeks to develop and evaluate next-generation HLCs that offer good environmental and thermal performance and scalability for modern construction applications. The holistic approach addresses key technical and ecological barriers to the broader adoption of bio-based materials and supports the transformation of the construction industry toward a more sustainable and regenerative future.

1.2. Research Scope and Objectives

Hemp-lime composites have captured significant attention in the construction industry due to their sustainability, availability, and excellent hygrothermal performance. However, their widespread adoption has been hindered by notable variability and inconsistent performance and the availability of raw material that leads to a higher embodied energy and cost. To overcome these challenges, the integration of a sustainable and locally available binder and a deeper comprehension of the material's performance are essential steps toward unlocking HLC's full potential and addressing its underutilization. This research introduces a promising method to produce hydrated lime through an electrical decarbonation process using different sources of $CaCO_3$. This research also presents

a novel approach to improve the uniformity and hygrothermal characteristics of HLC, aiming for reproducibility and consistency comparable to traditional insulation materials. This method consists of reducing hemp particle size and maximizing the hemp proportion while using vibration as a compaction method. The main objectives of this study are:

- To improve the consistency and repeatability of HLC performance by reducing the hemp shiv particle size and introducing vibration as a new compaction method for HLC. Traditional hemp-lime composites can suffer from inconsistency in density and insulation properties due to manual mixing and placement methods. This objective aims to systematically improve uniformity in the mixture and optimize mechanical and hygrothermal characteristics (e.g., thermal conductivity, moisture buffering, and compressive strength) so that HLC can rival or exceed the performance of conventional insulation materials.

- To investigate the effect of impurities in the form of hemp fibres on the mechanical and hygrothermal properties of HLC. This objective aims to evaluate how different proportions and lengths of hemp fibres influence the performance of hemp-lime composites. Varying fibre ratios can affect the density, internal structure, and bonding within the composite, which in turn impacts compressive strength. Similarly, fibre length can alter the capillary structure and connectivity within the material, potentially enhancing or hindering thermal insulation and moisture regulation. The study will systematically assess the mechanical behaviour and hygrothermal characteristics of HLC formulations with different fibre configurations to identify optimal combinations for structural and hygrothermal performance.

- To investigate the effectiveness of producing low-carbon hydrated lime from different inorganic (limestone) and organic (eggshells and mussel shells) $CaCO_3$ sources using electrolysis. This objective focuses on replacing the conventional fossil-fuel-based lime production method with an

electrically powered process. By applying controlled electrochemical reactions, the decarbonation of calcium carbonate can be achieved with significantly reduced carbon emissions. The study aims to test this method across multiple $CaCO_3$ sources, such as limestone and organic waste, to ensure broad applicability and sustainability.

- To integrate the proposed production methods to produce carbon-negative HLC with good mechanical and hygrothermal properties. All findings are combined into a unified production approach aimed at delivering a high-performance, carbon-negative building material. Ultimately, this work will demonstrate how synergy between low-emission lime production, optimized hemp usage, and vibration-assisted compaction can meet or exceed both sustainability and building performance benchmarks.

- To conduct a life cycle assessment (LCA) of the proposed lime production and HLC fabrication processes in a wall assembly. This objective evaluates the environmental impact of the entire production chain, including raw material sourcing, energy use during electrical decarbonation, hemp processing, and composite fabrication. The LCA will measure carbon emissions, aiming to validate the proposed system as a carbon-negative alternative to conventional insulation building materials.

1.3. Scientific publications

The outcomes of this thesis, published in peer-reviewed journals and conference proceedings, are as follows:

Journal papers:

1- Mahmood, O., Kavgic, M., & Noel, M. (2024). Hygrothermal and mechanical characterization of novel hemp-lime composites with enhanced consistency. *Construction and Building Materials*, *450*, 138720. https://doi.org/10.1016/j.conbuildmat.2024.138720

2- Ramírez-Amaya, D., Mahmood, O., Noël, M., Kavgic, M., Martinez, N. P., Troncoso P., F., Gazzano, V., Dreyse, P., Canales, R., & González, M. (2025). Assessing the Technical Suitability of Precipitated Materials from the Electrochemical Decarbonation of Limestones for Cement and Hydrated Lime Production: A Reproducibility Study Performed in Canada and Chile. *Journal of Materials in Civil Engineering, 37(9), 05025007*. https://doi.org/10.1061/JMCEE7.MTENG-19673

3- Mahmood, O.; Kavgic, M.; Noël, M. (2025). Electrochemical production of hydrated lime from organic waste: A feasibility study. *Journal of Materials in Civil Engineering*. https://doi.org/10.1061/JMCEE7.MTENG-21939

4- Mahmood, O., Kavgic, M., & Noel, M. Influence of Fibre Content and Length on the Hygrothermal and Mechanical Performance of Hemp-Lime Composites. *Energy and Buildings* (forwarded for review).

Conference papers:

1- Mahmood, O., Noël, M., & Kavgic, M. (2025). Physical and Mechanical Properties of Innovative Lime-Pozzolanic Hempcrete Binder. In S. Desjardins, G. J Poitras, M. S. Alam, & X. Sanchez-Castillo (Eds.), *Proceedings of the Canadian Society for Civil Engineering Annual Conference 2023, Volume 6* (pp. 67–75). Springer Nature Switzerland. https://doi.org/10.1007/978-3-031-61507-8_6

1.4. Outline of The Thesis

The thesis is divided into nine chapters, structured in a paper-based format as follows:

Chapter 1 presents a general context and research objectives.

Chapter 2 surveys the current state of knowledge on hemp-lime composite systems, performance-determining variables, sustainable lime production technologies such as electro-decarbonation, and identifies the gaps this research aims to address.

Chapter 3 outlines the general methodological approach adopted in the study.

Chapter 4 examines the influence of reduced hemp shiv particle size, increased hemp content, and the application of vibration techniques to standardize dry density on the mechanical, thermal, and moisture buffering properties of hemp-lime composites. It details the material composition, experimental methodology, and key findings. The content of this chapter is based on the journal article *"Hygrothermal and mechanical characterization of novel hemp-lime composites with enhanced consistency"* published in *Construction and Building Materials*.

Chapter 5 evaluates the role of hemp fibre content and length on key performance metrics of hemp-lime composites, including thermal and hygric properties as well as compressive strength. It includes an overview of the material mix designs, testing methods, and results. This chapter is adapted from the article that has been submitted in *Energy and Buildings*, titled *"Influence of Fiber Content and Length on the Hygrothermal and Mechanical Performance of Hemp-Lime Composites."*

Chapter 6 investigates the feasibility of applying the electro-decarbonation process to various limestone feedstocks for lime production, and assesses the suitability of the resulting precipitates as final hydrated lime products. It outlines the experimental setup, materials used, and key

findings. The chapter is based on the published article in the *Journal of Materials in Civil Engineering* titled *"Assessing the Technical Suitability of Precipitated Materials from the Electrochemical Decarbonation of Limestones for Cement and Hydrated Lime Production – A Reproducibility Study Performed in Canada and Chile."*

Chapter 7 evaluates the feasibility of producing hydrated lime from organic waste feedstocks—eggshells and mussel shells—using electrochemical decarbonation of $CaCO_3$. The study considers process efficiency, energy use, and product purity. Material preparation, methodology, and results are detailed, based on the published article *"Electrochemical Production of Hydrated Lime from Organic Waste: A Feasibility Study"* in the *Journal of Materials in Civil Engineering*.

Chapter 8 Examines the environmental performance of hemp-lime composites incorporating electro-decarbonation-derived lime, highlighting reductions in embodied carbon and energy use compared to conventional production methods. The chapter presents a comparative analysis of the life-cycle environmental impacts of HLCs made with conventional versus electro-decarbonation-derived lime, focusing on key indicators such as GHG emissions. In addition, the performance of HLCs is benchmarked against conventional insulation materials (low-density glass wool), providing a broader perspective on their relative environmental impacts. The study quantifies the carbon sequestration potential of the composites, the net greenhouse gas savings, and the broader sustainability implications of integrating this novel lime production method into HLC manufacturing. The findings highlight the potential for electro-decarbonation to support the development of truly carbon-negative construction materials and contribute meaningfully to decarbonization in the building sector. It is based on a paper that will be submitted to *Building and Environment* titled *"The Sustainability of Hemp-Lime Composites in Construction: A Comparative Life Cycle Analysis of External Wall."*

In conclusion, **Chapter 9** brings together the main insights from the research, acknowledges existing limitations, and proposes areas for continued study.

1.5. References

Amaducci, S., Scordia, D., Liu, F. H., Zhang, Q., Guo, H., Testa, G., & Cosentino, S. L. (2015). Key cultivation techniques for hemp in Europe and China. *Industrial Crops and Products*, *68*, 2–16. https://doi.org/10.1016/j.indcrop.2014.06.041

Bourdot, A., Moussa, T., Gacoin, A., Maalouf, C., Vazquez, P., Thomachot-Schneider, C., Bliard, C., Merabtine, A., Lachi, M., Douzane, O., Karaky, H., & Polidori, G. (2017). Characterization of a hemp-based agro-material: Influence of starch ratio and hemp shive size on physical, mechanical, and hygrothermal properties. Energy and Buildings, 153, 501–512. https://doi.org/10.1016/j.enbuild.2017.08.022

Brzyski, P., Gładecki, M., Rumińska, M., Pietrak, K., Kubiś, M., & Łapka, P. (2020). Influence of Hemp Shives Size on Hygro-Thermal and Mechanical Properties of a Hemp-Lime Composite. Materials, 13(23), 5383. https://doi.org/10.3390/ma13235383

Brzyski, P., Gleń, P., Gładecki, M., Rumińska, M., Suchorab, Z., & Łagód, G. (2021). Influence of the Direction of Mixture Compaction on the Selected Properties of a Hemp-Lime Composite. Materials, 14(16), 4629. https://doi.org/10.3390/ma14164629

Chen, T., Yao, S., Merlin, M., Mai, H., Qiu, Z., Hu, Y., Wang, B., Wang, C., & Jiang, H. (2014). Identification of Cannabis Fiber from the Astana Cemeteries, Xinjiang, China, with Reference to Its Unique Decorative Utilization. Economic Botany, 68(1), 59–66. https://doi.org/10.1007/s12231-014-9261-z

Cîrţînă, D., & Tudorache, A. (2019). ENVIRONMENTAL EFFECTS DUE TO THE TECHNOLOGICAL PROCESSES OF LIME PRODUCTION. Journal of Research and Innovation for Sustainable Society, 1(2), 44–51. https://doi.org/10.33727/JRISS.2019.2.6:44-51

Elfordy, S., Lucas, F., Tancret, F., Scudeller, Y., & Goudet, L. (2008). Mechanical and thermal properties of lime and hemp concrete (“hempcrete”) manufactured by a projection process. Construction and Building Materials, 22(10), 2116–2123. https://doi.org/10.1016/j.conbuildmat.2007.07.016

Goveremnt of Canada. (2020, November 19). Net-zero emissions by 2050. https://www.canada.ca/en/services/environment/weather/climatechange/climate-plan/net-zero-emissions-2050.html

Hirst, E. A. J. (2013). Characterisation Of Hemp-Lime As A Composite Building Material. [*Phd thesis*, University of Bath]. https://researchportal.bath.ac.uk/files/187944938/UnivBath_PhD_2013_E_Hirst.pdf

Hussain, A., Calabria-Holley, J., Lawrence, M., & Jiang, Y. (2019). Hygrothermal and mechanical characterisation of novel hemp shiv based thermal insulation composites. Construction and Building Materials, 212, 561–568. https://doi.org/10.1016/j.conbuildmat.2019.04.029

Ip, K., & Miller, A. (2012). Life cycle greenhouse gas emissions of hemp–lime wall constructions in the UK. *Resources, Conservation and Recycling*, *69*, 1–9. https://doi.org/10.1016/j.resconrec.2012.09.001

Laveglia, A., Sambataro, L., Ukrainczyk, N., De Belie, N., & Koenders, E. (2022). Hydrated lime life-cycle assessment: Current and future scenarios in four EU countries. Journal of Cleaner Production, 369, 133224. https://doi.org/10.1016/j.jclepro.2022.133224

Lawrence, M. (2015). Reducing the Environmental Impact of Construction by Using Renewable Materials. Journal of Renewable Materials, 3(3), 163–174. https://doi.org/10.7569/JRM.2015.634105

Niygena, C., Amziane, S., & Chateauneuf, A. (2018). Multicriteria analysis demonstrating the impact of shiv on the properties of hemp concrete. Construction and Building Materials, 160, 211–222. https://doi.org/10.1016/j.conbuildmat.2017.11.026

Pretot, S., Collet, F., & Garnier, C. (2014). Life cycle assessment of a hemp concrete wall: Impact of thickness and coating. *Building and Environment*, *72*, 223–231. https://doi.org/10.1016/j.buildenv.2013.11.010

Sagastume Gutiérrez, A., Van Caneghem, J., Cogollos Martínez, J. B., & Vandecasteele, C. (2012). Evaluation of the environmental performance of lime production in Cuba. Journal of Cleaner Production, 31, 126–136. https://doi.org/10.1016/j.jclepro.2012.02.035

Saleem, H. A., & Ayalew, A. T. (2025). Enhancing environmental sustainability and operational efficiency in a case study of limestone quarry in an arid climate. Scientific Reports, 15(1), 18884. https://doi.org/10.1038/s41598-025-01230-9

Simoni, M., Wilkes, M. D., Brown, S., Provis, J. L., Kinoshita, H., & Hanein, T. (2022). Decarbonising the lime industry: State-of-the-art. Renewable and Sustainable Energy Reviews, 168, 112765. https://doi.org/10.1016/j.rser.2022.112765

Stevulova, N., Cigasova, J., Estokova, A., Terpakova, E., Geffert, A., Kacik, F., Singovszka, E., & Holub, M. (2014). Properties Characterization of Chemically Modified Hemp Hurds. *Materials*, *7*(12), 8131–8150. https://doi.org/10.3390/ma7128131

Tronet, P., Lecompte, T., Picandet, V., & Baley, C. (2016). Study of lime hemp concrete (LHC) – Mix design, casting process and mechanical behaviour. Cement and Concrete Composites, 67, 60–72. https://doi.org/10.1016/j.cemconcomp.2015.12.004

Walker, R., & Pavía, S. (2014). Moisture transfer and thermal properties of hemp–lime concretes. *Construction and Building Materials*, *64*, 270–276. https://doi.org/10.1016/j.conbuildmat.2014.04.081

Williams, J., Lawrence, M., & Walker, P. (2017). The Influence of the Casting Process on the Internal Structure and Physical Properties of Hemp-Lime. Mater Struct, 50, 108. https://doi.org/10.1617/s11527-016-0976-4

Chapter 2 : Literature Review

2.1. Introduction

This chapter briefly summarizes available literature and empirical research concerning HLC and its constituents, with a specific emphasis on areas pertinent to the primary goals of this investigation. This includes aspects such as manufacturing methods, hemp shivs particle size, and hemp fibre content. Additionally, it will delve into literature related to the electrochemical decarbonation process as an alternative manufacturing method for hydrated lime. The findings from this review are anticipated to unveil research gaps requiring further investigation and clarification.

2.2. Hemp-Lime Composites

Hemp-lime composites have emerged as a promising lightweight bio-composite material. This material holds significant potential for enhancing energy efficiency, indoor environmental quality, and overall sustainability of buildings [Lawrence, 2015]. Notably, HLC is regarded as a low-carbon construction material due to the carbon sequestration properties of hemp, which compensate for GHG emissions produced during lime production. The growth of hemp plants facilitates CO_2 absorption, with the plant structure effectively integrating carbon within it [Lawrence, 2015]. Lime also absorbs CO_2 throughout its service life through a process known as carbonation. HLC is typically used as a non-load-bearing infill within structural frames in low- and mid-rise buildings, where it enhances hygrothermal regulation and supports passive climate control indoors [Collet & Pretot, 2014; Abdellatef et al., 2020]. It meets code compliance and facilitates simpler timber-frame construction [Magwood, 2016]. Additionally, due to similar thermal conductivity, HLCs and timber together help reduce thermal bridging [Stanwix & Sparrow, 2014; Jami et al., 2016].

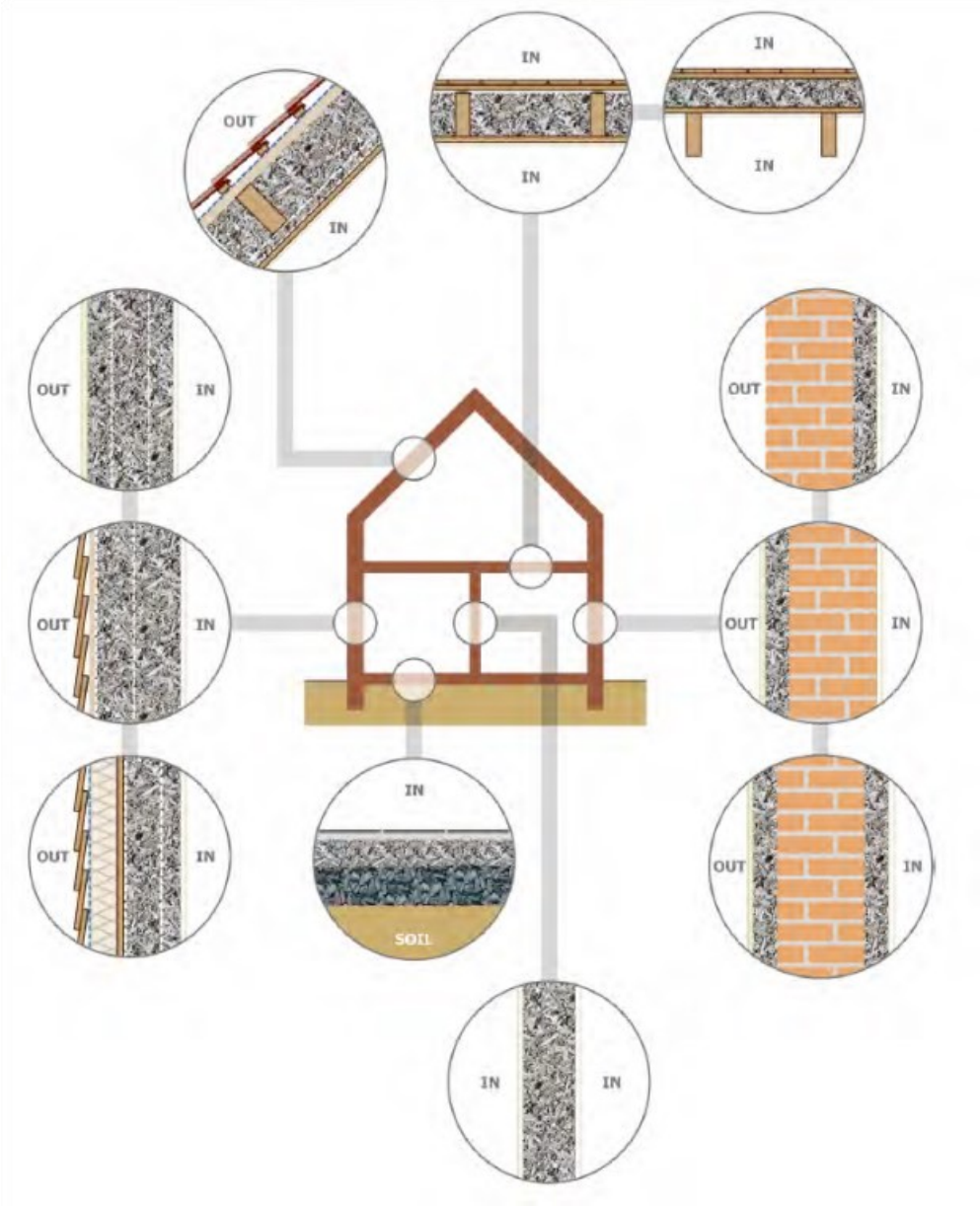

Figure 2.1 HLC walls surrounding a timber structure at different locations of the envelope [Kenneth & Miller, 2012].

Despite its potential, HLC remains underutilized in the construction sector, largely due to inconsistencies in their formulations and the absence of standardized mixes using widely available, locally sourced materials. For instance, in Canada, production costs and embodied energy can be significantly higher than in Europe because of the reliance on imported components [Magwood,

2016]. Advancing the use of innovative binders and deepening knowledge of hempcrete's performance are key to increasing its adoption.

2.3. HLC Manufacturing Methods

Manufacturing and casting methods are a crucial factor affecting HLC performance due to the material's anisotropic behaviour, which may yield different mechanical and thermal properties based on the direction in which the material is tested [Brzyski et al., 2021]. In real-world applications, HLC are applied via spraying, casting on-site, or installing precast products (e.g., panels, blocks) [Williams et al., 2016]. Regardless of the method, the compaction level, the depth of the layer, and the direction of compaction can significantly affect the distribution of density, thermal conductivity, compressive and tensile strength, and capillary rise [Brzyski et al., 2021; Williams et al., 2016; Nguyen et al., 2009]. Nguyen et al. [Nguyen et al., 2009] investigated the effect of compaction on the mechanical and thermal properties of hemp-lime composites for different densities ranging from 320 kg/m³ to 810 kg/m³ and binder types. The study considered four different parameters including initial density (684, 899, and 963 kg/m^3), binder to hemp (B/H) ratio (1.11, 2.15, and 3.48), water to binder ratio (0.55, 0.86, and 0.93), and three levels of compaction (low, medium, and high). Samples were tested for thermal conductivity and compressive strength. To evaluate the anisotropic properties of the HLC, samples were tested in two directions: parallel (λ1 and λ4) and perpendicular (λ2 and λ3) to the compaction direction as shown in Figure 2.2. The study showed that thermal conductivity was in the range of 0.071-0.185 W/m K and it has a linear relationship with density. The study also concluded that the thermal conductivity tested perpendicular to compaction was 50% higher than those tested in a direction parallel to compaction, Figure 2.3. This behaviour was attributed to the friction of the material along the inner surface of the mold as shown in Figure 2.4-a. The study reported a variation in the

HLC dry density with a coefficient of variation up to 14.89%. A variation in the dry density of the samples cut from different heights was also noticed and the gradient of the density was very low in the upper part and more significant at the lower part of the specimen as shown in Figure 2.4-b. Finally, the study reported an improvement in the compressive strength of the HLC when the compaction level was increased, ranging from 0.16 to 1.7 MPa.

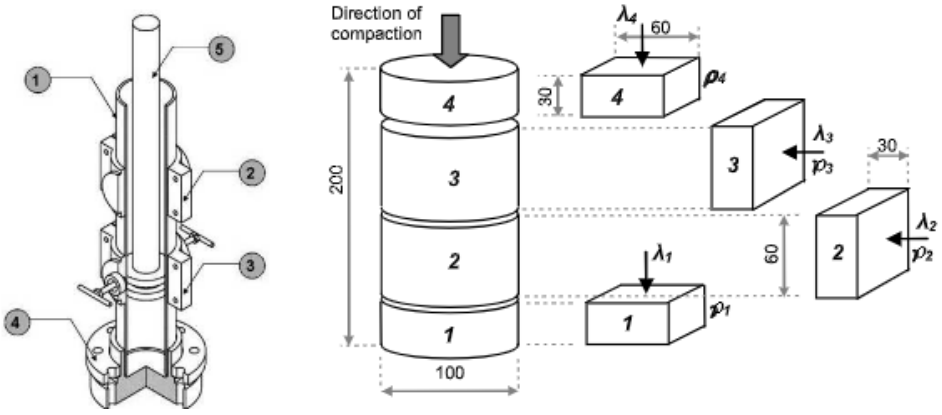

Figure 2.2 Compaction setup and location of HLC samples cut from cast cylindrical specimen [Nguyen et al., 2009].

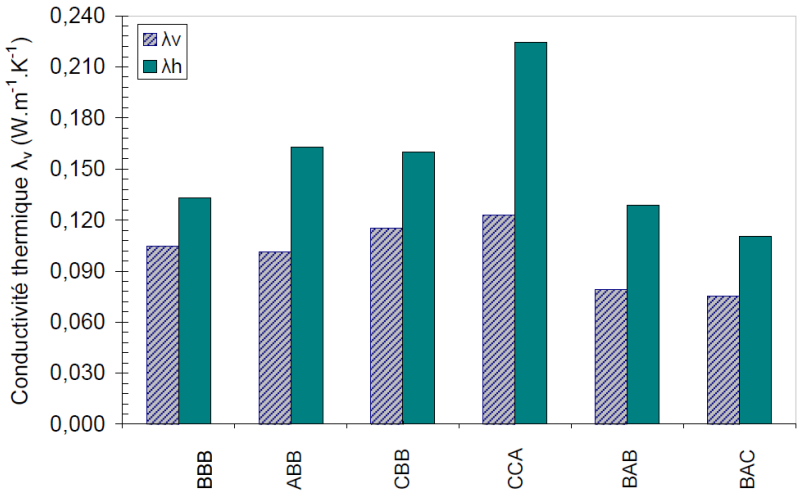

Figure 2.3 Comparison between vertical and horizontal thermal conductivity in the case of hemp concrete [Nguyen et al., 2009].

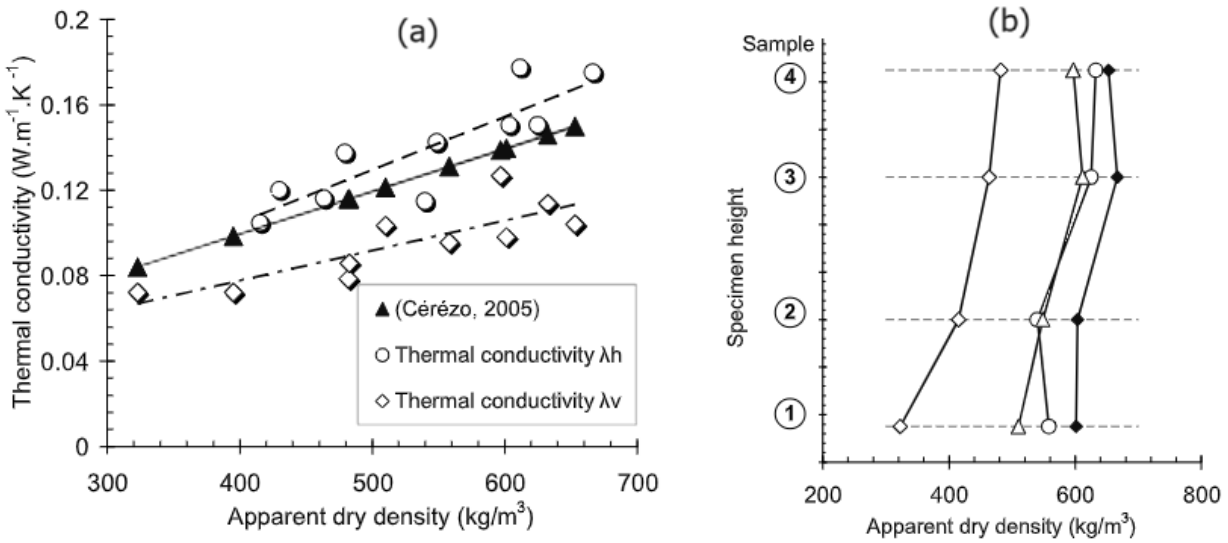

Figure 2.4 Effect of dry density on thermal conductivity (a), density according to height of specimen (b) [Nguyen et al., 2009].

Brzyski et al. [Brzyski et al., 2021] also studied the effect of compaction direction on hemp-lime composites' thermal and mechanical properties for two different hemp shiv sizes averaging 2.7 mm and 8.4 mm. Compaction was done by hand using a wooden compacter with a cross section of 30 mm x 30 mm. The samples were first cast in a 250 mm x 250 mm x 600 mm mold to produce an average dry density of 380 kg/m^3 and then specimens were cut to produce two sets of samples: parallel and perpendicular to compaction direction as shown in Figure 2.5.

The study reported a variation in the thermal conductivity values for samples with parallel (0.094 and 0.087 W/m K) and perpendicular (0.105 and 0.101 W/m K) heat flow to the compaction direction. The compressive strength for the 8.4 mm shivs was about 20% higher than the 2.7 mm shivs. The stress-strain behaviour was also different for the 2.7 mm shivs from the 8.4 mm shivs, characterized by a clear peak corresponding to the maximum destructive force as shown in Figure 2.6. Additionally, the water absorption coefficient in the parallel direction was reported to be 17.6%

and 18.4% higher than the coefficient determined in the perpendicular direction for 2.7 and 8.4-mm shivs, respectively.

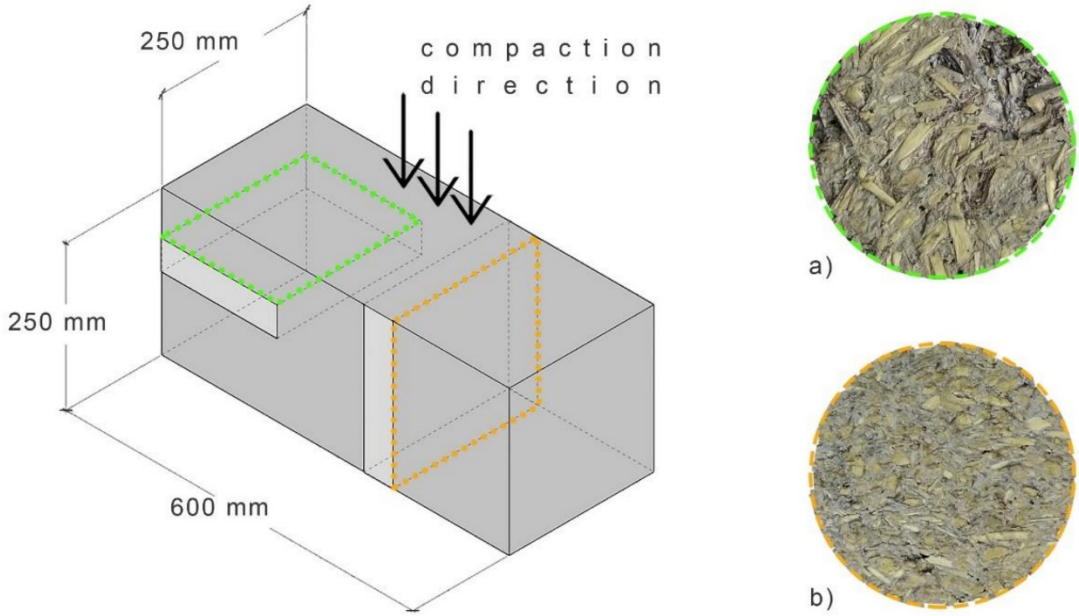

Figure 2.5 The method of cutting out samples, (a) perpendicular ⊥ (b) parallel II [Brzyski et al., 2021].

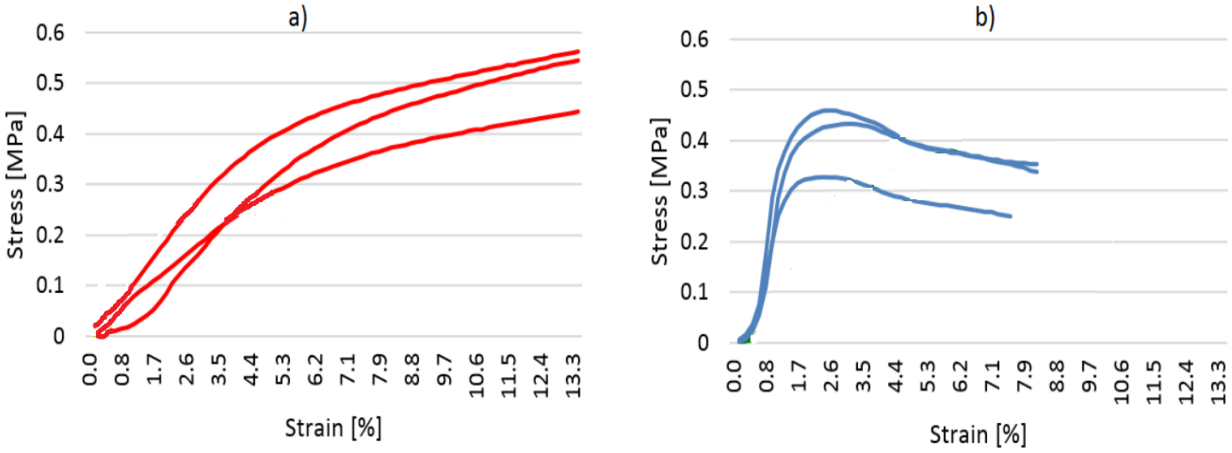

Figure 2.6 Stress-strain relationship, (a) 8.4 mm shivs , (b) 2.7 mm shivs [Brzyski et al., 2021].

Williams et al. [Williams et al., 2017] studied the effect of the casting process on the mechanical and thermal properties of three hemp-lime layers, 25, 50, and 150 mm, and three compaction levels, 30, 40, and 60% of volumetric decrease with two sets of tests, one parallel to compaction

and one perpendicular to it. The study produced samples using B/H ratio of 2.25:1.0 to produce samples with a dry density ranging between 304 to 379 kg/m^3. The study showed that the layer thickness did not significantly impact the HLC properties. In contrast, an increase in the compaction level from 30 to 60% increased thermal conductivity by 16.5% and 8.4% for perpendicular and parallel directions, respectively. The results also showed a linear relationship between thermal conductivity and compaction level as shown in Figure 2.7.

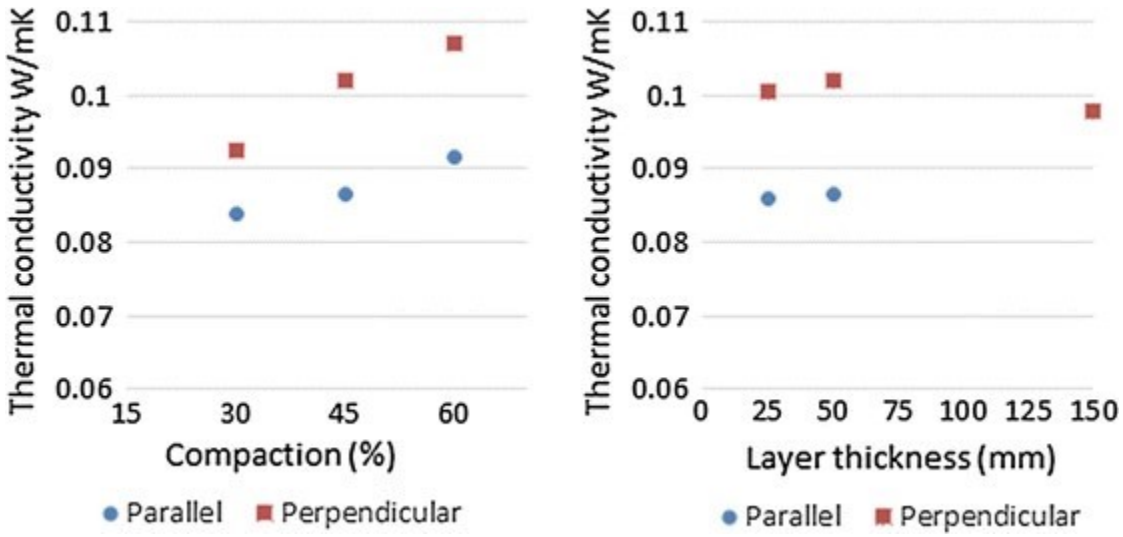

Figure 2.7 Thermal conductivity at (a) different compaction levels and (b) different layer thicknesses [Williams at al., 2017].

Furthermore, Holcroft & Shea [Holcroft & Shea, 2015] investigated how different compaction levels affect the moisture buffering capacity of HLC. Their study used a 1:1.65 H/B ratio creating samples with densities ranging from 210 kg/m³ to 333 kg/m³. These densities were achieved by compacting the samples with weights varying from 1 kg to 10 kg. The study found that the sample with the lowest density (210 kg/m^3) had the highest moisture buffering value (3.06 g/m² RH). This value decreased by just 6% when the density increased to 278 kg/m³ but fell by 39% at the highest 333 kg/m³ density.

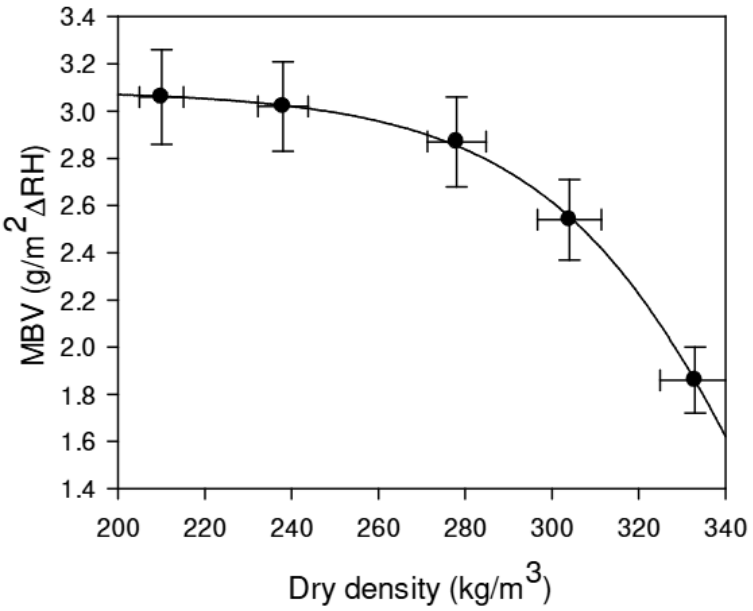

Figure 2.8 Relationship between dry density and moisture buffer value [Holcroft & Shea, 2015].

Additionally, Collet et al. evaluated the effect of the manufacturing method on the hygric behaviour of HLC [Collet et al., 2013]. The study considered three types of HLC for wall construction, where each type varied in composition and manufacturing technique: precast, sprayed on, and molded, with average produced densities of 460, 430, and 430 kg/m^3, respectively. The study showed that the moisture buffering values were 1.94, 2.15, and 2.15 gm/m^2 RH, corresponding to precast, sprayed-on, and molded samples. The study also indicated a negative correlation between HLC density and moisture buffering value.

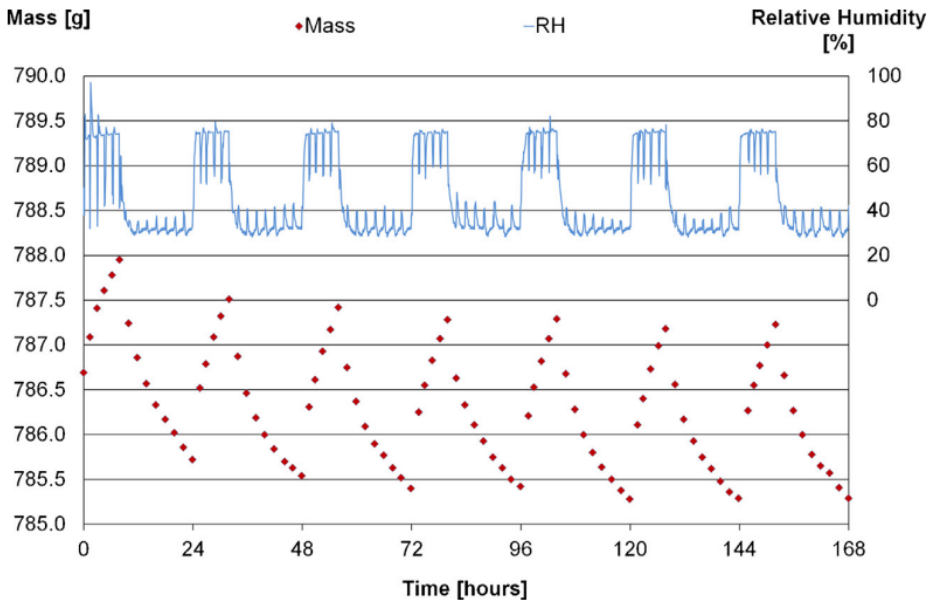

Figure 2.9 Moisture uptake and release for the specimen and monitored relative humidity [Collet et al., 2013].

2.4. Hemp Shivs Size

Analogous to other bio-based construction materials with high porosity, HLC are known to be sensitive to the properties of natural lignocellulosic constituencies (shiv/hurd) which affect their performance [Sáez-Pérez et al., 2020; Niyigena et al., 2016]. In this respect, hemp shiv exhibits highly variable granulations and sizes depending on the decortication process and the industrial hemp variety [Brzyski et al., 2020]. Simultaneously, the distribution of hemp shiv particle sizes has a crucial effect on the hygrothermal and mechanical properties of the resulting composite [Bourdot et al., 2017]. Several studies have investigated the impact of shiv particle size on the hygrothermal and mechanical properties of hemp-lime composites. While they all reported the relevance of this impact, their findings may seem discrepant. For example, Bourdot et al. [Bourdot et al., 2017] evaluated hygrothermal and mechanical properties of lightweight (126-143 kg/m³) hemp composites made of two shiv sizes (0-5 mm and 0-20 mm) using two proportions with 0-20 mm particles as dominant share (15%-85% and 30%-70%), as shown in Figure 2.10.

The findings showed a 10.5% increase in compressive strength and an 11.5% decrease in thermal conductivity when the fine particles (0-5 mm) ratio increased from 15% to 30%. In contrast, shiv size had a lesser impact on the specific heat and moisture buffer capacities of the HLC and shiv geometry did not significantly affect the other properties.

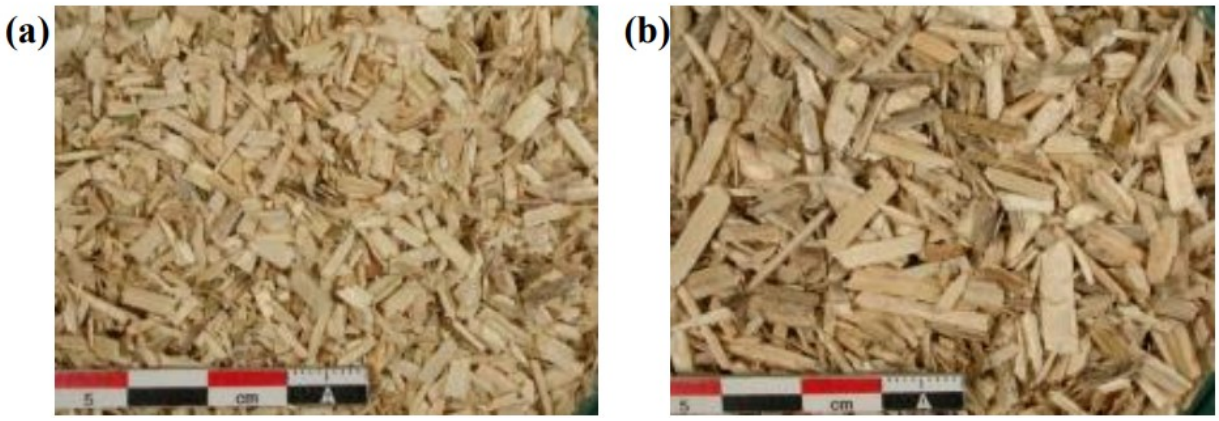

Figure 2.10 Photographs of (a) 0-5 mm hemp shive and (b) 0-20 mm hemp shive [Bourdot et al., 2017].

Brzyski et al. [Brzyski et al., 2020] investigated the impact of two hemp shiv sizes with an average length of 2.74 mm (FHS) and 8.4 mm (THS), as shown in Figure 2.11, on the mechanical and hygrothermal behaviour of HLC with an average density of 382 kg/m³ and 377 kg/m³, respectively. The results suggest that the samples with 8.4 mm shiv exhibited a higher compressive strength of around 0.51 MPa than those with 2.74 mm particles, which had a compressive strength of approximately 0.40 MPa. Additionally, samples made with larger shivs had higher capillary uptake of 8.82 kg/m² $h^{1/2}$ compared to 7.27 kg/m² $h^{1/2}$ for small shivs. On the other hand, small size shivs had an average thermal conductivity of 0.105 while the large shivs where 0.099 W/m K.

Figure 2.11 Hemp shives used in the investigation: (a) fine shives and (b) thick shives [Brzyski et al., 2020].

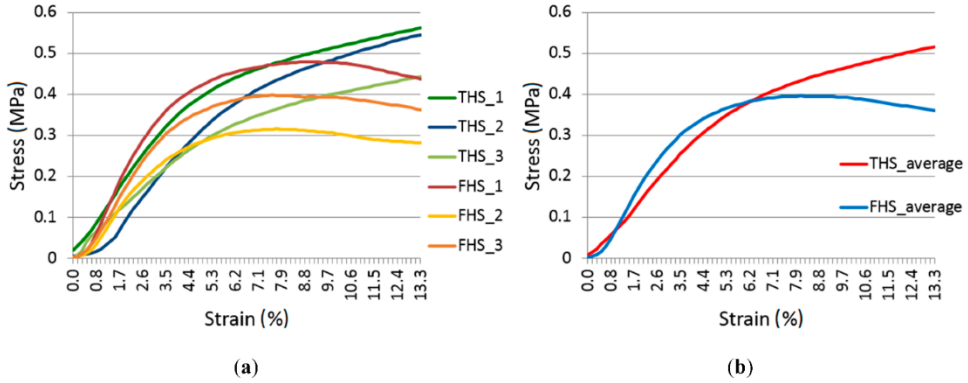

Figure 2.12 Stress–strain relationship: (a) all samples and (b) average values [Brzyski et al., 2020].

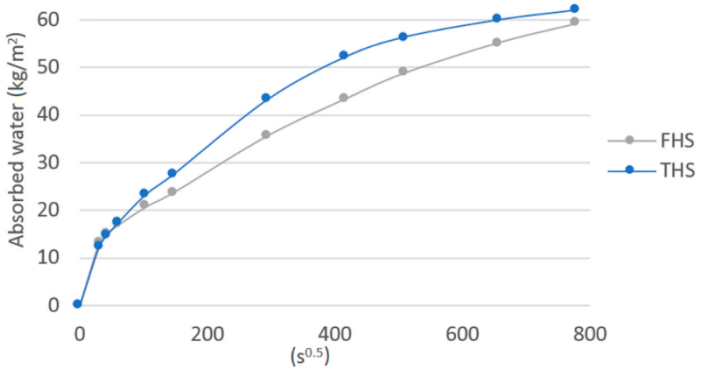

Figure 2.13 Capillary uptake of tested composites [Brzyski et al., 2020] .

Another study by Arnaud & Gourlay [Arnaud & Gourlay, 2012] explored the effect of using hemp shivs of 3.1 mm, 7.6 mm, and 8.9 mm, conforming to dry densities of 390 kg/m³, 400 kg/m³, and 430 kg/m³, respectively, on the mechanical properties of hemp-lime composites. This study concluded that large shivs showed a higher compressive strength when tested at 28 days by about 52.4% compared with small shivs. However, the study also concluded that the samples with a smaller shiv size produced higher strength by 30.5% to 50% than those with larger and medium-sized shivs after 4 months, respectively, as fine shivs were better wrapped with binder particles.

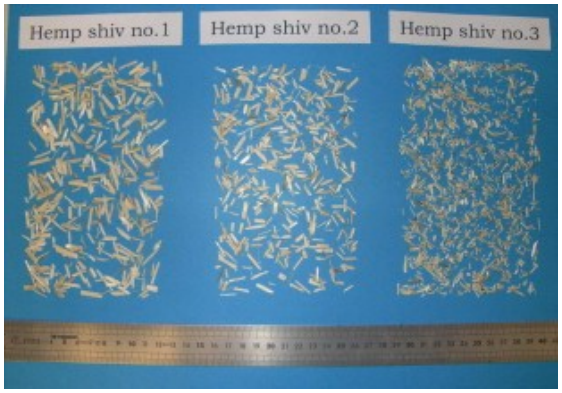

Figure 2.14 Hemp shiv in bulk [Arnaud & Gourlay, 2012].

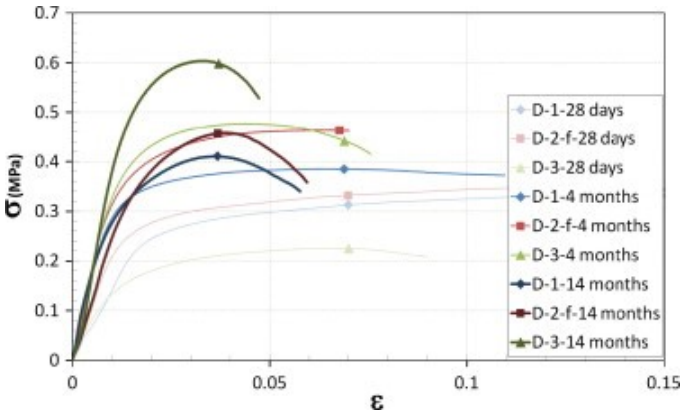

Figure 2.15 Compressive strength tests for increasing ages on hemp concretes based on different shiv [Arnaud & Gourlay, 2012] .

Stevulova et al. [Stevulova et al., 2012] studied the mechanical and thermal properties of hemp-lime composites using three different shiv sizes of 7.3 mm, 27.7 mm, and 33.7 mm, corresponding to 1,150 kg/m³, 1,070 kg/m³, and 1,040 kg/m³ densities. While their study concluded an increase in compressive strength from 2.73 MPa to 5.20 MPa when particle size reduced from 33.7 mm to 7.3 mm, thermal conductivity values were around 0.11 W/m K regardless of the particle size.

2.5. Hemp Fibre Content

The stem of the hemp plant consists of two primary components: the outer layer, which contains the hemp fibres, and the inner woody core, known as hemp shivs. Hemp fibres, characterized by their high porosity and low density, are commonly used as insulation materials, with thermal conductivity values ranging from 0.040 to 0.076 W/m·K [Chen et al., 2014]. However, separating these fibres from the shivs is a complex, costly, and energy-intensive process. The efficiency and quality of separation can vary significantly depending on the decortication equipment and techniques employed [de Bruijn et al., 2009]. Additionally, the economic viability of fibre production depends heavily on the existence of a stable and profitable market. Due to a lack of standard specifications and test methods to determine hemp shiv purity and fibre content, limited research has been conducted to evaluate the effect of the fibre content ratio in the shiv on the produced HLC properties.

de Bruijn et al. [de Bruijn et al., 2009] determined the mechanical properties of HLC made of a lime binder and the entire fragmented hemp stalk with 1:3 B/H volumetric ratio producing HLC with dry density ranging between 587-733 kg/m^3. The composition of the hemp was 35% fibres, 61% shivs, and 4% dust. However, it is worth mentioning that no standard or methodology was reported to determine the fibre content in the hemp shives. The study concluded that the compressive strength ranged from 0.15-0.83 MPa, tensile strength from 0.021-0.111 MPa, and

0.15 kg/m^2 S^{½} water sorption coefficient. The study concluded that no clear difference was observed in terms of mechanical behaviour between samples containing fibres and samples with pure shivs reported from previous literature.

Similarly, Nguyen [Nguyen, 2014] investigated the effect of hemp fibre, along with other factors, on the compressive strength and the thermal conductivity of HLC. However, the study did not report the fibre content in the hemp shives. Three hemp-to-binder mass ratios were used, 1:1.11, 1:2.15, and 1:3.48, to produce samples at different densities ranging from 440-730 kg/m^3. No significant difference was reported as samples with pure shiv had a compressive strength ranging between 0.96-2.97 MPa, while samples containing hemp fibre had a compressive strength between 0.95-3.10 MPa. Additionally, samples incorporating hemp fibres exhibited thermal conductivities between 0.066 and 0.099 W/m·K, demonstrating lower values compared to those composed solely of hemp shives.

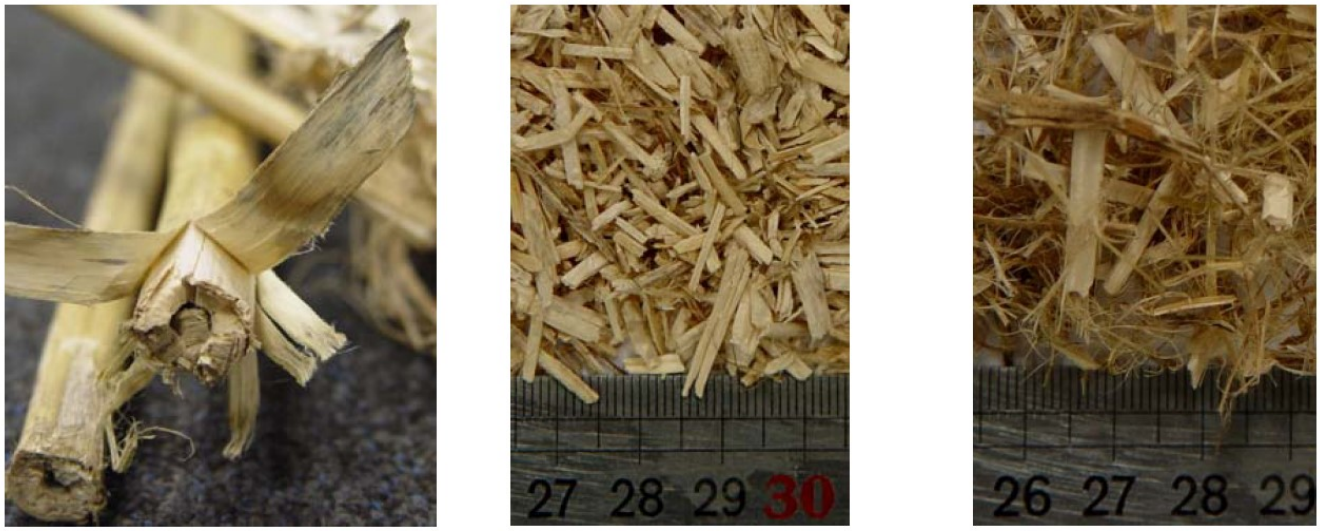

(a) (b) (c)

Figure 2.16 The aggregates studied a) Hemp stem, b) Pure hemp shiv , c) Fibred hemp shiv [Nguyen, 2014] .

Another study by Nguyen et al. [Nguyen et al., 2009] assessed the influence of compactness and hemp shiv characteristics on the mechanical performance of HLC, comparing pure hurd chips with a finer mixture of chips and fibres across lime-to-binder ratios of 1.11–2.32. Contrary to previous studies, the results indicated that samples containing hemp fibres exhibited lower compressive strength compared to those containing only pure hemp shives. Specifically, fibre-reinforced HLC samples displayed reductions in compressive strength ranging from 25.12% to 44.44%, accompanied by an elastic modulus approximately 2.5 times lower. Additionally, these samples exhibited substantial deformation (exceeding 50%) without failure. The observed behaviour was attributed to the inherent tensile strength of hemp fibres (~800 MPa) combined with their smooth surface texture, resulting in reduced shear resistance at the binder-fibre interface.

2.6. Electrochemical Decarbonation Process

Another important constituent of HLC is the binder, which is responsible for creating a connective matrix between the hemp shivs. The mechanical and thermal properties of the composite are strongly dependent on the B/H ratio. When using high binder content in the mix, the hemp particles are enclosed by a continuous binder matrix and the HLC will possess good compressive strength and high thermal conductivity. Conversely, when low binder content is used, the HLC will have a low thermal conductivity close to that of pure hemp and marginal strength. Between those two extremes, the HLC properties are transitional between the hemp and binder properties [Walker & Pavía, 2010]. Therefore, based on the application of the HLC with regard to thermal insulation and strength, a tradeoff between the hemp and binder content in the mix will be adopted.

The literature review shows that HLC can be made with a broad range of binders in varying relative proportions. Hydrated lime has been the most used binder in plant-based building materials. The use of hydrated lime in the formulation offers several advantages. First, it has a high pH, making

it suitable for preventing biological corrosion development when used with organic materials [Brzyski et al., 2020]. Second, lime's large surface area due to its fine particle size and ability to regulate the pH levels within the mixture [Walker & Pavía, 2010] promotes optimal conditions for forming stable mineral bonds between hemp shiv and lime, thus enhancing the resulting material's cohesion and strength. Third, it aids in carbonation, whereby carbon dioxide from the atmosphere reacts with lime during curing, forming calcium carbonate and effectively sequestering carbon, enhancing the material's sustainability and durability. Nevertheless, because hydrated lime gains strength through slow carbonation progress, the binder formulation can be enriched using different pozzolanic and cementitious materials such as metakaolin, fly ash, natural pozzolans, and slag. These materials are used due to their fast setting, high reactivity, and lower embodied energy to reduce CO_2 emissions [Abdellatef et al., 2020; Walker & Pavía 2010].

Hydrated lime ($Ca(OH)_2$) is produced from limestone after being crushed, milled, and sieved until the desired grain size is achieved. The next stage after limestone preparation is the decomposition of calcium carbonate into calcium oxide (quicklime) and carbon dioxide under high temperature in a process called calcination [Stork et al., 2014]. Then quicklime is carefully mixed with water (approximately 1% of quicklime) to yield hydrated lime. Equations 2.1-2.2 [Laveglia et al., 2022] describe the calcination reaction and the hydration reaction:

$$CaCO_{3(s)} + \text{Heat} \xrightarrow{\text{heat}} CO_{2(g)} + CaO_{(s)} \tag{2.1}$$

$$CaO_{(s)} + H_2O_{(l)} \rightarrow Ca(OH)_{2(s)} \tag{2.2}$$

Several strategies have been considered to address the emissions resulting from the calcination process such as carbon capture and storage technologies (e.g., amine scrubbing) [Costa & Ribeiro, 2020], or alternative raw materials other than limestone (e.g., construction and demolition wastes)

[Costa & Ribeiro, 2020; Abdul-Wahab et al., 2020]. However, those strategies have several barriers for their widespread adoption (e.g., cost-effectiveness, performance, policy, and availability issues) [Benhelal et al., 2021]. In 2020, Ellis et al. [Ellis et al., 2020] reported a promising method to directly target the CO_2 emission related to limestone calcination through electrochemical decarbonation (ED) of $CaCO_3$. ED employs a water electrolysis cell to decompose $CaCO_3$ at room temperature and precipitate $Ca(OH)_2$ while emitting two gas streams: hydrogen, and a mixture of oxygen and CO_2 in suitable concentrations to favour the implementation of carbon capture and storage technologies as shown in Figure 2.17. While the conventional limestone calcination process emits CO_2 at a concentration of about 25% alongside dust and other gases like NO_x and SO_x [Micari et al., 2021], which can interfere with the effectiveness of carbon capture and storage technologies [Kenneth & Miller, 2012], the ED process stands out for its significantly higher CO_2 concentration of around 67% [Barker et al., 2009]. This elevated concentration offers advantages in reducing the energy penalty associated with CCS implementation and enhancing overall efficiency. Additionally, the green hydrogen (H_2) produced in the cathode chamber of the electrolysis cell presents a valuable energy source with diverse industrial applications, including potential use in providing heat and electricity for the production process. The ED cell's deposited material (DM) comprised mainly of $Ca(OH)_2$ can be considered as an alternative source of hydrated lime as shown in Equation 2.3 [Ramirez-Amaya et al., 2023].

$$2CaCO_{3(s)} + 4H_2O_{(l)} \xrightarrow{ED} 2Ca(OH)_{2(s)} + 2H_{2(g)} + O_{2(g)} + 2CO_{2(g)} \quad (2.3)$$

Ellis et al. [Ellis et al., 2020] showed that the DMs obtained from ED of a high-purity (>99.0%) $CaCO_3$ can serve as an intermediate material for the synthesis of Alite (Ca_3SiO_2), the primary hydraulic clinker phase crucial for cement performance [Mehta & Monteiro, 2006]. Several laboratory H-cell reactors were assembled, featuring platinum electrodes as depicted in Figure

2.18. These reactors utilized an electrolyte comprising 1 M $NaNO_3$ in distilled water, supplemented with a few drops of universal pH indicator. Within the anode chamber, $CaCO_3$ powder was introduced, with a porous separator separating the chambers. The cells operated under potentiostatic conditions, maintaining a cell voltage of 2.5 V for about 12 hours. X-ray diffraction (XRD) analysis confirmed that the precipitate material primarily consisted of $Ca(OH)_2$, with about 6% presence of $CaCO_3$ and Brunauer–Emmett–Teller (BET) analysis showed that the precipitate has a specific surface area of 0.8 m^2/g.

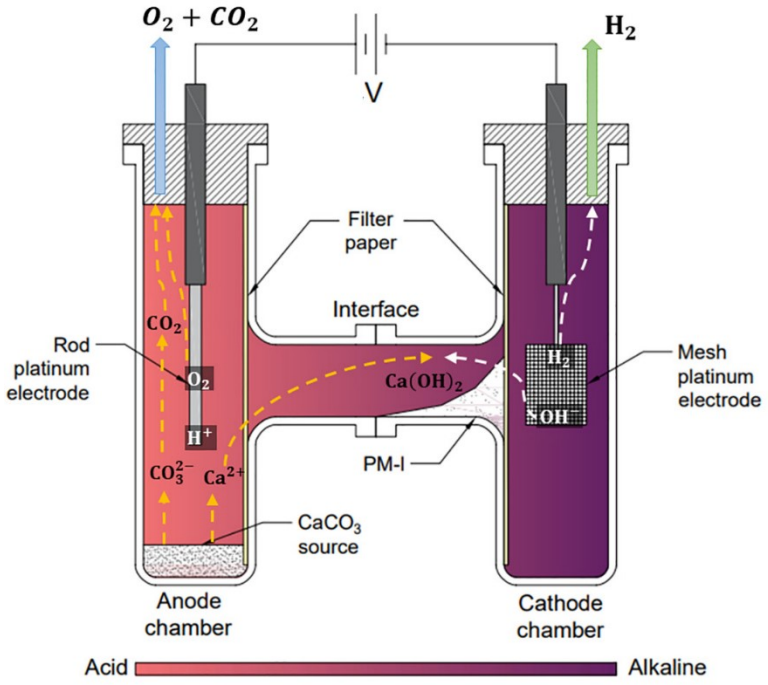

Figure 2.17 Schematic of electrolyzer-based decarbonation cell [Ramirez-Amaya et al., 2023].

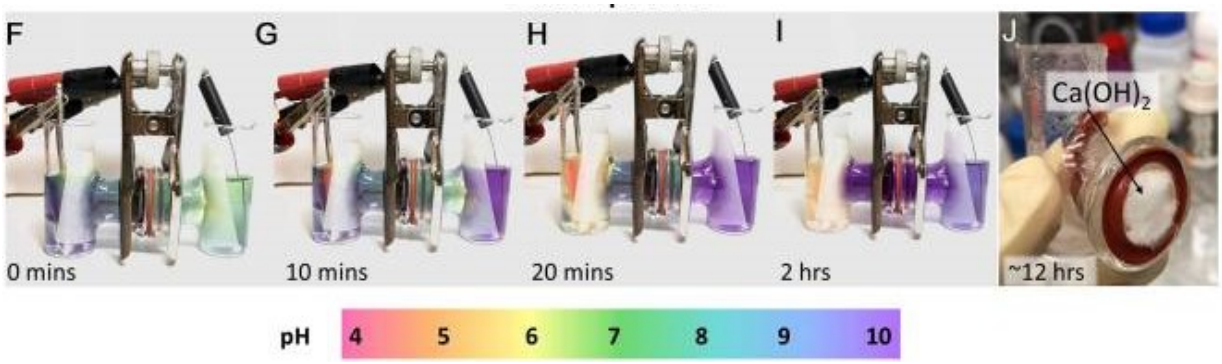

Figure 2.18 Time-lapse images of decarbonation H-cells [Ellis et al., 2020].

Another study by Ramirez-Amaya et al. [Ramirez-Amaya et al., 2023] conducted ED on three different limestone sources L-84, L-74, and L-68 (with $CaCO_3$ content of 84, 74, and 68%) and compared the ED efficiency, CaO recovery, and energy consumption during the electrolysis. H-cell reactors as shown in Figure 2.19 were used to perform the ED using 1M $NaNO_3$ in distilled water as the electrolytic solution. In each ED test, a sample of 0.70 ± 0.01 g of powder material from the $CaCO_3$ source was introduced in the anode chamber, then a constant direct current with a voltage of 9.0 V was applied for a continuous cycle of 5 hours. The study concluded that the efficiency and the energy consumption of the ED were (20, 18.5, and 25%) and (19.95, 22.5, and 22.5 kJ/gm) for the limestone samples L-84, L74, and L-68, respectively. It also concluded that although limestone is largely composed of two carbonate minerals, calcite ($CaCO_3$) and dolomite ($CaMg(CO_3)_2$), most natural limestone sources are not pure carbonates and include other components that can affect the performance of the ED process.

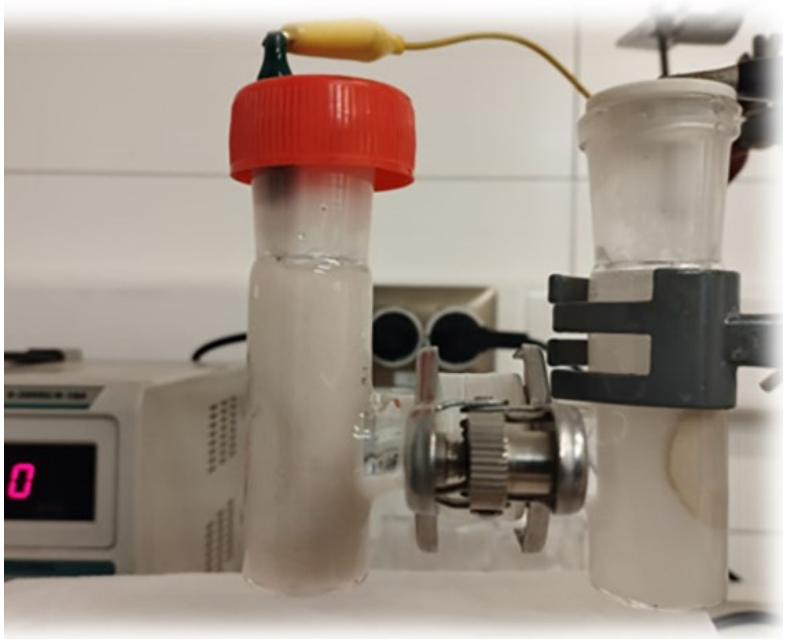

Figure 2.19 H-cell reactor used to conduct the ED process 3 [Ramirez-Amaya et al., 2023].

In another study, Martínez et al. [Martínez et al., 2024] detailed the development of an affordable electrochemical reactor and the optimization parameters necessary for producing high-purity DMs. The parameters studied in this work were: concentration of supporting electrolyte (i.e., $NaNO_3$, 1.0 M and 3.0 M), working potential (i.e., 9.0 and 12.0 V), mass of high purity $CaCO_3$ or limestone (i.e., 8.0 and 16.0 g) and time of electrolysis (i.e., 16 and 23 h). The research concluded that a DMs purity of approximately 95% could be attained by utilizing specific conditions of 23 hours for operation time, 9V for applied potential, and 3M for electrolyte concentration.

Another promising approach to reduce the environmental impact of hydrated lime production involves using alternative raw materials and by-products as feedstock. An increasing world population, urbanization, and income engender higher food production [Consoli et al., 2020]. Poultry is an example of a fast-growing industry worldwide for meat and eggs. Even though China dominates the world's egg market, Canada's egg industry is dynamic, constantly increasing annual

production rates [FAO, 2013]. Additionally, in Canada, mussel shells are the primary type of farmed shellfish, accounting for 14% of the total volume [Government of Canada, 2016]. While an increasing market is economically appealing, growing food production induces higher waste, where the waste management system is not necessarily optimized. Consequently, landfills are the most common option for eggs or mussels' wastes, potentially causing environmental and health issues [Eziefula et al., 2018; Kamkum et al., 2015; Kanani et al., 2020; Mo et al., 2018; Waheed et al., 2020]. A solution to reduce landfills and decrease lime's carbon footprint is valorizing the food industry by-products. Eggshells, which account for around 10% of the egg's total weight, are mainly comprised of $CaCO_3$ [Hincke et al., 2011]. Literature reviews on eggshell valorization present various uses, such as food supplements for animals and humans, medicine, agriculture, water and soil decontamination, or a catalyst for bioethanol production [Waheed et al., 2020; Hart, 2020; Oliveira, et al., 2013]. Because of their high $CaCO_3$ content, several studies have explored using eggshells in lime, cement, and concrete production as partial replacement, filler, or aggregates [Chong et al., 2020; Hamada et al., 2020]. In their investigation, Consoli and colleagues [Consoli et al., 2020] analyzed the feasibility of deriving quicklime and hydrated lime from eggshell by-products for soil stabilization. The production process involved the calcination of eggshells at 1,000°C. The study demonstrated that both lime variants exhibited excellent physical, mineralogical, and chemical attributes, making them viable alternatives to traditional pozzolanic materials for soil stabilization. Another study by Ferraz et. al. [Ferraz et al., 2018] investigated the use of chicken eggshell waste as an alternative source for producing calcitic lime. The eggshells, collected from an industrial supplier, were analyzed for their mineralogical, chemical, and thermal properties, then calcined at 1000 °C. The resulting calcium oxide was tested for reactivity in wet slaking and compared to that produced from commercial limestone. Both materials fell under the

highest reactivity class, but eggshell-derived lime showed slower reaction times due to larger, smoother particles and lower specific surface area. The study also assessed the industrial, environmental, and economic feasibility of this approach, concluding that eggshell waste could potentially replace up to 2.6% of limestone use in a Portuguese lime factory, contributing to waste valorization and resource sustainability. Similarly to eggshells, seashells are excellent sources of $CaCO_3$, typically containing 95-97% of this compound. This high calcium carbonate content makes them valuable for various applications [Buasri et al., 2013; Her et al., 2021]. Buasri et al. [[Buasri et al., 2013] explored the utilization of mussel, cockle, and scallop shells to produce CaO catalysts intended for biodiesel production. The catalysts were prepared through calcination at temperatures of 700 to 1,000°C for 4 hours. The study demonstrated that the CaO catalysts derived from these shell wastes exhibited notable reusability and possessed significant potential for catalyzing the transesterification of palm oil with methanol in biodiesel synthesis.

2.7. Research Gaps

In the last decade, many studies have been conducted to understand hemp-lime composites' properties and performance. While hemp-lime composites demonstrate promising properties such as thermal insulation and carbon sequestration, they face several notable gaps that warrant further investigation. As a result of the review of literature the following gaps in research have been identified:

- Research into HLC has progressed significantly over the past decade. However, several critical areas remain underexplored and require further investigation. These include: i) enhancing the consistency of produced HLC, as current practices yield significant variability in densities. This variability introduces fluctuations and uncertainties in HLC performance, given the strong correlation between density and mechanical as well as hydrothermal properties. ii) Limited

research has addressed the identification and comprehensive understanding of how impurities in hemp shivs, specifically in the form of hemp fibres, influence HLC properties. Understanding this impact could lead to cost reductions, lower environmental impact associated with hemp shiv production, and potentially eliminate the need for fibre separation processes, allowing for the utilization of the entire fragmented hemp stalk.

- While the ED method holds promise for reducing carbon emissions in hydrated lime production, several gaps remain to be addressed for assessing its viability as a large-scale industrial process. Firstly, previous studies have mainly focused on the potential use of the ED process as an intermediate step within the chain of cement production. No studies have specifically focused on the chemical and physical suitability of precipitated materials obtained from the ED process as a final hydrated lime product. Furthermore, the potential use of alternative local sources of $CaCO_3$ (mineral and organic) feedstock for hydrated lime production has not been explored, which could potentially transform certain forms of organic waste into valuable resources for the construction industry. Addressing this research gap requires conducting comprehensive experiments to assess key process variables, such as lime yield, secondary products, and energy consumption. Bridging these research gaps will be instrumental in realizing the full potential of electrochemical decarbonation as a sustainable alternative to conventional lime production methods.

2.8. References

Abdellatef, Y., Khan, M. A., Khan, A., Alam, M. I., & Kavgic, M. (2020). Mechanical, Thermal, and Moisture Buffering Properties of Novel Insulating Hemp-Lime Composite Building Materials. *Materials*, *13*(21), 5000. https://doi.org/10.3390/ma13215000

Abdul-Wahab, S. A., Al-Dhamri, H., Ram, G., & Chatterjee, V. P. (2020). An overview of alternative raw materials used in cement and clinker manufacturing. *International Journal of Sustainable Engineering*, *14*(4), 743–760. https://doi.org/10.1080/19397038.2020.1822949

Arnaud, L., & Gourlay, E. (2012). Experimental study of parameters influencing mechanical properties of hemp concretes. *Construction and Building Materials*, *28*(1), 50–56. https://doi.org/10.1016/j.conbuildmat.2011.07.052

Barker, D. J., Turner, S. A., Napier-Moore, P. A., Clark, M., & Davison, J. E. (2009). CO2 Capture in the Cement Industry. *Energy Procedia*, *1*(1), 87–94. https://doi.org/10.1016/j.egypro.2009.01.014

Benhelal, E., Shamsaei, E., & Rashid, M. I. (2021). Challenges against CO2 abatement strategies in cement industry: A review. *Journal of Environmental Sciences*, *104*, 84–101. https://doi.org/10.1016/j.jes.2020.11.020

Bourdot, A., Moussa, T., Gacoin, A., Maalouf, C., Vazquez, P., Thomachot-Schneider, C., Bliard, C., Merabtine, A., Lachi, M., Douzane, O., Karaky, H., & Polidori, G. (2017). Characterization of a hemp-based agro-material: Influence of starch ratio and hemp shive size on physical, mechanical, and hygrothermal properties. *Energy and Buildings*, *153*, 501–512. https://doi.org/10.1016/j.enbuild.2017.08.022

Brzyski, P., Gładecki, M., Rumińska, M., Pietrak, K., Kubiś, M., & Łapka, P. (2020). Influence of Hemp Shives Size on Hygro-Thermal and Mechanical Properties of a Hemp-Lime Composite. *Materials*, *13*(23), 5383. https://doi.org/10.3390/ma13235383

Buasri, A., Chaiyut, N., Loryuenyong, V., Worawanitchaphong, P., & Trongyong, S. (2013). Calcium oxide derived from waste shells of mussel, cockle, and scallop as the heterogeneous catalyst for biodiesel production. *TheScientificWorldJournal*, *2013*, 460923. https://doi.org/10.1155/2013/460923

Chen, T., Yao, S., Merlin, M., Mai, H., Qiu, Z., Hu, Y., Wang, B., Wang, C., & Jiang, H. (2014). Identification of Cannabis Fiber from the Astana Cemeteries, Xinjiang, China, with Reference to Its Unique Decorative Utilization. *Economic Botany*, *68*(1), 59–66. https://doi.org/10.1007/s12231-014-9261-z

Chong, B. W., Othman, R., Ramadhansyah, P. J., Doh, S. I., & Li, X. (2020). Properties of concrete with eggshell powder: A review. *Physics and Chemistry of the Earth, Parts A/B/C*, *120*, 102951. https://doi.org/10.1016/j.pce.2020.102951

Collet, F., & Pretot, S. (2014). Thermal conductivity of hemp concretes: Variation with formulation, density and water content. *Construction and Building Materials*, *65*, 612–619. https://doi.org/10.1016/j.conbuildmat.2014.05.039

Collet, F., Chamoin, J., Pretot, S., & Lanos, C. (2013). Comparison of the hygric behaviour of three hemp concretes. *Energy and Buildings*, *62*, 294–303. https://doi.org/10.1016/j.enbuild.2013.03.010

Consoli, N. C., Caicedo, A. M. L., Beck Saldanha, R., Filho, H. C. S., & Acosta, C. J. M. (2020). Eggshell Produced Limes: Innovative Materials for Soil Stabilization. *Journal of Materials in Civil Engineering*, *32*(11), 06020018. https://doi.org/10.1061/(ASCE)MT.1943-5533.0003418

Costa, F. N., & Ribeiro, D. V. (2020). Reduction in CO2 emissions during production of cement, with partial replacement of traditional raw materials by civil construction waste (CCW). *Journal of Cleaner Production*, *276*, 123302. https://doi.org/10.1016/j.jclepro.2020.123302

de Bruijn, P. B., Jeppsson, K.-H., Sandin, K., & Nilsson, C. (2009). Mechanical properties of lime–hemp concrete containing shives and fibres. *Biosystems Engineering*, *103*(4), 474–479. https://doi.org/10.1016/j.biosystemseng.2009.02.005

Ellis, L. D., Badel, A. F., Chiang, M. L., Park, R. J.-Y., & Chiang, Y.-M. (2020). Toward electrochemical synthesis of cement—An electrolyzer-based process for decarbonating CaCO3 while producing useful gas streams. *Proceedings of the National Academy of Sciences*, *117*(23), 12584–12591. https://doi.org/10.1073/pnas.1821673116

Eziefula, U. G., Ezeh, J. C., & Eziefula, B. I. (2018). Properties of seashell aggregate concrete: A review. *Construction and Building Materials*, *192*, 287–300. https://doi.org/10.1016/j.conbuildmat.2018.10.096

FAO. (2013). *Poultry production | Gateway to poultry production and products*. PoultryProduction. Retrieved September 4, 2025, from https://www.fao.org/poultry-production-products/production/

Ferraz, E., Gamelas, J. A. F., Coroado, J., Monteiro, C., & Rocha, F. (2018). Eggshell waste to produce building lime: Calcium oxide reactivity, industrial, environmental and economic implications. *Materials and Structures*, *51*(5), 115. https://doi.org/10.1617/s11527-018-1243-7

Government of Canada, Fisheries and Oceans Canada. (2016, October 6). *Aquaculture Production Quantities and Value*. https://www.dfo-mpo.gc.ca/stats/aqua/aqua-prod-eng.htm

Hamada, H. M., Tayeh, B. A., Al-Attar, A., Yahaya, F. M., Muthusamy, K., & Humada, A. M. (2020). The present state of the use of eggshell powder in concrete: A review. *Journal of Building Engineering*, *32*, 101583. https://doi.org/10.1016/j.jobe.2020.101583

Hart, A. (2020). Mini-review of waste shell-derived materials' applications. *Waste Management & Research*, *38*(5), 514–527. https://doi.org/10.1177/0734242X19897812

Her, S., Park, T., Zalnezhad, E., & Bae, S. (2021). Synthesis and characterization of cement clinker using recycled pulverized oyster and scallop shell as limestone substitutes. *Journal of Cleaner Production*, *278*, 123987. https://doi.org/10.1016/j.jclepro.2020.123987

Hincke, M., Gautron, J., Rodriguez-Navarro, A. B., & McKee, M. D. (2011). 8 - The eggshell: Structure and protective function. In Y. Nys, M. Bain, & F. Van Immerseel (Eds.), *Improving the Safety and Quality of Eggs and Egg Products* (pp. 151–182). Woodhead Publishing. https://doi.org/10.1533/9780857093912.2.151

Holcroft, N., & Shea, A. (2015). Effect of compaction on moisture buffering of hemp-lime insulation. *Academic Journal of Civil Engineering*, *33*(2), 542–546. https://doi.org/10.26168/icbbm2015.84

Ip, K., & Miller, A. (2012). Life cycle greenhouse gas emissions of hemp–lime wall constructions in the UK. *Resources, Conservation & Recycling*, *69*(C), 1–9.

Jami, T., Rawtani, D., & Agrawal, Y. K. (2016). Hemp concrete: Carbon-negative construction. *Emerging Materials Research*, *5*(2), 240–247. https://doi.org/10.1680/jemmr.16.00122

Kamkum, P., Atiwongsangthong, N., Muanghlua, R., & Vittayakorn, N. (2015). Application of chicken eggshell waste as a starting material for synthesizing calcium niobate (Ca4Nb2O9) powder. *Ceramics International*, *41*, S69–S75. https://doi.org/10.1016/j.ceramint.2015.03.189

Kanani, F., Heidari, M. D., Gilroyed, B. H., & Pelletier, N. (2020). Waste valorization technology options for the egg and broiler industries: A review and recommendations. *Journal of Cleaner Production*, *262*, 121129. https://doi.org/10.1016/j.jclepro.2020.121129

Laveglia, A., Sambataro, L., Ukrainczyk, N., De Belie, N., & Koenders, E. (2022). Hydrated lime life-cycle assessment: Current and future scenarios in four EU countries. *Journal of Cleaner Production*, *369*, 133224. https://doi.org/10.1016/j.jclepro.2022.133224

Lawrence, M. (2015). Reducing the Environmental Impact of Construction by Using Renewable Materials. *Journal of Renewable Materials*, *3*(3), 163–174. https://doi.org/10.7569/JRM.2015.634105

Magwood, C. & Feigin, J. (2016). Essential Hempcrete Construction: The Complete Step-by-Step Guide. *New Society Publishers.*

Martínez, N. P., Troncoso P, F., Gazzano, V., Ramírez-Amaya, D., González, M., Navarrete, I., Canales, R., & Dreyse, P. (2024). High-performance and low-cost electrochemical reactor for limestone decarbonation applied to clinker production – A validation at laboratory scale. *Journal of Cleaner Production*, *468*, 143112. https://doi.org/10.1016/j.jclepro.2024.143112

Mehta, P. K., & Monteiro, P. J. M. (2014). *Concrete: Microstructure, Properties, and Materials* (4th Edition). McGraw-Hill Education. https://www.accessengineeringlibrary.com/content/book/9780071797870

Micari, M., Dakhchoune, M., & Agrawal, K. V. (2021). Techno-economic assessment of postcombustion carbon capture using high-performance nanoporous single-layer graphene membranes. *Journal of Membrane Science*, *624*, 119103. https://doi.org/10.1016/j.memsci.2021.119103

Mo, K. H., Alengaram, U. J., Jumaat, M. Z., Lee, S. C., Goh, W. I., & Yuen, C. W. (2018). Recycling of seashell waste in concrete: A review. *Construction and Building Materials*, *162*, 751–764. https://doi.org/10.1016/j.conbuildmat.2017.12.009

Nguyen, T. T. (2010). *Contribution à l'étude de la formulation et du procédé de fabrication d'éléments de construction en béton de chanvre* [Phdthesis, Université de Bretagne Sud]. https://doi.org/10/document

Nguyen, T. T., Picandet, V., Amziane, S., & Baley, C. (2009). Influence of compactness and hemp hurd characteristics on the mechanical properties of lime and hemp concrete. *European Journal of Environmental and Civil Engineering*, *13*(9), 1039–1050. https://doi.org/10.1080/19648189.2009.9693171

Niyigena, C., Amziane, S., Chateauneuf, A., Arnaud, L., Bessette, L., Collet, F., Lanos, C., Escadeillas, G., Lawrence, M., Magniont, C., Marceau, S., Pavia, S., Peter, U., Picandet, V., Sonebi, M., & Walker, P. (2016). Variability of the mechanical properties of hemp concrete. *Materials Today Communications*, *7*, 122–133. https://doi.org/10.1016/j.mtcomm.2016.03.003

Oliveira, D. A., Benelli, P., & Amante, E. R. (2013). A literature review on adding value to solid residues: Egg shells. *Journal of Cleaner Production*, *46*, 42–47. https://doi.org/10.1016/j.jclepro.2012.09.045

Ramirez-Amaya, D., Dreyse, P., Martínez, N. P., Troncoso P., F., Navarrete, I., Noël, M., Canales, R. I., & González, M. (2023). Comparison of the electrochemical decarbonation of different-grade limestones used in cement manufacturing. *Cement and Concrete Research*, *174*, 107307. https://doi.org/10.1016/j.cemconres.2023.107307

Sáez-Pérez, M. P., Brümmer, M., & Durán-Suárez, J. A. (2020). A review of the factors affecting the properties and performance of hemp aggregate concretes. *Journal of Building Engineering*, *31*, 101323. https://doi.org/10.1016/j.jobe.2020.101323

Stanwix, W. & Sparrow, A. (2014). The Hempcrete Book: Designing and building with hemp-lime. *Green Books.*

Stevulova, N., Kidalova, L., Junak, J., Cigasova, J., & Terpakova, E. (2012). Effect of Hemp Shive Sizes on Mechanical Properties of Lightweight Fibrous Composites. *Procedia Engineering*, *42*, 496–500. https://doi.org/10.1016/j.proeng.2012.07.441

Stork M., Meinderstma W., Overgaag, M., Neelis M. (2014): A Competitive and Efficient Lime Industry, Cornerstone for a Sustainable Europe (Lime Roadmap). (n.d.). *European Lime Association*. Retrieved September 4, 2025, from https://eula.eu/resources/stork-m-meinderstma-w-overgaag-m-neelis-m-2014-a-competitive-and-efficient-lime-industry-cornerstone-for-a-sustainable-europe-lime-roadmap/

Waheed, M., Yousaf, M., Shehzad, A., Inam-Ur-Raheem, M., Khan, M. K. I., Khan, M. R., Ahmad, N., Abdullah, & Aadil, R. M. (2020). Channelling eggshell waste to valuable and utilizable products: A comprehensive review. *Trends in Food Science & Technology*, *106*, 78–90. https://doi.org/10.1016/j.tifs.2020.10.009

Walker, R., Pavía, S. (2011). Physical properties and reactivity of pozzolans, and their influence on the properties of lime–pozzolan pastes. *Mater Struct, 44, 1139–1150*. https://doi.org/10.1617/s11527-010-9689-2

Williams, J., Lawrence, M., & Walker, P. (2016). A method for the assessment of the internal structure of bio-aggregate concretes. *Construction and Building Materials*, *116*, 45–51. https://doi.org/10.1016/j.conbuildmat.2016.04.088

Williams, J., Lawrence, M., & Walker, P. (2017). The Influence of the Casting Process on the Internal Structure and Physical Properties of Hemp-Lime. *Mater Struct.* https://doi.org/10.1617/s11527-016-0976-4

Chapter 3 : Research Methodology

3.1. Research Method Overview

To Figure 3.1 depicts the overall approach used, broken down into three phases: (1) production of HLC with improved consistency and performance, (2) producing hydrated lime binder through electrolysis, and (3) technical and environmental assessment of carbon-negative HLC in a wall assembly. Further explanation of each phase appears in the upcoming pages with additional details covered in later chapters.

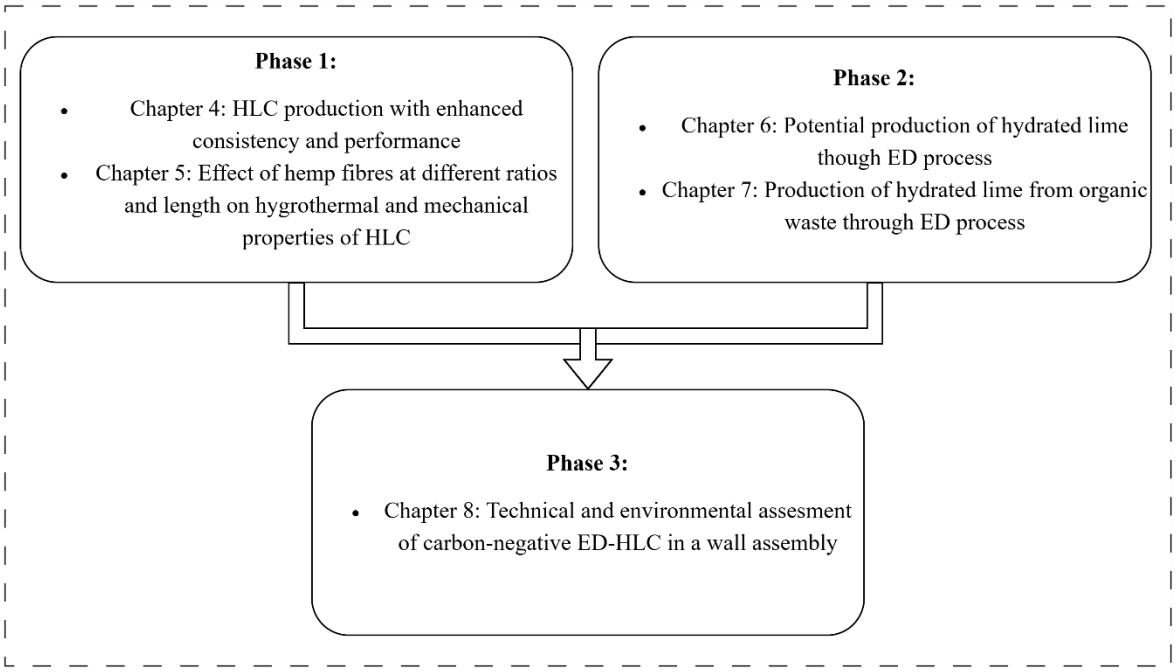

Figure 3.1 Schematic view for the research methodology.

3.2. Phase 1- Production of HLC with Improved Consistency and Performance

3.2.1. Hemp

The hemp shivs used in this study were provided by a local Canadian producer located in Alberta (Terrafibre). Two main groups of hemp shivs were considered in this study. The first group (G1) includes four types of hemp shivs with different particle size fractions as shown in Figure 3.2. The

first type was the received (R) shiv, while other types were reduced in size to various degrees: coarse-size (C), medium-size (M), and fine-size (F), produced by grinding the received shivs using an industrial grinder (JTANGL Electric Grain Grinder Mill, 3000 W) with particle sizes (D_{90}) of 4.52, 1.33, 0.96, and 0.72 mm, respectively.

The second group (G2) consists of hemp shives and fibres. The hemp shivs were milled to 0.73 mm using an industrial grinder to improve the consistency and performance of the produced HLC. Subsequently, two types of fibres were created: fine fibres (1.15 mm) produced using an industrial grinder and long fibres (6, 12, 25 mm ± 0.5 mm) produced by manual cutting, as illustrated in Figure 3.3. Lastly, hemp samples with different fibre ratios were produced by adding the cut fibres to the hemp shivs to achieve the desired mass ratios (10, 20, and 40%). A more detailed description of the materials will be provided in the chapters that follow.

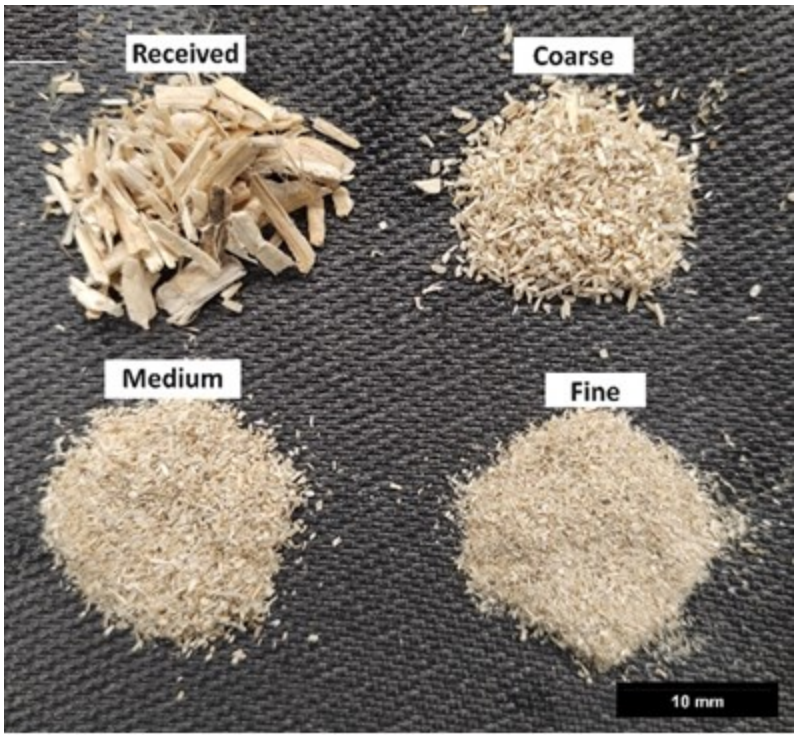

Figure 3.2 Hemp shivs (G1) that were used in this study.

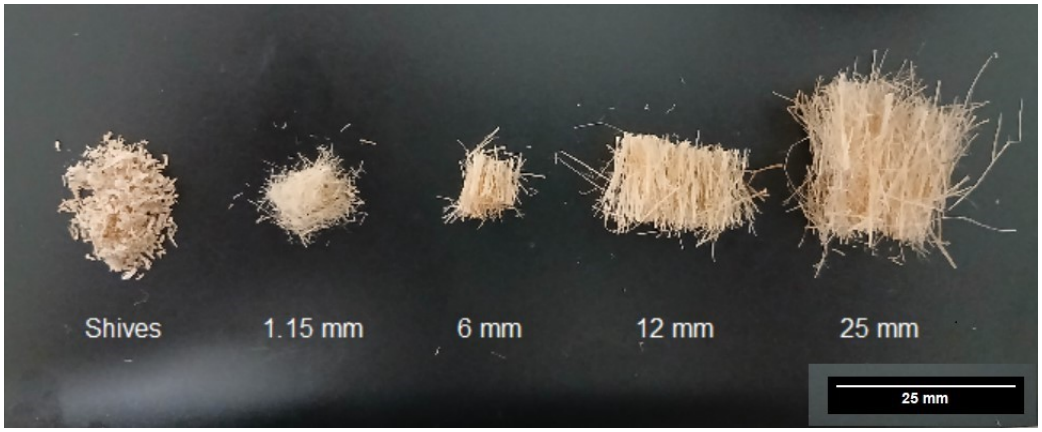

Figure 3.3 Hemp shivs and fibres (G2) in this study.

3.2.2. Characterization Techniques

Various approaches have been employed in the literature to characterize hemp shiv and fibre [Niyigena et al., 2018]. A laboratory investigation by Amziane and Collet [Amziane and Collet, 2017] on establishing characterization methods for hemp demonstrated strong repeatability. Consequently, this study adhered to the prescribed protocols [Amziane and Collet, 2017] for assessing density, water absorption, particle size distribution, fibre content, and moisture content.

- **Bulk Density**

The bulk density was determined using the following procedure. Firstly, enough material was selected to fill out at least half of the cylindrical mold expected to be used to measure the bulk density. Secondly, the material was oven-dried at 60 °C using a convection oven fitted with an extraction fan to remove the humidity until a constant mass was achieved when the variation between two consecutive readings at 24 h was less than 0.1%. Then, the sample was placed in a sealed plastic bag until it reached room temperature. Then, the hemp sample was placed in the cylindrical mold to reach half of the volume of the cylinder. After that, the cylinder was upended ten times and shaken to achieve a horizontal surface. The following step included marking the

level of the sample in the cylinder and then removing the sample from the mold to determine the mass of the sample. Finally, the occupied volume was determined by filling the mold with water up to the previously marked level and measuring the weight of the water. The test was repeated three times with three different samples. The bulk density was calculated using Equation (3.1) [Amziane and Collet, 2017]:

$$\rho = M/V \tag{3.1}$$

Where ρ is the bulk density, M is the mass of the shiv, and V is the sample volume.

- **Moisture Content**

The following procedure was followed to determine the initial moisture content in the hemp sample. A sample of 200 g was selected. Subsequently, the sample was oven-dried at 60 °C until a constant mass was achieved when the variation between two consecutive readings at 24 h was less than 0.1%, and the dry mass of the sample was determined. The test was repeated three times with three different samples. The bulk density was calculated using Equation (3.2) [Amziane and Collet, 2017]:

$$W = 100 \times (m_0 - m_d)/m_d \tag{3.2}$$

Where W is the initial water content, m_0 is the initial mass of the sample, and m_d is the dry mass of the sample.

- **Water Absorption**

The following procedure is used to assess water absorption in the hemp. Initially, a 25 g hemp sample was selected. Then, the sample underwent oven-drying at 60 °C until reaching a consistent mass, indicated by a variation of less than 0.1% between two consecutive readings taken 24 hours

apart, and their dry mass was measured. Subsequently, the sample was submerged in a plastic pail filled with water for 1 minute. After that, the water in the pail was drained, the sample was placed in a "salad spinner" and turned 100 times at a rate of 2 rotations per second. Finally, the weight of the spun sample was determined. The same steps were repeated using another 25 g of sample but with different immersion times of 15, 240, and 2,880 minutes. The test was repeated 3 times with 3 different samples of shivs. The absorption (water content) value using Equation (3.2) was determined each time. The initial rate of absorption, measured at 1 minute, and (K_1) representing the absorption curve's slope as a logarithmic time function was determined. The water absorption at any given time (W_t) was calculated using Equation (3.3) [Amziane and Collet, 2017]:

$$W_t = \text{IRA} + K_1 Log\ (t) \tag{3.3}$$

Where W_t is the water absorption at any given time, IRA is the initial rate of absorption, and K_1 is the slope of the absorption curve.

- **Fibre Content**

It is essential to report the purity level of the hemp shiv used to produce HLC because hemp fibre content can affect the properties and performance of the HLC. To the authors' knowledge, no standards exist that directly report how to measure the fibre content in the hemp shiv; therefore, a new methodology was developed based on the flotation technique, as it is widely used in industries where materials can be separated through density differences caused by the difference in absorption rate between hemp shiv and fibres. The methodology's effectiveness in determining fibre content was assessed through previous testing using hemp shiv samples with different fibre contents ranging from 2-44%, and the results were crosschecked using a handpicking method

where fibres were separated manually from the shiv. The proposed method predicted fibre content within ±5% of the results obtained from the handpicking method (see Appendix A).

A 10 g hemp shiv sample was selected to determine the fibre content. Then, the sample was oven-dried at 60°C until a constant mass was achieved when the variation between two consecutive readings at 24 h was less than 0.1%, and the dry mass was measured. After that, the sample was ground to achieve the desired length (2-5 mm). This step can be skipped if the particle size matches the desired length. Subsequently, the sample was entirely submerged in a plastic pail containing 3 liters of water at room temperature. The sample was then stirred for 5 minutes using a magnetic stirrer at medium speed (750 RPM) and left to settle for another 10 minutes. The floating hemp shiv particles were then removed using a fine mesh strainer. The remaining part of the sample in the pail was sieved through sieve No. 200 (75 μm), and what was left on the sieve was placed in a container and transferred to a drying oven at 60°C until a constant mass was achieved when the variation between two consecutive readings at 24 h was less than 0.1%, and the dry mass of the fibres was measured. The fibre content was calculated using Equation (3.4):

$$f_c = 100 \times m_f / m_d \tag{3.4}$$

Where f_c is the fibre content, m_f is the dry mass of the fibres, and m_d is the dry mass of the sample.

- **Particle Size Distribution**

The particle size distribution was obtained using a combination of two approaches. An image analysis method was used to determine the diameter of large shivs as well as fibre length [Nozahic, 2012]. The analysis procedure was conducted on 5 g samples using image analysis software ImageJ [Igathinathane et al., 2009], with outputs being the fibre length and Feret's diameter (i.e.,

the diameter of the smallest circle that confines the shiv particle outline). Meanwhile, the particle size distribution of small shivs was determined using a combination of mechanical sieving for particles bigger than 0.3 mm and laser diffraction for particles less than 0.3 mm, as there was a limitation on detecting the larger particle sizes with laser diffraction apparatus.

3.2.3. Binder Mix Design

Before preparing the HLC samples, a pilot study [Mahmood et al., 2023] was carried out to examine the effects of incorporating by-products and locally available pozzolanic and cementitious materials at various replacement ratios and different water-to-binder ratios on the physical and mechanical properties of the lime binder. The results indicated that a binder containing 20% slag and a 100% water-to-binder ratio exhibited the best mechanical performance compared to the other mixtures. Therefore, the binder mix design was fixed in this study and was comprised of hydrated lime, in compliance with the ASTM C207-18 [ASTM C207, 2018] standards, at an 80% ratio, and slag, in compliance with ASTM C989/C989M-18a [ASTM C989/C989M, 2018], at a 20% ratio of the total binder weight. Table 3.1 summarizes their chemical composition and physical properties.

The use of hydrated lime in the formulation offered several advantages. First, hydrated lime has a high pH level, making it suitable for preventing biological corrosion when used with organic materials [Brzyski et al., 2020]. Second, lime's large surface area (see Table 3.1) due to its fine particle size and ability to regulate the pH levels within the mixture [Walker & Pavía, 2010] promoted optimal conditions for forming stable mineral bonds between hemp shiv and lime, thus enhancing the resulting material's cohesion and strength. Third, hydrated lime aids in carbonation, whereby carbon dioxide from the atmosphere reacts with lime during curing, forming calcium carbonate and effectively sequestering carbon, enhancing the material's sustainability and

durability. Nevertheless, because hydrated lime gains strength through slow carbonation progress, the binder formulation was enriched with slag, a by-product of metal smelting processes, and a cementitious material that provides early strength and moisture resistance [Walker & Pavía, 2010; Asghari and Memari, 2024]. The addition of slag offered the following benefits. First, high silica content in slag improved cohesion within the hemp-lime matrix, resulting in increased compressive strength and reduced brittleness. Additionally, using slag in HLC increased sustainability by diverting industrial waste from landfills and reducing the environmental footprint associated with traditional construction materials.

Table 3-1 The chemical composition and physical properties of hydrated lime and slag.

Material	Chemical composition Mass %									Physical properties	
	CaO	Na_2O	MgO	Al_2O_3	SiO_2	P_2O_5	K_2O	TiO_2	Fe_2O_3	Specific gravity	Surface area g/m²
Hydrated lime	67.56	0.05	0.42	0.04	0.75	0.02	0.03	0.02	0.11	2.39	13.72
Slag	37.82	0.37	11.82	10.20	36.80	0.00	0.49	1.43	0.43	2.74	1.63

3.2.4. Composition and Preparation of Hemp-Lime Specimens

This study aimed to produce hemp-lime composites with consistent performance, high thermal resistance, and a minimized environmental impact, suitable for sustainable buildings exposed to cold climates. This aim was achieved by (i) maximizing the share of hemp shiv using binder-to-hemp (B/H) ratios of 1:1, 1:1.5, and 1:2.4, (ii) producing lightweight samples with dry densities of 140 kg/m³, 170 kg/m³, and 200 kg/m³, and (iii) using a mechanical process to manufacture uniform samples with consistent dry density.

The preparation of the samples included placing the hemp shiv in a plastic pail and adding the binder mix composed of hydrated lime and slag. A hand-operated drill mixer was used for the dry components for 3-4 minutes until a homogenous mixture was achieved. Water was then added to

the dry components, and further hand-operated mixing was applied for another 10 minutes to ensure that the moistened binder encapsulated all shiv particles. Fine hemp particles allowed easier mix preparation and more uniform samples than the received hemp shiv product. Considering the lack of standards to measure the workability of hemp-lime composites, a "test ball" procedure was followed where the mixture was stuck together in hand, forming a ball without excess water, as shown in Figure 3.4-b. Since most previous studies that manually produced hemp-lime samples reported significant variations in the density [Williams et al., 2017; Abdellatef et al., 2020], the vibration technique was chosen to ensure consistent properties of the HLC samples. Hence, when a desired mixture was obtained, the molds were filled, placed on a vibration table, and vibrated for 30 seconds using 60 Hz frequency to achieve the targeted wet density, as shown in Figure 3.4-a. It is important to note that a preliminary study was conducted to determine the maximum density that could be achieved using vibration before stratification occurs. Our composite was intentionally designed to be lightweight and highly bio-based, prioritizing thermal performance, sustainability, and workability rather than mechanical strength. In this respect, depending on the B/H ratio, the maximum target dry densities achieved by vibration were 200 kg/m³, 170 kg/m³, and 140 kg/m³ for 1:1, 1:1.5, and 1:2.4, respectively. The decrease in dry density corresponds to the increase in the share of hemp shiv with consistent vibration technique applied to all samples.

Two mold shapes were utilized to assess the hemp-lime samples' hygrothermal and mechanical properties. In this respect, 160 mm (width) x 160 mm (length) x 80 mm (height) samples were used to measure the thermal conductivity, specific heat capacity, thermal diffusivity, and moisture buffering potential. Additionally, cubic samples (100 mm x 100 mm x 100 mm) were used to measure the compressive strength. As fresh hemp-lime composites have marginal strength, the mold size can affect the de-molding process, as samples might collapse while being removed from

the mold. Therefore, samples cast for compressive strength were de-molded immediately, whereas other larger samples for hygrothermal tests were de-molded after 48 hours.

Samples were placed in a curing chamber for 28 days under 70% RH and 22±1 °C temperature until testing. Samples intended for thermal conductivity, specific heat, thermal diffusivity, and moisture buffering value analysis were oven-dried at 65-80 °C until a constant weight was achieved. In contrast, samples tested for compressive strength were tested directly after removal from the curing chamber. Previous studies reported that the direction of casting and compaction affect the thermal and mechanical properties of the hemp-lime composites [Williams et al., 2017; Nguyen et al., 2009]. In this study, all mixes were initially cast in a direction perpendicular to heat flow (i.e., vertically). Selected HLC mixes were also cast in a parallel direction (i.e., horizontally) to investigate the effect of casting direction on the thermal properties, and the results were compared with the corresponding mixes cast in the perpendicular direction, as shown in Figure 3.4-a.

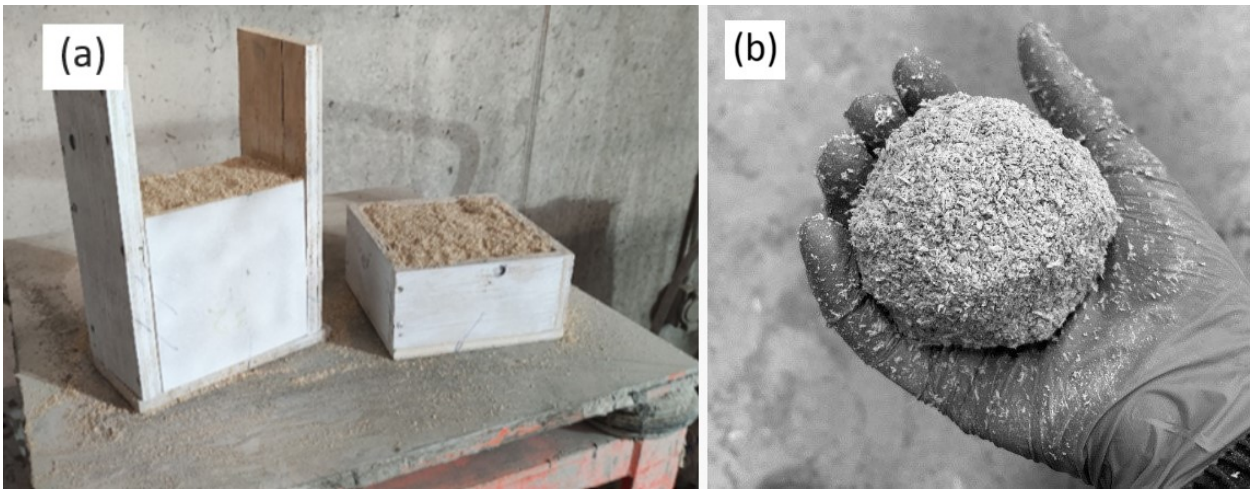

Figure 3.4 The molds filled with HLC were placed on the vibration table (a) to produce the samples and the test ball method (b).

3.2.5. Experimental Tests

- **Physical and Mechanical Properties Tests**

The apparent dry and wet densities were determined due to a significant correlation between the hemp-lime density and its mechanical and hygrothermal properties. Three cubic samples of each mix were used to determine the apparent densities. Given the absence of specific standards governing the measurement and calculation of compressive strength and stiffness in hemp-lime composites, protocols outlined in BS EN 12390-1 [BS EN 12390, 2021] and BS EN 826:2013 [BS EN 826, 2013], devised for concrete and thermal insulation materials in building applications were adhered to for the preparation, testing of samples, determination of compressive strength, and material stiffness [Walker et al., 2014]. The compressive strength was determined as an average value of six samples for each mix and tested at 30 days using a hydraulic press machine MTS 103. The load was applied in a displacement control manner at a rate of 2 mm/min, and the failure mode was determined when the load-displacement curve reached the maximum value [Abdellatef et al., 2020]. Figure 3.5 illustrates the compressive strength testing setup.

Figure 3.5 Compressive strength testing setup.

- **Thermal Conductivity**

This test was performed on four samples for each hemp-lime mix using a FOX 304 Heat Flow Meter Apparatus (HFMA) following ASTM C518 standard [ASTM C518, 2017] for both perpendicular and parallel cast samples. The apparatus was first calibrated using NIST 1450b SRM (Standard Reference Material of the National Institute of Standards and Technology) to convert the voltage signals into heat flux. Then, the test was conducted using Fourier's law of heat conduction by applying a steady one-dimensional heat flux through the sample by setting a different but constant temperature for the upper and lower plates [Abdellatef et al., 2020]. For all samples, the thermal conductivity was determined in oven-dry conditions at an average temperature of 12.5 °C where the hot plate was 25°C and the cold plate was 0°C. For all samples, a high thermal resistance material was placed surrounding the sample to fill up the gap between

the chamber walls and the samples to ensure heat flowed through the sample in one direction, as shown in Figure 3.6.

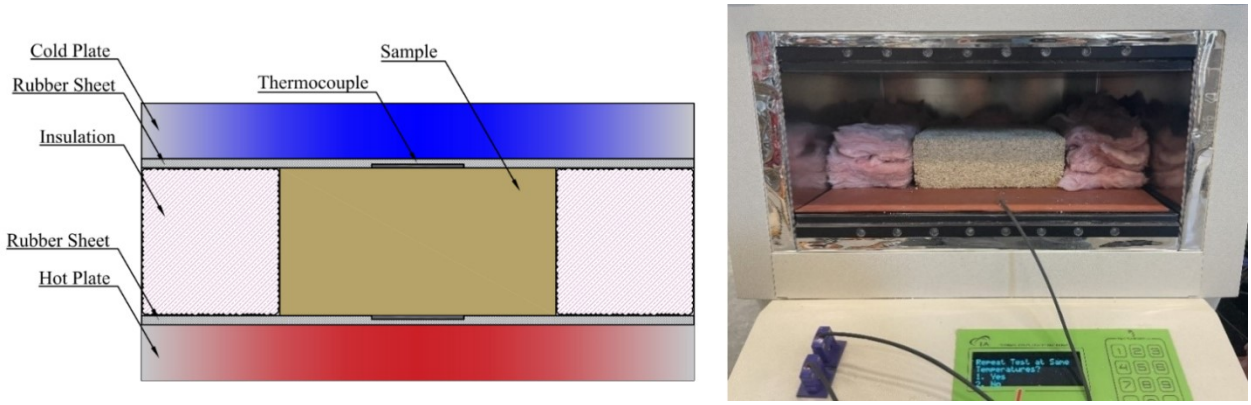

Figure 3.6 Thermal conductivity setup using FOX 304 Heat Flow Meter.

- **Specific Heat Capacity**

The specific heat capacity of a material is its ability to store thermal energy [Tleoubaev & Brzezinski, 2007]. The specific heat capacity was indirectly measured by first measuring the volumetric specific heat using LaserComp FOX 304, as a new method was integrated into the software to measure the volumetric specific heat directly. WinTherm32 software records all the readings of the heat HFMA and calculates the time interval between the readings (typically ~1-1.3 seconds). Then, the software calculates the amount of the total heat per unit square absorbed by both the sample and the instrument using Equation (3.5):

$$H = \sum\left[S_U\left(QU_i - QU_{equil}\right) + S_L\left(QL_i - QL_{equil}\right)\right]\tau, \quad (3.5)$$

Where S_U and S_L are upper and lower calibration factors, QU_i and QL_i are the HMFAs readings, and QU_{equil} and QL_{equil} are the final equilibrium values of the HFMA signals, which are subtracted to eliminate drift of the sum due to edge heat losses (or gains), and τ is the time interval

between the readings. Then, the software calculates volumetric specific heat value as the amount of heat (per unit of square area and degree °C) absorbed by the sample, divided by the sample's thickness as shown in Equation (3.6) [Tleoubaev & Brzezinski, 2007; 35. Carslaw & Jaeger, 1959; Flynn & Gorthala, 1997; Tikhonov & Samarskii, 1963]:

$$C_{p\rho} = [H_{total}/(\Delta T - H_{HFMs})]/L, \quad (3.6)$$

Where $C_{p\rho}$is the volumetric specific heat, H_{total} is the total heat absorbed, ΔT is the temperature change, H_{HFMs} is the heat absorbed by the heat flow meter, and L is the sample thickness. Finally, the specific heat capacity was manually calculated using Equation (3.7):

$$C_p = C_{p\rho}/\rho, \quad (3.7)$$

Where $C_p$is the specific heat capacity, and ρ is density.

- **Thermal Diffusivity**

This property indicates how fast the material temperature would change when subjected to heating or cooling loads, where the higher the thermal diffusivity, the faster the material would heat or cool and vice versa. Therefore, it is imperative to characterize this property, especially when considering the unsteady state of the heat transfer environment [Abdellatef et al., 2020]. Thermal diffusivity can be determined using Equation (3.8):

$$\alpha = k/(\rho.C_p), \quad (3.8)$$

Where α is the thermal diffusivity and k is the thermal conductivity.

• **Moisture Buffering Value**

Since the hygroscopic behaviour of materials subjected to a dynamic humid environment is more realistic than a steady state condition, the Nordtest project introduced an experimental procedure to estimate the moisture buffering behaviour of hygroscopic materials using a universal coefficient known as Moisture Buffer Value (MBV) [Rode et al., 2005]. This coefficient indicates the quantity of water transferred in or out of a material per open surface area in a defined time interval when subjected to varying humidity loading conditions. Under Nordtest, the tested material is subjected to at least three consecutive humidity cycles. The MBV is determined when the test satisfies two conditions: (1) in the last three cycles, the mass difference should be less than 5%, and (2) within the same cycle, the mass difference in loss or gain should be less than 5%. Following the Nordtest procedure, four samples of each mix were tested. All sample sides except one (160 mm x 160 mm) were sealed. The samples were then placed in an environmental chamber and exposed to a dynamic humidity cycle of 24 hours between high (75%) and low humidity levels (33%) for 8 and 16 hours, respectively, at 23±1 °C.

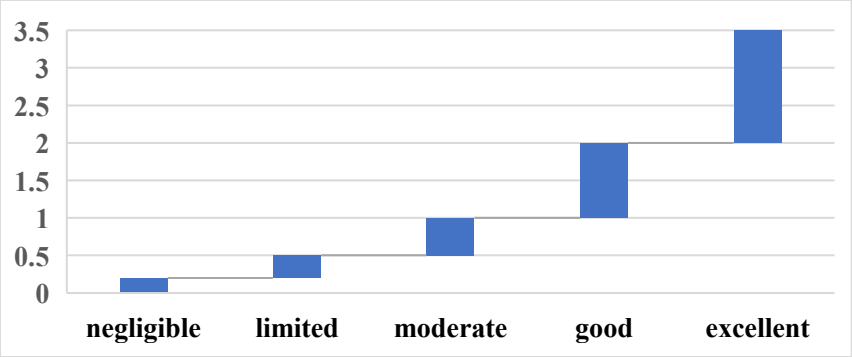

Figure 3.7 Graphic presentation of practical Moisture Buffer Value classes [77].

The environmental chambers were built using sealed plastic containers with dimensions of (37.4 x 47.6 x 60.3 cm) and saturated salt solutions to produce 33% and 75% relative humidities (RH).

ASTM E104-20a standard was followed to produce the humidity levels; 33% RH was produced by mixing magnesium chloride ($MgCl_2$) with distilled water at a 10:1 weight ratio, while 75% RH was produced by mixing sodium chloride (NaCl) with distilled water at 2:1 weight ratio [ASTM E104, 2020]. Two humidity sensors were positioned at the top and bottom of each chamber to continuously monitor the humidity levels and ensure the required RH levels and uniform humidity. According to recent research, air velocity can significantly impact the MBV, especially regarding bio-based materials, which can exhibit an increase in MBV by about 150% when airspeed is increased from 0.108 m/s to 1.91 m/s [Khaled et al., 2023]. In this respect, it is essential to mention that environmental chambers employed in this study use the passive method (i.e., saturated salt solutions) to provide the required moisture conditions while minimizing air movement, unlike conventional climate-controlled environmental chambers with fans or blowers to circulate air within the chamber. The environmental chambers were kept sealed during the test, except when taking weight measurements, and also placed in a climate-controlled lab environment with consistent conditions, including an ambient temperature of 20 ºC (±1ºC), relative humidity of 45% (±5%), and air velocity of 0.2 m/s (±0.05m/s), to minimize further the air movement caused by natural convection due to the variations in ambient conditions. Figure 3.8 illustrates the samples and climate chamber. When the test conditions were satisfied, the MBV for each sample was determined using Equation (3.9):

$$MBV = \Delta m/(A.\Delta RH), \tag{3.9}$$

Where MBV is the moisture buffer value, Δm is the moisture uptake/release during the cycle, A is the sample exposed area, and ΔRH is the difference between the highest and the lowest relative humidity.

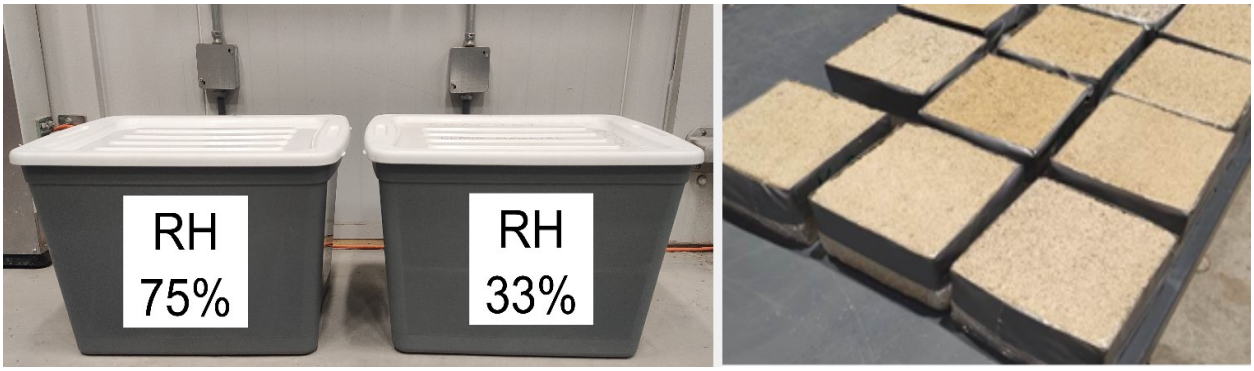

Figure 3.8 Test assembly and setup of hemp-lime samples in a climate chamber for MBV testing.

3.3. Phase 2- Production of Hydrated Lime Through ED Process

3.3.1. Materials

Three main groups of feedstocks were considered in this study. In the first group is a Fisher Chemical high-purity calcium carbonate (CAS-No: 471-34-1, Ref-No: 64-500) which was utilized as a control sample (C). The second group consists of three inorganic powdered limestone samples supplied by a local lime industry with different purity levels: CA-1235, CA-792, and CA-687. The precursor materials were oven-dried to 105°C for 24 hours and then subjected to physical and chemical analysis. The last group consists of two organic $CaCO_3$ sources: mussel shells (MS) and eggshells (ES). These materials were washed multiple times with distilled water to eliminate impurities, dust, and organic residues, then oven-dried at 200°C for 6 hours to remove excess moisture and remaining organic matter (e.g., membranes) [Ballester et al., 2007; Barros et al., 2009]. The dried materials were manually crushed with a hammer to break them into smaller pieces, followed by further grinding with a ceramic mortar to achieve a fine powder. The finely ground powder was then sieved through 90 μm [Strother, 2019]. The feedstock was oven-dried at 105°C for 24 hours and then physically and chemically analyzed. A more detailed description of the materials will be provided in the chapters that follow.

3.3.2. Characterization Techniques

- **Thermogravimetric and Differential Thermogravimetric Analysis (TG/DTG)**

For this test, 20 - 25 mg of dry powder sample was placed into an alumina crucible. The sample was heated to 1000°C at a rate of 10°C/min. The heating was selected as a compromise between thermal resolution, experimental duration, and data comparability. Lower heating rates (e.g., 2–5 °C/min) can improve peak separation but significantly increase test time and may amplify baseline drift, while higher heating rates (>20 °C/min) can cause thermal lag, peak shifting, and incomplete heat transfer, leading to inaccurate determination of onset and completion temperatures. Moreover, using this heating rate enhances comparability with published literature and ensures reproducibility of the measured mass-loss behavior. A continuous flow of nitrogen (N_2) to 50 ml/min was applied as an inert atmosphere to avoid oxidation. Samples were tested in a Setsys 24 from SETARAM. TG/DTG was performed to identify and quantify the content of $CaCO_3$ and $Ca(OH)_2$ by mass in precursor and DMs using the equations below [Ramirez-Amaya et al., 2023]:

$$\%CaCO_3 = \%L_{(550-900)}\left(\frac{\mathrm{Mw_{CaCO_3}}}{\mathrm{Mw_{CO_2}}}\right) \tag{3.10}$$

$$\%Ca(OH)_2 = \%L_{(310-500)}(\mathrm{Mw_{Ca(OH)_2}}/\mathrm{Mw_{H_2O}}) \tag{3.11}$$

where $\%L_{(550\text{-}900)}$ is the sample's weight loss in the decarbonation zone, $\%L_{(310\text{-}500)}$ is the sample's weight loss in the dehydration zone, $\mathrm{Mw_{CaCO_3}}$ is the calcium carbonate molecular weight (100.087 g/mol), $\mathrm{Mw_{Ca(OH)_2}}$ is the molecular weight of calcium hydroxide (74.093 g/mol), $\mathrm{Mw_{CO_2}}$ is the molecular weight of carbon dioxide (44.01 g/mol), and $\mathrm{Mw_{H_2O}}$ is the molecular weight of water (18.015 g/mol)[Ramirez-Amaya et al., 2023].

- **X-Ray Diffraction (XRD)**

XRD was performed on dry powder samples of precursor and DMs in order to identify crystalline phases. Samples were tested in a Bruker D8 (Cu K,= 1.5418 Å, operation voltage 40 kV, current 25 mA). For all samples, the range of 2θ was 10-70°, and the test speed was 0.02° per second. The COD inorganic database was employed in MATCH software for candidate phase selection.

- **X-Ray Fluorescence (XRF)**

XRF was performed to quantify the elemental composition by mass of precursor and DMs. Each sample was calcined to 1050°C for 150 minutes to reduce all compounds to an oxidation state and quantify the loss on ignition (LOI). The sample was fused into a homogeneous vitreous disc, which was later analyzed for 10 minutes using the Fast-Vac34 method. The results were expressed in the content of elemental oxides by mass. Rigaku SuperMini200 WDXRF spectrometers were used for testing.

- **Particle Size Distribution (PSD)**

The PSD of precursor and DMs were studied by laser diffraction using a MasterSizer 2000 from Malvern Instruments. A Hydro 2000Mu ultrasonicator was used as the dispersion unit, and distilled water and isopropyl alcohol were utilized as the dispersant of precursor and precipitated samples, respectively. The percentiles D_{90}, D_{50}, and D_{10} were computed from the cumulative sum of volume fractions.

- **Specific Surface Area: Brunauer, Emmett and Teller Method (SSABET)**

The specific surface area by BET technique (SSABET) of precursor and precipitated materials was quantified by physical nitrogen adsorption in a BET model. Samples were tested in an ASAP 2020 from Micrometrics.

- **Field Emission Scanning Electron Microscopy (FE-SEM) with Energy Dispersive X-Ray Spectroscopy (EDX)**

FE-SEM studied the surface and morphology of precursor and DMs. Samples were coated with 5 nm of gold and palladium; carbon tape was used as the sample holder. Images were taken for samples using a JEOL JSM-7500F FE-SEM.

3.3.3. Electrochemical Decarbonation Process

Figure 3.9 shows the scheme of the H-type electrolysis cell used, which comprises an anode and cathode chamber interconnected by an interface. Two paper filters (Whatman grade 1) were installed between each chamber and the cell's interface to avoid cathode electrode passivation [Ellis et al., 2020]. The filter material was chosen because it has a high resistance to the acid and alkaline conditions generated in the electrolysis cell during the ED process [Jena et al., 2013]. It is worth mentioning that the filter papers did not become clogged during the test runs; however, to ensure consistency and prevent any contamination or buildup, clean filter papers were used for each individual run. A platinum plate (10 mm x15 mm x 0.2 mm) and mesh (10 mm x 20 mm x 0.2 mm) electrode were placed in the anode and cathode chambers, respectively, and sodium nitrate ($NaNO_3$) dissolved in distilled water to 3M concentration was employed as an electrolyte. This electrolyte was chosen because it does not decompose at high voltage [Ellis et al., 2020]. A more detailed description of the process will be provided in the chapters that follow.

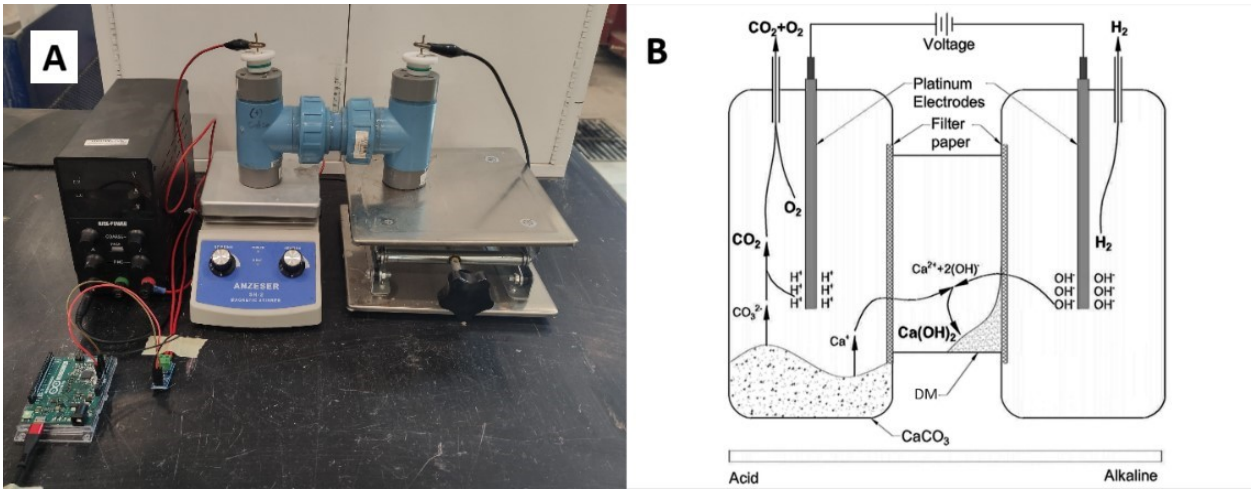

Figure 3.9 Electrochemical reactor setup (A), Electrolysis cell scheme (B).

3.4. Phase 3 - The Sustainability of Hemp-Lime Composites in Construction: A Comparative Life Cycle Analysis of External Walls

In this phase, a quantitative evaluation of the sustainability of hemp-lime composites incorporating ED-produced hydrated lime is presented. The composites are benchmarked against (i) traditional HLC made with industrially hydrated lime and (ii) glass fibre insulation, a conventional external wall material. The objective is to assess both technical feasibility and sustainability performance, using a cradle-to-gate life cycle assessment (LCA) normalized to thermal functionality. The findings provide insights into the viability of bio-based composites with alternative binders as scalable insulation solutions for low-carbon construction.

3.4.1. Methods

A two-stage methodology was used to investigate the techno-sustainability performance of HLC prepared with a binder that includes hydrated lime produced through the ED process. The first stage focused on a comprehensive hygrothermal and mechanical characterization of the hemp-lime composites. HLC samples were tested for thermal conductivity (W/m·K), compressive strength

(MPa), and moisture buffering value (g/m²·RH) following the protocols detailed in Section 3.2.5. In the second stage, a Life Cycle Assessment (LCA) framework was used to evaluate the environmental footprint and sustainability performance of the hemp-lime composites, with a comparative analysis against traditional insulation materials. The sustainability assessment employed a cradle-to-gate LCA framework, with the functional unit defined as 1 m² of material providing a thermal transmittance (R=2.88 m²·K/W). A more comprehensive description of the methodology is presented in Chapter 8.

3.5. References

Abdellatef, Y., Khan, M. A., Khan, A., Alam, M. I., & Kavgic, M. (2020). Mechanical, Thermal, and Moisture Buffering Properties of Novel Insulating Hemp-Lime Composite Building Materials. *Materials*, *13*(21), 5000. https://doi.org/10.3390/ma13215000

Amziane, S. Z& Collet, Fl. (2017). Hygric and thermal properties of bio-aggregate based building materials. Bio-aggregates Based Building Materials: State-of-the-Art Report of the RILEM Technical Committee 236-BBM. *Springer Nature Link*.

Asghari, N., & Memari, A. M. (2024). State of the Art Review of Attributes and Mechanical Properties of Hempcrete. *Biomass*, *4*(1), 65-91. https://doi.org/10.3390/biomass4010004

ASTM International. (2017). Standard Test Method for Steady-State Thermal Transmission Properties by Means of the Heat Flow Meter Apparatus (ASTM C518).

ASTM International. (2018). Standard Specification for Hydrated Lime for Masonry Purposes (ASTM C207-18).

ASTM International. (2018). Standard Specification for Slag Cement for Use in Concrete and Mortars (ASTM C989/C989M).

ASTM International. (2020). Standard Practice for Maintaining Constant Relative Humidity by Means of Aqueous Solutions (ASTM E104-20a).

Ballester, P., Mármol, I., Morales, J., & Sánchez, L. (2007). Use of limestone obtained from waste of the mussel cannery industry for the production of mortars. *Cement and Concrete Research*, *37*(4), 559–564. https://doi.org/10.1016/j.cemconres.2007.01.004

Barros, M. C., Bello, P. M., Bao, M., & Torrado, J. J. (2009). From waste to commodity: Transforming shells into high purity calcium carbonate. *Journal of Cleaner Production*, *17*(3), 400–407. https://doi.org/10.1016/j.jclepro.2008.08.013

British Standards Institution. (2013). Thermal insulating products for building applications. Determination of compression behaviour (BS EN 826:2013).

British Standards Institution. (2021). British Standard for Testing Hardened Concrete—Part 1: Shape, Dimensions and Other Requirements for Specimens and Moulds (BS EN 12390-1:2021).

Brzyski, P., Gładecki, M., Rumińska, M., Pietrak, K., Kubiś, M., & Łapka, P. (2020). Influence of Hemp Shives Size on Hygro-Thermal and Mechanical Properties of a Hemp-Lime Composite. *Materials*, *13*(23), 5383. https://doi.org/10.3390/ma13235383

Ellis, L. D., Badel, A. F., Chiang, M. L., Park, R. J.-Y., & Chiang, Y.-M. (2020). Toward electrochemical synthesis of cement—An electrolyzer-based process for decarbonating CaCO3 while producing useful gas streams. *Proceedings of the National Academy of Sciences*, *117*(23), 12584–12591. https://doi.org/10.1073/pnas.1821673116

Graves, R. S., & Zarr, R. R. (1997). *Insulation Materials, Testing and Applications, 3rd Volume*. ASTM International.

Igathinathane, C., Pordesimo, L. O., Columbus, E. P., Batchelor, W. D., & Sokhansanj, S. (2009). Sieveless particle size distribution analysis of particulate materials through computer vision. *Computers and Electronics in Agriculture*, *66*(2), 147–158. https://doi.org/10.1016/j.compag.2009.01.005

Jena, M. S., Sahu, P., Dash, P., & Mohanty, J. K. (2013). Beneficiation of limestone plant rejects for value addition. *Journal of Hazardous Materials*, *262*, 218–227. https://doi.org/10.1016/j.jhazmat.2013.08.048

Khaled, S., Collet, F., Prétot, S., & Bart, M. (2023). Effect of Air Velocity and Initial Conditioning on the Moisture Buffer Value of Four Different Building Materials. *Materials*, *16*(8), 3284. https://doi.org/10.3390/ma16083284

Mahmood, O., Noël, M., & Kavgic, M. (2023). Physical and Mechanical Properties of Innovative Lime-Pozzolanic Hempcrete Binder. In S. Desjardins, G. J Poitras, M. S. Alam, & X. Sanchez-Castillo (Eds.), *Proceedings of the Canadian Society for Civil Engineering Annual Conference 2023, Volume 6* (pp. 67–75). Springer Nature Switzerland. https://doi.org/10.1007/978-3-031-61507-8_6

Nguyen, T. T., Picandet, V., Amziane, S., & Baley, C. (2009). Influence of compactness and hemp hurd characteristics on the mechanical properties of lime and hemp concrete. *European Journal of Environmental and Civil Engineering*, *13*(9), 1039–1050. https://doi.org/10.1080/19648189.2009.9693171

Niyigena, C., Amziane, S., & Chateauneuf, A. (2018). Multicriteria analysis demonstrating the impact of shiv on the properties of hemp concrete. *Construction and Building Materials*, *160*, 211–222. https://doi.org/10.1016/j.conbuildmat.2017.11.026

Nozahic, V. (2012). *Vers une nouvelle démarche de conception des bétons de végétaux lignocellulosiques basée sur la compréhension et l'amélioration de l'interface liant / végétal: Application à des granulats de chenevotte et de tige de tournesol associés à un liant ponce / chaux* [Phdthesis, Université Blaise Pascal - Clermont-Ferrand II]. https://theses.hal.science/tel-00822142

Ramirez-Amaya, D., Dreyse, P., Martínez, N. P., Troncoso P., F., Navarrete, I., Noël, M., Canales, R. I., & González, M. (2023). Comparison of the electrochemical decarbonation of different-grade limestones used in cement manufacturing. *Cement and Concrete Research*, *174*, 107307. https://doi.org/10.1016/j.cemconres.2023.107307

Rode, C., Peuhkuri, R., Hanssen, K., Time, B., Svennberg, K., Arfvidsson, J. A., & Ojanen, T. (2005). NORDTEST - Project on moisture buffer value of materials: 26th AIVC Conference. *Ventilation in Relation to the Energy Performance of Buildings*.

Strother, P.(2019). 2 - Manufacture of Portland Cement, Fifth ed. pp. 31-56.

Tleoubaev, A., & Brzezinski, A. (n.d.). *Title: Thermal Diffusivity and Volumetric Specific Heat Measurements Using Heat Flow Meter Instruments for Thermal Conductivity 29 / Thermal Expansion 17 Conference*.

Walker, R., & Pavía, S. (2011). Physical properties and reactivity of pozzolans, and their influence on the properties of lime–pozzolan pastes. *Materials and Structures*, *44*(6), 1139–1150. https://doi.org/10.1617/s11527-010-9689-2

Walker, R., Pavia, S., & Mitchell, R. (2014). Mechanical properties and durability of hemp-lime concretes. *Construction and Building Materials*, *61*, 340–348. https://doi.org/10.1016/j.conbuildmat.2014.02.065

Williams, J., Lawrence, M., & Walker, P. (2017). The influence of the casting process on the internal structure and physical properties of hemp-lime. *Materials and Structures*, *50*(2), 108. https://doi.org/10.1617/s11527-016-0976-4

Chapter 4 : Hygrothermal and Mechanical Characterization of Novel Hemp-lime Composites with Enhanced Consistency[1]

4.1. Introduction

Bio-based construction materials have captured the attention of research and industry sectors over the last decade, mainly due to their carbon sequestration ability and superior hygrothermal properties [Barnat-Hunek et al., 2015]. As such, they pose a sustainable solution for developing an energy-efficient, carbon-zero built environment with a healthy indoor environment [Sinka et al., 2015]. HLC, or hempcrete, are among the most recognized and broadly used bio-based materials globally [Abdellatef et al., 2020]. Analogous to other bio-based construction materials with high porosity, hemp-lime composites are known to be sensitive to many factors affecting their performance that fall into two broad categories: properties of natural lignocellulosic constituencies (shiv/hurd) and manufacturing or construction approaches [Sáez-Pérez et al., 2020]. In this respect, hemp shiv exhibits highly variable granulations and sizes depending on the decortication process and the industrial hemp variety [Brzyski et al., 2020]. Simultaneously, the distribution of hemp shiv particle sizes has a crucial effect on the thermal and mechanical properties of the resulting composite [Stevulova et al., 2012].

Several studies investigated the impact of shiv particle size on the hygrothermal and mechanical properties of hemp-lime composites. While they all reported the relevance of this impact, their findings may seem discrepant, raising the need for further investigation of the impact of particle size on hygrothermal and mechanical properties of hemp-lime composites [Sáez-Pérez et al., 2020].

[1] This chapter is an abridged version of the published paper: Mahmood O., Kavgic M., Noel M. (2024). Hygrothermal and mechanical characterization of novel hemp-lime composites with enhanced consistency. *Construction and Building Materials, Volume 450*. https://doi.org/10.1016/j.conbuildmat.2024.138720.

Manufacturing is another crucial factor affecting hemp-lime performance due to the material's anisotropic behavior, which may yield different mechanical and thermal properties based on the direction in which the material is tested [Brzyski et al., 2021]. In real-world applications, hemp-lime composites are applied via spraying, casting on-site, or installing precast products (e.g., panels, blocks) [Williams et al., 2016]. Regardless of the method, the compaction level, the depth of the layer, and the direction of compaction can significantly affect the distribution of density, thermal conductivity, compressive and tensile strength, and capillary rise [Nguyen et al., 2009].

Previous studies indicate that hemp-lime composites' mechanical and hygrothermal properties significantly vary depending on the hemp particle size, orientation, and compaction level, hindering their reproducibility and consistent quality. Commercial, large-scale application of hemp-lime composites requires natural constituent properties and manufacturing procedures to be standardized and easily controlled. This study addresses these challenges by proposing a new integrated approach combining uniformly reduced-in-size hemp shivs with vibration as a casting process to produce consistent quality and performance hemp-lime samples. Hence, this is the first study to address the following critical research objectives: (i) to combine finely ground hemp particles and vibration techniques to develop consistent hemp-lime composite materials, (ii) to investigate the impact of uniformly reduced hemp shiv particle sizes obtained through a grinding process on the hygrothermal and mechanical performance of hemp-lime composites, (iii) to evaluate the effectiveness of the vibration process in producing hemp-lime samples with consistent physical properties, and (iv) to decrease the hemp-lime composites' thermal conductivity and carbon footprint through the increased content of natural constituencies. Hemp-lime samples were created using hemp shives that were ground to four different particle sizes (4.52, 1.33, 0.96, and 0.72 mm) and three different binder-to-hemp ratios (1:1, 1:1.5, 1:2.4). All hemp-lime samples were

manufactured through a vibration process to achieve three different target dry densities within a tolerance of +/-3.5%. The samples' hygrothermal and mechanical behaviors were experimentally investigated following relevant standards.

4.2. Materials and Methods

4.2.1. Hemp Shiv

The hemp-lime samples were created from hemp shiv, hydrated lime, slag, and water. The hemp shivs used in this study were provided by a local Canadian producer (Terrafibre). Four types of hemp shiv with different fractions were considered in this study, as shown in Figure 4.1-a. The first type was the received (R) shiv, while other types were reduced in size to various degrees: coarse-size (C), medium-size (M), and fine-size (F), produced by grinding the received shivs using an industrial grinder (JTANGL Electric Grain Grinder Mill, 3000W).

Figure 4.1-b shows the particle size distribution, and Table 4.1 summarizes the physical properties of the hemp shiv used in this study. The sieve sizes at which 90% (D_{90}) of the total particles pass were 4.52, 1.33, 0.96, and 0.72 mm, and the sieve sizes corresponding to 50% pass particle sizes (D_{50}) were 2.59, 0.74, 0 .54, and 0.30 mm for R, C, M, and F shiv particles, respectively.

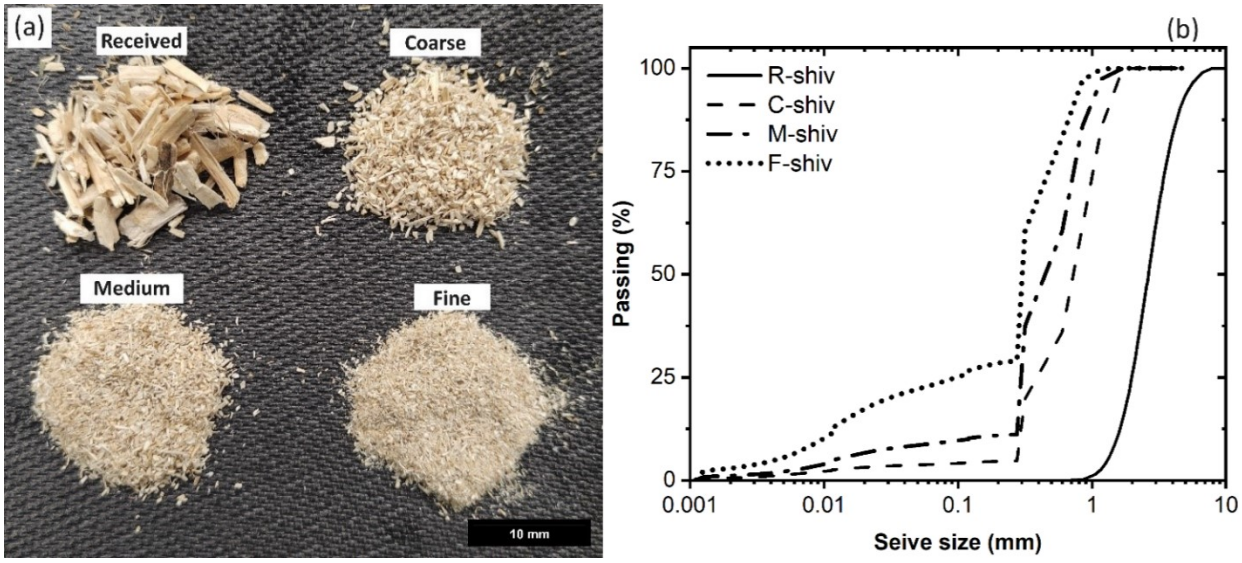

Figure 4.1 Hemp shivs that were used in this study (a) and their particle size distribution were determined by image analysis, mechanical sieving, and laser diffraction (b).

Table 4-1 Physical properties of four hemp shiv types.

Property	Hemp shiv type			
	Received	Coarse	Medium	Fine
Bulk density (kg/m^3)	94	104	107	114
Initial moisture content (%)	7.20	6.94	7.38	7.52
Hemp fibre content (%)	8.91	8.32	9.03	9.12
Water absorption				
IRA %	150.08	137.26	142.91	139.91
K_1	47.42	51.88	52.94	52.79
*D_{90} (mm)	4.52	1.33	0.96	0.72
**D_{50} (mm)	2.59	0.74	0.54	0.30

*90% of the total particles are smaller than the specified sizes.
** A cumulative 50% point of diameter (or 50% pass particle size).

4.2.2. Composition of Hemp-Lime Specimens

Table 4.2 summarizes the mix ratios and percentages by mass of hemp-lime samples produced from four types of shiv particle sizes (R, C, M, and F) using three B/H ratios (50/50, 40/60, and 30/70). It should be mentioned that it was unfeasible to create a robust sample with a 1:2.4 (30/70) ratio with the R-shiv received from the manufacturer because the samples kept collapsing when demolding and handling. This finding indicates that reducing and standardizing the shiv particle

size is necessary to increase the share of the bio-based component in the hemp-lime mix design. Such behavior could be attributed to the improved cohesion forces, contact, interfacial bonding, packing, and connection between the lignocellulosic particles and the cementitious binder by reducing hemp particle sizes and enhancing homogeneity. Simultaneously, voids and gaps were reduced, resulting in a more robust and compact material less prone to collapse, even with a hemp content of 70%. Furthermore, the hygroscopic nature of hemp shivs helps regulate moisture levels within the material, contributing to a healthier indoor environment and moisture management by absorbing excess moisture and releasing it when humidity levels decrease. Nevertheless, the hygroscopic properties of hemp shiv can lead to the binder's incompletion of the hydration process. Hence, the quantity of water incorporated into the mixture was calculated considering both the requisite amount for binder hydration and the water absorption capacity of the hemp shiv.

Table 4-2 Composition of the hemp-lime samples.

B/H ratio	*Name	Mix % by mass			
		Lime	Slag	Hemp	Water
50/50	R50	13.40	3.35	16.75	67.00
	C50				
	M50				
	F50				
40/60	R60	10.00	2.50	18.75	68.75
	C60				
	M60				
	F60				
**30/70	C70	7.05	1.77	20.58	70.60
	M70				
	F70				

* R-received; C-coarse; M-medium; F-fine.

**It was impossible to create a robust 30/70 sample with the shiv received from the manufacturer.

4.3. Results and Discussion

4.3.1. Dry Density

Table 4.3 summarizes the descriptive statistics of dry densities of the hemp-lime samples created using three B/H ratios (1:1, 1:1.5, and 1:2.4) and three hemp shiv particle sizes (received - R, coarse - C, medium - M, and fine - F). Results show a low variability between the dry densities for all B/H ratio categories and sizes of hemp shiv particles. In this regard, all samples' coefficient of variation (CV) is between 0.16 and 2.36%. The samples with the F-shiv type exhibited the lowest variability, averaging a CV of 0.56%. The hemp-lime samples with the highest targeted density of 200 kg/m³ and B/H ratio of 1:1 exhibited the highest variability, averaging 1.84 kg/m³. The consistency achieved in dry densities shows the efficiency of the applied production method, potentially leading to a consistent, repeatable, and reliable mechanical and hygrothermal performance of hemp-lime composites.

Table 4-3 Descriptive statistics of samples' dry densities.

Mix ID	Target density (kg/m^3)	Dry density (kg/m^3)			
		Mean	Maximum	Minimum	Coefficient of variation %
R50	200	193.30	193.90	192.72	0.31
C50		200.75	202.49	198.97	0.88
M50		199.80	203.27	196.20	1.77
F50		200.12	201.80	199.10	0.73
R60	170	166.02	167.73	164.80	0.92
C60		166.89	167.18	166.70	0.16
M60		168.97	173.50	166.02	2.36
F60		169.87	170.51	169.24	0.37
*C70	140	140.67	143.80	138.53	1.97
M70		142.38	143.12	141.15	0.75
F70		143.92	144.98	142.89	0.59

*It was impossible to create a robust 30/70 sample with the shiv received from the manufacturer.

Figure 4.2 compares the variation in dry density of the samples produced in this study against the previous research that focused on similar densities. The vibrated hemp-lime samples exhibited

superior dry density consistency within the targeted weight categories. For example, when using manual tamping as a compaction method to achieve the required density [Abdellatef et al., 2020], a variation of 17.83 kg/m³ was introduced. Moreover, when machine press compaction and projection process were used [Elfordy et al., 2008; Nguyen et al., 2009] to produce hemp-lime samples, a significant variation in densities was produced with a CV of around 16%. Variations in density were reported within the same sample types where an axial gradient of compactness is observed inside the specimen. Specifically, the density of material near the piston (upper part of the cylinders) was higher than that of material in the lower part. Similar density fluctuations were also noted in the projection process [Elfordy et al., 2008; Nguyen et al., 2009]. Having such high variation can cause a significant impact on the mechanical and thermal properties as they are both heavily dependent on the density.

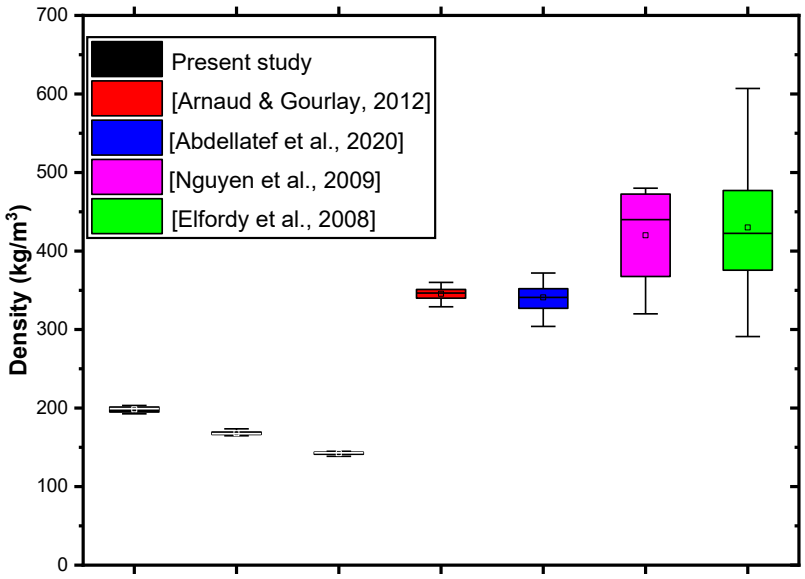

Figure 4.2 Density variation comparison with other studies.

4.3.2. Compressive Strength

When examining low-strength construction materials such as hemp-lime composites, it is essential to understand the insights gained from testing the material's compressive strength, especially in non-structural applications. While not intended for load-bearing, compressive strength can be a useful measure of relative performance or quality between similar materials. Hence, compressive strength may indicate how well the material can fulfill its intended purpose within its specific environment, considering aspects like durability, constructability in handling, transporting, and installing, and compatibility with other components in the construction assembly. Figure 4.3-a depicts the hemp-lime samples' two distinct mechanical failure behaviors under continuously applied compressive load. Samples with received shiv behaved as bilinear materials, whereby the curve could be divided into two distinct regions. The first linear phase occurs when the binder fails, and initial cracks propagate. The second linear phase represents significant deformation with less stress development increase than the first. In this phase, the cracking noises became louder, indicating the collapse of the hemp particles, providing additional strength by increasing the contact between those particles. In contrast, hemp-lime samples made of hemp shiv powder exhibited collapse similar to a shear failure, regardless of the particle size. Three different regions can be observed in the stress-strain response: the ascending portion, the peak point or the maximum compressive stress point where the behavior is no longer linear, and finally, the descending portion, where the curve shows a descending trend after reaching maximum stress.

The stress-strain curve for all samples shows a significant ability of the material to deform under loading before total failure, registering a high level of strains in the range of 0.087-0.26 mm/mm. This behavior could make the hemp-lime composite resilient in earthquake regions as it sustains

high deformation before failure. Similar findings were also confirmed by previous literature [Brzyski et al., 2020].

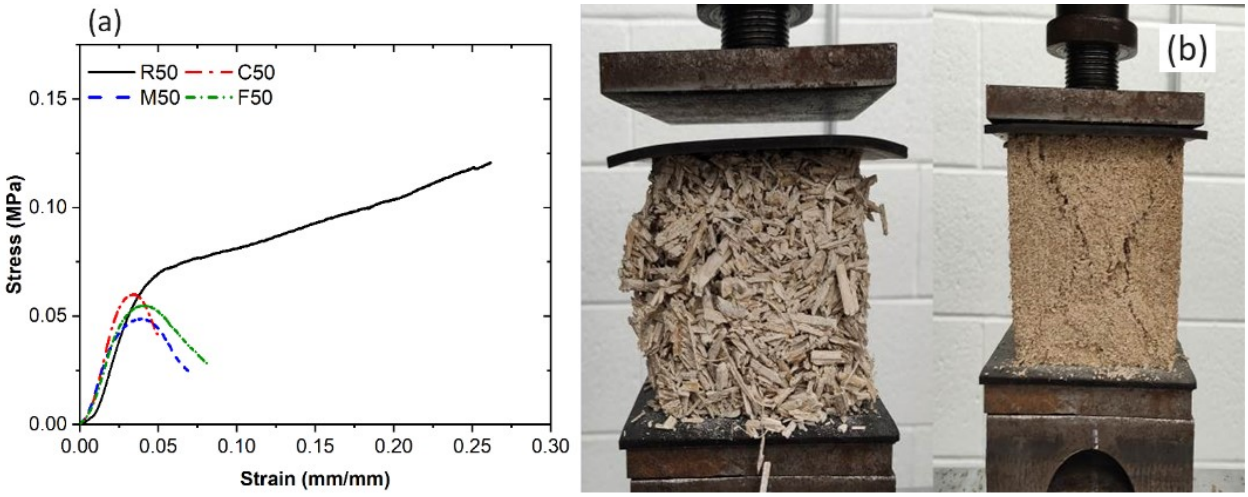

Figure 4.3 Typical stress-strain curve for hemp-lime samples (a); Compressive Strength test, hemp-lime cubes after crushing (b).

As shown in Table 4.4, the prepared hemp-lime samples displayed satisfactory mechanical performance for such low densities when compared with faced rigid thermal insulation boards [ASTM C1289, 2022]. Thus, the average compressive strength ranged between 0.033 MPa and 0.11 MPa. Similar to the findings of other studies [Elfordy et al., 2008; Williams et al., 2017; Abdellatef et al., 2020], the compressive strength is directly proportional to dry density and inversely proportional to the increase in hemp shiv share. In this respect, samples with B/H ratios 1:1 producing 200 kg/m³ density exhibit the highest compressive strength value. A 35% and 45% reduction in the compressive strength was recorded when the density reduced from 200 kg/m³ to 170 kg/m³ and 140 kg/m³, respectively. The results also show the production method's effectiveness in reducing the variability between the mechanical behavior of hemp-lime composites. The C-type shiv exhibited the lowest variation in compressive strength, with a CV ranging between 4.24 and 8.94%. The findings also show a 32-36% reduction in compressive

strength in the 200 kg/m³ and 170 density groups when received particles were replaced with ground particles. The behavior observed is consistent with the findings of [Brzyski et al., 2020; Stevulova et al., 2012], which reported decreases in strength of 21.6% and 34.4% when larger hemp shivs were used instead of smaller ones.

In contrast, Arnaud & Gourlay [Arnaud & Gourlay, 2012] Show more found that using larger shivs resulted in a 47.5% decrease in compressive strength compared to smaller shivs. The discrepancy may be attributed to the average densities: large shivs had an average density of 1040 kg/m³, while small shivs had an average density of 1150 kg/m³, a 10.57% difference. Such a variation in density can significantly influence compressive strength, as shown in this study, where a 15% reduction in density from 200 kg/m³ to 170 kg/m³ led to about a 40% decrease in average compressive strength.

Table 4-4 Descriptive statistics of samples' compressive strength.

Mix ID	Density category (kg/m³)	Compressive Strength (MPa)		Young's modulus (MPa)	
		Mean	Coefficient of variation %	Mean	Coefficient of variation %
R50	200	0.111	9.91	3.96	7.38
C50		0.070	5.71	3.76	5.01
M50		0.070	7.86	3.27	5.43
F50		0.071	19.72	3.22	13.82
R60	170	0.072	13.89	2.81	8.63
A60		0.047	8.94	2.74	7.62
M60		0.045	19.56	2.93	11.89
F60		0.049	10.00	2.61	6.31
C70	140	0.033	4.24	2.09	3.28
M70		0.036	24.44	1.91	16.32
F70		0.042	14.29	1.82	7.54

Table 4.4 also presents approximate Young's modulus values calculated using the displacement values of the actuator, as it was challenging to mount the compressometer directly to the sample. As shown in Table 4.4, the average modulus of elasticity ranged between approximately 1.82 and 3.96 MPa. Results show a direct relationship between HLC dry density and Young's modulus. In

this respect, a 15% reduction in density from 200 kg/m^3 to 170 kg/m3 led to an approximately 22% decrease in average Young's modulus. Similarly, a further decrease in density from 170 kg/m^3 to 140 kg/m^3 resulted in around 30% reduction in average Young's modulus. Findings also show a negative correlation between Young's modulus and hemp shiv particle size.

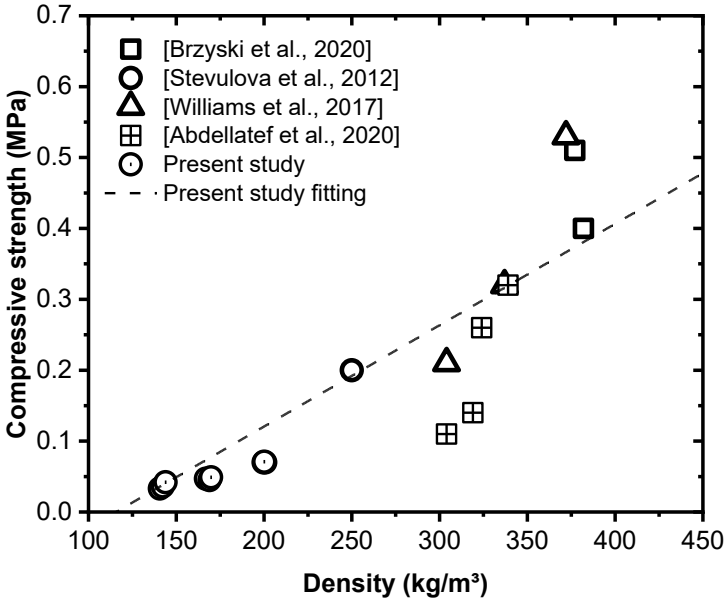

Figure 4.4 Comparison of density and compressive strength with the previous literature.

Figure 4.4 compares the relationship between the density and the compressive strength results obtained from this study and the previous studies that used a hydrated lime-based binder [Brzyski et al., 2020], [Stevulova et al., 2012], [Williams et al., 2017], and [Abdellatef et al., 2020]. As documented in prior studies, the compressive strength and density are directly and inversely proportional [Elfordy et al., 2008; Abdellatef et al., 2020]. Therefore, Figure 4.9 illustrates that when the results of this study are extrapolated to the available range of densities, they align with the findings reported in the previous literature. Bryziki [Brzyski et al., 2020] and Williams [Williams et al., 2017] have reported higher compressive strength values than other studies, which

can be explained using a B/H ratio of 2:1 and 2.25:1, respectively. As reported by previous literature, an increase in binder content in the formulation leads to an almost linear increase in compressive strength [Sáez-Pérez et al., 2020].

4.3.3. Thermal Properties

- **Thermal Conductivity**

Table 4.5 summarizes the results of thermal conductivity measurements. As expected, thermal conductivity is positively linearly correlated with the dry density of the hemp-lime composites [Abdellatef et al., 2020]. Hence, samples with the lowest dry density (140 kg/m³) had the lowest thermal conductivity, ranging from 0.054 to 0.056 W/m K, followed by 170 kg/m³ samples with 0.056-0.062 W/m K, and 200 kg/m³ with the highest thermal conductivity ranging from 0.061 to 0.067 W/m K. It can also be observed that samples made of received shiv particles exhibited the highest thermal conductivity values within density category. Furthermore, the hemp-lime samples made with fine hemp particles tend to have the lowest thermal conductivity despite having the highest or as high density within their respective density categories. In this regard, thermal conductivity was reduced by 8.1-10.4% when using the fine fragments compared to the received. A likely explanation for these findings is a discontinuity in the binder thermal path when using small hemp shiv particles, reducing the overall thermal conductivity of hemp-lime composites. These findings suggest that reducing the hemp shiv particle size benefits the thermal performance of hemp-lime composites.

Table 4.5 also shows the low variability in the thermal conductivity values across the samples at different densities, achieved using the vibration casting technique. Therefore, the CV of all samples was between 3.87 and 8.77%. The samples with the finest particle size exhibited the lowest

variability, recording 3.87, 4.63, and 5.6 % for samples with 200, 170, and 140 kg/m³ density, respectively.

Table 4-5 Descriptive statistics of samples' thermal conductivity.

Mix ID	Mean dry density (kg/m³)	Thermal conductivity (W/m K)			
		Mean	Maximum	Minimum	Coefficient of variation %
R50	193	0.0667	0.0713	0.0612	6.66
C50	201	0.0638	0.0701	0.0589	8.76
M50	200	0.0616	0.0674	0.0581	6.70
F50	200	0.0605	0.0625	0.0572	3.87
R60	166	0.0617	0.0683	0.0573	7.75
C60	167	0.0587	0.0622	0.0562	4.96
M60	169	0.0579	0.0621	0.0555	5.11
F60	170	0.0564	0.0597	0.0532	4.63
C70	141	0.0559	0.0593	0.0538	6.05
M70	142	0.0545	0.0589	0.0522	5.71
F70	144	0.0535	0.0572	0.0502	5.40

Figure 4.5 compares the correlation between dry density and thermal conductivity from this research with other studies [Nguyen et al., 2009], [Brzyski et al., 2020], [Williams et al., 2016], and [Abdellatef et al., 2020]. It can be seen that the thermal conductivity values from this study are 25-65% lower than those reported in previous studies, and correspondingly, the dry densities are also 28-65% lower. To facilitate a seamless comparison, the thermal conductivity results from this study have been extrapolated, considering the nearly linear relationship between density and thermal conductivity [Abdellatef et al., 2020], to match the average densities reported in the other studies presented in Figure 4.5. The extrapolated thermal conductivity values were 0.0775, 0.0828, 0.0778, and 0.07425 W/m K, which correspond to the average densities of (335, 380, 340, and 310 kg/m^3) reported in studies [Nguyen et al., 2009], [Brzyski et al., 2020], [Williams et al., 2017] and [Abdellatef et al., 2020], in that order. The extrapolated values from this study are 18.82%, 11.22%, and 19.16% lower in thermal conductivity compared to the values documented in [Brzyski et al., 2020], [Williams et al., 2017], and [Abdellatef et al., 2020], respectively. The extrapolated thermal

conductivities are only 1.35% higher than those reported by [Nguyen et al., 2009]. These findings suggest that a decrease in hemp particle sizes reduces hemp-lime composites' thermal conductivity, thus improving the material's thermal performance even at higher densities.

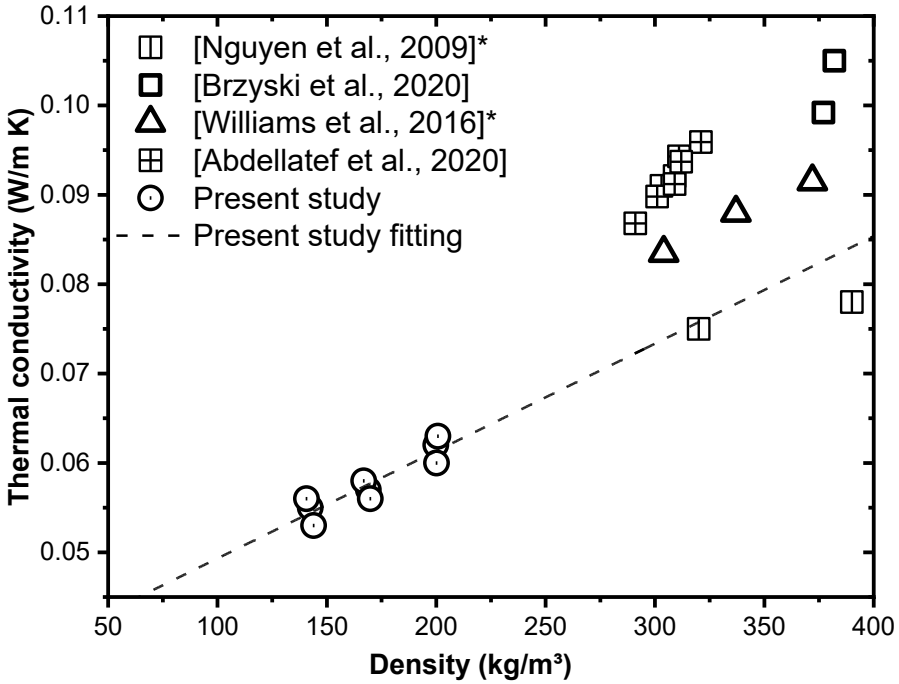

* Samples were tested at 20 °C.
Figure 4.5 Comparing thermal conductivity results with other studies.

- **Thermal Conductivity as a Function of Temperature**

Thermal conductivity was assessed at three distinct temperature levels (12.5°C, 22.5°C, and 32.5°C) to evaluate the performance of hemp-lime composites across various climate zones. The study included selected hemp-lime mixes (F50, F60, and F70) with dry densities of 200 kg/m³, 170 kg/m³, and 140 kg/m³, respectively. These mixes represent the optimal thermal performance within their respective groups, exhibiting the lowest thermal conductivity. Figure 4.6 shows a nearly linear increase in thermal conductivity across all the samples, ranging from 6.6% to 9.8%, with a rise in testing temperature from 12.5 °C to 32.5 °C. These results echo the findings from

previous studies that reported an increase in conductivity of 8.9-10.78 % when the temperature increased from 10 °C to 30°C [Bennai et al., 2017]. This behavior is attributed to the increased thermal conductivity of air entrapped in the sample from 0.0253 W/m K at 12.5°C to 0.0268 W/m K at 32.5°C [Witt, 2002].

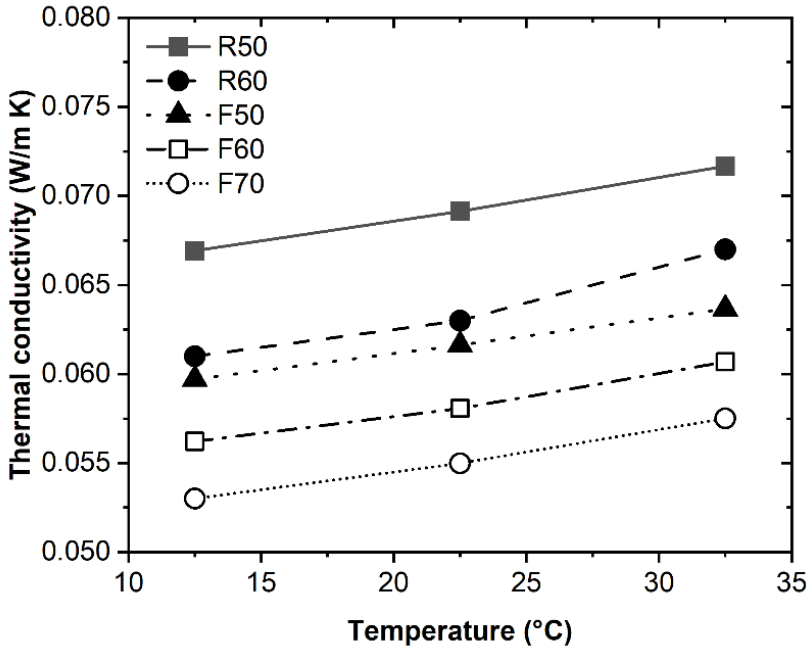

Figure 4.6 Thermal conductivity of different hemp-lime mixes at different testing temperatures.

- **Anisotropy of Thermal Conductivity**

The effect of hemp shiv orientation due to compaction via vibration on thermal conductivity is also investigated due to the inherently anisotropic nature of hemp particles, where thermal conductivity in the direction parallel to the capillaries is higher than in the transversal direction [Nguyen et al., 2009]. In this respect, ISO 10456 standard [ISO 10456, 2023] reports two values with a significant difference reaching up to 27% for the thermal conductivity of wood particles when heat flows along the material fibres versus when heat transfers across the fibres. Previous studies showed a significant effect of the compaction direction of hemp-lime composites on their

thermal conductivity coefficients. For example, Brzyski [Brzyski et al., 2021] has reported a 12% and 16% difference in thermal conductivity in the parallel and perpendicular direction for short (2.74 mm) and long (8.40 mm) hemp shivs, respectively. Williams [Williams et al., 2017] reported that the average thermal conductivity for perpendicularly tested samples was 16% higher than that of parallel-tested samples. Tronet et al. [Tronet et al., 2016] has also reported a 33% directional difference in thermal conductivity, similar to what was reported in [Amziane et al., 2015; Dinh et al., 2015].

In contrast, as presented in Figure 4.7, this study significantly improved the directional difference in thermal conductivity to only 1.2-2.75% when using fine hemp fragments and approximately 6.8% when using R-shiv. The results confirm the previously reported trend as the smaller the hemp shiv, the lower the difference [Brzyski et al., 2021]. It also shows the significant effect of using compaction via vibration, leading to a consistent performance of the hemp composite. The perpendicular thermal conductivity results also have a linear relationship with the dry density, as the lower the density, the lower the conductivity.

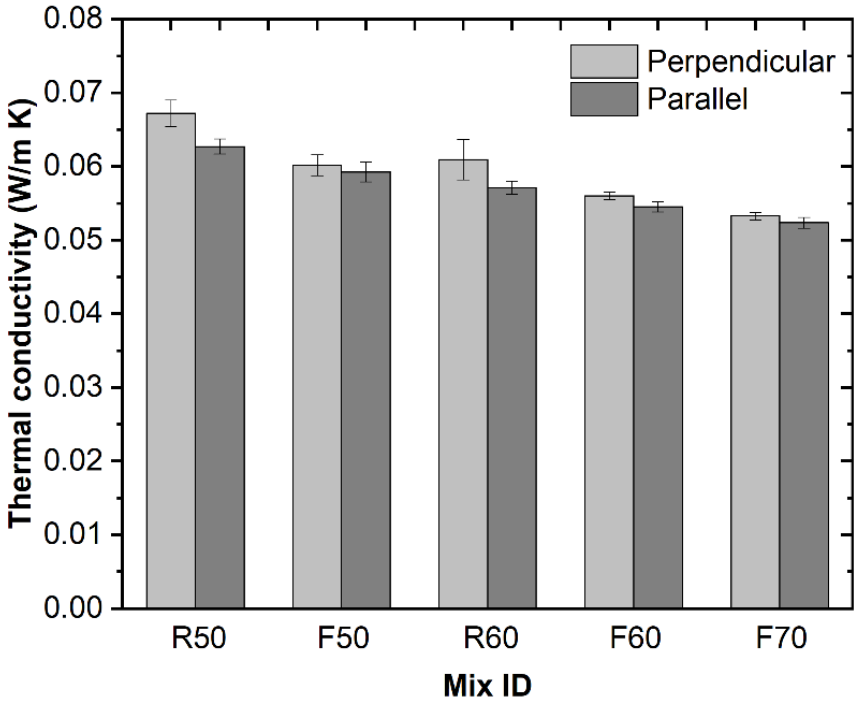

Figure 4.7 Thermal conductivity for different testing directions.

- **Specific Heat Capacity and Thermal Diffusivity**

As shown in Table 4.6, the specific heat capacity of the hemp-lime samples ranged from 672 to 957 J/kg K. As expected, mixes with higher dry density and binder content had higher specific heat capacity, meaning more heat energy is needed to raise their temperature. For instance, 200 kg/m³ samples had around 28% higher average specific heat capacity than 140 kg/m³ samples and approximately 15% higher than 170 kg/m³ samples. The findings also show no tangible effect of the hemp shiv size on the specific heat values, concluding that hemp composites are more susceptible to density and binder ratio than hemp shiv size [Brzyski et al., 2020]. The results also confirm the general trend of the linear relationship between hemp-lime's density and specific heat capacity. Previous studies echoed these findings. For example, in [de Bruijn et al., 2009], two different mixes, A (394.8 kg/m³) and B (298.1 kg/m³), with binder-to-hemp mass ratios of 1.8 and 1.13, respectively, have been investigated. The study found that mix B, which had a higher hemp

content and lower dry density, exhibited an average specific heat capacity of 333 J/kg K, approximately 13.5% lower than mix A, which had a lower hemp content and higher dry density, with a specific heat capacity of 385 J/kg K.

Thermal diffusivity measures a material's ability to conduct heat relative to its ability to store thermal energy, quantifying the rate at which temperature changes propagate through the material over time [de Bruijn et al., 2009] . Building materials with low thermal diffusivity reduce heat exchange with their surroundings, leading to improved energy efficiency and thermal comfort for occupants [Abdellatef et al., 2020]. Thermal diffusivity of all samples ranged between 0.321 (m^2/s) $x10^{-6}$ and 0.585 (m^2/s) $x10^{-6}$, with averages of 0.338, 0.433, and 0.565 (m^2/s) $x10^{-6}$ for samples with 200, 170, and 140 kg/m^3 density categories, respectively. The densest (200 kg/m^3) samples exhibited around 40% lower thermal diffusivity than the lightest (140 kg/m^3) and approximately 22% lower than the 170 kg/m^3 hemp-lime samples. These findings were expected considering the interdependency between thermal diffusivity, thermal conductivity, and density (see Equation 3.8). Furthermore, the high thermal diffusivity of air of 18.69 (m^2/s) $x10^{-6}$ [Massman, 1999] increased the thermal diffusivity of low-density samples. These findings echo previous studies [Abdellatef et al., 2020; de Bruijn et al., 2009; Reilly et al., 2019]. The results also show a lower diffusivity value for samples with smaller hemp fragments. For example, F-type shiv particles were around 13% and 11% lower than R-type shiv for 200 and 170 kg/m^3 density samples. Such reduction could be attributed to filling the air gap between constituents when small hemp shiv particles were used.

Table 4-6 Average specific heat capacity and thermal diffusivity.

Mix ID	Dry density category (kg/m³)	Ave. Specific heat capacity (J/kg K)	Coefficient of variation %	Ave. Thermal diffusivity (m^2/s) $x10^{-6}$	Coefficient of variation %
R50	200	942	4.21	0.368	3.23
C50		931	6.79	0.337	5.75
M50		957	3.01	0.324	4.39
F50		933	2.26	0.321	3.56
R60	170	803	6.43	0.458	6.93
C60		798	5.27	0.436	4.22
M60		782	2.68	0.431	3.71
F60		811	4.11	0.406	5.03
C70	140	681	5.79	0.585	4.68
M70		672	4.38	0.575	3.41
F70		689	4.17	0.534	3.79

- **Moisture Buffer Value**

Moisture buffering ability plays a vital role in regulating the fluctuation in humidity in internal spaces. As illustrated in Figure 4.8, all the samples showed an excellent moisture buffering capacity [Rode et al., 2005], as the MBV ranged between 2.06 g/m² RH and 2.53 g/m² RH. The results show a negative correlation between dry density and MBV of hemp-lime composites. In this regard, average MBV values of 140, 170, and 200 kg/m³ samples were 2.47, 2.28, and 2.12 g/m² RH, respectively. A similar trend is confirmed by previous literature, as a high hemp ratio in the composite produces lower density and higher permeability, leading to a high moisture transfer and storage of the material [Mazhoud et al., 2021; Rahim et al., 2015]. Therefore, an increase in the hemp ratio in the hemp composite results in an increase in the moisture capacity, which causes an increase in the MBV. The results also showed an improvement in the MBV when using a smaller hemp shiv size.

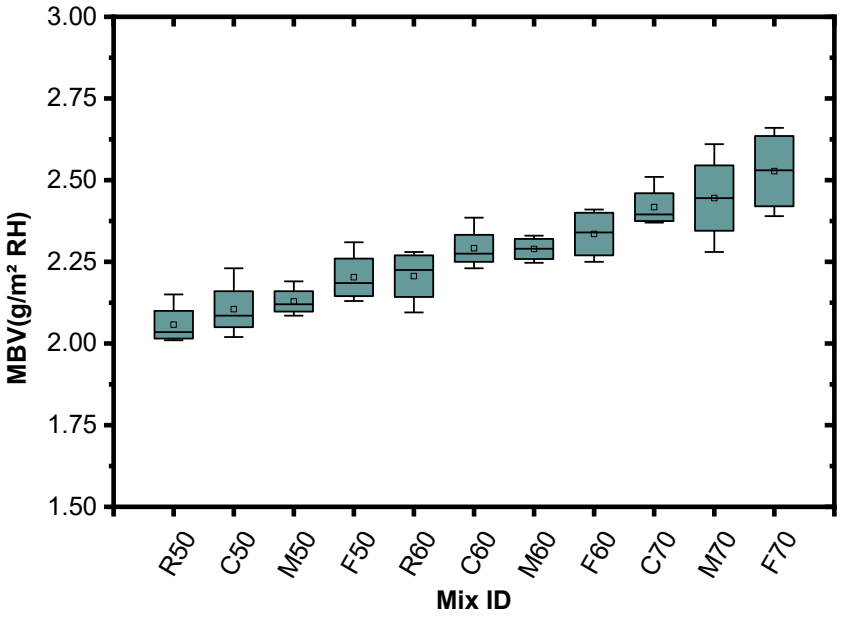

Figure 4.8 MBV values of the hemp-lime samples using the NORDTEST procedure.

Additionally, Figure 4.9 shows the mass change percentage concerning the original sample mass for the F-type shiv when exposed to the humidity cycles during the MBV test. The mass change was determined per the exposed surface area and was measured every four hours. It can be seen that regardless of the B/H ratio, all samples showed similar mass change behavior. The mass change profile consists of two phases: the mass phase increases when the humidity level is 75%, while the decreasing phase occurs at a 33% humidity level. For both phases, the initial hours 0-8 hours record the highest rate of mass change, and then the change rate decreases with time. It can also be seen that the higher the hemp shiv ratio, the higher the mass change gain; thus, F70 samples have the highest mass gain. This behavior is attributed to the high absorption capacity of the hemp compared to the binder.

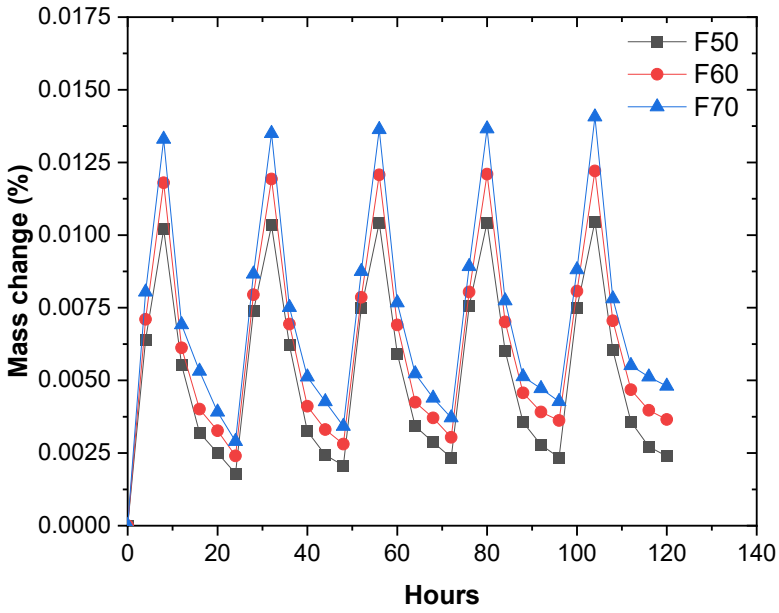

Figure 4.9 Mass change of the hemp-lime samples when subjected to varying relative humidity at room temperature.

Figure 4.10 compares the uptake moisture buffering capacity at oven-dry as an initial condition for the three groups used in the study with B/H ratios 1:1, 1:1.5, and 1:2.4. It can be seen that the moisture buffering capacity starts at high values ranging between 2.5 g/m² RH and 3.6 g/m² RH then it starts decreasing until reaching steady-state by the third cycle. This increase is attributed to the high absorption capacity of the hemp-lime samples when they have low moisture content, whereas higher initial moisture content leads to lower absorption. Figure 4.10 shows a distinct behavior for the R-type hemp-lime samples where the decrease in the absorption from the first cycle takes longer than that of other types as they have a lower surface area. It can be concluded that hemp-lime composites with lower particle size can achieve moisture stability faster, leading to better moisture control performance.

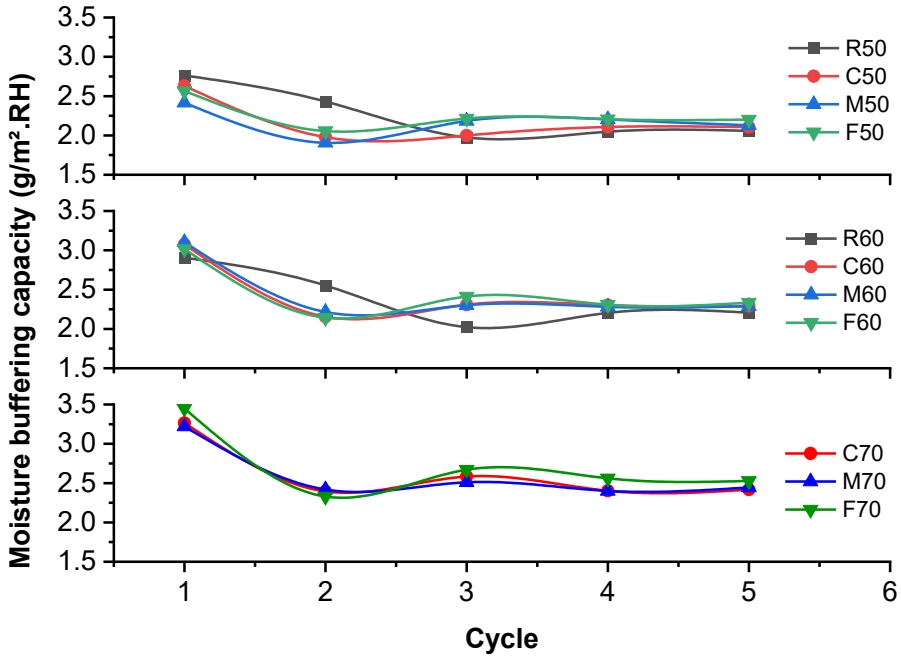

Figure 4.10 Moisture buffering capacity with cycles.

4.4. Conclusions

The principal conclusions drawn from this study and limitations that guide future research directions can be summarized as follows:

- The experimental findings highlight the significance of reducing and standardizing the shiv particle size, resulting in a notable enhancement in material consistency and a reduction in variations across mechanical and hygrothermal properties among samples of the same targeted density. Furthermore, this reduction in particle size was pivotal in achieving a 70% weight share of the bio-based component in the hemp-lime mix design. Subsequent research endeavors should delve into the effects of particle size reduction and augmented hemp shive content on properties such as fire resistance, freeze-thaw behavior, biological degradation, and durability.

- Employing vibration as a compaction method significantly enhanced the consistency and repeatability of the produced densities, showcasing a less than 3.5% variation. Hence, the density disparities between the initial and fine hemp fragments were also negligible. Given the substantial influence of density on the hygrothermal and mechanical properties of hemp-lime composites, attaining such uniformity facilitates the material's adoption in the construction industry and large-scale applications. Consequently, future endeavors should prioritize optimizing hemp-lime composite mix designs tailored for various applications in building envelopes (walls, floors, ceilings), envelope component designs (blocks, panels), and installation methods (sprayed-in, precast).
- Although the hemp-lime composite may not match the structural capabilities of other load-bearing construction materials, it does fall within the compressive strength range of faced rigid insulation materials ranging between 0.11 and 0.965 MPa. Future research could explore alternative binder mix designs, incorporating pozzolans such as metakaolin, silica fume, and fly ash. In addition to enhancing mechanical properties, these pozzolans have the potential to positively influence the long-term alkalinity and durability of hemp-lime composites. Subsequent research should further optimize the binder mix design and distribution between hydrated lime and added pozzolans. Additionally, adjustments to the binder-to-hemp ratio could be made to meet specific mechanical requirements.
- The received shiv exhibited a 60% increase in strength compared to fine fragments and demonstrated a distinct failure pattern characterized by bi-linear behavior, contrasting with the shear failure mode observed in fine fragments. Subsequent investigations should prioritize optimizing the particle size distribution by exploring various ratios of coarse and fine particles, aiming to enhance compressive strength while minimizing thermal conductivity.

- Hemp-lime samples containing fine hemp fragments displayed an approximate 13% decrease in thermal conductivity compared to those with received shivs. This observation suggests that thermal conductivity is influenced by shiv size since uniformly reducing hemp particle size diminished areas containing predominant binder content with an inherently higher thermal conductivity than hemp shivs. Future research should focus on optimizing the smallest particle size of hemp shivs and determining its threshold to prevent unnecessary expenditure of energy and resources on grinding and preprocessing. Furthermore, developing a detailed and validated finite element or finite volume thermal model could provide further insight and explanation of the experimental results.
- The results demonstrate a noteworthy enhancement in the directional difference of thermal conductivity, reduced to less than 3% when employing fine hemp fragments. These findings suggest that the proposed hemp shiv reduction approach could facilitate the creation of building envelope components with uniform thermal properties. In addition, it could enable the development of building envelopes with predictable thermal performance, accommodating various installation methods such as projection, precast, and printing.
- Hemp-lime mixes with a higher hemp-to-binder ratio demonstrate improved moisture control, attributed to hemp's greater moisture storage capacity than the binder mixture. Additionally, reducing the hemp size enhances the moisture buffer value by increasing the exposed surface area to the outside environment. However, further investigation is warranted to confirm this behavior conclusively. Additionally, the impact of air velocity on the variations in moisture buffer values should be investigated.

4.5. References

Abdellatef, Y., Khan, M. A., Khan, A., Alam, M. I., & Kavgic, M. (2020). Mechanical, Thermal, and Moisture Buffering Properties of Novel Insulating Hemp-Lime Composite Building Materials. *Materials*, *13*(21), 5000. https://doi.org/10.3390/ma13215000

Amziane, S., Nozahic, V., & Sonebi, M. (2015). Design of mechanically enhanced concrete using hemp shiv. *Academic Journal of Civil Engineering*, *33*(2), 422–426. https://doi.org/10.26168/icbbm2015.65

Arnaud, L., & Gourlay, E. (2012). Experimental study of parameters influencing mechanical properties of hemp concretes. *Construction and Building Materials*, *28*(1), 50–56. https://doi.org/10.1016/j.conbuildmat.2011.07.052

ASTM International. (2022). Standard Specification for Faced Rigid Cellular Polyisocyanurate Thermal Insulation Board (ASTM C1289-22a).

Barnat-Hunek, D. , Smarzewski, P. & FicS. (2015). Mechanical and Thermal Properties of Hemp-Lime Composites. Compos. *Theory Pract. , vol. 15.*

Bennai, F., Issaadi, N., Abahri, K., Belarbi, R., & Tahakourt, A. (2018). Experimental characterization of thermal and hygric properties of hemp concrete with consideration of the material age evolution. *Heat and Mass Transfer*, *54*(4), 1189–1197. https://doi.org/10.1007/s00231-017-2221-2

Bourdot, A., Moussa, T., Gacoin, A., Maalouf, C., Vazquez, P., Thomachot-Schneider, C., Bliard, C., Merabtine, A., Lachi, M., Douzane, O., Karaky, H., & Polidori, G. (2017). Characterization of a hemp-based agro-material: Influence of starch ratio and hemp shive size on physical, mechanical, and hygrothermal properties. *Energy and Buildings*, *153*, 501–512. https://doi.org/10.1016/j.enbuild.2017.08.022

Brzyski, P., Gładecki, M., Rumińska, M., Pietrak, K., Kubiś, M., & Łapka, P. (2020). Influence of Hemp Shives Size on Hygro-Thermal and Mechanical Properties of a Hemp-Lime Composite. *Materials*, *13*(23), 5383. https://doi.org/10.3390/ma13235383

Brzyski, P., Gleń, P., Gładecki, M., Rumińska, M., Suchorab, Z., & Łagód, G. (2021). Influence of the Direction of Mixture Compaction on the Selected Properties of a Hemp-Lime Composite. *Materials*, *14*(16), 4629. https://doi.org/10.3390/ma14164629

de Bruijn, P. B., Jeppsson, K.-H., Sandin, K., & Nilsson, C. (2009). Mechanical properties of lime–hemp concrete containing shives and fibres. *Biosystems Engineering*, *103*(4), 474–479. https://doi.org/10.1016/j.biosystemseng.2009.02.005

Dinh, T. M., Magniont, C., Coutand, M., & Escadeillas, G. (2015). Hemp concrete using innovative pozzolanic binder. *Academic Journal of Civil Engineering*, *33*(2), 265–270. https://doi.org/10.26168/icbbm2015.40

Elfordy, S., Lucas, F., Tancret, F., Scudeller, Y., & Goudet, L. (2008). Mechanical and thermal properties of lime and hemp concrete ("hempcrete") manufactured by a projection process. *Construction and Building Materials*, *22*(10), 2116–2123. https://doi.org/10.1016/j.conbuildmat.2007.07.016

European Committee for Standardization. (2007). Building materials and products — Hygrothermal properties — Tabulated design values and procedures for determining declared and design thermal values (ISO 10456:2007).

Incropera, DeWitt, Bergman, & Lavine. (2006). *Fundamentals of Heat Transfer*. Wiley.

Massman, W. J. (1999). Molecular diffusivities of Hg vapor in air, O2 and N2 near STP and the kinematic viscosity and thermal diffusivity of air near STP. *Atmospheric Environment*, *33*(3), 453–457. https://doi.org/10.1016/S1352-2310(98)00204-0

Mazhoud, B., Collet, F., Prétot, S., & Lanos, C. (2021). Effect of hemp content and clay stabilization on hygric and thermal properties of hemp-clay composites. *Construction and Building Materials*, *300*, 123878. https://doi.org/10.1016/j.conbuildmat.2021.123878

Nguyen, T.-T., Picandet, V., Amziane, S., & Baley, C. (2009). Influence of compactness and hemp hurd characteristics on the mechanical properties of lime and hemp concrete. *European Journal of Environmental and Civil Engineering*, *13*(9), 1039–1050. https://doi.org/10.1080/19648189.2009.9693171

Rahim, M., Douzane, O., Tran Le, A. D., Promis, G., Laidoudi, B., Crigny, A., Dupre, B., & Langlet, T. (2015). Characterization of flax lime and hemp lime concretes: Hygric properties and moisture buffer capacity. *Energy and Buildings*, *88*, 91–99. https://doi.org/10.1016/j.enbuild.2014.11.043

Reilly, A., Kinnane, O., Lesage, F. J., McGranaghan, G., Pavía, S., Walker, R., O'Hegarty, R., & Robinson, A. J. (2019). The thermal diffusivity of hemplime, and a method of direct measurement. *Construction and Building Materials*, *212*, 707–715. https://doi.org/10.1016/j.conbuildmat.2019.03.264

Rode, C., Peuhkuri, R., Hanssen, K., Time, B., Svennberg, K., Arfvidsson, J. A., & Ojanen, T. (2005). NORDTEST - Project on moisture buffer value of materials: 26th AIVC Conference. *Ventilation in Relation to the Energy Performance of Buildings*.

Sáez-Pérez, M. P., Brümmer, M., & Durán-Suárez, J. A. (2020). A review of the factors affecting the properties and performance of hemp aggregate concretes. *Journal of Building Engineering*, *31*, 101323. https://doi.org/10.1016/j.jobe.2020.101323

Sinka, M., Radina, L., Sahmenko, G., Korjakins, A., & Bajare, D. (2015). Enhancement of lime-hemp concrete properties using different manufacturing technologies. *Academic Journal of Civil Engineering*, *33*(2), 301–308. https://doi.org/10.26168/icbbm2015.46

Stevulova, N., Kidalova, L., Junak, J., Cigasova, J., & Terpakova, E. (2012). Effect of Hemp Shive Sizes on Mechanical Properties of Lightweight Fibrous Composites. *Procedia Engineering*, *42*, 496–500. https://doi.org/10.1016/j.proeng.2012.07.441

Tronet, P., Lecompte, T., Picandet, V., & Baley, C. (2016). Study of lime hemp concrete (LHC) – Mix design, casting process and mechanical behaviour. *Cement and Concrete Composites*, *67*, 60–72. https://doi.org/10.1016/j.cemconcomp.2015.12.004

Williams, J., Lawrence, M., & Walker, P. (2016). A method for the assessment of the internal structure of bio-aggregate concretes. *Construction and Building Materials*, *116*, 45–51. https://doi.org/10.1016/j.conbuildmat.2016.04.088

Williams, J., Lawrence, M., & Walker, P. (2017). The influence of the casting process on the internal structure and physical properties of hemp-lime. *Materials and Structures*, *50*(2), 108. https://doi.org/10.1617/s11527-016-0976-4

Chapter 5 : Influence of Fibre Content and Length on the Hygrothermal and Mechanical Performance of Hemp-Lime Composites[2]

5.1. Introduction

Despite the growing interest in hemp-lime composites, the lack of standardized methods for determining hemp shiv purity and fibre content presents a significant barrier to understanding the role of fibre inclusions in HLC performance. As a result, limited research has systematically examined how residual fibre content within commercially processed shiv influences the thermal and mechanical properties of HLC. Addressing this gap is essential not only for advancing material performance but also for promoting more sustainable and economically viable bio-based construction practices.

Addressing this gap, the present study provides the first controlled experimental investigation into the combined influence of hemp fibre content and length on the hygrothermal and mechanical properties of HLC. Unlike prior work, this study employs rigorously defined formulations and standardized testing methods to assess performance metrics across a wide range of fibre conditions. The primary novelty and research objectives of this study are defined as follows: (i) identifying how varying hemp fibre contents (10%, 20%, and 40%) influence the hygrothermal and mechanical properties of HLC; (ii) investigating the impact of fibre length (1.15 mm, 6 mm, 12 mm, and 25 mm) on these same performance properties; and (iii) assessing the effectiveness of reducing hemp fibre size to achieve more consistent and desirable HLC properties [Mahmood et al., 2024]. For this purpose, hemp-lime samples were produced using a consistent binder-to-hemp ratio of 1:1, deliberately chosen to enhance sustainability by increasing natural content and reducing the overall carbon footprint. All samples were fabricated using a vibration compaction

[2] This chapter has been submitted for review in Energy and Buildings.

method to consistently attain a specified dry density, maintaining a tolerance margin of ±3.0%. The mechanical and hygrothermal performance of the composites were systematically evaluated using standardized testing protocols, providing critical new insights that support the development of high-performance, sustainable, and scalable bio-based building materials.

5.2. Materials and Methods

5.2.1. Hemp Fibres and Shives

The hemp shivs used in this study were provided by a local Canadian producer (Terrafibre). Hemp fibres were initially separated from hemp shivs using the floating technique [Mahmood et al., 2024], enabling the preparation of hemp samples with precisely controlled fibre content ratios. Secondly, the hemp shivs were milled to 0.73 mm using an industrial grinder (JTANGL Electric Grain Grinder Mill, 3000W) to improve the consistency and performance of the produced HLC (the effect of hurd size is reported in Chapter 4 [Mahmood et al., 2024]. Subsequently, two types of fibres were created: fine fibres (1.15 mm) produced using an industrial grinder and long fibres (6, 12, 25 mm ± 0.5 mm) produced by manual cutting, as illustrated in Figure 5.1. Lastly, hemp samples with different fibre ratios were produced by adding the cut fibres to the hemp shivs to achieve the desired mass ratios (10, 20, and 40%). Different approaches have been explored in the literature to analyze hemp shivs and fibres [Mahmood et al., 2024]. The hemp shivs and fibre samples underwent tests to assess density, water absorption, particle size distribution, and moisture content. These tests adhered to the same methodologies described in Chapter 4, specifically Section 3.2.2.

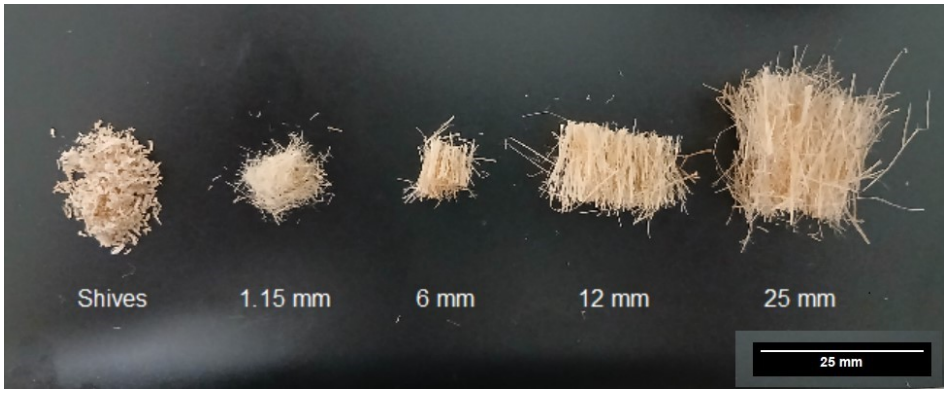

Figure 5.1 Hemp shivs and fibres in this study.

Table 5-1 Physical properties of hemp shivs and fibres.

Property	Hemp				
	Shivs	Fibres			
		1.15 mm	6 mm	12 mm	25 mm
Bulk density (kg/m^3)	114	57.32	53.91	51.76	51.15
Initial moisture content (%)	6.94	7.52	8.65	7.13	8.03
Water absorption					
IRA %	137.26	139.91	134.23	135.48	132.67
K_1	51.88	52.79	50.18	49.05	51.32

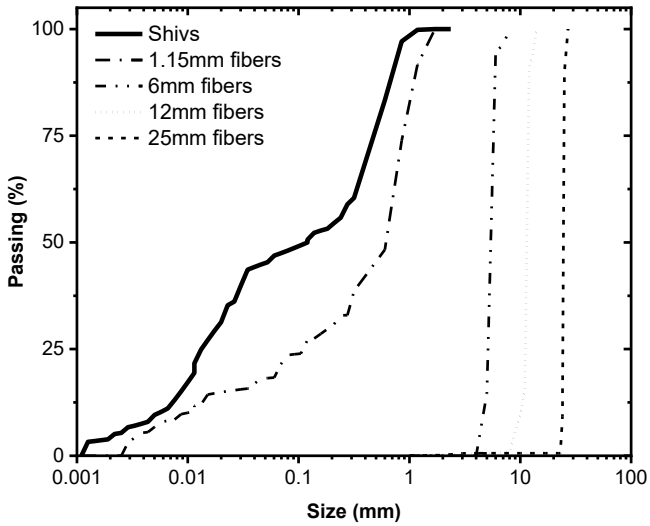

Figure 5.2 Particle size distribution of hemp shivs and fibres in this study.

5.2.2. Composition of Hemp-Lime Samples

The primary objective of this study was to develop HLC that exhibit consistent performance, high thermal resistance, and minimal environmental impact, making them suitable for sustainable buildings in cold climates. These goals were accomplished by maximizing the proportion of hemp shiv with B/H ratios of 1:1, resulting in lightweight samples with dry densities of 200 kg/m³, and employing a mechanical process to produce uniform samples with consistent dry density [Mahmood et al., 2024]. The binder mix used in this study is the same as the one used in Chapter 3 (section 3.2.3). Table 5.2 summarizes the mix ratios and percentages by mass of hemp-lime samples produced in this study. The mixture includes fibres of different lengths and proportions. CS refers to the control specimen, and the mix properties are represented as 10F6L, where F stands for the fibre percentage, and L indicates the fibre length in mm.

Table 5-2 Composition of the hemp-lime samples.

Mix ID	Mix% by mass				
	Hemp shivs	Hemp fibres	Lime	Slag	Water
CS	16.67	-	13.34	3.33	66.67
10F1.15L	15.00	1.67			
10F6L					
10F12L					
10F25L					
20F1.15L	13.34	3.33			
20F6L					
20F12L					
20F25L					
40F1.15L	10.00	6.67			
40F6L					
40F12L					
40F25L					

5.2.3. Experimental Tests

The HLC samples underwent tests to assess their thermal, mechanical, and moisture properties, including measurements of thermal conductivity (W/m·K), specific heat capacity (J/kg·K),

thermal diffusivity (m^2/s), MBV ($g/m^2 \cdot RH$), and compressive strength (MPa). These tests adhered to the same methodologies described in Chapter 3, specifically Section 3.2.5. `

5.2.4. Potential CO_2 Mitigation

Ideally, hemp shivs used in bio-based construction should be free of fibres following mechanical separation; however, in practice, the decortication process often yields shivs with varying fibre content depending on equipment and processing intensity. This research hypothesizes that avoiding complete fibre removal—thereby accepting a certain percentage of residual fibres—can lead to a measurable reduction in carbon footprint by eliminating energy-intensive cleaning and refining steps. Therefore, a focused LCA evaluation was conducted to estimate potential CO_2 emission reductions specifically associated with upstream hemp processing. The simplified LCA relies on data from previous studies detailing emissions associated with different stages of decortication. The analysis considers a cradle-to-gate system boundary, as shown in Figure 5.3, with a functional unit of 1 kg of hemp and compares three scenarios with increasing shiv purity levels: high-purity (~0% fibres), medium-purity (5-20% fibres), and low-purity (>20% fibres). The carbon footprint associated with each scenario is derived from published CO_2-equivalent emissions per kg of processed hemp [Shanbhag et al., 2024] (see Table 5.3), enabling a comparative assessment of the trade-offs between environmental impact and fibre removal. This methodology allows the quantification of the avoided emissions resulting from incomplete decortication and supports the broader evaluation of whether the environmental gains justify minor compromises in mechanical and hygrothermal performance.

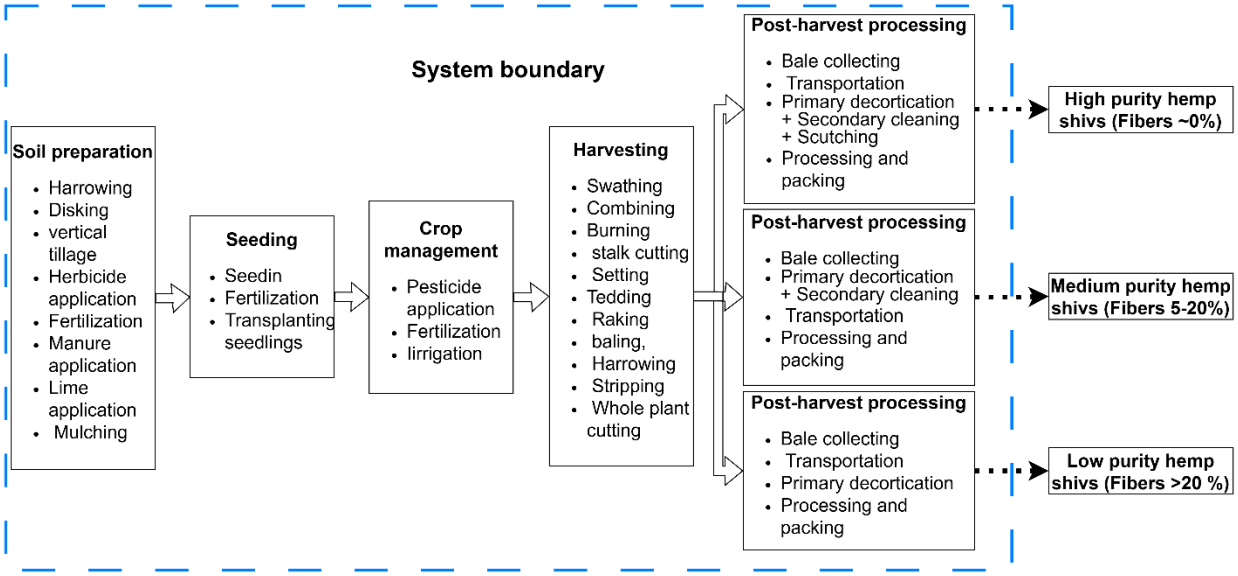

Figure 5.3 System boundary.

Table 5-3 Embodied Carbon of Industrial hemp processing [Shanbhag et al., 2024].

Process	GWP ($kgCO_2e$)/kg
Hemp straw production	0.0027
Transportation	0.0452
Hemp processing	0.0667

In the absence of detailed energy consumption data for each step of hemp shiv processing, the carbon footprint of medium- and low-purity scenarios can be reasonably estimated by proportionally reducing the emissions associated with omitted processing stages. To do so, the total emissions reported for the high-purity scenario were distributed across the main processing phases—primary decortication, secondary cleaning, and fibre refining (scutching)—based on their relative energy intensity and mechanical complexity as reported in the literature, Table 5.4. Specifically, primary decortication was assigned approximately 30% of the total emissions, reflecting the moderate energy requirements of initial fibre–shiv separation through mechanical milling and breaking. Secondary cleaning, which involves multiple stages of mechanical and

pneumatic separation to remove fine fibres and dust, was allocated the highest share at 40%, given its high operational energy demand and extended processing time. Finally, fibre refining or scutching was estimated to contribute the remaining 30%, as it is mechanically intensive and often comparable in complexity to the decortication stage itself. These proportional allocations are supported by previous LCA studies [Nazari &Woods, 2025; Qifan, 2024] and technical assessments of hemp processing systems, providing a transparent and literature-backed approach for estimating emissions in partially processed shiv scenarios.

Table 5-4 Estimated distribution of carbon emissions across key hemp shiv processing stages.

Process stage	Description	Emission Share (%)	Justification summary
Primary decortication	Initial fibre–shiv separation	~ 30	Moderate energy demand for mechanical milling and breaking
Secondary cleaning	Dust and fine fibre removal	~ 40	High energy usage due to multi-stage pneumatic and mechanical separation
Scutching	Final fibre removal	~ 30	Mechanically intensive; comparable to decortication in complexity

5.3. Results and Discussion

5.3.1. Thermal Conductivity

Table 5.5 summarizes the results of thermal conductivity measurements, , which ranged from 0.0526 to 0.0648 W/m·K, demonstrating a clear linear decrease with increasing hemp fibre content. Specifically, thermal conductivity was reduced by approximately 6%, 15%, and 20% for fibre ratios of 10%, 20%, and 40%, respectively. This improvement is primarily attributed to the low thermal conductivity and high porosity of hemp fibres relative to shivs, which introduce more air pockets into the composite and effectively disrupt heat transfer pathways [Kosiński et al., 2017]. These findings align with previous research, which confirms that incorporating fibre enhances the thermal resistance of hemp-lime composites [Nguyen, 2010]. However, increasing fibre content introduces important trade-offs. Hemp fibres are a high-value resource used across

multiple industries, whereas shiv is typically considered a lower-value by-product. The overuse of fibres can therefore raise concerns about sustainability and economics. Additionally, although research directly addressing the impact of fibre content in HLC is limited, studies on other fibre-rich composites indicate that excessive fibre levels may compromise mechanical performance, reducing compressive strength, workability, and homogeneity, while increasing water absorption and the risk of inhomogeneities [Kaplan & Bayraktar, 2021]. Therefore, while higher fibre content improves thermal insulation, it must be carefully optimized to maintain a balance between hygrothermal performance, mechanical integrity, and sustainability objectives.

Low variation in thermal conductivity among samples is also evident in Table 5.5, particularly those containing short fibres (1.15 mm), with coefficients of variation ranging from 2.22% to 5.35%. This consistency underscores the effectiveness of the adopted method in producing uniform HLC samples at high fibre contents. These results build upon previous work [Mahmood et al., 2024], where we demonstrated that controlling hemp shiv particle size and using vibration during casting significantly reduced variability in the physical properties of hempcrete. Standardizing the hurd size promoted uniform packing, resulting in consistent porosity and enhanced thermal and mechanical performance. Meanwhile, vibration minimized voids and improved the bonding between binder and fibre.

In contrast, samples with longer fibres (6, 12, and 25 mm) exhibited considerably higher variability, with average coefficients of variation reaching 7%, 13%, and 22% for hemp ratios of 10%, 20%, and 40%, respectively. This increased inconsistency is likely due to the balling effect, where longer fibres clump together during mixing instead of dispersing evenly throughout the matrix [Salehi et al., 2022], as illustrated in Figure 5.4. These fibre clumps create denser regions that facilitate heat transfer, while poorly dispersed zones retain more air pockets, which improves

insulation and results in heterogeneous thermal behavior—an undesirable trait for reliable building applications.

Figure 5.4 Balling effect of hemp fibres.

Table 5-5 Descriptive statistics of samples' thermal conductivity.

Mix ID	Mean dry density (kg/m³)	Thermal conductivity (W/m K)	Coefficient of variation (%)
CS	200.79	0.0685	3.60
10F1.15L	200.87	0.0644	2.22
10F6L	199.01	0.0648	5.93
10F12L	197.92	0.0641	7.84
10F25L	200.12	0.0638	7.12
20F1.15L	198.71	0.0583	4.56
20F6L	200.36	0.0580	10.92
20F12L	198.29	0.0564	13.29
20F25L	199.15	0.056	14.28
40F1.15L	199.93	0.0546	5.35
40F6L	201.65	0.0541	18.93
40F12L	199.18	0.0528	22.38
40F25L	200.73	0.0526	21.93

Figure 5.5 evaluates the dry density–thermal conductivity correlation in this research relative to existing literature [Mahmood et al., 2024], [Abdellatef et al., 2020], and [Williams et al., 2017].

Compared to previous research with similar dry density [Mahmood et al., 2024], this study shows 0.13–18.45% lower thermal conductivity values. To allow accurate comparison, thermal conductivity results from the literature [Abdellatef et al., 2020], and [Williams et al., 2017] were extrapolated considering their linear dependence on density to align with the average value of density in this study. The thermal conductivity values are 5.29-19.07% lower than the extrapolated values reported in [Abdellatef et al., 2020], and [Williams et al., 2017]. These findings emphasize the role of fibre-rich formulations in optimizing the thermal performance of HLC. However, it is important to consider that variations in raw material properties, binder types, compaction levels, and sample preparation methods across different studies may also influence the thermal behavior.

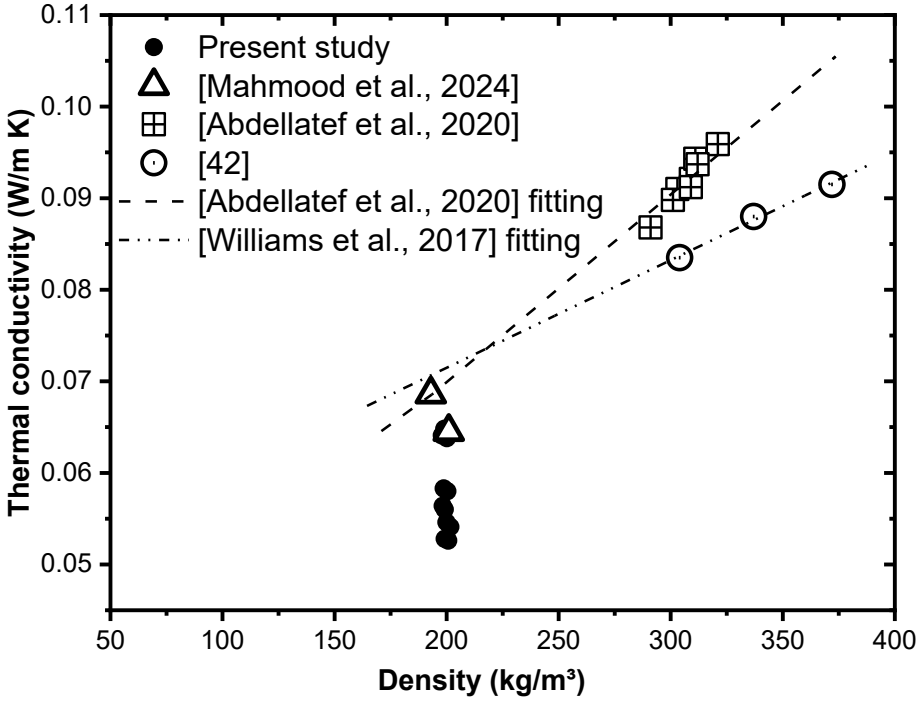

Figure 5.5 Comparing thermal conductivity results with other studies.

The significantly lower density of our HLC samples, compared to those reported in most other studies, can be attributed to our intentional use of a high hemp-to-binder ratio and the adoption of

a vibration-based compaction technique. The high hemp-to-binder ratio results in a greater volume of hemp aggregate within the mix, which inherently leads to a lower density, as there is more air space between the hemp particles and less binder material to fill the gaps. This approach was chosen to prioritize insulation properties and reduce material weight. Additionally, the use of vibration during compaction improves homogeneity and reduces air pockets, but it does not achieve the same degree of compaction as more traditional methods, such as hand packing or mechanical pressing. This results in a less densely packed structure, contributing further to the overall lower density of the final product [Mahmood et al., 2024].

The effect of hemp fibre length on the thermal conductivity of the hemp-lime composite was assessed at four different fibre lengths (1.15, 6, 12, and 25 mm) to evaluate the performance of HLC across various fibre production processes. In general, Figure 5.6 shows a slight decrease in thermal conductivity with increasing fibre length, ranging from 0.62% to 0.93% for 10F samples, from 0.5% to 3.9% for 20F samples, and from 0.9% to 3.6% for 40F samples, relative to the samples containing 1.15 mm fibres. Such a trend can be explained by the longer hemp fibres creating a more interconnected, porous structure within the matrix, which enhances air entrapment, reduces heat transfer, and improves insulation. On the other hand, short fibres result in a denser matrix with fewer air pockets, leading to increased thermal conductivity as heat transfer occurs more efficiently through the material. However, the experimental results show that the differences in thermal conductivity observed with varying hemp fibre lengths fall within the experimental coefficient of variation, indicating that fibre length does not have a statistically significant effect on the thermal performance of the hemp-lime composite.

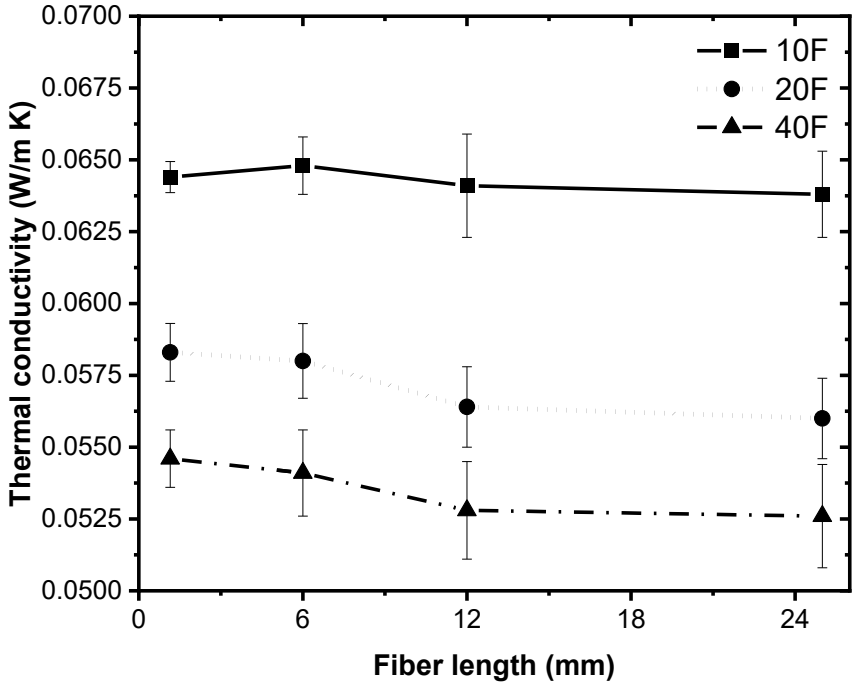

Figure 5.6 Thermal conductivity vs. different fibre lengths.

5.3.2. Specific Heat Capacity and Thermal Diffusivity

The specific heat capacity of HLC samples varied between 931 and 976 J/kg K, as detailed in Table 5.6. The results align with previous literature where sample densities falling within a similar range (200 kg/m^3) [Mahmood et al., 2024]. The findings reveal no significant influence of the hemp fibre ratio on the measured specific heat capacities, indicating that HLC are more influenced by other parameters, such as B:H ratio and density, than the hemp fibre ratio.

Defined as the ratio of thermal conductivity to heat storage capacity, thermal diffusivity indicates the speed of temperature change transmission through a material [Gourlay et al., 2017]. Materials exhibiting low thermal diffusivity minimize heat flow, promoting better energy efficiency and comfort [Abdellatef et al., 2020]. The range of thermal diffusivity across all samples was 0.277 (m²/s) x10^{-6} and 0.361 (m²/s) x10^{-6}. Samples that incorporated hemp fibre into the mix exhibited

lower thermal diffusivity by about 8%, 13%, and 22% for fibre ratios of 10%, 20%, and 40%, respectively. These findings reflect the established correlation among thermal diffusivity, thermal conductivity, and density. Moreover, the higher CV observed for longer fibre samples was anticipated due to the inherent relationship among thermal diffusivity, thermal conductivity, and density. As fibre length increases, the variability in fibre distribution and orientation likely becomes more pronounced, which affects the consistency of thermal pathways within the composite. This is reflected in the increasing CV of thermal conductivity with longer fibres, contributing directly to the higher CV in thermal diffusivity.

Table 5-6 Average specific heat capacity and thermal diffusivity.

Mix ID	Ave. Specific heat capacity (J/kg K)	Coefficient of variation (%)	Ave. Thermal diffusivity (m^2/s) $x10^{-6}$	Coefficient of variation (%)
CS	943	3.57	0.361	3.72
10F1.15L	961	2.19	0.333	2.61
10F6L	976	3.89	0.334	6.81
10F12L	958	4.01	0.338	8.32
10F25L	966	3.23	0.330	7.10
20F1.15L	931	4.09	0.315	4.66
20F6L	949	5.11	0.305	12.52
20F12L	971	3.76	0.293	11.89
20F25L	962	5.98	0.292	13.67
40F1.15L	957	4.61	0.285	5.12
40F6L	969	2.79	0.277	16.14
40F12L	938	3.29	0.283	19.94
40F25L	951	3.83	0.276	18.79

5.3.3. Moisture Buffer Value

Moisture buffering capacity is a key indicator of a material's ability to regulate indoor humidity and contribute to passive hygrothermal comfort. As presented in Figure 5.7, HLC samples demonstrated excellent MBV, ranging from 2.12 to 2.73 $g/m^2 \cdot RH$, which meets the threshold for the "excellent" classification as defined in [Khaled et al., 2023] and [Collet and Pretot, 2012]. A clear upward trend is observed with increasing fibre content: MBV values increased by approximately 3%, 10%, and 24% for fibre ratios of 10%, 20%, and 40%, respectively, relative to

the lowest fibre content. This enhancement is attributed to the greater porosity and vapor permeability introduced by the incorporation of hemp fibres, which facilitate higher rates of moisture absorption and release. Similar trends have been reported in studies highlighting the role of bio-based aggregates in enhancing the moisture buffering performance of building materials [Collet and Pretot, 2012].

Importantly, fibre length had a negligible effect on MBV, as the variations across different lengths fell within the experimental range of variability for each fibre content group. These findings align with prior observations indicating that microstructural characteristics, such as pore distribution and connectivity, rather than aggregate geometry alone, govern moisture buffering performance in hemp-lime composites [Walker et al., 2014]. It can be concluded that fibre volume fraction is the dominant parameter influencing moisture regulation in HLCs, making it a critical variable for optimizing mix designs in applications requiring passive indoor humidity control, such as breathable or low-energy wall systems.

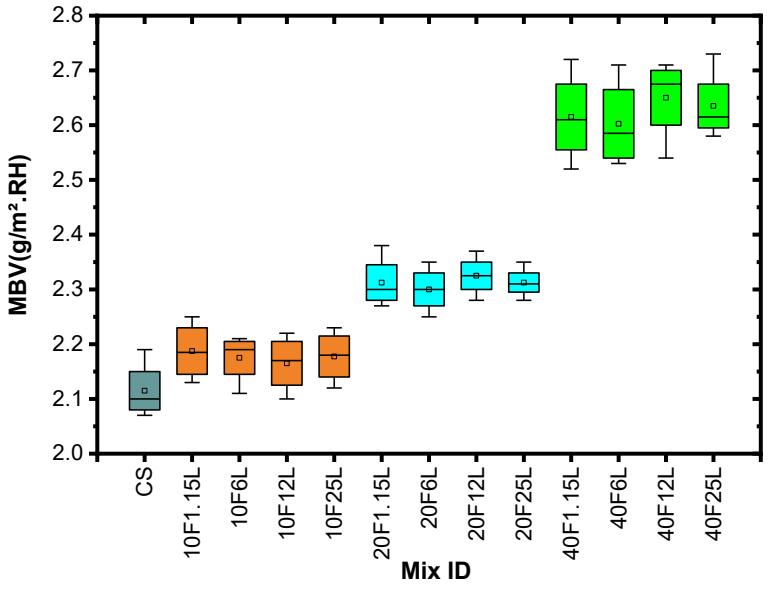

Figure 5.7 MBV values of the hemp-lime samples using the NORDTEST procedure.

Figure 5.8 evaluates the MBV results in this research relative to previous litterature [Mahmood et al., 2024], [Abdellatef et al., 2020], and [Collet and Pretot, 2012]. The results demonstrate that the MBV values from the present study are consistently higher across comparable dry density ranges. Specifically, MBV values are 2.5–23.6% higher than those reported in [Mahmood et al., 2024] at similar dry densities, and 4.0–26.4% higher than those reported by [Collet and Pretot, 2012], which used a higher average sample density of approximately 440 kg/m³. In comparison, the study by [Abdellatef et al., 2020], which used a density of 300 kg/m³, reported an average MBV of 2.77 g/m² RH, which closely aligns with the results for our lower-density samples containing 40% hemp fibres. These comparisons underscore the positive impact of increased hemp fibre content on moisture buffering performance, particularly in lower-density composites. The improved MBV in the present samples can be attributed to the enhanced porosity and permeability introduced by higher fibre ratios, which facilitate more effective moisture exchange with the ambient environment [Collet and Pretot, 2012]. It is well established that moisture buffering in porous bio-based materials is governed by vapor diffusion through interconnected pores, the hygroscopic nature of the plant aggregates, and the specific surface area available for moisture adsorption [Collet et al., 2013; Hoxha et al., 2022]. Furthermore, the results suggest that optimized low-density formulations can achieve MBV values comparable to or exceeding those of higher-density systems reported in the literature, offering a performance advantage in passive moisture regulation applications such as interior wall linings and breathable insulation systems.

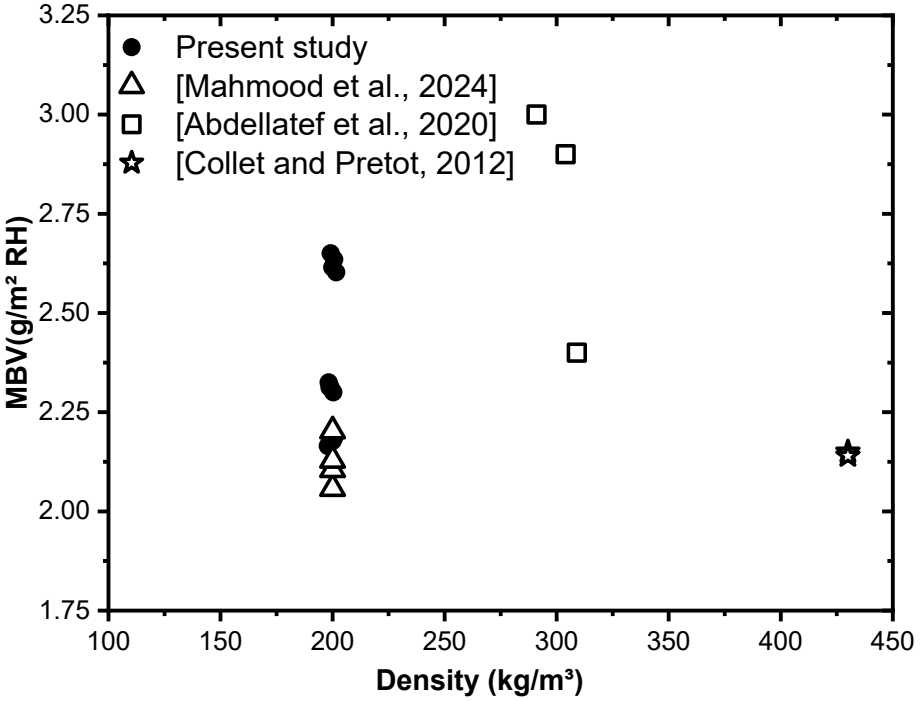

Figure 5.8 Comparing MBV results with other studies.

Figure 5.9 illustrates the evolution of MBV under oven-dry initial conditions across different fibre ratios. At the onset of testing, all samples exhibit high MBV values ranging from 2.5 to 4.35 g/m²·RH, which gradually decrease and stabilize by the fourth sorption–desorption cycle. This initial peak results from the elevated moisture uptake potential of dry hemp-lime composites, which decreases as the material becomes progressively conditioned with moisture. This behavior is consistent with previous observations, which indicate that materials with a low initial moisture content exhibit a greater hygroscopic response, while elevated starting humidity reduces their subsequent absorption capacity [Mahmood et al., 2024]. Figure 5.9 also highlights a distinct influence of fibre ratio on moisture uptake behavior. During the first cycle, samples with 20% and 40% fibre content absorb approximately 30% and 75% more moisture, respectively, compared to those with 0% and 10% fibre content. This behavior enhances absorption, delaying the time to reach moisture equilibrium and resulting in more gradual stabilization. In contrast, HLC samples

with lower fibre content achieve stable MBV values more rapidly, suggesting a more immediate regulatory response to indoor humidity fluctuations.

Notably, variations in fibre length did not significantly alter this behavior, as all fibre length groups followed similar moisture equilibration trends. These findings indicate that fibre content, rather than fibre length, is the dominant factor influencing moisture buffering dynamics and stabilization in hemp-lime composites.

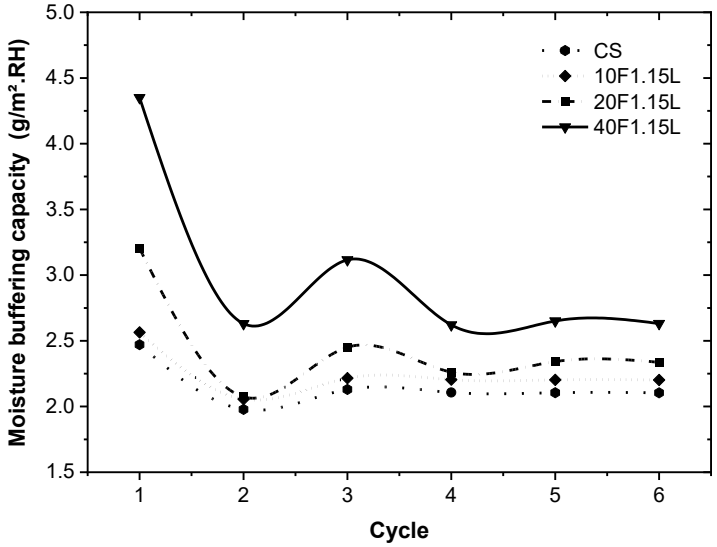

Figure 5.9. Typical moisture buffering capacity of different fibre ratios with cycles.

5.3.4. Compressive Strength

HLC samples exhibited a collapse pattern similar to that of a shear failure, as shown in Figure 5.10. The stress-strain response exhibits three regions: an ascending linear portion, a peak at maximum compressive stress marking the end of linearity, and a descending segment where stress decreases. Similar behavior has been reported in previous literature [Mahmood et al., 2024; Ataebi et al., 2025]. The fine particle size of hemp is the key element inducing such behavior, as smaller

particles may lack structural integrity, resulting in interconnected pores that promote premature shear-like failure [Mahmood et al., 2024; Sparrow, 2014].

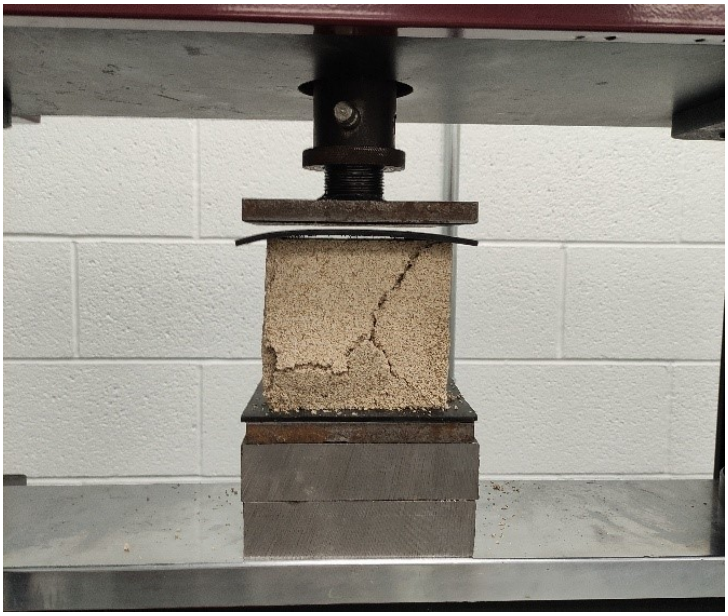

Figure 5.10 Compressive Strength test,HLC cubes after failure.

Figure 5.11 exhibits the stress–strain response of HLCs with varying fibre contents. All samples demonstrate substantial strain capacity at peak load, ranging from 0.032 to 0.048 mm/mm, indicating a pronounced quasi-ductile behavior rather than brittle failure. Such ductility is advantageous in seismic contexts, where materials that undergo controlled deformation can dissipate energy and avoid sudden collapse. The stress–strain curves reveal a gradual post-peak strength reduction, particularly in fibre-reinforced samples, suggesting strain softening rather than sudden collapse. This behavior is attributed to the role of hemp fibres in bridging microcracks and delaying crack propagation. In particular, the 10% fibre sample demonstrates both enhanced deformability and a relatively stable strength level, indicating a favorable balance between strength and ductility. However, it is important to note that the 40% fibre sample, while exhibiting the

highest strain capacity, showed a reduced compressive strength at peak load compared to samples with lower fibre content. This trend reflects a well-known trade-off in natural-fibre-reinforced composites: increasing fibre content can improve energy dissipation and post-peak behavior but may weaken matrix integrity and load-bearing capacity due to higher porosity and reduced packing density [Laborel-Préneron et al., 2016]. Therefore, optimizing the fibre ratio is crucial for balancing mechanical resilience and structural performance.

Overall, the findings suggest that moderate fibre addition (e.g., less than 20%) offers the best compromise between compressive strength and ductility, making such formulations particularly suitable for non-load-bearing or infill applications in earthquake-prone buildings. Excessive fibre content, although beneficial for deformability, may compromise strength and should be used with caution, depending on the structural requirements.

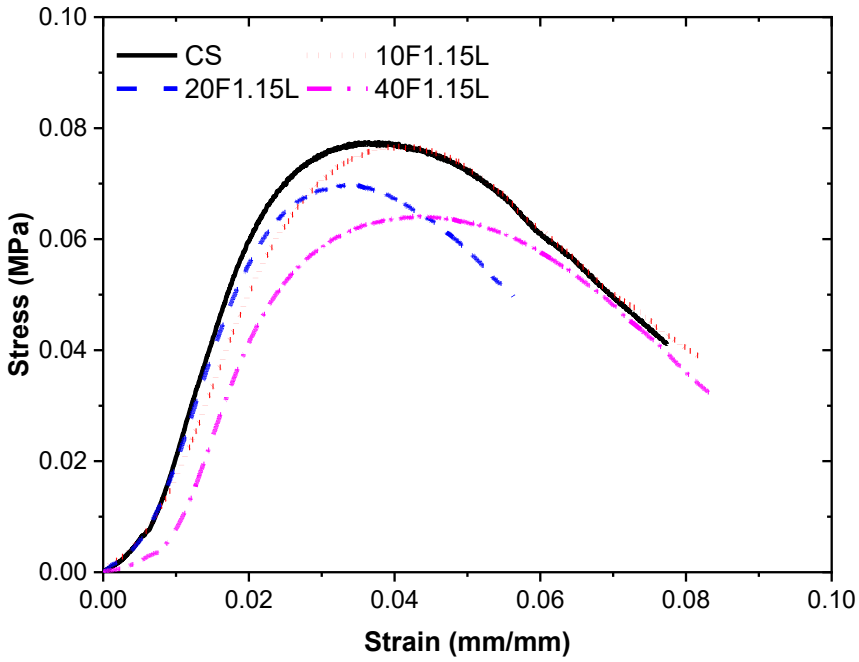

Figure 5.11 Typical stress-strain curve for hemp-lime samples.

The mean compressive strength values and the associated coefficients of variation for each mix are compiled in Table 5.7. When compared to rigid thermal insulation boards [ASTM C1289, 2022], the hemp-lime samples exhibited commendable mechanical performance despite their lower densities. The average compressive strength values range from 0.055 to 0.079 MPa, with coefficients of variation ranging between 7.91% and 19.45%. Results show that adding hemp fibre has reduced the compressive strength by approximately 13%, 15%, and 25% for fibre ratios of 10%, 20%, and 40%, respectively. Such behavior was expected, as hemp fibres have much lower compressive strength compared to the hemp shivs, and it could also interfere with the cohesion between the hemp shivs and the binder, thereby reducing the ability to withstand pressure. The average compressive strength in this study falls within the range reported in the literature. For example, Mahmood et al. [Mahmood et al., 2024] reported an average compressive strength of 0.70 MPa with a bind-to-hemp ratio of 1:1 and an average dry density of 200 kg/m³. Moreover, based on the experimental data, the hemp fibre length does not appear to produce a notable or consistent impact on the compressive strength of the HLC, indicating that this parameter does not play a critical role in determining structural performance. While hemp-lime composites may not match the structural capacity of conventional load-bearing materials, their compressive strength (0.11–0.965 MPa) aligns with that of faced rigid insulation.

Tensile strength was not assessed in this study, as prior research indicates that the tensile strength of HLC is generally around 10% of its compressive strength. In the context of our mix, which was formulated with a high hemp-to-binder ratio to optimize thermal performance and reduce density, the compressive strength is relatively low. Therefore, the tensile strength would likely be similarly diminished. Given that tensile strength is not a key performance indicator for hempcrete's primary

applications, such as thermal insulation, we determined that testing for this property was not essential to the objectives of our research.

Due to difficulties in attaching a compressometer, Young's modulus was estimated using actuator displacement, with values ranging between 3.07 and 3.96 MPa, as shown in Table 8. Results show a reduction of approximately 5%, 17%, and 18% for fibre ratios of 10%, 20%, and 40%, respectively. A similar finding was reported in the previous literature [Nguyen, 2010], which showed that Young's modulus was approximately 50% lower in samples containing hemp fibres. It can be seen that a high fibre ratio has a negative effect on material stiffness, as higher fibre ratios not only increase flexibility but also make the samples more prone to strain under loading.

Table 5-7 Descriptive statistics of samples' compressive strength and Young's modulus.

Mix ID	Compressive Strength		Young's modulus	
	Mean (MPa)	Coefficient of variation %	Mean (MPa)	Coefficient of variation %
CS	0.079	17.89	3.96	7.38
10F1.15L	0.071	19.45	3.76	5.01
10F6L	0.063	15.82	3.51	8.95
10F12L	0.067	16.41	3.56	11.31
10F25L	0.074	18.92	3.81	8.73
20F1.15L	0.065	9.88	3.27	5.43
20F6L	0.072	12.69	3.58	10.52
20F12L	0.069	8.42	3.31	9.31
20F25L	0.061	17.95	3.10	13.69
40F1.15L	0.058	7.91	3.22	13.82
40F6L	0.055	15.41	2.93	14.92
40F12L	0.061	9.72	3.16	12.28
40F25L	0.057	10.63	3.07	12.98

5.4. Potential CO_2 mitigation

The comparative analysis of the three hemp shiv processing scenarios reveals significant differences in carbon footprint depending on the level of fibre removal. In the high-purity scenario, where full decortication, secondary cleaning, and fibre refining are performed to eliminate nearly

all residual fibres, the estimated carbon footprint reaches 0.1146 kg CO_2e per kg of hemp. This represents the most emission-intensive approach due to the energy demands of both fine cleaning and scutching stages. In contrast, the medium-purity scenario, which excludes the scutching phase but retains secondary cleaning, results in a reduced footprint of approximately 0.0946 kg CO_2e/ton, reflecting a 17.5 % reduction in emissions. The most substantial savings occur in the low-purity scenario, where only primary decortication is conducted, yielding an estimated footprint of 0.0679 kg CO_2e/ton, or a 40.7 % reduction compared to the high-purity reference. These results clearly demonstrate that the more intensive the fibre removal process, the higher the associated environmental impact. Therefore, from an environmental standpoint, minimizing processing intensity—by accepting a higher fibre content in shiv—can lead to substantial emission reductions. This finding underscores the need to balance the pursuit of material purity with the environmental costs of achieving it, especially in applications where moderate fibre content does not significantly compromise composite performance.

Such an approach enhances resource efficiency and aligns well with circular economy principles by minimizing biomass waste and maximizing the value derived from each harvested plant. The environmental benefit is particularly relevant given the growing demand for low-carbon construction materials. However, it is important to acknowledge that these findings are preliminary. While the initial results demonstrate promising carbon mitigation potential, further comprehensive research is needed to assess detailed and long-term environmental impacts. Thus, while the early data points to a viable path for emissions reduction, a deeper and more systematic investigation is essential before this method can be broadly recommended or standardized.

5.5. Conclusions

The key findings from this study, along with the limitations that inform prospects for continued research, can be outlined as follows:

- The study demonstrates that increasing the hemp fibre ratio notably enhances the thermal insulation performance of hempcrete. Specifically, the samples exhibited thermal conductivity values ranging from 0.0546 to 0.0685 W/m·K, with reductions of 6%, 15%, and 20% observed at fibre ratios of 10%, 20%, and 40%, respectively. This trend indicates a direct correlation between higher fibre content and improved thermal properties. Future research should focus on assessing the long-term thermal stability of these composites under various environmental conditions and exploring optimized mix design ratios that balance thermal performance with mechanical strength for enhanced energy efficiency in building applications.
- The investigation into the effect of hemp fibre length on the thermal properties of hemp-lime composites revealed a decrease in thermal conductivity, ranging from 0.5% to 3.9% for F20 samples and from 0.9% to 3.6% for F40 samples relative to the samples containing 1.15 mm fibres. However, these variations fall within the experimental coefficient of variation, suggesting that the differences were not statistically significant. In summary, fibre length does not have a measurable impact on the thermal performance of the composite. Future work could explore the influence of fibre surface treatments or orientation, as well as the use of different hemp shiv sizes, given that previous studies have reported a potential effect of hemp shiv size on the material's overall performance.
- Specific heat capacity ranged between 931 to 976 J/kg K while thermal diffusivity ranged between 0.277 (m^2/s) $x10^{-6}$ and 0.361 (m^2/s) $x10^{-6}$. The results show no significant effect of the hemp fibre ratio or the fibre length on the specific heat capacity and thermal diffusivity. Future

work should consider different density ranges and H:B ratios, as the current findings are limited to a 1:1 H:B ratio and a dry density of 200 kg/m³.

- The study reports an excellent moisture buffering capacity in hemp-lime composites, with average values ranging from 2.12 to 2.73 g/m² RH. A positive correlation was observed, with MBV increasing by about 24% for fibre ratios of 40%. This behavior can be attributed to the increased permeability of the hemp-lime composite caused by the incorporation of fibre particles, which enhances both moisture transfer and storage within the material. Future research should investigate the long-term environmental performance and durability of these composites.
- The study indicates that incorporating hemp fibre into hemp-lime composites markedly influences their mechanical properties, specifically their compressive strength. The average compressive strength values, which range from 0.055 to 0.079 MPa, exhibit coefficients of variation from 7.91% to 19.45%. Despite their low densities, the hemp-lime samples exhibit mechanical performance comparable to that of other insulation materials, such as rigid thermal insulation boards. Importantly, the addition of hemp fibre reduces compressive strength by about 13%, 15%, and 25% for fibre ratios of 10%, 20%, and 40%, respectively. Future research should focus on optimizing the fibre-to-matrix interface and exploring alternative mix designs or fibre treatments to counteract the reduction in compressive strength while preserving the material's beneficial thermal and moisture buffering properties.
- The findings suggest notable potential for lowering direct CO_2 emissions by approximately 17% and 40% when using medium- and low-purity hemp shivs, respectively, compared to high-purity ones with emissions of 0.1146 kg CO_2e/kg. Nonetheless, although the initial results

are promising, further comprehensive and systematic LCA research is needed before this approach can be widely adopted or standardized.

5.6. References

Abdellatef, Y., Khan, M. A., Khan, A., Alam, M. I., & Kavgic, M. (2020). Mechanical, Thermal, and Moisture Buffering Properties of Novel Insulating Hemp-Lime Composite Building Materials. *Materials*, *13*(21), 5000. https://doi.org/10.3390/ma13215000

ASTM International. (2022). Standard Specification for Faced Rigid Cellular Polyisocyanurate Thermal Insulation Board (ASTM C1289-22a).

Ataebi, E., Mahmood, O., & Kavgic, M. (2025). Impact of Varying Proportions of Slag on the Thermal and Mechanical Performance of Hempcrete. In S. Amziane, R. D. Toledo Filho, M. Y. R. da Gloria, & J. Page (Eds.), *Bio-Based Building Materials—Proceedings of ICBBM 2025* (pp. 298–315). Springer Nature Switzerland. https://doi.org/10.1007/978-3-031-92777-5_25

Bourdot, A., Moussa, T., Gacoin, A., Maalouf, C., Vazquez, P., Thomachot-Schneider, C., Bliard, C., Merabtine, A., Lachi, M., Douzane, O., Karaky, H., & Polidori, G. (2017). Characterization of a hemp-based agro-material: Influence of starch ratio and hemp shive size on physical, mechanical, and hygrothermal properties. *Energy and Buildings*, *153*, 501–512. https://doi.org/10.1016/j.enbuild.2017.08.022

Collet, F., & Pretot, S. (2012). Experimental investigation of moisture buffering capacity of sprayed hemp concrete. *Construction and Building Materials*, *36*, 58–65. https://doi.org/10.1016/j.conbuildmat.2012.04.139

Collet, F., Chamoin, J., Pretot, S., & Lanos, C. (2013). Comparison of the hygric behaviour of three hemp concretes. *Energy and Buildings*, *62*, 294–303. https://doi.org/10.1016/j.enbuild.2013.03.010

de Bruijn, P. B., Jeppsson, K.-H., Sandin, K., & Nilsson, C. (2009). Mechanical properties of lime–hemp concrete containing shives and fibres. *Biosystems Engineering*, *103*(4), 474–479. https://doi.org/10.1016/j.biosystemseng.2009.02.005

Gourlay, E., Glé, P., Marceau, S., Foy, C., & Moscardelli, S. (2017). Effect of water content on the acoustical and thermal properties of hemp concretes. *Construction and Building Materials*, *139*, 513–523. https://doi.org/10.1016/j.conbuildmat.2016.11.018

Hoxha, D., Ismail, B., Rotaru, A., Izabel, D., & Renaux, T. (2022). Assessment of the Usability of Some Bio-Based Insulation Materials in Double-Skin Steel Envelopes. *Sustainability*, *14*(17), 10797. https://doi.org/10.3390/su141710797

Kaplan, G., & Bayraktar, O. Y. (2021). The effect of hemp fiber usage on the mechanical and physical properties of cement based mortars. *Research on Engineering Structures & Materials*, *7*(2), 245–258.

Khaled, S., Collet, F., Prétot, S., & Bart, M. (2023). Effect of Air Velocity and Initial Conditioning on the Moisture Buffer Value of Four Different Building Materials. *Materials*, *16*(8), 3284. https://doi.org/10.3390/ma16083284

Kosiński, P., Brzyski, P., Szewczyk, A., & Motacki, W. (2018). Thermal Properties of Raw Hemp Fiber as a Loose-Fill Insulation Material. *Journal of Natural Fibers*, *15*(5), 717–730. https://doi.org/10.1080/15440478.2017.1361371

Laborel-Préneron, A., Aubert, J. E., Magniont, C., Tribout, C., & Bertron, A. (2016). Plant aggregates and fibers in earth construction materials: A review. *Construction and Building Materials*, *111*, 719–734. https://doi.org/10.1016/j.conbuildmat.2016.02.119

Mahmood, O., Kavgic, M., & Noel, M. (2024). Hygrothermal and mechanical characterization of novel hemp-lime composites with enhanced consistency. *Construction and Building Materials*, *450*, 138720. https://doi.org/10.1016/j.conbuildmat.2024.138720

Nazari, F., & Woods, L. D. (2025). Environmental life cycle assessment of hemp-based thermal insulation: From agricultural growth to manufacturing in the United States. *Journal of Cleaner Production*, *506*, 145509. https://doi.org/10.1016/j.jclepro.2025.145509

Nguyen, T. T. (2010). *Contribution à l'étude de la formulation et du procédé de fabrication d'éléments de construction en béton de chanvre* [Phdthesis, Université de Bretagne Sud]. https://doi.org/10/document

Salehi, P., Dabbagh, H., & Ashengroph, M. (2022). Effects of microbial strains on the mechanical and durability properties of lightweight concrete reinforced with polypropylene fiber. *Construction and Building Materials*, *322*, 126519. https://doi.org/10.1016/j.conbuildmat.2022.126519

Shanbhag, S. S., Dixit, M. K., & Sideris, P. (2024). Examining the global warming potential of hempcrete in the United States: A cradle-to-gate life cycle assessment. *Developments in the Built Environment*, *20*, 100572. https://doi.org/10.1016/j.dibe.2024.100572

Stanwix, W. & Sparrow, A. (2014). The hempcrete book, designing and building with hemp-lime. *Green Books*.

Walker, R., Pavia, S., & Mitchell, R. (2014). Mechanical properties and durability of hemp-lime concretes. *Construction and Building Materials*, *61*, 340–348. https://doi.org/10.1016/j.conbuildmat.2014.02.065

Williams, J., Lawrence, M., & Walker, P. (2016). The influence of the casting process on the internal structure and physical properties of hemp-lime. *Materials and Structures*, *50*(2), 108. https://doi.org/10.1617/s11527-016-0976-4

Wu, Q. (2024). *Life Cycle Assessment of Industrial Hemp and Hemp-Based Products in Canada*. https://ualberta.scholaris.ca/items/024f4c32-1562-41c6-8b6e-eebe8eae7bc4

Chapter 6 : Assessing The Technical Suitability of Precipitated Materials from the Electrochemical Decarbonation of Limestones for Hydrated Lime Production[3]

6.1. Introduction

Lime production is a major contributor to industrial CO_2 emissions, primarily due to the calcination of limestone at high temperatures. Electrochemical decarbonation offers a low-carbon alternative by releasing CO_2 in a capturable stream and generating calcium-based precipitates under milder, potentially renewable-powered conditions. These precipitates could serve as hydrated lime, but their technical suitability must be verified.

The effectiveness of ED-derived lime depends on properties such as purity, crystallinity, particle size, which may differ from conventional lime and influence binder performance in construction applications. This chapter evaluates the physical and chemical characteristics of ED precipitates and compares them with conventional hydrated lime, providing insight into their potential as a sustainable alternative for carbon-conscious building materials.

To guarantee an extensive generalization of the research results, several limestones' sources were studied under a similar ED process (i.e., identical electrochemical cell and working parameters). Consequently, for the first time, this study presents a technical suitability analysis of the deposited materials (DMs) obtained by the ED of limestones from different sources, which provides evidence of the reproducibility of this technology and supports its further deployment in worldwide chains of hydrated lime production.

[3] An abridged version of this chapter has been published as: Ramírez-Amaya, D., Mahmood, O., Noël, M., Kavgic, M., Martinez, N. P., Troncoso P., F., Gazzano, V., Dreyse, P., Canales, R., & González, M. (2025). Assessing the Technical Suitability of Precipitated Materials from the Electrochemical Decarbonation of Limestones for Cement and Hydrated Lime Production: A Reproducibility Study Performed in Canada and Chile. *Journal of Materials in Civil Engineering, 37(9), 05025007*. https://doi.org/10.1061/JMCEE7.MTENG-19673

6.2. Materials and Methods

In this chapter, four sources of $CaCO_3$ were used as precursor materials for the ED process. Fisher Chemical (CAS-No: 471-34-1, Ref-No: 64-500) calcium carbonate reagents were utilized as control sample (C). In addition, powdered limestone samples supplied by a local lime industry were used: L1, L2, and L3. The precursor materials (i.e. feedstcoks) were oven-dried to 105°C for 24 hours and then subjected to physical and chemical analysis [Ramirez-Amaya et al., 2023]. The precursor materials and the DMs samples underwent tests to assess their physical and chemical properties, including measurements of PSD, SSA_{BET}, FE-SEM, TGA/DTGA, XRD, XRF. These tests adhered to the methodologies described in Chapter 3, specifically Section 3.3.2.

For each ED performed, 10.0g of precursor material was introduced into the anode chamber and stirring (< 200rpm) was applied to enhance the sample diffusion. ED was performed by applying a 12V direct current for 16 hours (non-interrupted). The voltage operation and ED duration were chosen to guarantee the whole dissolution of the precursor materials based on previous trials. After ED, precipitated material was extracted from the cell's interface and isolated by filtration through a paper filter placed on a Büchner funnel. Then, the DM samples were oven-dried to 105°C for 24 hours and stored in a chamber desiccant at room temperature for further analysis.

6.3. Results and Discussion

6.3.1. Precursor Materials Characterization

- **Chemical Characteristics**

Table 6.1 presents the chemical characterization of the precursor materials, including the oxide composition and chemical modules obtained by XRF, as well as the purity of $CaCO_3$ computed using Equation 3.10 and the TG/DTG results shown in Figure 6.2. The control sample C is high-purity $CaCO_3$ sources (>99% by mass) and consequently have very low or negligible content of

other primary and secondary oxides (i.e., other than CaO).L1, L2, and L3 are classified as high-grade limestone (i.e., CaO > 45%, carbonates >80%, SiO_2 < 12%, and Fe_2O_3< 5% by mass) with a $CaCO_3$ content exceeding 95% by mass and low levels of other primary oxides, making them chemically suitable for hydrated lime production [ILIÇ & Shaw, 1995].

Table 6-1 Chemical characteristics of the precursors.

Test	C	L1	L2	L3
XRF [wt. %]				
CaO	56.24	51.61	53.01	52.64
SiO_2	0.16	1.37	2.33	2.66
Al_2O_3	-	0.22	0.09	0.12
Fe_2O_3	0.01	0.11	0.08	0.09
MgO	-	0.79	1.05	1.06
Na_2O	0.05	0.08	0.06	0.06
K_2O	0.01	0.07	0.07	0.08
P_2O_5	0.01	0.01	0.03	0.03
MnO	-	-	-	-
TiO_2	0.01	0.02	0.01	0.01
SO_3	-	-	-	-
LOI	43.48	45.68	43.28	43.21
Total	99.97	99.96	99.93	99.96
TG/DTG [wt.%]				
$L_{(550-900)}$	43.77	43.27	42.87	42.53
$CaCO_3$	99.53	98.41	97.49	96.71

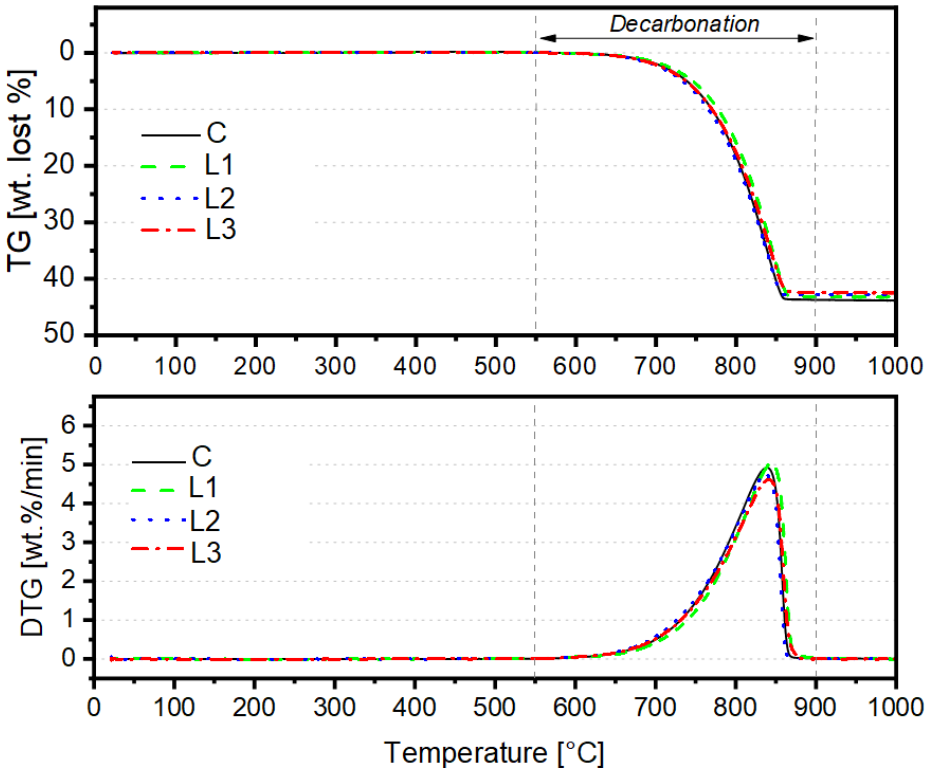

Figure 6.1 Thermogravimetric analysis of the precursors.

XRD analysis of precursors is shown in Figure 6.2. Samples were mainly comprised of calcite as the primary source of CaO. Quartz and dolomite were also identified, which explains the minor contents of SiO_2 and MgO, respectively. Regarding the content of secondary constituents, all the precursor samples met the chemical requirements for hydrated lime production [Abdel Moneim et al., 2013], with the MgO being the main secondary constituent in all the limestone samples.

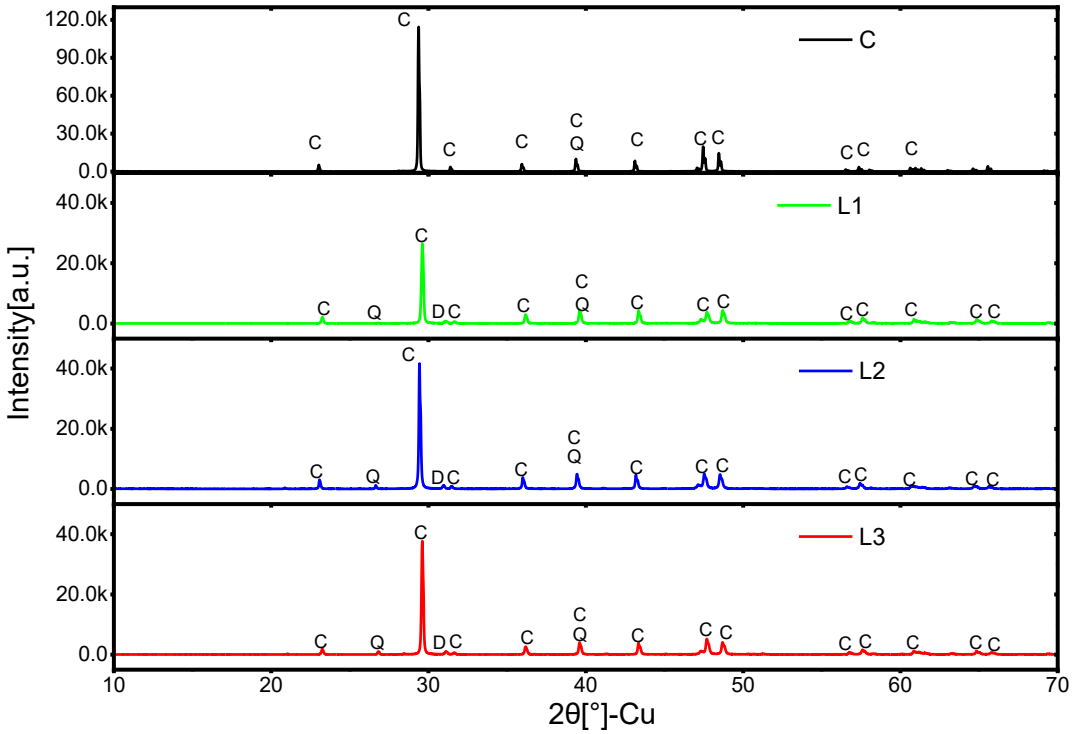

Figure 6.2 XRD analysis of the precursors. C: Calcite ($CaCO_3$), Q: Quartz (SiO_2), D: Dolomite ($CaMg(CO_3)_2$).

- **Physical Characteristics**

The main physical characteristics of the precursor materials are listed in Table 6.2. There was a high variability in the PSD (see Figure 6.3) and SSA_{BET} among precursor samples. These differences, together with the initial masses of the samples, explain the lower temperature and rate of decomposition of $CaCO_3$ observed in the DTG analysis of Figure 6.1. A similar observation was also reported in this kind of raw material by [Suleiman et al., 2013].

Table 6-2 Physical characteristics of the precursors.

Sample	C	L1	L2	L3
PSD				
$d_{90}[\mu m]$	236.40	162.71	292.46	188.73
$d_{50}[\mu m]$	19.43	26.71	18	36.22
$d_{10}[\mu m]$	3.03	3.08	1.78	2.59
BET				
$SSA_{BET}\ [m^2/g]$	0.64	1.11	1.32	0.74

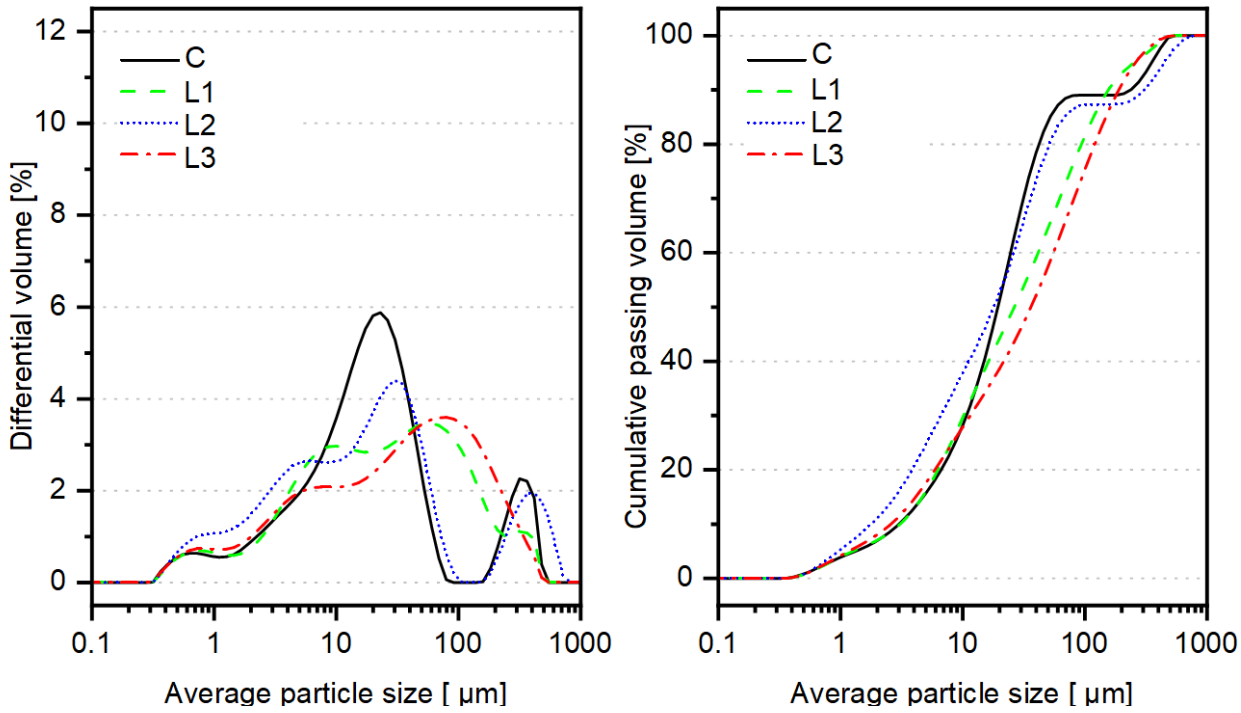

Figure 6.3 Particle size distribution of the precursors.

Figure 6.4 shows SEM images of all the precursor materials. At low magnification, the images corroborate the differences observed in the particle size and fineness among the studied samples, also showing a greater frequency of larger particles with a regular and smooth surface in the sample C, which is consistent with its low SSA_{BET}.

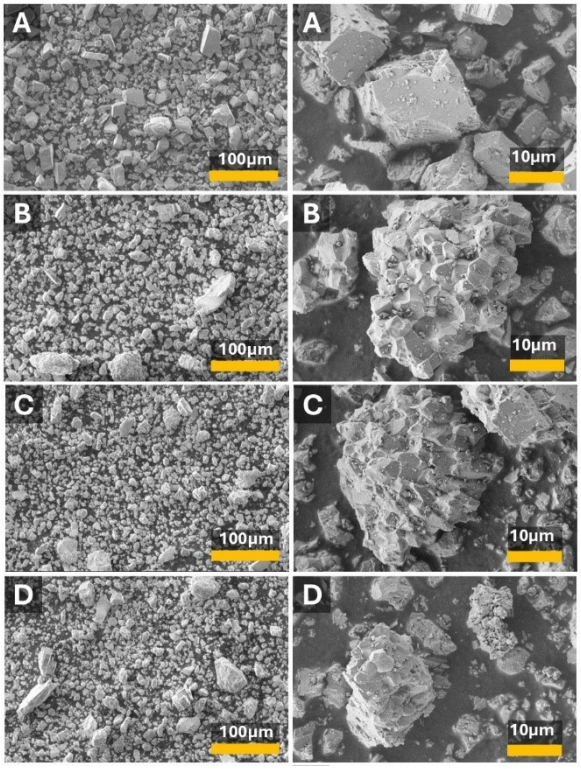

Figure 6.4 SEM images of precursors C (A), L1 (B), L2 (C), L3 (D).

6.3.2. Deposited Materials Characterization

- **Chemical Characteristics**

Table 6.3 summarizes the chemical composition of the DMs. The majority primary oxide in all samples was CaO, whose percentage by mass was between 65.39% to 69.46% representing a significant increase in comparison to the CaO content of the precursors. Likewise, the other primary oxides (SiO_2, Al_2O_3, Fe_2O_3) were below 1%, while the loss on ignition also decreased for all the samples. In this sense, ED acted as a lime concentrator where the initial content of the other primary oxides and secondary constituents were significantly reduced. The results indicate that the ED of calcite was possible despite impurities from the natural rock, which can be separated through the ED and successfully isolated in the anode chamber. This residual material, or anodic sludge, primarily consists of the other primary and secondary oxides found in the precursor material. For

example, subsequent electrolysis conducted on approximately 20g of limestone sample for a duration of 23 hours resulted in anodic sludge composed of: CaO 2.14%, SiO_2 62.6%, Al_2O_3 15.1%, Fe_2O_3 5.7%, Na_2O 3.36%, K_2O 2.76%, MgO 1.83%, TiO_2 0.81%, and LOI 5.6%, by mass. In contrast, control samples did not produce anodic sludge which is expected due to its high purity of $CaCO_3$.

Table 6-3 Chemical characteristics of the deposited materials.

Test	C	L1	L2	L3
XRF [wt. %]				
CaO	69.46	68.50	65.39	65.62
SiO_2	0.18	0.22	0.51	0.79
Al_2O_3	-	0.04	0.41	0.03
Fe_2O_3	0.02	0.07	0.07	0.07
MgO	0.01	0.03	1.64	1.28
Na_2O	0.53	1.80	1.05	3.35
K_2O	0.01	0.01	0.03	0.02
P_2O_5	0.01	0.01	0.03	0.03
MnO	-	-	0.01	-
TiO_2	0.02	0.02	-	0.01
LOI	29.74	28.3	30.82	28.76
Total	99.98	99.99	99.95	99.97
TG/DTG [wt.%]				
$L_{(30-310)}$	0.76	1.01	1.65	1.56
H_2O	0.76	1.01	1.65	1.56
$L_{(310-500)}$	19.16	20.85	20	20.33
$Ca(OH)_2$	78.80	85.73	82.27	83.63
$L_{(550-900)}$	9.42	4.31	5.67	4.41
$CaCO_3$	21.42	9.79	12.89	10.03

Regarding the secondary constituent's content (MgO, K_2O, Na_2O, and P_2O_5) in DMs from limestones, there were different behaviors according to the kind of impurity and sample. In general, K_2O and P_2O_5 were reduced, while MgO suffered a slight increase. However, for all the samples, the MgO content still meets the limits of this secondary constituent (MgO < 2.5%). DMs' MgO content variability can be attributed to the movement of impurities toward the cell's interface motivated by the stirring and the reduction of the particle sizes during the calcite dissolution, as well as the presence of aqueous magnesium ions (Mg^{2+}) because of the dolomite dissolution, which

could facilitate the movement of the magnesium to the cell's interface. Dolomite dissolution under acid conditions can be represented by the following reaction [Saldi et al., 2021]:

$$CaMg(CO_3)_2 + 4H^+ \rightarrow Ca^{2+} + Mg^{2+} + 2H_2CO_3 \quad (6.1)$$

The Na_2O content is augmented in all samples, being the main impurity of the DMs. This increase is attributed to the remaining electrolytic solution that was not completely isolated during the filtering protocol. In this sense, a washing protocol needs to be applied to DMs to reduce their sodium content. Although the high solubility of $NaNO_3$ is beneficial in terms of reducing the amount of water that is necessary to isolate DMs completely, the water consumption of this ancillary process, together with water and electrolyte reutilization, should be considered in a deep sustainability analysis of ED for further industrial applications.

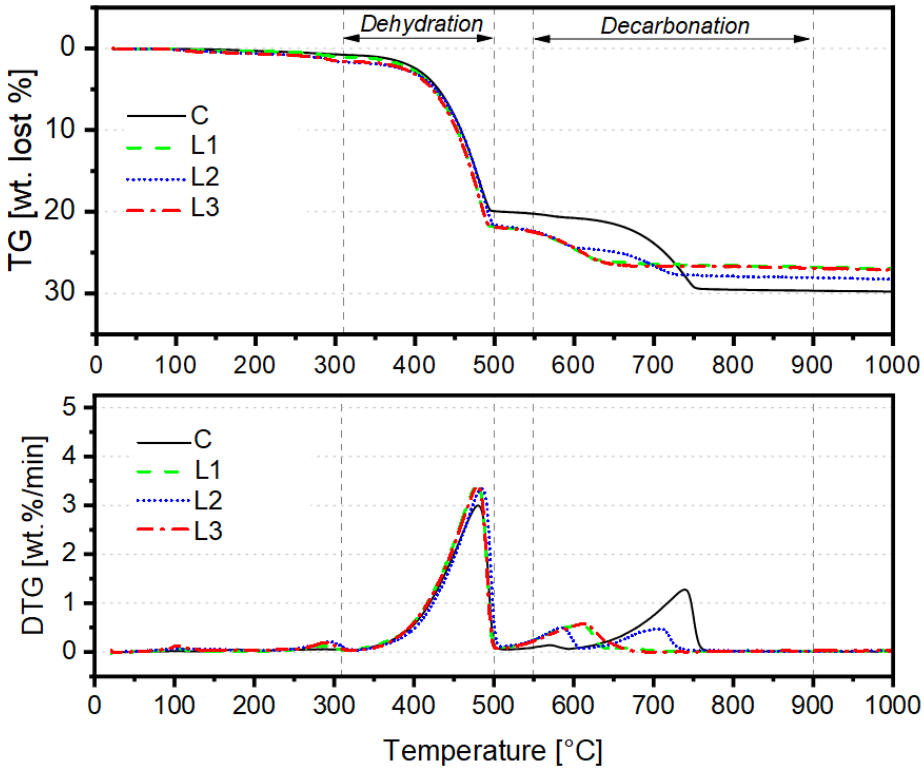

Figure 6.5 Thermogravimetric analysis of the deposited materials.

Figure 6.5 shows the TG/DTG analysis of the DMs from which mass loss for each temperature range are also detailed in Table 6.3. Most of the total weight loss occurred in the dehydration zone, where a new DTG peak associated with the precipitated $Ca(OH)_2$ can be observed. Likewise, the total weight loss and DTG peak in the decarbonation zone decreased because of the $CaCO_3$ reduction. This shows that the main phases present in the DMs are the deposited $Ca(OH)_2$ and the remaining $CaCO_3$ (i.e., unreacted or recombined), which also can be corroborated by the XRD results in Figure 6.6.

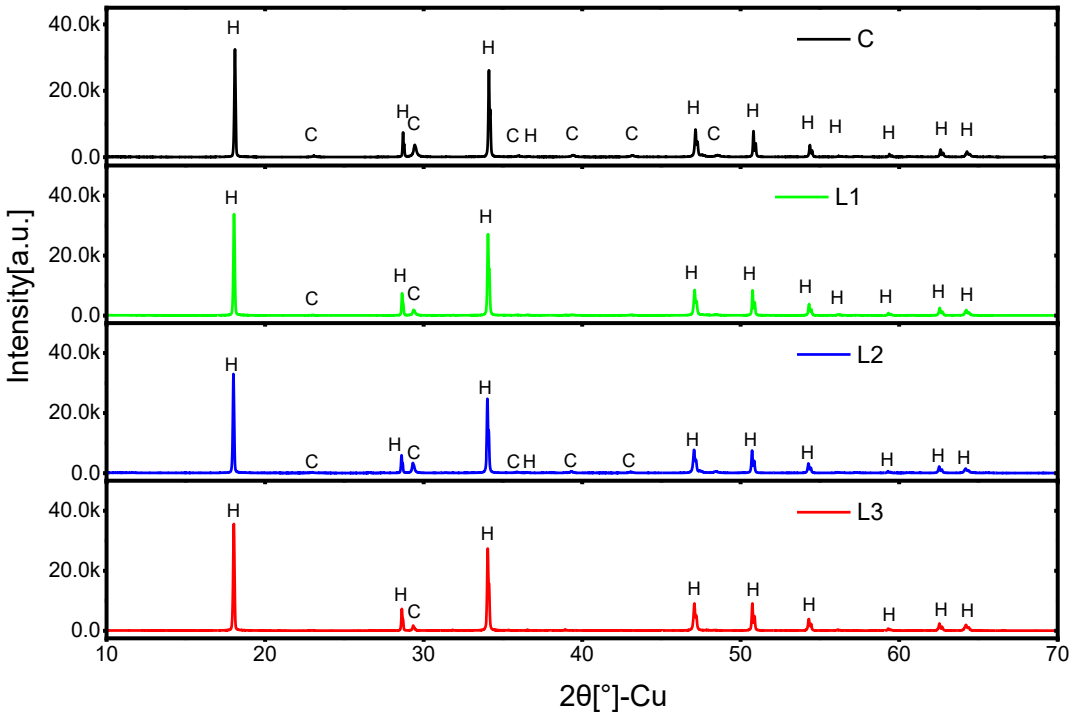

Figure 6.6 XRD analysis of the deposited materials. H: Calcium hydroxide ($Ca(OH)_2$), C: Calcite ($CaCO_3$).

Figure 6.7 compares the content of $Ca(OH)_2$ and $CaCO_3$ by mass among DMs and their respective precursors computed from the TG/DTG results. Furthermore, the percentage of Others phases includes the rest of the primary oxides, the secondary constituents, and occluded water. The $Ca(OH)_2$ content was between 78.8% to 85.73%. The content of $Ca(OH)_2$ in DMs from the

limestones having different sources showed a high similarity, demonstrating that ED enables precipitation of materials with similar chemical composition, even using natural limestones from diverse sources and chemical characteristics as precursors. This is evidence of the reproducibility of the process, which benefits its future scalability.

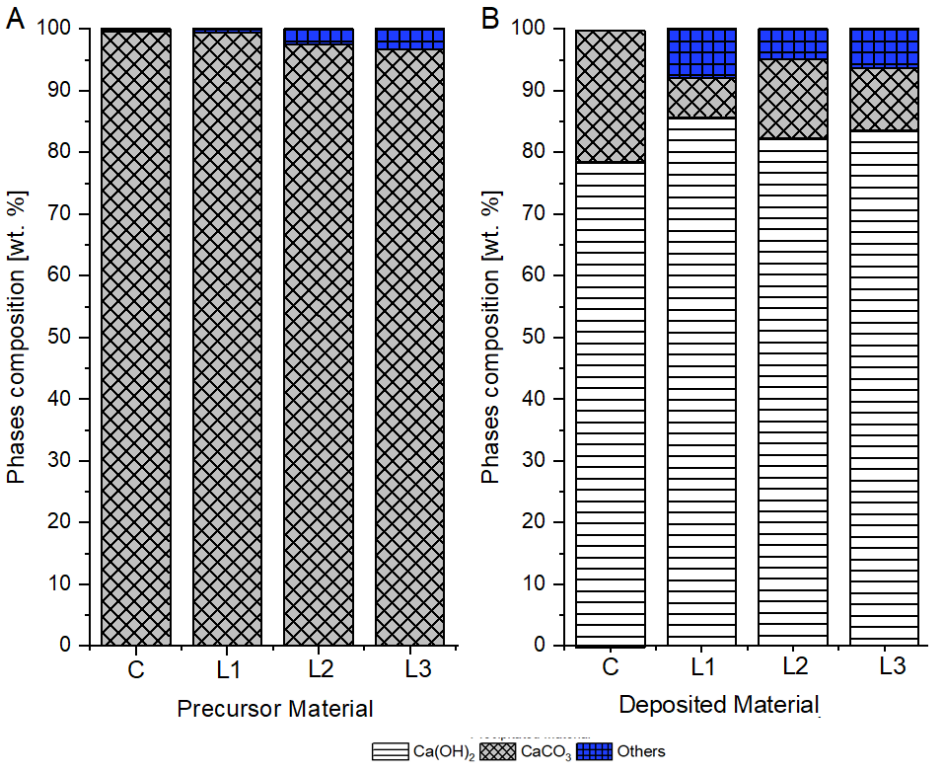

Figure 6.7 Comparison of the chemical composition of precursor materials (A), and deposited materials (B).

Variability was observed on the remaining $CaCO_3$ content among all the studied DMs. As previously mentioned, the physical characteristics of the precursors could explain the differences in the DMs chemical composition [Ramirez-Amaya et al., 2023].

Regarding the quality of DMs as hydrated lime products, ASTM-C207 [ASTM-C207, 2018] and ASTM-C206 [ASTM-C206, 2014] define a suitable chemical composition of hydrated lime for masonry and finishing products for construction. The requirements for typical hydrated lime (Type

N) are a minimum content of CaO of 95% (no LOI basis) and a maximum content of CO_2 of 5% if the sample is taken from the production chain.

Table 6-4 Main chemical characteristics of DM regarding requirements for normal hydrated lime for construction applications.

DM	%CaO[a] LOI basis	%LOI[a]	%CaO no LOI basis	$\%CO_2^b$
C	69.46	29.74	98.86	9.42
L1*	68.50	28.30	95.54	4.31
L2	65.39	30.82	94.52	5.67
L3	65.62	28.76	92.11	4.41

a. According to the oxides content by XRF analysis.
b. According to TG/DTG analysis, and is considered equal to $\%L_{(550\text{-}900)}$.
* Complies with requirements about chemical composition for Type N hydrated lime for construction applications.

Table 6.4 compares the properties of the various DMs from this study with the chemical requirements for Type N hydrated lime. DMs obtained from the ED of L1 could be considered chemically suitable as a hydrated lime product. In this sense, the main issue regarding the chemical composition of the rest of the DMs was the remaining content of $CaCO_3$, the variability of which was previously explained by the physical properties of the precursor materials.

- **Physical Characteristics**

The main physical characteristics of DMs are listed in Table 6.5. The differences in the PSD percentiles were reduced compared to the precursors, and the PSD curves show a slight homogenization and increase of the particle gradation (see Figure 6.8), meaning that DM includes a broader range of particle sizes than its precursor. The SSA_{BET} increased significantly for all the samples linked to better gradation, and mainly due to the presence of more porous structures produced by the fast precipitation of $Ca(OH)_2$ along the electrolysis process.

Table 6-5 Physical characteristics of the deposited materials.

Test	C	L1	L2	L3
PSD				
d_{90}[µm]	167.38	267.01	152.17	184.18
d_{50}[µm]	13.90	32.86	27.72	20.35
d_{10}[µm]	1.51	3.06	3.01	3.24
Retained on the 600µm sieve [vt %]	0.26	0.20	0	0
Retained on the 90µm sieve [vt %]	15.76	32.43	19.33	25.08
Retained on the 75µm sieve [vt %]	17.96	35.93	23.46	28.43
BET				
SSA_{BET} [m^2/g]	1.14	2.42	4.41	5.13

Regarding the fineness requirements for lime production, ASTM-C206 [ASTM-C206, 2018] mandates that no more than 0.5% of the material should remain on a 600 µm sieve and no more than 15% remain on a 75 µm sieve. These values are presented in Table 6.5 according to the PSD results. This means that DM may need an additional ancillary grinding process.

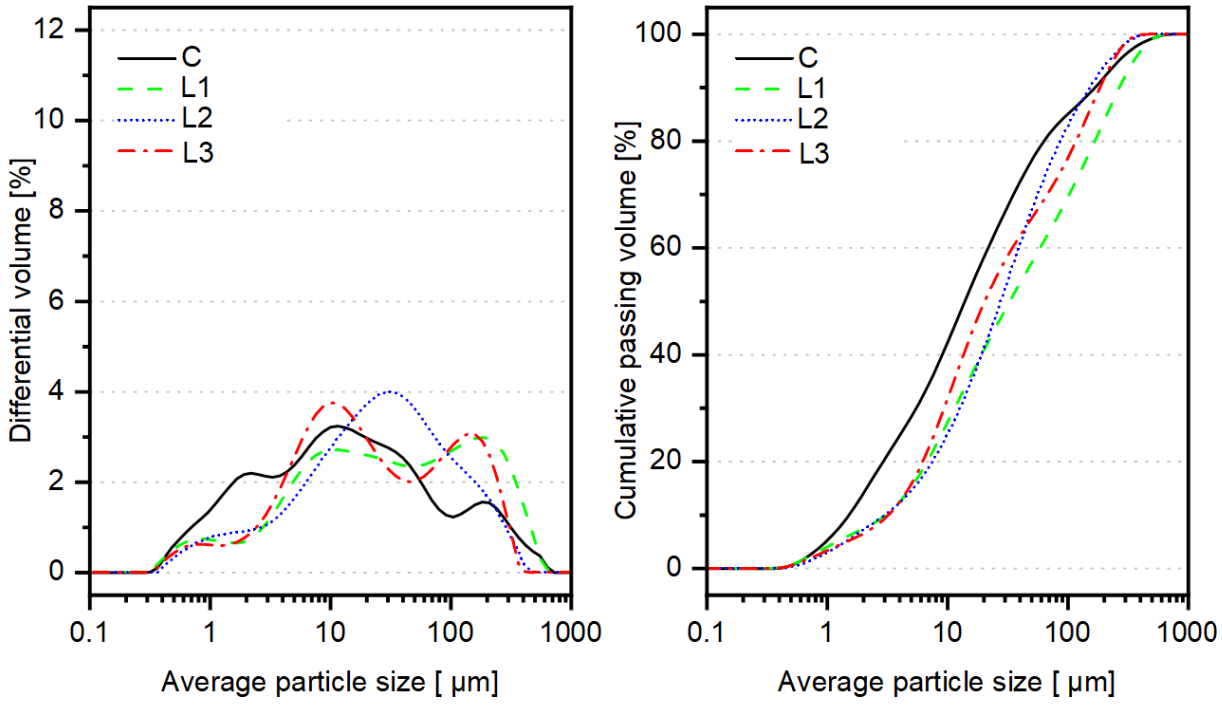

Figure 6.8 Particle size distribution of the deposited materials.

Figure 6.9 shows the different particle structures observed in DMs by FE-SEM. For all samples, low-carbon rich-calcium structures associated with $Ca(OH)_2$ formations were observed whose chemical composition was identified by EDX (see Figure C1). Particle clusters and large crystals with hexagonal cross-sections and smooth surfaces can be observed at low magnification. The latter is consistent with the morphologies of $Ca(OH)_2$ crystals with hexagonal plate and hexagonal column shape [Ma et al., 2022], and portlandite [Aïtcin, 2016], formed at a high pH. At high magnification, it can be observed that there are two standard classes of particle clusters. The first mainly comprises the agglomeration of prismatic structures with irregular shapes and smooth surfaces, including some smaller hexagonal crystals. The second type of cluster observed is mainly comprised of the agglomeration of smaller grains with irregular shapes (<1μm) whose chemical composition is similar to the hexagonal crystals (see Figure C2). Carbonate structures were also detected, which have an irregular shape and surface and are associated with the remanent $CaCO_3$ (see Figure C3).

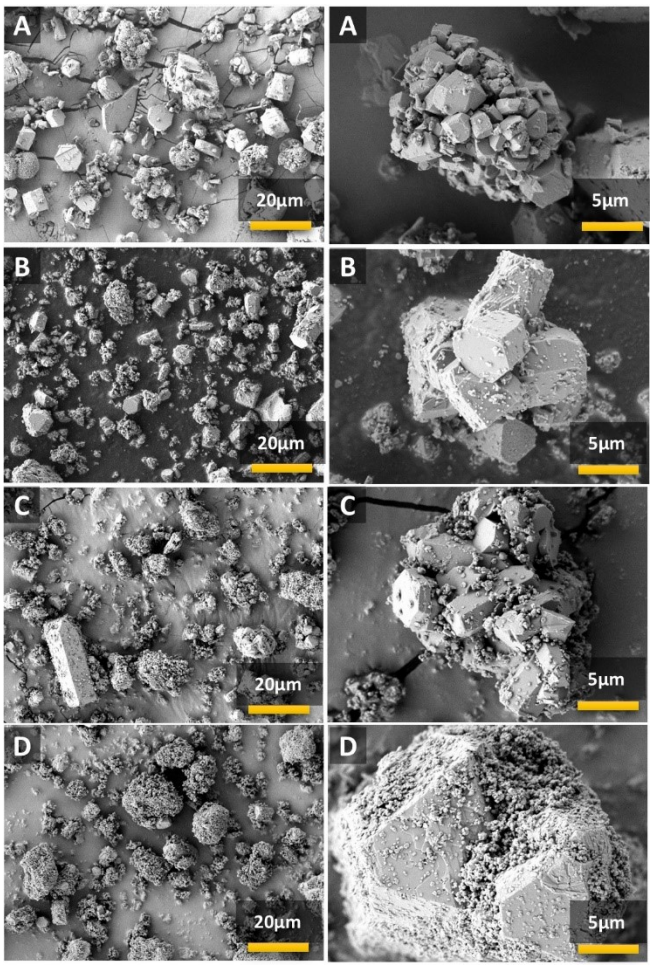

Figure 6.9 SEM images of DM from C (A), L1 (B), L2 (C), L3 (D).

The formation mechanism of the different structure morphologies and particle sizes depends on several factors that are also time variant during the ED, such as the ions concentration and the electrolyzed solution pH. In this sense, the pH along the interface has a wide variation, coming from acid levels in the anode chamber to alkaline levels in the cathode chamber, which creates a pH gradient in the interface that can precipitate different $Ca(OH)_2$ morphologies and structures that are consistent with the SEM observations. Although there was not a clear association between the physical or chemical characteristics of precursors and the physical characteristics of DMs, the better gradation and specific surface area of all samples mean an upgrade of the physical

characteristics of DMs compared with their precursors. For hydrated lime applications, a high specific surface benefits paste workability and hardening process, including carbonation [Romagnoli et al., 2013].

6.4. Conclusion

Electrochemical decarbonation is a disruptive technology with the potential to introduce several synergistic strategies to deep-decarbonize lime production. However, its early cost-effective incorporation in the current production chains needs evidence of its reproducibility and technical suitability under the wide range of operation conditions (e.g., feedstock materials availability and characteristics) that the lime industry offer around the world. This reproducibility study performed successfully applied the ED on different limestone feedstock used for lime production. The obtained precipitated materials were chemically and physically characterized, and their technical suitability to be considered an intermediary for hydrated lime production was assessed according to requirements established by the state of practice in the industry. The following conclusions can be drawn from the presented results:

- Several samples of high-grade limestone from lime industry were successfully decarbonated using two electrolysis cells operated at 12V. Regardless of the chemical composition, and physical characteristics of samples, from the electrochemical decarbonation of each precursor, the resultant material was a precipitate mainly comprised of $Ca(OH)_2$ (78.80% to 85.73% by mass), which also had a higher CaO content, reduced content of other primary oxides (SiO2, Al_2O_3, Fe_2O_3), and lower loss on ignition (LOI) than their respective precursors.

- The MgO from dolomite mineral, the majority secondary constituent in the precursors studied, was slightly increased in DMs. However, the MgO content for all samples remained under limits established by industry (<2.5%).
- Evidence was found that suggests that the physical characteristics of the precursor materials are associated with the variability in the remaining content of $CaCO_3$ in DMs. In this sense, as in the conventional thermal calcination, the electrochemical decarbonation is favored by a smaller average maximum particle size. This association can be employed to optimize the grinding process of limestones before ED. However, generalizing the variables' dependence and effects requires further investigation.
- DMs are mainly comprised of portlandite crystals and particle clusters of $Ca(OH)_2$ with a wide spectrum of sizes and morphologies. Likewise, DMs achieved a better gradation and SSA_{BET} than their respective precursors thus representing an upgrade of the physical characteristics for hydrated lime production.
- DMs from the ED of limestones L1 met requirements for chemical composition and particle size established by the standards ASTM-C206-14 and ASTM-C207-18 for Type N hydrated lime, which shows the potentiality of ED to produce a final product for construction applications. However, it is essential to highlight that other performance parameters from the presented standard, which were beyond the scope of this study, must be evaluated before DMs are considered a final product to be commercialized.

6.5. References

Aranda Usón, A., López-Sabirón, A. M., Ferreira, G., & Llera Sastresa, E. (2013). Uses of alternative fuels and raw materials in the cement industry as sustainable waste management options. *Renewable and Sustainable Energy Reviews*, *23*, 242–260. https://doi.org/10.1016/j.rser.2013.02.024

ASTM International. (2014). Standard Specification for Finishing Hydrated Lime (ASTM C206-14).

ASTM International. (2018). Standard Specification for Hydrated Lime for Masonry Purposes (ASTM C207-18).

Belaïd, F. (2022). How does concrete and cement industry transformation contribute to mitigating climate change challenges? *Resources, Conservation & Recycling Advances*, *15*, 200084. https://doi.org/10.1016/j.rcradv.2022.200084

Benhelal, E., Shamsaei, E., & Rashid, M. I. (2021). Challenges against CO2 abatement strategies in cement industry: A review. *Journal of Environmental Sciences*, *104*, 84–101. https://doi.org/10.1016/j.jes.2020.11.020

Ellis, L. D., Badel, A. F., Chiang, M. L., Park, R. J.-Y., & Chiang, Y.-M. (2020). Toward electrochemical synthesis of cement—An electrolyzer-based process for decarbonating CaCO3 while producing useful gas streams. *Proceedings of the National Academy of Sciences*, *117*(23), 12584–12591. https://doi.org/10.1073/pnas.1821673116

El-Salamony, A.-H. R., Mahmoud, H. M., & Shehata, N. (2020). Enhancing the efficiency of a cement plant kiln using modified alternative fuel. *Environmental Nanotechnology, Monitoring & Management*, *14*, 100310. https://doi.org/10.1016/j.enmm.2020.100310

Iliç, M., & Shaw, C. t. (1995). Evaluation of the quality of the raw materials for cement manufacture during geological exploration: Some observations on eastern and western european practice. *Mineral Resources Engineering*, *04*(01), 3–14. https://doi.org/10.1142/S0950609895000023

Jiang, Y., Liao, P., van Gestel, N., Sun, Y., Zeng, Y., Huang, S., Zhang, W., & van Groenigen, K. J. (2018). Lime application lowers the global warming potential of a double rice cropping system. *Geoderma*, *325*, 1–8. https://doi.org/10.1016/j.geoderma.2018.03.034

Laveglia, A., Sambataro, L., Ukrainczyk, N., De Belie, N., & Koenders, E. (2022). Hydrated lime life-cycle assessment: Current and future scenarios in four EU countries. *Journal of Cleaner Production*, *369*, 133224. https://doi.org/10.1016/j.jclepro.2022.133224

Ma, X., Wu, H., Chang, L., Wang, J., Wang, Y., & Cui, S. (2022). The influence of calcium hydroxide crystal morphology on the desulfurization of cement kiln flue gas. *Journal of Materials Science*, *57*(39), 18287–18297. https://doi.org/10.1007/s10853-022-07801-9

Moneim, A. A. A., Aziz, E. H. A., & Magd, S. A. A. E. (2013). Assessment of raw materials for cement industry in Sohag area, upper Egypt. *International Journal of Mining and Mineral Engineering*, *4*(4), 333. https://doi.org/10.1504/IJMME.2013.056868

Ramirez-Amaya, D., Dreyse, P., Martínez, N. P., Troncoso P., F., Navarrete, I., Noël, M., Canales, R. I., & González, M. (2023). Comparison of the electrochemical decarbonation of different-grade limestones used in cement manufacturing. *Cement and Concrete Research*, *174*, 107307. https://doi.org/10.1016/j.cemconres.2023.107307

Romagnoli, M., Gualtieri, M. L., Hanuskova, M., Rattazzi, A., & Polidoro, C. (2013). Effect of drying method on the specific surface area of hydrated lime: A statistical approach. *Powder Technology*, *246*, 504–510. https://doi.org/10.1016/j.powtec.2013.06.009

Sagastume Gutiérrez, A., Van Caneghem, J., Cogollos Martínez, J. B., & Vandecasteele, C. (2012). Evaluation of the environmental performance of lime production in Cuba. *Journal of Cleaner Production*, *31*, 126–136. https://doi.org/10.1016/j.jclepro.2012.02.035

Saldi, G. D., Causserand, C., Schott, J., & Jordan, G. (2021). Dolomite dissolution mechanisms at acidic pH: New insights from high resolution pH-stat and mixed-flow reactor experiments associated to AFM and TEM observations. *Chemical Geology*, *584*, 120521. https://doi.org/10.1016/j.chemgeo.2021.120521

Simoni, M., Wilkes, M. D., Brown, S., Provis, J. L., Kinoshita, H., & Hanein, T. (2022). Decarbonising the lime industry: State-of-the-art. *Renewable and Sustainable Energy Reviews*, *168*, 112765. https://doi.org/10.1016/j.rser.2022.112765

Suleiman, I. E., Abubakar, A., Otuoze, H. S., Suleiman, M. A., Momoh, R. O., & Aliyu, S. N. (2013). *Effects of Particle Size Distribution on the Burn Ability of Limestone*. https://www.semanticscholar.org/paper/Effects-of-Particle-Size-Distribution-on-the-Burn-Suleiman-Abubakar/afabf6e50d35b27cd01b3f08e78439e833c7ea30

Chapter 7 : Electrochemical production of hydrated lime from organic waste: A feasibility study[4]

7.1. Introduction

Pursuing sustainable hydrated lime production addresses environmental concerns and aligns with broader goals of resource efficiency and economic viability. By adopting innovative technologies and practices, the lime industry can contribute to a more sustainable future while meeting the growing demand for this essential material. This research makes a significant contribution by demonstrating that the ED process can produce quality hydrated lime equivalent to that obtained through conventional methods. This study explores an innovative approach of utilizing bio-based feedstock (eggshells and mussel shells) with ED to reduce waste diverted to landfills, as well as the extraction of raw materials. This novel combination not only proves the feasibility and versatility of ED in lime production but also leverages bio-based materials, which effectively reduce the carbon footprint associated with hydrated lime production, offering a more environmentally friendly alternative to conventional techniques. This advancement holds promise for making hydrated lime—a fundamental component in building materials—more sustainable, thereby contributing to the broader goal of reducing the environmental impact of the construction industry.

7.2. Materials and Methods

7.2.1. Materials

Three sources of $CaCO_3$ were used as feedstocks in the ED process as shown in Figure 7.1. Fisher Chemical's calcium carbonate reagent (CAS-No: 471-34-1, Ref-No: 64-500), similar to that used

[4] This chapter is an abridged version of the paper that has been published as: Mahmood, O.; Kavgic, M.; Noël, M. (2025). Electrochemical production of hydrated lime from organic waste: A feasibility study. *Journal of Materials in Civil Engineering*. https://doi.org/10.1061/JMCEE7.MTENG-21939

by Ellis et al. [Ellis et al., 2020], served as the control sample as it has a high purity level of $CaCO_3$ (>99%) to minimize the effect of any impurities on the chemical reaction. Additionally, powdered organic $CaCO_3$ sources from mussel shells (MS) and eggshells (ES) were employed as feedstocks. These materials were washed multiple times with distilled water to eliminate impurities, dust, and organic residues, then oven-dried at 200°C for 6 hours to remove excess moisture and remaining organic matter (e.g., membranes) [Ballester et al., 2007; Barros et al., 2009]. The dried materials were manually crushed with a hammer to break them into smaller pieces, followed by further grinding with a ceramic mortar to achieve a fine powder. The finely ground powder was then sieved through 90 μm [Strother, 2019]. The feedstock was oven-dried at 105°C for 24 hours and then physically and chemically analyzed.

Figure 7.1 Feedstocks used in the study (C) High purity $CaCO_3$, (ES) Eggshells,(MS) Mussel shells.

7.2.2. Electrochemical Decarbonation Process and Experimental Design

The H-type electrolysis reactor used in this study was similar to that used in chapter 3 (see section 3.3.3). For each ED procedure, 10.0 grams of the feedstock were introduced into the anode

chamber, and stirring was maintained at 200 rpm to enhance diffusion. A 9V direct current was applied continuously for 15 hours to ensure complete dissolution of the feedstock, based on prior experimentation. The electrical current was continuously monitored every 60 seconds during the ED process with an ACS712 current sensor and Arduino Leonardo microcontroller board. Once the ED was completed, the DMs were removed from the cell and isolated by filtration. The samples underwent additional washing with distilled water to remove any residual sodium nitrates in the deposited material. This step was essential because, as demonstrated in the previous chapter, unwashed samples exhibited a noticeably higher sodium nitrate content. This indicates that residual sodium nitrates from the deposition process remain adhered to the material surface unless actively removed. Washing with distilled water ensures the elimination of these residues, thereby improving the purity of the samples and ensuring consistency and accuracy in subsequent characterization or application. Subsequently, samples were filtered through a paper filter using a Büchner funnel, oven-dried at 105°C for 24 hours, and stored in a desiccant chamber at room temperature for future analysis [Ramirez-Amaya et al., 2023; Martínez et al., 2024].

A completely randomized design was used to determine statistically significant variations in the chemical composition and physical properties of the DMs, the performance of the ED process, and the energy consumption for each $CaCO_3$ source. The design involved three replicates for the feedstocks, which served as the explanatory variable. Each replicate encompassed a distinct ED process using a sample of powdered raw material, leading to 9 ED trials conducted in a randomized sequence. Although the number of trials was limited ($n = 9$), the order in which they were conducted was randomized to reduce systematic bias. Randomization was implemented using the RAND function in Microsoft Excel to assign each trial a random value, and the trials were then ordered accordingly. Throughout the experiments, the same electrodialysis cell and operational

parameters, including voltage, electrolyte concentration, initial sample mass, and process duration, were consistently applied to maintain uniformity across the trials.

7.2.3. Characterisation of Feedstock and Deposited Materials

The feedstocks and DMs samples underwent tests to assess their physical and chemical properties, including measurements of PSD, SSA_{BET}, FE-SEM, TGA/DTGA, XRD, XRF. These tests adhered to the methodologies described in Chapter 3, specifically Section 3.3.2.

7.2.4. Electrochemical Decarbonation Performance

This investigation employed three principal performance metrics previously proposed by Ramirez-Amaya et al. [[Ramirez-Amaya et al., 2023]: 1) Efficiency, indicating the extent to which the actual quantity of $Ca(OH)_2$ in the DMs aligns with the theoretically anticipated amount; 2) Energy, which measures the total electrical energy consumed throughout the electrolysis process; and 3) $Ca(OH)_2$ Purity, denoting the fraction of $Ca(OH)_2$ moles retrieved in the DMs.

TG/DTG was employed to measure the amounts of $CaCO_3$ and $Ca(OH)_2$ purity in the feedstocks and DMs, following Equations 7.1 and 7.2 [Ramirez-Amaya et al., 2023]:

$$\%CaCO_3 = \%WL_{(550-900)}(MW_{CaCO_3}/MwW_{CO_2}) \quad (7.1)$$

$$\%Ca(OH)_2 = \%WL_{(310-500)}(MW_{Ca(OH)_2}/MW_{H_2O}) \quad (7.2)$$

where $\%WL_{(550-900)}$ and $= \%WL_{(310-500)}$ represent weight loss in the decarbonation and dehydration zones, respectively. Molecular weights were as follows: $CaCO_3$ (100.087 g/mol), $Ca(OH)_2$ (74.093 g/mol), CO_2 (44.01 g/mol), and H_2O (18.015 g/mol). ED efficiency was calculated using Equation 7.3, and the energy consumption was determined by integrating the power curve.

$$\%\text{Efficiency} = \frac{W_{DM}\,\text{MW}_{\text{CaCO}_3} DM_{\%\text{Ca(OH)}_2}}{W_C C_{\%\text{CaCO}_3} \text{MW}_{\text{Ca(OH)}_2}} \text{x}100 \quad (7.3)$$

Where W_{DM} is the dry weight of DMs, $DM_{\%\text{Ca(OH)}_2}$ is the percentage of $Ca(OH)_2$ in the DMs, W_C is the initial weight feedstock, and $C_{\%\text{CaCO}_3}$ is the percentage of $CaCO_3$ in the feedstock.

7.2.5. Statistical Analysis

A comprehensive statistical approach was implemented to analyze ED performance. The investigation commenced with a one-way ANOVA to evaluate whether significant differences in performance metrics existed [Ramirez-Amaya et al., 2023]. This test allowed for the comparison of mean values across different feedstock groups. Before this, the Shapiro-Wilk test was utilized to verify the normality of the data, thereby ensuring that the ANOVA's assumptions were valid [Jena et al., 2013]. Following the ANOVA, a post-hoc analysis using the Tukey test, adjusted for multiple comparisons through the Bonferroni correction, was performed to identify specific group differences [Haynes, 2013]. This meticulous approach ensured a rigorous and detailed examination of performance variations, providing a robust basis for interpreting the effects of different conditions on ED performance.

7.2.6. Evaluating Potential CO_2 Reduction

Although a comprehensive life cycle analysis (LCA) of the electrochemical decarbonation process is outside of the scope of this study, a preliminary assessment of the potential reduction in CO_2 emissions was conducted. It is important to note that the potential CO_2 reduction calculations were confined to the calcination reaction in the production process (i.e., chemical emissions) and do not include the energy demand to heat the kiln nor the embodied energy to transport raw materials or final products. Consequently, the reduction in CO_2 emissions can be determined based on the theoretical CO_2 emissions values for the conventional approach (CA) and the ED method. For the

conventional approach, the CO_2 emitted can be determined based on Equations 7.1 and 7.3 [Martínez et al., 2024]:

$$CO_{2_{CA}} = \frac{W_C \times \%\mathrm{CaCO_3}}{\mathrm{MW_{CaCO_3}}} \tag{7.3}$$

Conversely, the role of the ED process in lowering the carbon footprint of hydrated lime can be broken down into two components: the first component accounts for the CO_2 sequestered by the DMs in the form of remaining (unreacted or recombined) $CaCO_3$. This accounts for a small proportion of unreleased CO_2 when the ED efficiency is maximized. This portion can be calculated using Equation 7.4 [Martínez et al., 2024]:

$$CO_{2_{ED-Seq.}} = \frac{W_{DM} \times [1 - \%\mathrm{Ca(OH)_2}]}{\mathrm{MW_{CaCO_3}}} \tag{7.4}$$

The second component refers to the CO_2 gas that is captured during the ED process; this constitutes one of the key benefits of the process, namely to facilitate more efficient carbon capture by achieving a higher CO_2 concentration (approximately 67%). This enhances the process and reduces the energy needed for CO_2 capture [Ellis et al., 2020]. Therefore, it is assumed in this study that all CO_2 produced by the ED process will be captured, such that the amount of CO_2 captured can be calculated using Equation 7.5:

$$CO_{2_{ED-Capt.}} = \frac{\{W_C \times \%\mathrm{CaCO_3}\} - \{W_{DM} \times [1 - \%\mathrm{Ca(OH)_2}]\}}{\mathrm{MW_{CaCO_3}}} \tag{7.5}$$

7.3. Results and Discussion

7.3.1. Feedstock Characterization

Table 7.1 shows the chemical composition of the feedstocks used in this study. The main oxide was CaO content with 56.24%, 52.01%, and 53.89 % for C, ES, and MS, respectively, which are

chemically suitable for hydrated lime production [Abdel Moneim et al., 2013]. When comparing the CaO content of the ES and MS with that of mineral-based limestone reported in previous studies employing the ED process, which was 40.85-48.09% for [Ramirez-Amaya et al., 2023] and 48.55% for [Martínez et al., 2024], it can be seen that organic-based feedstocks show a higher $CaCO_3$ purity level, which is expected to lead to a higher yield of DMs. The loss on ignition (LOI) indicates the content of $CaCO_3$ as the mass loss occurs due to the release of CO_2 gas from the feedstocks. The LOI values for the feedstocks were higher than 40%, confirming a high content of $CaCO_3$ in the feedstocks.

Table 7-1 Chemical characteristics of the feedstock.

Test	Control (C)	Eggshells (ES)	Mussel shells (MS)
XRF [wt. %]			
CaO	56.24	52.01	53.89
SiO_2	0.16	0.20	0.19
Al_2O_3	0.00	0.00	0.00
Fe_2O_3	0.01	0.01	0.02
MgO	0.00	0.49	0.09
Na_2O	0.05	0.20	0.41
K_2O	0.01	0.09	0.01
LOI	43.48	46.74	45.22
Total	99.95	99.72	99.85
TGA[wt. %]			
$WL_{(550-900)}$	43.77	43.85	43.52
$\%CaCO_3$	99.53	99.72	98.97
XRD Rietveld (wt%)			
Calcite ($CaCO_3$)	100.00	100.00	58.10
Aragonite ($CaCO_3$)	-	-	41.9

TG analysis was employed to determine the decomposition temperatures of the feedstocks (Figure 7.2), and this information was utilized to evaluate the electrolysis performance. The thermogravimetric data reveal that weight losses between 550-900 °C were 43.77%, 43.85%, and 43.52%, translating to $CaCO_3$ contents of 99.53%, 99.72%, and 98.87% for the C, ES, and MS samples, respectively. It can also be seen that the MS exhibits lower decomposition temperatures than the other feedstocks. This difference is because the primary mineral in MS is aragonite,

whereas calcite is the predominant mineral in C and ES. While calcite and aragonite share the same chemical composition, their different crystal structures lead to their physical properties and stability variations. Calcite decomposes at a higher temperature compared to aragonite. It typically decomposes into CaO and CO_2 at around 700°C to 800°C, while aragonite decomposes at a lower temperature around 650°C [Ballester et al., 2007]. Figure 7.3 presents the XRD analysis of the feedstock samples, confirming that the C and ES samples primarily consist of calcite, the primary CaO source. Meanwhile, MS contains a significant amount of aragonite (41.9%).

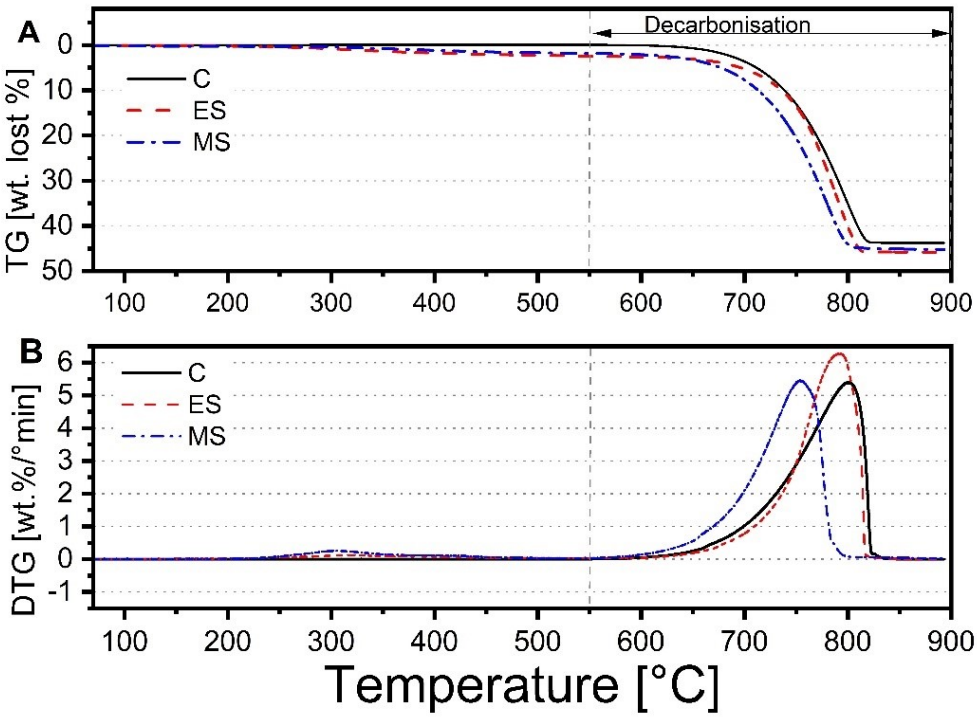

Figure 7.2 TG (A), DTG (B) analysis of the feedstocks.

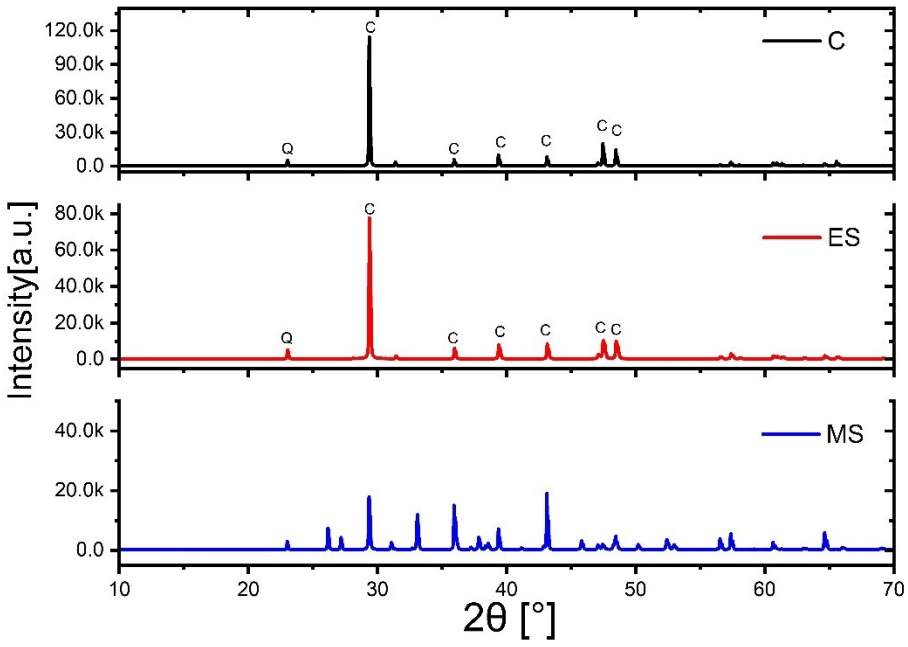

Figure 7.3 XRD analysis of feedstock. C: Calcite (CaCO3), A: Aragonite (CaCO3).

The main physical characteristics of the feedstocks are listed in Table 7.2, and the PSD is shown in Figure 7.4. There was high variability in the PSD and SSA_{BET} among feedstock samples; ES and MS samples showed a smaller average maximum particle size and higher specific surface area than the C sample. A more uniform particle size distribution was observed in C compared to ES and MS, as depicted in Figure 7.4. This finding is expected because the C sample is a commercial material with high purity. In contrast, ES and MS are natural materials composed of various minerals and were powdered manually. Table 7.2 also indicates a high surface area with an SSA_{BET} value of 4.54 m^2/gm, attributed to the numerous tiny pores in the eggshells that facilitate gas exchange for the embryo's respiration [Mortola, 2009]. This porous structure is visible in the FE-SEM images shown in Figure 7.5. Finer $CaCO_3$ particles, along with a higher surface area to volume ratio, can enhance the efficiency of the calcination in the conventional method. A finer particle size can lead to a more effective reaction, resulting in complete calcination and greater

CO_2 generation due to the increased surface area and reaction kinetics [Suleiman et al., 2013]. The volume percentage of particles larger than 90 μm did not surpass 15% for any of the sources, maintaining an acceptable level in line with the fineness recommendations to ensure optimum calcination [Stanˇek, 2019].

Table 7-2 Physical properties of the feedstocks

Test	Control (C)	Eggshells (ES)	Mussel shells (MS)
PSD			
Retained on $90\mu m$ [vt. %]	10.97	0.00	0.00
d_{90} $[\mu m]$	239.88	13.36	13.18
SSA_{BET} $[m^2/g]$	0.64	4.54	1.93

In this feasibility study, the organic sources of $CaCO_3$ were powderized by hand. Consequently, there are differences in PSD among the used material sources. While particle size may influence surface area and reaction kinetics, this effect has not been investigated in this study. As a result, it is acknowledged that the findings may not comprehensively reflect the nuanced interactions between particle size and process efficiency. Nevertheless, the differences in particle size are not believed to influence the overall feasibility of this approach. It is recommended that future investigations should incorporate a more detailed examination of particle size effects to provide a holistic understanding of their role in optimizing decarbonation performance.

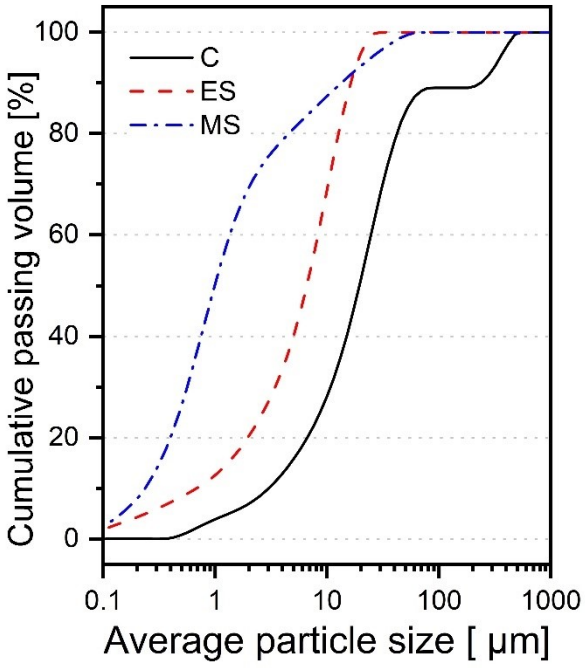

Figure 7.4 Particle size distribution of the feedstock.

FE-SEM was performed to evaluate the morphology of the feedstocks, and the results are shown in Figure 7.5. At low magnification, agglomeration of particles in cubic shapes is observed for sample C; these agglomerations do not exceed 90 µm, and the particle size is relatively homogeneous. In contrast, in ES and MS, a heterogeneous particle size distribution can be observed in irregular and undefined agglomerates, which could result from the crushing process. High FE-SEM magnification shows the pores in ES particles as fine, well-defined openings. These pores are distributed throughout the shell and vary in size, with some appearing as small, round holes while others may be elongated or irregular. The porous matrix of ES is consistent with its high SSA_{BET}. High magnification also shows that MS is primarily composed of $CaCO_3$ in the form of aragonite crystals appearing as needle-like or elongated prisms.

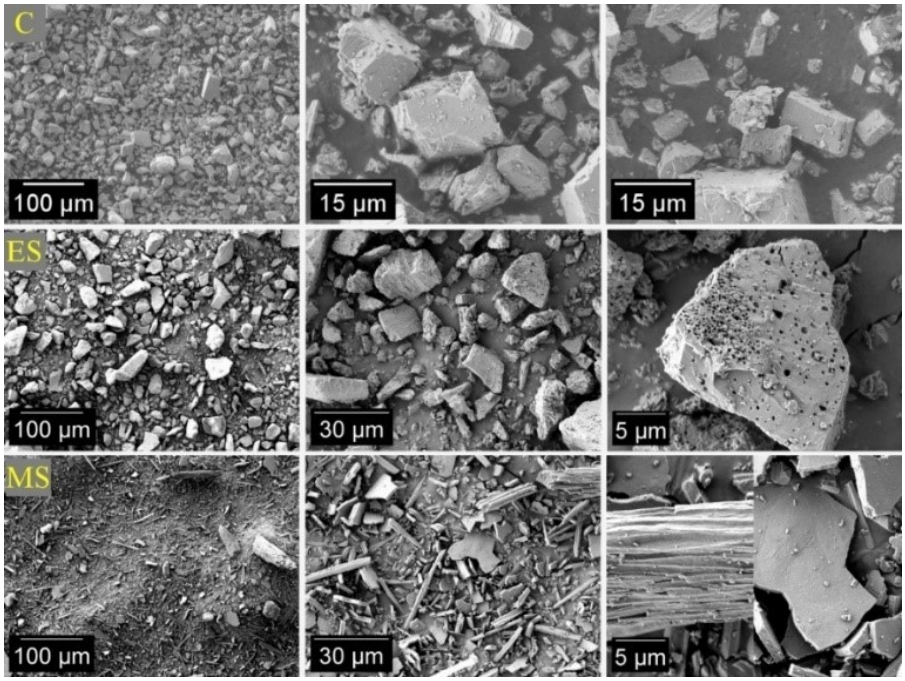

Figure 7.5 FE-SEM of the feedstock.

7.3.2. Deposited Materials Characterization

Table 7.3 presents the chemical composition of the DMs, which defines the end products upon the conclusion of the ED process. The dominant oxide in all samples was CaO, with its mass percentage ranging from 70.84% to 73.72%, reflecting a significant increase compared to the CaO content in the feedstocks. In contrast, the other primary oxides (SiO_2, Fe_2O_3, MgO) were below 1%, and the loss on ignition was reduced across all samples. This outcome is attributed to the electrolysis process in the anode chamber, where calcite dissolution occurs. Calcium ions (Ca^{2+}) migrate toward the cell interface and react with hydroxyl ions (OH^-) generated from water reduction in the cathode chamber, resulting in the deposition of $Ca(OH)_2$ at the cell interface [Martínez et al., 2024]. These results indicate that calcite electrolysis was effective despite

impurities separated and isolated in the anode chamber. This result is consistent with previous studies [Ramirez-Amaya et al., 2023].

Table 7-3 The chemical composition of the deposited materials.

Test	Control (C)	Eggshells (ES)	Mussel shells (MS)
XRF [wt. %]			
CaO	73.72	70.84	73.12
SiO_2	0.22	0.19	0.18
Al_2O_3	0.00	0.00	0.00
Fe_2O_3	0.02	0.01	0.01
MgO	0.00	0.88	0.17
Na_2O	0.04	0.11	0.15
K_2O	0.00	0.01	0.00
LOI	25.86	27.48	26.23
Total	99.85	99.53	99.86
TGA [wt. %]			
$WL_{(550-900)}$	3.80	4.56	3.75
$\%CaCO_3$	8.64	10.37	8.53
XRD Rietveld (wt%)			
Calcite ($CaCO_3$)	7.96	4.24	3.25
Portlandite ($Ca(OH)_2$)	92.04	95.76	96.75

The content of secondary constituents (K_2O, MgO, and Na_2O) in the DMs showed varying behaviors depending on the type of impurity and the sample. K_2O was reduced across all samples, whereas MgO experienced a slight increase. Nevertheless, the MgO content in all samples remains within the acceptable limits for hydrated lime production [Strother, 2019]. Notably, the Na_2O content was also decreased despite the use of $NaNO_3$ as the electrolytic solution due to the isolation process during the filtering procedure.

Figure 7.6 shows the TG/DTG analysis of the DMs. The weight loss at 310-500 °C was 21.21%, 20.15%, and 21.52% for the C, ES, and MS, respectively. This weight loss occurred in the dehydration zone, where a new DTG peak associated with $Ca(OH)_2$ can be observed. Likewise, the weight loss and DTG peak in the decarbonation zone at 550-900 °C decreased significantly to 3.80%, 4.56%, and 3.75% for C, ES, and MS because of the $CaCO_3$ reduction in the DMs. The

significant decrease in $CaCO_3$ content indicates the efficiency of the ED process in producing high-purity $Ca(OH)_2$ regardless of the impurity level, crystalline phase, and type of feedstocks. The TGA also confirms that the main phases present in the DMs are $Ca(OH)_2$ and the remaining $CaCO_3$ (i.e., unreacted or recombined), as corroborated by the XRD results in Figure 7.7.

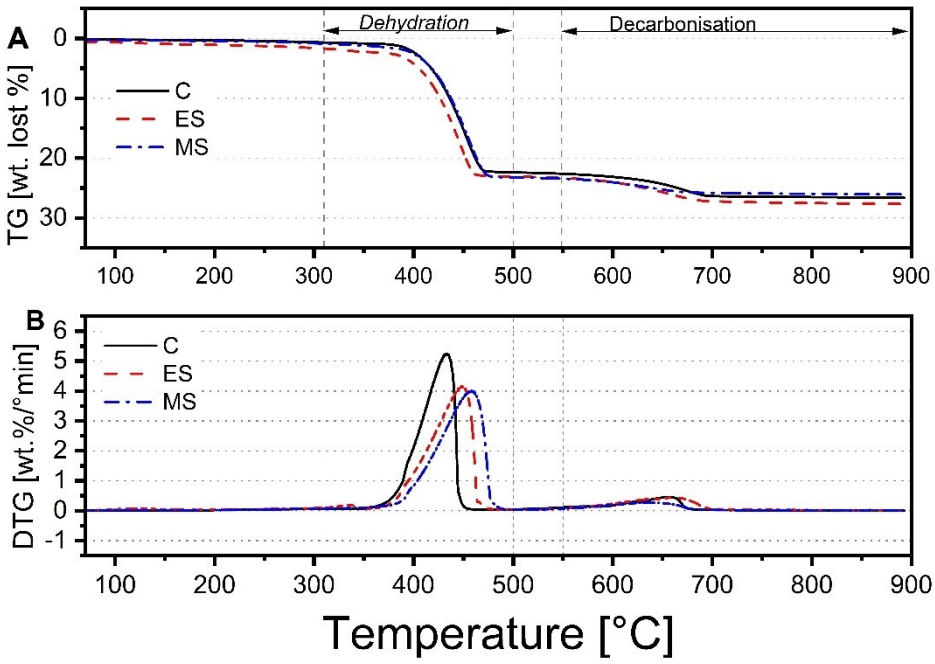

Figure 7.6 TG (A), DTG (B) analysis of the deposited materials.

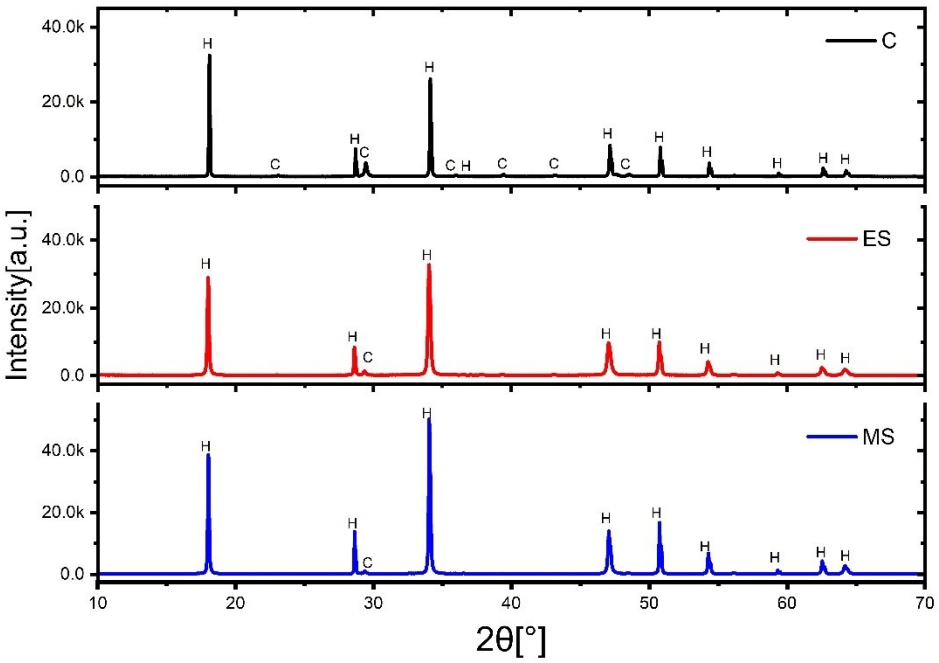

Figure 7.7 XRD analysis of the deposited materials.

ASTM-C207 [ASTM-C207, 2018] outlines the chemical composition criteria for hydrated lime used in masonry and finishing products. Specifically, Type N hydrated lime must have at least 95% CaO (on a no-LOI basis) and no more than 5% CO_2 if sampled from the production line. Table 7.4 compares the different DMs examined in this study with these standards for typical hydrated lime. All the DMs sourced from the ED satisfy these chemical requirements and are thus deemed suitable as a final hydrated lime product.

Table 7-4 The main chemical characteristics of the deposited materials regarding the requirements of hydrated lime for construction applications.

DMs	%CaO no LOI basis	$\%\mathbf{CO_2^*}$
Control (C)**	99.50	3.80
Eggshells (ES)**	98.31	4.56
Mussel shells (MS)**	99.27	3.75

* according to TG/DTG analysis, and is considered equal to $L_{(550-900)}$.
** complies with requirements about chemical composition for Type N hydrated lime for construction applications.

The Specific Surface Area (SSA_{BET}) and PSD of DMs are presented in Figure 7.8 and Table 7.5. The PSD curves reveal a modest degree of homogenization and an enhanced particle gradation, indicating that DMs encompass a broader spectrum of particle sizes than their raw materials. The specific surface area exhibited a significant increase across all samples, primarily due to improved gradation and the development of more porous structures resulting from the rapid precipitation of $Ca(OH)_2$ during the electrolysis process [Ramirez-Amaya et al., 2023]. ASTM-C206 [ASTM-C206, 2014] mandates that no more than 0.5% of the material should remain on a 600 μm sieve and no more than 15% should remain on a 75 μm sieve. ES and MS DMs comply with this standard, meeting the physical criteria for hydrated lime, while DMs from C slightly exceed the latter requirement. It is worth mentioning that when the feedstocks meet the fineness requirement before the ED process, their corresponding DMs also meet this physical standard, consistent with findings reported by [Ramirez-Amaya et al., 2023]. This finding indicates the importance of optimizing the milling process of feedstocks in the chain of hydrated lime production, which includes ED.

Table 7-5 Physical properties of the deposited materials.

Test	Control (C)	Eggshells (ES)	Mussel shells (MS)
PSD			
Retained on $600\mu m$ [vt. %]	0.00	0.00	0.00
Retained on $90\mu m$ [vt. %]	14.76	0.5	1.14
Retained on $75\mu m$ [vt. %]	18.77	2.85	3.66
d_{90} $[\mu m]$	158.59	13.31	13.36
SSA_{BET} $[m^2/g]$	1.14	5.01	3.26

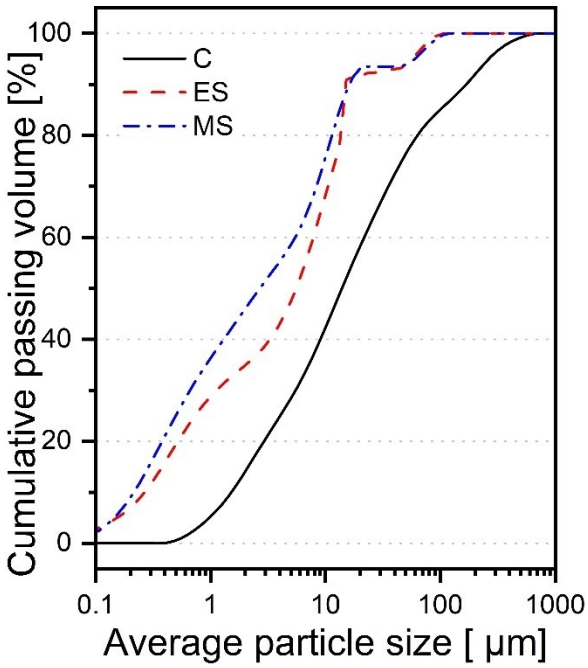

Figure 7.8 Particle size distribution of the deposited materials.

Figure 7.9 showcases the various particle structures within DMs as revealed by FE-SEM. The images display low-carbon calcium-rich structures associated with $Ca(OH)_2$. At lower magnifications, particle clusters and sizable crystals with hexagonal cross-sections and smooth surfaces are evident. These observations correspond to the morphologies of $Ca(OH)_2$ crystals, including both hexagonal plate and columnar shapes, as well as portlandite [Ma et al., 2022], which typically emerge under high pH conditions. At increased magnification, two primary classes of particle clusters are discerned. The first class consists mainly of agglomerated prismatic structures with irregular shapes and smooth surfaces interspersed with smaller hexagonal crystals. The second class features predominantly smaller grains with irregular shapes (<1 µm), whose chemical composition is comparable to hexagonal crystals.

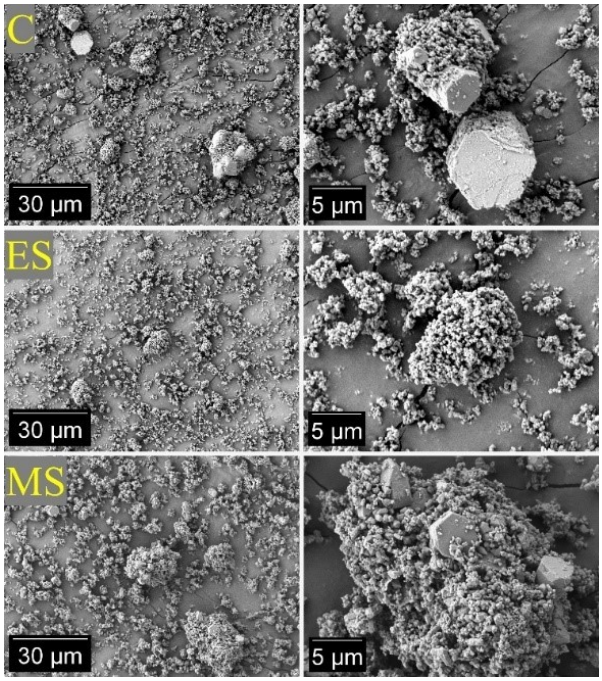

Figure 7.9 FE-SEM images of the deposited materials.

The diverse structural morphologies and particle sizes are influenced by several factors that evolve during the electrolysis process, including ion concentration and the pH of the electrolytic solution [Ellis et al., 2020]. The pH gradient across the interface, ranging from acidic in the anode chamber to alkaline in the cathode chamber, induces varying precipitation patterns of $Ca(OH)_2$ morphologies and structures, corroborated by the FE-SEM observations. It can be seen that the electrolysis process significantly enhances the particle gradation and specific surface area of all samples, thereby improving the physical attributes of the DMs compared to their raw materials.

7.3.3. Electrochemical decarbonation performance

Figure 7.10 displays the average efficiency values for the ED along with their standard error bars. The current ED design achieved efficiencies of 85.96%, 82.65%, and 83.18% for C, ES, and MS, respectively, representing a significant improvement over previous studies, which reported efficiencies ranging from 19-25% [Ramirez-Amaya et al., 2023] and 27%-80% [Martínez et al.,

2024]. The improvement might be due to more ideal experimental conditions. Previous studies have highlighted that longer operation times enable the system to approach steady-state conditions, enhancing ion transport across membranes while reducing losses caused by factors such as membrane fouling. In contrast, shorter durations may only reflect the initial, unsteady phase of operation, which can result in lower efficiency outcomes. Therefore, extended run times allow for more thorough extraction of target ions, leading to improved recovery rates and energy performance [Martínez et al., 2024].

Nevertheless, it is essential to carefully optimize the duration of operation to balance energy consumption and avoid placing excessive strain on the system. Another contributing factor to the observed performance improvement may be the feedstock-to-electrolytic solution ratio. Previous studies have shown that this ratio plays a critical role in determining the ion concentration gradient, which serves as the main driving force for ion transport in electrodialysis [Martínez et al., 2024]. Excessively high feedstock concentrations can lead to membrane clogging and lower ion selectivity, whereas overly diluted solutions may weaken the concentration gradient, reducing extraction efficiency [Martínez et al., 2024]. In this study, the chosen feedstock-to-electrolyte ratio appears to strike a suitable balance, supporting improved throughput and product purity.

This increased efficiency reflects a notable improvement in the mass recovery of $Ca(OH)_2$, which ranges from 86.86% to 90.26%. The ED's efficiency and mass recovery highlight the potential and sustainability of this new technology for hydrated lime production. Figure 7.10 also shows the ED process's energy consumption, which was in the range of 24.25-25.52 kJ/gm. The energy data reveals a 20% rise in consumption compared to earlier studies [Ramirez-Amaya et al., 2023]. This increase can be attributed to the fact that the previous experiments were limited to a 5-hour duration. The energy indicator demonstrated consistent performance across all $CaCO_3$ sources.

These findings indicate that using the same amount of energy in the electrolysis process results in comparable efficiency and mass conservation regardless of the specific $CaCO_3$ source used.

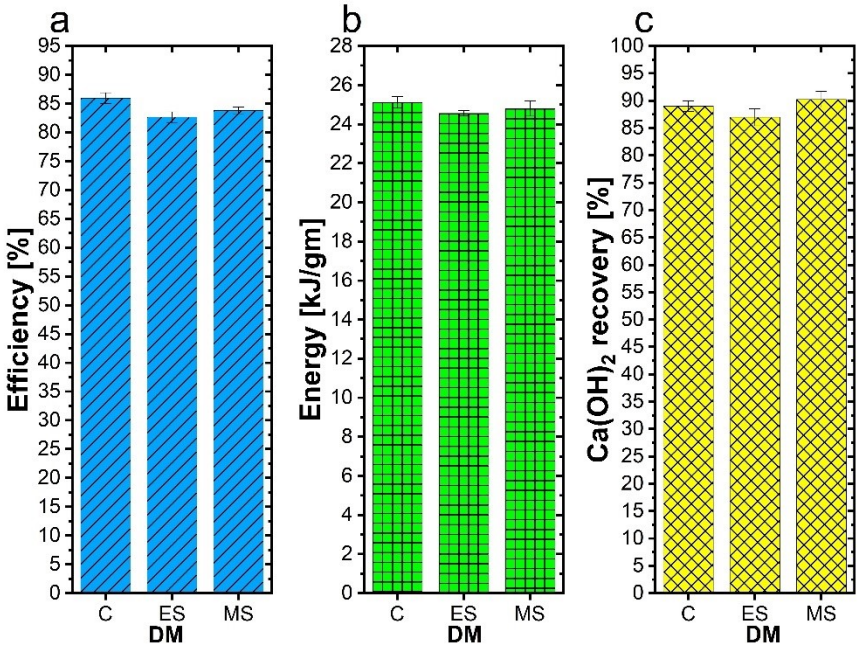

Figure 7.10 ED performance indicators: Efficiency (a), Energy consumption during electrolysis (b), and $Ca(OH)_2$ recovery (c).

Table 7.6 summarizes the statistical analysis used to assess the significance of differences among the properties of the studied feedstocks. The analysis reveals that only the efficiency of C was significantly different from that of the organic feedstocks. At the same time, no significant differences were found between ES and MS. This lack of difference is likely due to the high purity of C, producing only two solid phases in the DMs: deposited $Ca(OH)_2$ and unreacted $CaCO_3$ [Ellis et al., 2020]. In contrast, using ES and MS as $CaCO_3$ sources introduces additional mineralogical phases (e.g., SiO_2, MgO) into the electrolysis cell. These additional phases may remain in the anode chamber or move toward the cell's interface chamber, thereby reducing the purity of the DMs. Agitation also plays a role by keeping the particles in suspension, especially if the grain size

of the precursor is reduced during $CaCO_3$ decomposition [Ramirez-Amaya et al., 2023]. Table 7.6 shows no statistically significant differences in the %$Ca(OH)_2$ recovery or energy consumption across the various feedstock sources. This consistency in ED efficiency implies that there is no significant correlation with the different $CaCO_3$ sources, emphasizing the ED's compelling performance in decomposing $CaCO_3$ from various sources and crystalline forms (calcite and aragonite) and precipitating $Ca(OH)_2$ regardless of impurities.

Table 7-6 Statistical analysis results of the electrochemical decarbonation (ED) performance.

Parameter	Shapiro-Wilk test, P. Value			ANOVA		Post-hoc analysis		
	C	ES	MS	F. value	P. value	Group 1	Group 2	P. value
Efficiency [%]	0.593	0.918	0.401	8.342	*0.019	C	ES	*0.016
						C	MS	*0.089
						ES	MS	0.391
Energy consumption [kJ/gm]	0.488	0.737	0.264	1.911	0.228	C	ES	0.204
						C	MS	0.551
						ES	MS	0.677
$Ca(OH)_2$ [%]	0.534	0.487	0.801	3.094	0.119	C	ES	0.337
						C	MS	0.645
						ES	MS	0.106

* These differences can be considered as significant.

7.3.4. CO_2 mitigation from the ED process

Table 7.7 illustrates the theoretical CO_2 emissions from the conventional method and the ED process. Theoretical CO_2 emissions from the conventional method were computed based on the assumption that all feedstocks underwent a complete calcination reaction in the rotary kiln, leading to chemical CO_2 emissions of 221.90, 223.19, and 215.75 mL/gm from C, ES, and MS, respectively. Meanwhile, the potential CO_2 reduction achieved through the ED process is presented in two parts. The sequestered portion reflects the amount of CO_2 in the DMs in the form of impurities calculated using Equation 9. This part ranged between 24.38 and 29.17 mL/gm. The second portion, corresponding to the CO_2 that is emitted during the ED process at high

concentrations suitable for direct carbon capture, ranged from 191.37 to 197.36 mL/gm. Hence, based on the results of these experiments, 86.93% to 88.94% of CO_2 emissions would be directly captured, while the balance remained sequestered within the final product.

Table 7-7 Theoretical CO_2 mitigation in the conventional approach vs the electrochemical decarbonation (ED) process.

Feedstock	CO_2 [mL/gm]		
	Conventional approach / Emitted	ED process/ Captured	ED process/ Sequestered
C	221.90	197.36	24.54
ES	223.19	194.02	29.17
MS	215.75	191.37	24.38

7.4. Conclusions

This study pioneers the use of eggshells and mussel shells, abundant yet underutilized waste materials, as feedstocks for producing hydrated lime via electrochemical decarbonation. The results demonstrate that both materials can be efficiently converted into high-quality $Ca(OH)_2$ suitable for direct use. This approach not only valorizes organic waste but also advances sustainable, circular practices aligned with global climate and waste reduction goals. The main conclusions are as follows:

- The electrochemical decarbonation process effectively utilizes organic waste feedstocks like eggshells and mussel shells, despite differences in $CaCO_3$ content, crystal structure, and purity.
- All feedstocks showed significant $CaCO_3$ reduction and high $Ca(OH)_2$ yields, with mussel shells achieving the highest $Ca(OH)_2$ concentration at 90.26%, followed by control (89.03%) and eggshells (86.86%).
- The electrochemical decarbonation design achieved 82.65–85.96% efficiency, improving mass recovery over previous studies and outperforming the limestone flotation technique in efficiency and mass recovery, highlighting its feasibility and sustainability.

- The deposited materials from eggshells and mussel shells met ASTM-C206-14 and ASTM-C207-18 standards for Type N hydrated lime, suggesting suitability for construction. However, further performance assessments are needed to confirm commercial viability.
- The study shows that combining direct carbon capture with the ED process can capture up to 89% of CO_2, making the process emission-free with residual CO_2 stored as impurities.

Despite promising results, this study has several limitations. First, the effect of feedstock particle size on the electrochemical process was not considered, which may influence surface area and reaction kinetics. Second, a comprehensive life cycle analysis was not conducted to evaluate the broader environmental impacts, including upstream and downstream emissions. Additionally, the experiments were carried out under laboratory conditions, which may not fully reflect real-world challenges. Future research should address these limitations by examining the impact of feedstock particle size, conducting a life cycle analysis, and scaling up to pilot and industrial levels. Moreover, the long-term availability of eggshells and mussel shells as feedstocks should be assessed, and other calcium-rich waste materials, such as chicken bones or shellfish by-products, should be explored to increase sustainability. Finally, although the use of low-cost organic waste and room-temperature operation suggests economic advantages over conventional high-temperature lime production, this study did not include a techno-economic analysis. Future research should assess the financial feasibility of scaling this process, including cost comparisons with traditional production methods and potential savings from waste diversion and energy reduction. Such analysis will be critical to determine the commercial viability and broader adoption of this sustainable approach.

7.5. References

Acharya, P. K., Patro, S. K., & Moharana, N. C. (2016). Effect of Lime on Mechanical and Durability Properties of Blended Cement Based Concrete. *Journal of The Institution of Engineers (India): Series A*, *97*(2), 71–79. https://doi.org/10.1007/s40030-016-0158-y

ASTM International. (2014). Standard Specification for Finishing Hydrated Lime (ASTM C206-14).

ASTM International. (2018). Standard Specification for Hydrated Lime for Masonry Purposes (ASTM C207-18).

Ballester, P., Mármol, I., Morales, J., & Sánchez, L. (2007). Use of limestone obtained from waste of the mussel cannery industry for the production of mortars. *Cement and Concrete Research*, *37*(4), 559–564. https://doi.org/10.1016/j.cemconres.2007.01.004

Barros, M. C., Bello, P. M., Bao, M., & Torrado, J. J. (2009). From waste to commodity: Transforming shells into high purity calcium carbonate. *Journal of Cleaner Production*, *17*(3), 400–407. https://doi.org/10.1016/j.jclepro.2008.08.013

Bing, L., Ma, M., Liu, L., Wang, J., Niu, L., & Xi, F. (2023). An investigation of the global uptake of CO_2 by lime from 1930 to 2020. *Earth System Science Data*, *15*(6), 2431–2444. https://doi.org/10.5194/essd-15-2431-2023

Buasri, A., Chaiyut, N., Loryuenyong, V., Worawanitchaphong, P., & Trongyong, S. (2013). Calcium Oxide Derived from Waste Shells of Mussel, Cockle, and Scallop as the Heterogeneous Catalyst for Biodiesel Production. *The Scientific World Journal*, *2013*(1), 460923. https://doi.org/10.1155/2013/460923

Bustillo Revuelta, M. (2021). Lime. In M. Bustillo Revuelta (Ed.), *Construction Materials: Geology, Production and Applications* (pp. 167–193). Springer International Publishing. https://doi.org/10.1007/978-3-030-65207-4_7

Chong, B. W., Othman, R., Ramadhansyah, P. J., Doh, S. I., & Li, X. (2020). Properties of concrete with eggshell powder: A review. *Physics and Chemistry of the Earth, Parts A/B/C*, *120*, 102951. https://doi.org/10.1016/j.pce.2020.102951

Consoli, N. C., Caicedo, A. M. L., Beck Saldanha, R., Filho, H. C. S., & Acosta, C. J. M. (2020). Eggshell Produced Limes: Innovative Materials for Soil Stabilization. *Journal of Materials in Civil Engineering*, *32*(11), 06020018. https://doi.org/10.1061/(ASCE)MT.1943-5533.0003418

Dang, L. C., Fatahi, B., & Khabbaz, H. (2016). Behaviour of Expansive Soils Stabilized with Hydrated Lime and Bagasse Fibres. *Procedia Engineering*, *143*, 658–665. https://doi.org/10.1016/j.proeng.2016.06.093

Diez, D. M. , Barr, C. D., & Cetinkaya-Rundel, M. (2015). OpenIntro Statistics—Fourth Edition. Open Textbook Library. https://open.umn.edu/opentextbooks/textbooks/60

Ellis, L. D., Badel, A. F., Chiang, M. L., Park, R. J.-Y., & Chiang, Y.-M. (2020). Toward electrochemical synthesis of cement—An electrolyzer-based process for decarbonating CaCO3 while producing useful gas streams. *Proceedings of the National Academy of Sciences*, *117*(23), 12584–12591. https://doi.org/10.1073/pnas.1821673116

Eziefula, U. G., Ezeh, J. C., & Eziefula, B. I. (2018). Properties of seashell aggregate concrete: A review. *Construction and Building Materials*, *192*, 287–300. https://doi.org/10.1016/j.conbuildmat.2018.10.096

Ferraz, E., Gamelas, J. A. F., Coroado, J., Monteiro, C., & Rocha, F. (2018). Eggshell waste to produce building lime: Calcium oxide reactivity, industrial, environmental and economic implications. *Materials and Structures*, *51*(5), 115. https://doi.org/10.1617/s11527-018-1243-7

Government of Canada. 2016. "Aquaculture Production Quantities and Value." https://www.dfo-mpo.gc.ca/stats/aqua/aqua-prod-eng.htm

Government of Canada. 2022. "The Daily Poultry and egg statistics." https://www150.statcan.gc.ca/n1/daily-quotidien/220606/dq220606f-eng.htm

Hamada, H. M., Tayeh, B. A., Al-Attar, A., Yahaya, F. M., Muthusamy, K., & Humada, A. M. (2020). The present state of the use of eggshell powder in concrete: A review. *Journal of Building Engineering*, *32*, 101583. https://doi.org/10.1016/j.jobe.2020.101583

Hart, A. (2020). Mini-review of waste shell-derived materials' applications. *Waste Management & Research*, *38*(5), 514–527. https://doi.org/10.1177/0734242X19897812

Haynes, W. (2013). Tukey's Test. In *Encyclopedia of Systems Biology* (pp. 2303–2304). Springer, New York, NY. https://doi.org/10.1007/978-1-4419-9863-7_1212

Her, S., Park, T., Zalnezhad, E., & Bae, S. (2021). Synthesis and characterization of cement clinker using recycled pulverized oyster and scallop shell as limestone substitutes. *Journal of Cleaner Production*, *278*, 123987. https://doi.org/10.1016/j.jclepro.2020.123987

Hincke, M., Gautron, J., Rodriguez-Navarro, A. B., & McKee, M. D. (2011). 8 - The eggshell: Structure and protective function. In Y. Nys, M. Bain, & F. Van Immerseel (Eds.), *Improving the Safety and Quality of Eggs and Egg Products* (pp. 151–182). Woodhead Publishing. https://doi.org/10.1533/9780857093912.2.151

Jena, M. S., Sahu, P., Dash, P., & Mohanty, J. K. (2013). Beneficiation of limestone plant rejects for value addition. *Journal of Hazardous Materials*, *262*, 218–227. https://doi.org/10.1016/j.jhazmat.2013.08.048

Jhatial, A. A., Sohu, S., Memon, M. J., Bhatti, N.-K., & Memon, D. M. 3 A. (2019). Eggshell powder as partial cement replacement and its effect on the workability and compressive strength of concrete. *International Journal of Advanced and Applied Sciences*, *6*(9), 71–75. https://doi.org/10.21833/ijaas.2019.09.011

Kamkum, P., Atiwongsangthong, N., Muanghlua, R., & Vittayakorn, N. (2015). Application of chicken eggshell waste as a starting material for synthesizing calcium niobate (Ca4Nb2O9) powder. *Ceramics International*, *41*, S69–S75. https://doi.org/10.1016/j.ceramint.2015.03.189

Kanani, F., Heidari, M. D., Gilroyed, B. H., & Pelletier, N. (2020). Waste valorization technology options for the egg and broiler industries: A review and recommendations. *Journal of Cleaner Production*, *262*, 121129. https://doi.org/10.1016/j.jclepro.2020.121129

Laveglia, A., Sambataro, L., Ukrainczyk, N., De Belie, N., & Koenders, E. (2022). Hydrated lime life-cycle assessment: Current and future scenarios in four EU countries. *Journal of Cleaner Production*, *369*, 133224. https://doi.org/10.1016/j.jclepro.2022.133224

Ma, X., Wu, H., Chang, L., Wang, J., Wang, Y., & Cui, S. (2022). The influence of calcium hydroxide crystal morphology on the desulfurization of cement kiln flue gas. *Journal of Materials Science*, *57*(39), 18287–18297. https://doi.org/10.1007/s10853-022-07801-9

Martínez, N. P., Troncoso P, F., Gazzano, V., Ramírez-Amaya, D., González, M., Navarrete, I., Canales, R., & Dreyse, P. (2024). High-performance and low-cost electrochemical reactor for limestone decarbonation applied to clinker production – A validation at laboratory scale. *Journal of Cleaner Production*, *468*, 143112. https://doi.org/10.1016/j.jclepro.2024.143112

Mo, K. H., Alengaram, U. J., Jumaat, M. Z., Lee, S. C., Goh, W. I., & Yuen, C. W. (2018). Recycling of seashell waste in concrete: A review. *Construction and Building Materials*, *162*, 751–764. https://doi.org/10.1016/j.conbuildmat.2017.12.009

Moneim, A. A. A., Aziz, E. H. A., & Magd, S. A. A. E. (2013). Assessment of raw materials for cement industry in Sohag area, upper Egypt. *International Journal of Mining and Mineral Engineering*, *4*(4), 333. https://doi.org/10.1504/IJMME.2013.056868

Mortola, J. P. (2009). Gas exchange in avian embryos and hatchlings. *Comparative Biochemistry and Physiology Part A: Molecular & Integrative Physiology*, *153*(4), 359–377. https://doi.org/10.1016/j.cbpa.2009.02.041

Oliveira, D. A., Benelli, P., & Amante, E. R. (2013). A literature review on adding value to solid residues: Egg shells. *Journal of Cleaner Production*, *46*, 42–47. https://doi.org/10.1016/j.jclepro.2012.09.045

Ramirez-Amaya, D., Dreyse, P., Martínez, N. P., Troncoso P., F., Navarrete, I., Noël, M., Canales, R. I., & González, M. (2023). Comparison of the electrochemical decarbonation of different-grade

limestones used in cement manufacturing. *Cement and Concrete Research*, *174*, 107307. https://doi.org/10.1016/j.cemconres.2023.107307

Sagastume Gutiérrez, A., Van Caneghem, J., Cogollos Martínez, J. B., & Vandecasteele, C. (2012). Evaluation of the environmental performance of lime production in Cuba. *Journal of Cleaner Production*, *31*, 126–136. https://doi.org/10.1016/j.jclepro.2012.02.035

Simoni, M., Wilkes, M. D., Brown, S., Provis, J. L., Kinoshita, H., & Hanein, T. (2022). Decarbonising the lime industry: State-of-the-art. *Renewable and Sustainable Energy Reviews*, *168*, 112765. https://doi.org/10.1016/j.rser.2022.112765

Staněk, T. (2019). The Influence of Raw Meal Granulometry on the Formation and Properties of Clinker. *Solid State Phenomena*, *296*, 9–14. The 17th Conference Silicate Binders 2018. https://doi.org/10.4028/www.scientific.net/SSP.296.9

Strother, P. (2019). 2—Manufacture of Portland Cement. In P. C. Hewlett & M. Liska (Eds.), *Lea's Chemistry of Cement and Concrete (Fifth Edition)* (pp. 31–56). Butterworth-Heinemann. https://doi.org/10.1016/B978-0-08-100773-0.00002-2

Suleiman, I. E., Abubakar, A., Otuoze, H. S., Suleiman, M. A., Momoh, R. O., & Aliyu, S. N. (2013). *Effects of Particle Size Distribution on the Burn Ability of Limestone*. https://www.semanticscholar.org/paper/Effects-of-Particle-Size-Distribution-on-the-Burn-Suleiman-Abubakar/afabf6e50d35b27cd01b3f08e78439e833c7ea30

Waheed, M., Yousaf, M., Shehzad, A., Inam-Ur-Raheem, M., Khan, M. K. I., Khan, M. R., Ahmad, N., Abdullah, & Aadil, R. M. (2020). Channelling eggshell waste to valuable and utilizable products: A comprehensive review. *Trends in Food Science & Technology*, *106*, 78–90. https://doi.org/10.1016/j.tifs.2020.10.009

Chapter 8 : The Sustainability of Hemp-Lime Composites in Construction: A Comparative Life Cycle Analysis of External Walls

8.1. Introduction

The construction sector is one of the largest contributors to global carbon emissions, with building materials such as cement, lime, and glass fibre insulation driving a substantial portion of embodied energy and environmental impact. In parallel, increasing demand for thermally efficient building envelopes underscores the need for building materials that are not only effective but also environmentally sustainable.

In recent years, the construction industry has faced growing pressure to adopt sustainable practices and reduce its environmental footprint. One of the most impactful strategies for achieving this involves evaluating and optimizing building materials, particularly those used in exterior wall systems, which significantly influence a structure's overall energy performance and environmental impact.

Hemp-lime composites represent a promising solution to this challenge. Derived from renewable hemp shives bound with lime-based matrices, HLC combines thermal insulation, moisture buffering, and carbon sequestration potential. Previous research has demonstrated the hygrothermal benefits of HLC; however, their environmental performance is strongly influenced by the binder system. Conventional lime binders require high-temperature calcination, leading to high carbon dioxide emissions during both processing and decarbonation of limestone.

To address this limitation, recent studies have investigated electrochemical decarbonation processes, which produce hydrated lime from calcium carbonate feedstocks such as natural limestone or waste eggshells, while capturing and potentially valorizing the released CO_2.

Integrating such binder systems into HLC offers a pathway to further reduce the carbon footprint of construction materials.

This study evaluates the sustainability of hemp-lime composites incorporating ED-produced hydrated lime. The composites are benchmarked against (i) traditional HLC made with industrially hydrated lime and (ii) glass fibre insulation, a conventional external wall material. The objective is to assess both technical feasibility and sustainability performance, using a cradle-to-gate life cycle assessment (LCA) normalized to thermal functionality. The findings provide insights into the viability of bio-based composites with alternative binders as scalable insulation solutions for low-carbon construction.

8.2. Materials

Hemp shivs were sourced from a Canadian supplier (Terrafibre) and milled to an average particle size of 0.73 mm using an industrial grinder (JTANGL Electric Grain Grinder Mill, 3000 W) to improve the consistency and performance of the produced HLC (the effect of hurd size is reported in Chapter 4 [Mahmood et al., 2024]). Physical properties including density, water absorption, particle size distribution, and moisture content were measured according to procedures detailed in Chapter 3 (Section 3.2.2). Table 8.1 shows the physical properties of hemp shivs used in this study.

Table 8-1 Physical properties of hemp shivs.

Property	Hemp Shivs
Bulk density (kg/m^3)	114
Initial moisture content (%)	6.94
Water absorption	
IRA %	137.26
K_1	51.88
D90 (mm)	0.73

The binder used in this study was hydrated lime produced via the electrochemical decarbonation process. Figure 8.1 illustrates the schematic of the large-scale electrochemical decarbonation reactor developed in this study. The system was constructed using hardwood plywood panels (11.5 mm thick, 2 ft × 4 ft) coated with an epoxy layer to ensure full chemical resistance and watertight sealing. The assembled reactor measured 120 × 60 × 60 cm and consisted of separate anode and cathode chambers interconnected by a bridge section (10 × 60 × 60 cm). This configuration maintained effective ion exchange while preventing cross-contamination between the chambers. Stainless steel sheets were employed as electrodes, with dimensions of 15 × 20 × 0.1 cm for the anode and 10 × 15 × 0.1 cm for the cathode. Continuous stirring was provided by a brushless, cordless ½-inch mud mixer to enhance diffusion and maintain a uniform suspension throughout the electrolysis process. Each experimental run used 5 kg of raw precursor material, yielding about 2.5 kg of DMs.

A constant direct current of 9 V was applied for 48 hours to achieve complete electrochemical decarbonation and ensure high product purity. The operating voltage and duration were determined through preliminary optimization to maximize process efficiency and material quality.

The design and configuration of this reactor are illustrated in Figure 8.1. The binder mix used in this study is the same as the one described in Chapter 3 (Section 3.2.3).

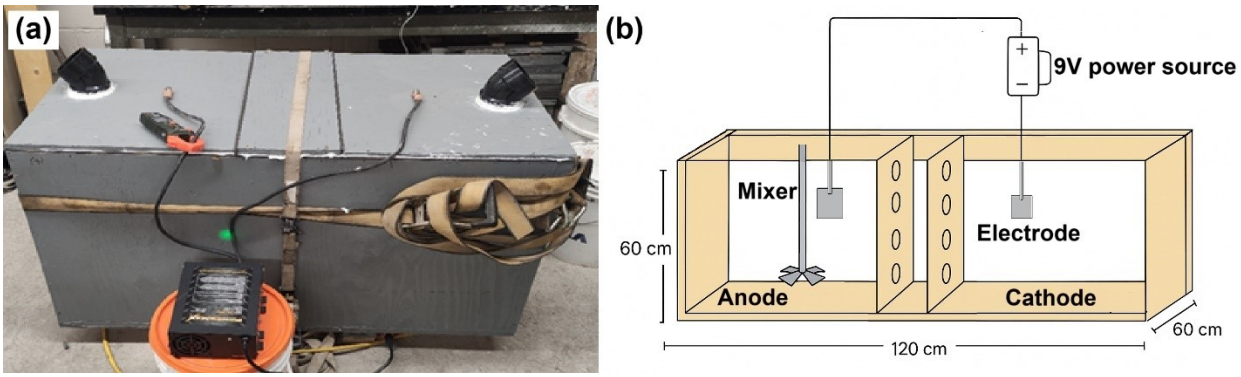

Figure 8.1 Scale-up electrochemical decarbonation (ED) reactor setup showing (a) the constructed large-scale reactor and (b) the corresponding schematic illustrating the main components and configuration.

Table 8-2 The chemical composition and physical properties of hydrated lime and slag.

Material	Chemical composition Mass %									Physical properties	
	CaO	Na_2O	MgO	Al_2O_3	SiO_2	P_2O_5	K_2O	TiO_2	Fe_2O_3	Specific gravity	Surface area g/m²
ED Hydrated Lime	65.13	1.01	1.13	0.02	0.81	0.01	0.01	0.01	0.04	2.43	5.18
Slag	37.82	0.37	11.82	10.20	36.80	0.00	0.49	1.43	0.43	2.74	1.63

A binder-to-hemp ratio of 1:2.4 was selected to produce lightweight composites with a target dry density of 140 kg/m³ [Mahmood et al., 2024]. The ratio was optimized to balance binder content and hemp shiv volume, ensuring adequate thermal performance and structural integrity. A mechanical mixing and casting process was employed to ensure uniformity and reproducibility across all samples [Mahmood et al., 2024]. The sample preparation followed the procedure described in Chapter 3 (Section 3.2.4). Table 8.3 summarizes the mass quantities of each constituent used in the mix design to produce 1 m^3 of HLC.

Table 8-3 Composition of the hemp-lime samples.

Component	Wright (kg)/1 m^3
ED Hydrated Lime	33.6
Slag	8.4
Hemp shivs	98.0
Water	336.0

8.3. Methods

8.3.1. Technical Evaluation

HLC samples were tested for thermal conductivity (W/m·K), thermal diffusivity (m^2/s), compressive strength (MPa), and moisture buffering value ($g/m^2 \cdot RH$). All tests followed protocols detailed in Chapter 3 (Section 3.2.5).

8.3.2. Sustainability Evaluation (LCA Framework)

After completing the key hygrothermal and mechanical tests to assess technical feasibility, the next step in the evaluation process focuses on the sustainability performance of the HLC. While mechanical properties such as strength and durability are crucial for determining the material's applicability in construction, it is equally important to assess its environmental impact, resource efficiency, and long-term sustainability.

The objective of this study is to evaluate and compare the environmental sustainability of two HLC formulations—each utilizing different lime binder production methods—through a cradle-to-gate LCA. By benchmarking these bio-based materials against conventional glass fibre insulation, the study aims to assess the potential of alternative binder sources, including ED-produced lime from limestone, to reduce the environmental impact of insulation materials used in external wall construction.

A performance-based functional unit (FU) was employed to enable a fair comparison across materials with differing physical properties. The FU was defined as 1 m^2 of material delivering a thermal transmittance of (RSI=2.88 $m^2 \cdot K/W$). For this definition, the thermal insulation values of 0.0347 and 0.052 W/m K were adopted for low-density glass fibre and HLC, respectively. This ensures that each material is assessed based on equivalent thermal functionality rather than mass or volume alone. Canadian building and energy codes regulate above-grade exterior walls

according to minimum effective thermal resistance requirements that vary by climate zone, with typical RSI values ranging approximately from 2.78 to 3.85 $m^2 \cdot K/W$ depending on heating degree days (HDD), construction type, and allowance for thermal bridging [Canadian Commission on Building and Fire Codes, 2020]. The selected RSI value of 2.88 $m^2 \cdot K/W$ falls within this range and represents a realistic, code-compliant level of thermal performance for above-grade wall assemblies in several Canadian climate zones when assembly effects are considered. By adopting an area- and performance-based functional unit aligned with building code practice, this study enables a fair and decision-relevant comparison between hemp–lime composites and conventional wall systems under realistic regulatory conditions. The defined FU for evaluating the wall systems is shown in Figure 8.2, which shows that the HLC wall is 50% thicker than the glass wool wall to achieve the same RSI-value.

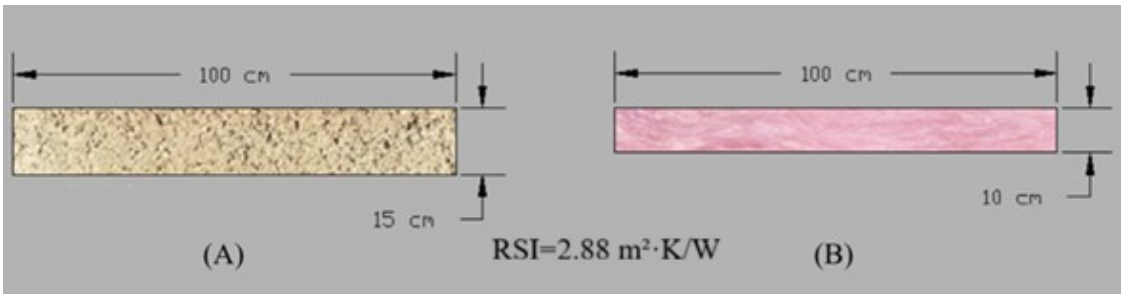

Figure 8.2 Performance-based functional unit for wall system comparison. (A) HLC wall, (B) low-density glass wool wall.

This study adopts a cradle-to-gate system boundary, which encompasses all life cycle stages from raw material extraction to the point at which the composite materials are ready for use at the factory gate as shown in Figure 8.3. Specifically, the boundary includes: (1) production and transportation of agricultural inputs such as hemp seeds, fertilizers, herbicides, farming machinery, and irrigation equipment; (2) hemp cultivation, harvesting, and transportation to processing facilities; (3)

decortication and processing of hemp stalks to obtain shives; (4) production of lime binders—either through conventional calcination and hydration processes or via electrochemical methods using limestone or eggshells as calcium feedstocks; and (5) the mixing, blending, and casting of the hemp-lime composites. For the glass wool insulation, the cradle-to-gate boundary encompasses: (1) extraction and processing of silica sand and other raw minerals (e.g., soda ash and limestone); (2) melting to form glass fibres; (3) addition of binders and processing additives; and (4) packaging and transportation of the finished insulation material to the factory gate. Downstream processes such as on-site construction, use phase, maintenance, and end-of-life treatment are excluded from the scope of this analysis as downstream processes can vary significantly depending on building design, usage patterns, and regional practices, introducing variability that is beyond the scope of this comparative study. The system boundary is cradle-to-grave as shown in Figure 8.3.

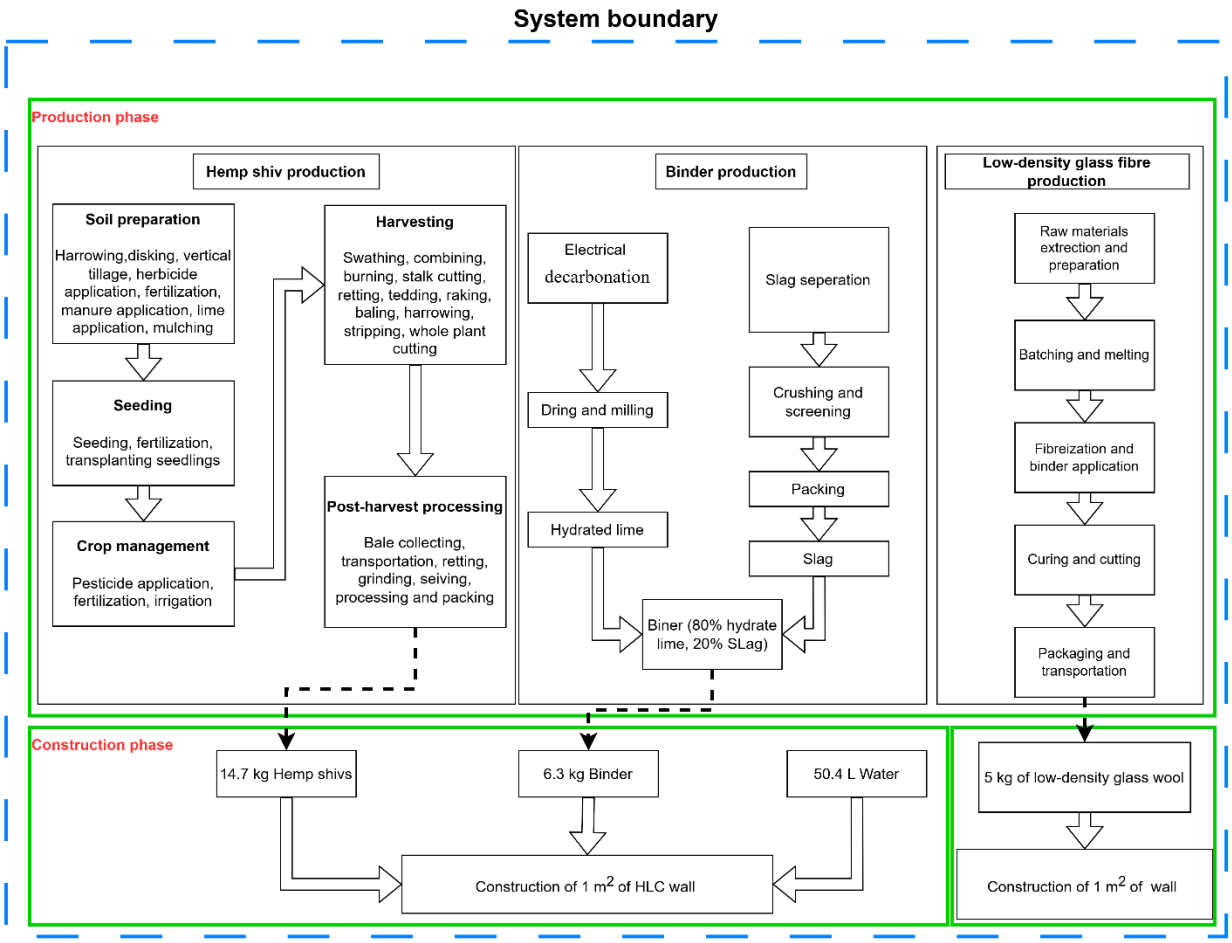

Figure 8.3 System boundary of the wall system.

The life cycle inventory (LCI) was developed using a combination of primary and secondary data sources to ensure accuracy and representativeness across all material systems. Primary data were collected specifically for the novel binder systems and focused on the production of hydrated lime via electrochemical processes. This included direct measurements of energy consumption and water inputs based on experimental trials and pilot-scale production data. As shown in Table 8-4.

Table 8-4 Inventory data for ED hydrated lime production.

Input	Quantity per 1 kg
Water	30 kg
Electricity	7.1 kWh

In the present research, the results of these published LCA studies were used as secondary data inputs to support the analysis and interpretation of the environmental performance of HLC. These secondary data were obtained from a wide range of reputable sources, including peer-reviewed LCA studies, industry publications, and established life cycle databases. The LCA data adopted in this research were originally generated in previous studies through a combination of primary data collection methods, including semi-structured interviews and questionnaires with hemp growers and manufacturers, as well as secondary data from industry figures and life cycle inventory databases.

In the referenced studies, literature reviews, site visits, interviews, and data analysis were used to develop process maps describing the life cycle inputs, outputs, and key processes involved in the production and construction of hemp–lime walls. The life cycle assessments in those studies were conducted in accordance with ISO 14040 and ISO 14044 standards using the LCA software SimaPr. Background inventory data in the original assessments were primarily sourced from the EcoInvent database (EcoInvent, 2010), supplemented where necessary with literature values and industry-specific information.

These data informed background processes such as hemp cultivation, agricultural input production, transport, conventional lime production, composite manufacturing, and the benchmark glass fibre insulation resulting greenhouse gas (GHG) emissions associated with each material are presented in Table 8-6.

Table 8-5 Inventory data for the FU.

Input	Item		Quantity
Materials	Hemp seed		0.21 kg
	Fertilizers	Ammonium nitrate	0.71 kg
		Triple superphosphate	0.76 kg
		Potassium chloride	0.96 kg
	Hemp shivs		14.70 kg
	Hydrated lime		5.03 kg
	Slag		1.26 kg
	Water		50.43 kg
	Low-density glass wool		5.0 kg
Electricity	Mixing		1.5 kWh
Transportation-factory to site	Lime binder		5000 kg km
	Hemp shivs		3000 kg km

Table 8-6 Carbon footprint per FU.

Input	GHG emissions (kg CO_2e)	Sequestration (kg CO_2e)
Hemp shivs [Ip & Miller, 2012]	2.23	− 22.45
Hydrated lime [Ip & Miller, 2012]	3.85	− 3.83
ED Hydrated lime	0.72	− 3.83
Slag [Zhang et al., 2025]	0.03	-
Water [Mohammadifardi et al., 2019]	0.0459	-
Electricity [G.o.C, 2025]	0.15	-
Low-density glass wool [Grazieschi et al., 2021]	4.32-8.64	-

8.4. Results and discussion

8.4.1. Technical Evaluation

The HLC prepared with hydrated lime produced through ED (ED-HLC) demonstrated competitive thermo-hygro-mechanical properties compared with those made using conventionally manufactured hydrated lime [Mahmood et al., 2024]. The average thermal conductivity of the ED-HLC was 0.0521 W/m·K, closely matching the 0.0535 W/m·K obtained for the conventional counterpart. This negligible difference highlights that the binder production route had little influence on thermal insulation performance, which is primarily governed by the porous structure of the hemp shiv phase. The similarity confirms that adopting the ED process does not compromise the insulating capacity of HLC.

Moisture buffering performance was also well preserved. The ED-HLC achieved an average moisture buffering value (MBV) of 2.61 g/m²·RH, slightly higher than the 2.47 g/m²·RH reported for conventional lime systems. Both values fall within the “excellent” category, underscoring the capacity of HLC to moderate indoor humidity. The marginal enhancement observed with the ED binder may be attributed to subtle differences in pore network connectivity arising from the alternative hydration and carbonation pathways. These findings suggest that the electrochemical process can deliver binders that maintain, or even improve, the hygric regulation benefits that make hemp–lime composites attractive for building applications.

Mechanical strength showed the most noticeable difference between the two systems. While both mixtures reflect the low load-bearing capacity characteristic of hemp–lime composites, the ED-HLC attained an average compressive strength of 0.061 MPa compared to 0.042 MPa for the conventional lime reference. This improvement suggests a denser or more reactive lime matrix in the ED binder, which could enhance structural stability without altering hygrothermal performance. Such gains are relevant for broadening the application potential of HLC in construction where minimal mechanical requirements must be met.

Overall, the results demonstrate that replacing conventionally manufactured hydrated lime with ED hydrated lime yields hemp–lime composites with nearly identical thermal conductivity, slightly higher moisture buffering capacity, and improved compressive strength. These outcomes highlight the feasibility of integrating an electrochemically decarbonized binder into bio-based composites, combining functional performance with the reduced carbon footprint inherent to the ED process.

8.4.2. Environmental Impact of HLC Wall

A component-level analysis of the ED-HLC wall provides insights into the sources of carbon savings and embodied emissions. Three carbon accounting approaches are determined: full sequestration including all components (WS – includes all carbon uptake and storage associated with both hemp shivs and lime binder over the material's lifetime, reflecting the full carbon-negative potential of the composite), ignoring all CO_2 uptake (NS – ignores all carbon uptake, accounting only for emissions from material production, processing, and energy use, without considering any CO_2 storage), and accounting only for the biogenic carbon in hemp shivs (HS – accounts only for the biogenic carbon stored in hemp shivs during plant growth, while no sequestration is considered for the lime binder or other components). The latter can be considered the embodied carbon at the time of a building's commissioning.

When full sequestration is considered (i.e. WS), the results show that the hemp shivs (–20.22 kg CO_2 eq.) and the ED hydrated lime (–3.11 kg CO_2 eq.) dominate the negative balance, together accounting for 86.6% and 13.4%, respectively. Water, slag, and electricity contribute marginally positive emissions, with shares of 0.6%, 0.1%, and 0.2%, respectively. The combined effect yields a net global warming potential (GWP) of –23.10 kg CO_2 eq., confirming the carbon-negative profile of the ED-HLC wall.

Table 8-7 Contribution of HLC–ED constituents to CO_2 eq.

Component	Full sequestration (WS) (kg CO_2 eq.)	No sequestration (NS) (kg CO_2 eq.)	Hemp sequestration (HS) (kg CO_2 eq.)
ED Hydrated lime	–3.11	+0.72	+0.72
Hemp shivs	–20.22	+2.23	–20.22
Water	+0.15	+0.15	+0.15
Slag	+0.03	+0.03	+0.03
Electricity	+0.05	+0.05	+0.05
Total	–23.10	+3.19	–19.26

When sequestration is not considered (i.e. NS), the hemp shivs (2.23 kg CO_2 eq.) and the ED hydrated lime (0.72 kg CO_2 eq.) are the main contributors to the overall emissions, accounting for approximately 70% and 22% of the total, respectively. Water, slag, and electricity contribute marginally with 0.16, 0.03, and 0.05 kg CO_2 eq., respectively, resulting in a total GWP of 3.19 kg CO_2 eq. per functional unit. When the biogenic carbon sequestration of hemp shivs is included i.e. HS), the system transitions to a carbon-negative balance of –19.26 kg CO_2 eq. This more realistic representation accounts for the CO_2 absorbed naturally by hemp during its growth phase prior to material processing. From this point onward, only WS and HS will be considered in the analysis. The result highlights that the carbon-negative nature of the ED-HLC wall primarily stems from the renewable and bio-based characteristics of the hemp component, which effectively stores atmospheric carbon within the composite over its lifespan.

Comparative results further highlight the environmental benefit of ED-HLC. When considering WS scenario, the ED-HLC wall performance surpassed that of the conventional lime-based HLC (–19.97 kg CO_2 eq.) by approximately 15.7%, reflecting the enhanced sequestration and lower emissions associated with the ED process.

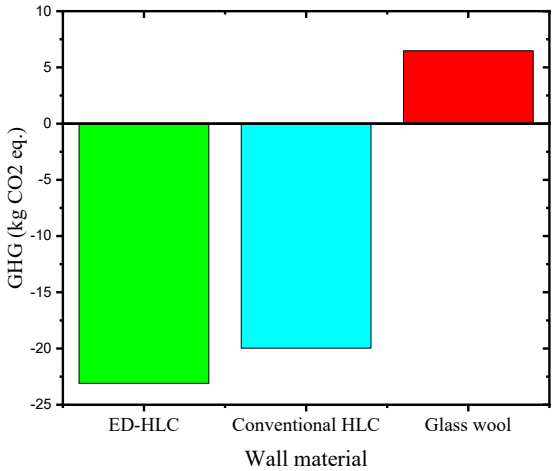

Figure 8.4 GHG impact per wall material (kg CO_2 eq) (WS).

With carbon sequestration included, the ED-HLC wall achieved a 457% lower carbon footprint compared to low-density glass wool insulation, transitioning to a strongly carbon-negative balance, a performance far beyond the reach of standard HLC or mineral-based insulation products, as shown in Figure 8.4. Under the HS scenario, the standard HLC wall already reached a carbon-negative balance of –16.12 kg CO_2 eq., while the ED-HLC wall further improved this to –19.26 kg CO_2 eq., highlighting the additional benefit of the electrochemical process. Compared to conventional low-density fibreglass insulation, the standard HLC wall achieves a 348% lower carbon footprint, and the ED-HLC wall achieves a 397% lower footprint, clearly illustrating the superior greenhouse-gas mitigation potential of hemp-lime composites (Figure 8.5).

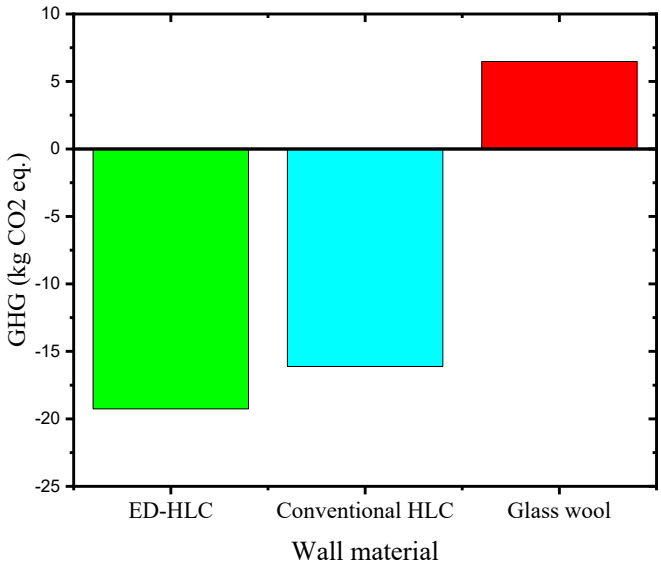

Figure 8.5 GHG impact per wall material (kg CO_2 eq) (HS).

Overall, these findings demonstrate that HLC made with ED hydrated lime combines the dual benefits of carbon sequestration and low embodied emissions, offering reductions of 15.7% (with sequestration) relative to conventional lime-based HLC, and up to 457% compared with glass

wool. This positions ED-HLC as an environmentally superior alternative for sustainable wall systems, achieving both high functional performance and significant carbon mitigation potential.

A one-way sensitivity analysis was performed to examine the effect of varying the B:H mass ratio (1:1, 1:1.5, and 1:2.4), corresponding to densities of 200, 170, and 140 kg/m³, on the GWP of ED-HLC walls (Figure 8.6 and Figure 8.7). When WS was considered, the net GHG balance improved from –23.10 kg CO_2 eq. at 1:2.4 to –27.73 kg CO_2 eq. at 1:1, representing a 20% reduction in GWP with increasing binder content. In contrast, the HS scenario exhibited an opposite trend, with values of –18.59, –19.59, and –19.24 kg CO_2 eq. for 1:1, 1:1.5, and 1:2.4, respectively — showing a modest 5% variation. This reversed pattern reflects the dominant role of hemp content in the HS case, where increasing the proportion of shivs enhances biogenic sequestration, while the contribution from the binder is negligible.

The previous findings indicate that the influence of the B:H ratio is much more pronounced when lime carbonation is included, emphasizing the binder's critical role in enhancing the composite's carbon-negative potential. The trend also suggests that the binder, produced through the ED process, contributes significantly to the overall carbon negativity through its carbonation potential. When hemp content is increased disproportionately, the relative contribution of binder carbonation decreases, leading to a less negative balance.

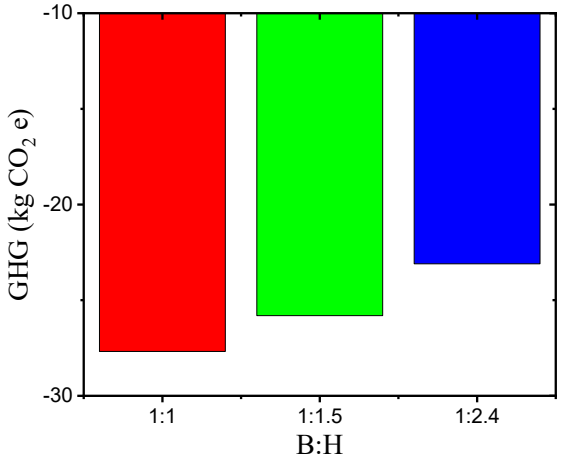

Figure 8.6 Sensitivity of net greenhouse-gas balance to B:H ratio (WS).

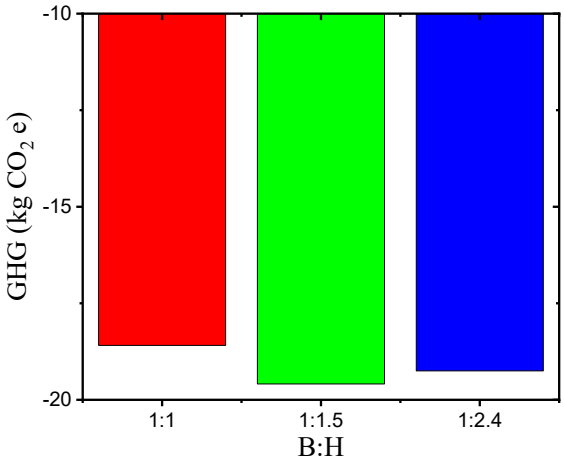

Figure 8.7 Sensitivity of net greenhouse-gas balance to B:H ratio (HS).

The results highlight that binder design and reactivity may play a stronger role in carbon performance than the simple addition of more bio-aggregate. Nevertheless, given typical LCA uncertainties (±10–30%), the relative ranking between the ratios should be interpreted cautiously. Further work should couple the carbon balance with mechanical and hygrothermal performance, as higher hemp fractions may still provide other functional advantages even if the climate impact is slightly less favourable.

8.5. Limitations of the Study

While this study provides a comparative environmental assessment of hemp-lime composites and conventional insulation materials, several limitations should be acknowledged.

Firstly, the analysis adopts a cradle-to-gate system boundary, which excludes downstream life cycle stages such as construction, operational use, maintenance, and end-of-life treatment. Although the use of a performance-based FU helps standardize thermal performance across materials, omitting the use and disposal phases limits the ability to fully assess long-term environmental impacts, including durability, recyclability, and carbon sequestration over the building's lifespan.

Secondly, the primary data for the electrochemical lime binders were based on pilot-scale or laboratory-scale production, which may not reflect the efficiencies or challenges of full industrial-scale implementation. Scaling assumptions were applied where needed, but actual energy demands and process emissions could vary in commercial settings.

Third, the secondary data used for conventional lime, agricultural inputs, and benchmark materials were drawn from existing databases and literature, some of which are not specific to the geographical context of the study. Regional differences in energy grids, farming practices, and transportation infrastructure may affect the transferability of results.

Lastly, the study does not assess other impact categories such as human toxicity, water depletion, or land occupation, which may be relevant in comprehensive sustainability evaluations. Future research should expand the scope to include these categories and integrate dynamic modeling to assess long-term environmental trade-offs.

8.6. Conclusions

This chapter evaluated the technical performance and environmental impacts of hemp–lime composites prepared with hydrated lime derived from electrochemical decarbonation. The results can be summarized as follows:

- Hemp–lime composites prepared with electrochemical decarbonation hydrated lime showed comparable thermal and hygric behaviour to those with conventional lime binders. Thermal conductivity was nearly identical (0.0521 W/m·K for ED-HLC vs. 0.0535 W/m·K for conventional HLC), confirming that the change in binder production route does not compromise insulation performance.
- Moisture buffering remained excellent, with ED-HLC (2.61 g/m²·RH) performing slightly better than conventional HLC (2.47 g/m²·RH). This suggests that ED-derived lime supports the intrinsic humidity-regulating properties of HLC.
- Compressive strength improved significantly (0.061 MPa vs. 0.042 MPa), indicating that ED lime may form a denser and more reactive matrix. While HLC remains a non-structural material, this gain broadens its robustness and potential use cases.
- ED-HLC confirmed its role as a carbon-conscious insulation solution with strong sequestration capacity.
- With carbon sequestration included (WS), the ED-HLC wall achieved a net GWP of –23.10 kg CO_2 eq., outperforming conventional lime-based HLC (–19.97 kg CO_2 eq.) by 15.7%.
- When benchmarked against glass wool, ED-HLC delivered a 457% lower embodied footprint without sequestration, and a carbon-negative profile when sequestration was accounted for — an outcome unattainable by mineral-based insulation.

- Under the Hemp Sequestration only (HS) scenario, where only the biogenic carbon in hemp shivs is considered, the ED-HLC wall still achieved a carbon-negative balance of –19.26 kg CO_2 eq., demonstrating that even without accounting for binder carbonation, the system remains strongly climate-positive. From this point onward, only WS and HS were considered in the analysis.
- The sensitivity analysis confirmed that all mixes remained carbon-negative, but higher hemp fractions reduced sequestration by up to 20%. Conversely, under HS, the trend was reversed, with a modest 5% variation, confirming that hemp content controls the carbon balance when binder sequestration is excluded. This dual trend illustrates that binder reactivity governs carbon performance under WS, whereas biogenic uptake dominates under HS. This underscores the dominant role of the ED binder in the carbon balance and the need to balance environmental gains with material performance.

8.7. References

Canadian Commission on Building and Fire Codes. (2020). *National Building Code of Canada: 2020*. National Research Council Canada. https://doi.org/10.4224/W324-HV93

Government of Canada, C. E. R. (2025, July 29). *CER – Ontario Energy Profile*. https://www.cer-rec.gc.ca/en/data-analysis/energy-markets/provincial-territorial-energy-profiles/provincial-territorial-energy-profiles-ontario.html?utm_source=chatgpt.com

Grazieschi, G., Asdrubali, F., & Thomas, G. (2021). Embodied energy and carbon of building insulating materials: A critical review. *Cleaner Environmental Systems*, *2*, 100032. https://doi.org/10.1016/j.cesys.2021.100032

Haik, R., Meir, I. A., & Peled, A. (2023). Lime Hemp Concrete with Unfired Binders vs. Conventional Building Materials: A Comparative Assessment of Energy Requirements and CO_2 Emissions. *Energies*, *16*(2), 708. https://doi.org/10.3390/en16020708

Ingrao, C., Lo Giudice, A., Bacenetti, J., Tricase, C., Dotelli, G., Fiala, M., Siracusa, V., & Mbohwa, C. (2015). Energy and environmental assessment of industrial hemp for building

applications: A review. *Renewable and Sustainable Energy Reviews*, *51*, 29–42. https://doi.org/10.1016/j.rser.2015.06.002

Ip, K., & Miller, A. (2012). Life cycle greenhouse gas emissions of hemp–lime wall constructions in the UK. *Resources, Conservation and Recycling*, *69*, 1–9. https://doi.org/10.1016/j.resconrec.2012.09.001

Mahmood, O., Kavgic, M., & Noel, M. (2024). Hygrothermal and mechanical characterization of novel hemp-lime composites with enhanced consistency. *Construction and Building Materials*, *450*, 138720. https://doi.org/10.1016/j.conbuildmat.2024.138720

Mohammadifardi, H., Knight, M. A., Unger, A. A. J. (2019). Sustainability Assessment of Asset Management Decisions for Wastewater Infrastructure Systems—Implementation of a System Dynamics Model. *Systems, Vol. 7, Iss. 3*. https://doi.org/10.3390/systems7030034

Nazari, F., & Woods, L. D. (2025). Environmental life cycle assessment of hemp-based thermal insulation: From agricultural growth to manufacturing in the United States. *Journal of Cleaner Production*, *506*, 145509. https://doi.org/10.1016/j.jclepro.2025.145509

van der Werf, H. M. G. (2004). Life Cycle Analysis of field production of fibre hemp, the effect of production practices on environmental impacts. *Euphytica*, *140*(1), 13–23. https://doi.org/10.1007/s10681-004-4750-2

Wu, Q. (2024). *Life Cycle Assessment of Industrial Hemp and Hemp-Based Products in Canada*. https://ualberta.scholaris.ca/items/024f4c32-1562-41c6-8b6e-eebe8eae7bc4

Zhang, L.-N., Kwon, S.-J., & Wang, X.-Y. (2025). Low-Carbon Slag Concrete Design Optimization Method Considering the Coupled Effects of Formwork Stripping, Strength Progress, and Carbonation Durability. *Buildings*, *15*(8), 1316. https://doi.org/10.3390/buildings15081316

Chapter 9 : Conclusions, limitations, and future recommendations

9.1. General conclusions

The research presented in this thesis addressed two complementary strategies for developing sustainable, carbon-conscious construction materials: (1) optimizing hemp–lime composites (HLCs) for improved technical performance, and (2) assessing the technical suitability and environmental benefits of hydrated lime produced via electrochemical decarbonation (ED) of limestone and waste feedstocks. The results can be summarized as follows:

- Reducing and standardizing hemp shiv particle size significantly improved material consistency, reducing variability in mechanical and hygrothermal properties and enabling a bio-based content of up to 70% by weight.
- Employing vibration as a compaction method enhanced density uniformity (<3.5% variation), which is critical given the influence of density on HLC properties.
- While HLCs remain non-structural, compressive strength (0.055–0.079 MPa) is comparable to rigid thermal insulation boards. Strength was influenced by hemp-to-binder ratio and shiv size; fine shivs increased uniformity and reduced thermal conductivity (~13%).
- Thermal performance improved with higher hemp content: fibre ratios of 10%, 20%, and 40% led to thermal conductivity reductions of 6%, 15%, and 20%, respectively. Fibre length had minimal influence on thermal properties. Specific heat capacity (931–976 J/kg·K) and thermal diffusivity (0.277–0.361×10^{-6} m^2/s) were largely unaffected by hemp ratio or fibre length.
- Moisture buffering was excellent (2.12–2.73 g/m^2·RH), increasing with higher fibre content (up to 24% for 40% fibre ratio). The combination of fine hemp and higher hemp-to-binder ratios enhanced hygric performance.

- Environmental assessment showed reductions in direct CO_2 emissions of 17–40% when using medium- and low-purity hemp shivs compared to high-purity ones.
- ED effectively decarbonated limestone feedstocks, producing precipitates with high $Ca(OH)_2$ content (78.8–85.7%), reduced impurities, and improved particle size distribution. Some products met ASTM standards for Type N hydrated lime.
- ED was successfully applied to waste feedstocks such as eggshells and mussel shells, yielding $Ca(OH)_2$ concentrations of up to 90.3% and demonstrating feasibility for circular economy applications.
- Combining ED with direct carbon capture captured up to 89% of CO_2, indicating near-zero emission potential.
- ED processes achieved efficiencies of 82.7–86.0%, outperforming previous mass recovery techniques and demonstrating potential for sustainable, low-carbon lime production.
- HLCs prepared with ED-derived lime maintained similar thermal conductivity (0.0521 W/m·K) and moisture buffering (2.61 g/m²·RH) compared to conventional lime composites.
- Compressive strength increased by ~45% (0.061 MPa vs. 0.042 MPa), indicating a denser and more reactive binder matrix.
- Environmental performance was enhanced when using ED-derived lime; including sequestration, net GWP = –23.10 kg CO_2 eq., which is 15.7% lower than conventional HLC.
- With sequestration, the ED-HLC wall achieved a 457% lower carbon footprint than a glass wool insulation, transitioning to a strongly carbon-negative balance — a performance beyond the reach of conventional mineral insulation products.
- The sensitivity analysis confirmed that all mixes remained carbon-negative, but higher hemp fractions reduced sequestration by up to 16%. This underscores the dominant role of the ED

binder in the carbon balance and the need to balance environmental gains with material performance.

- These results highlight the dual benefit of ED-HLC: maintaining technical performance while delivering significant carbon reductions, including carbon-negative potential.

9.2. Research contributions

This thesis provides several key contributions to sustainable construction materials:

1. Demonstrated that particle size, compaction method, and binder composition critically influence the thermal, mechanical, and hygric performance of hemp–lime composites.
2. Validated the technical suitability of ED-derived lime for construction applications, showing compliance with ASTM standards and improved compressive strength in HLCs.
3. Established the environmental benefits of ED lime, including reductions in embodied CO_2 emissions and the potential for carbon-negative building materials.
4. Showed the feasibility of using organic waste feedstocks (eggshells, mussel shells) for sustainable lime production, advancing circular economy practices.

9.3. Limitations and future work

Despite these contributions, several limitations should be acknowledged:

- Long-term durability, fire resistance, freeze-thaw behaviour, and biological degradation of HLC were not experimentally evaluated, leaving open questions regarding material performance under extreme or prolonged environmental conditions.
- Effects of fibre orientation, surface treatments, and complex particle size distributions on mechanical and thermal performance were not fully investigated.

- The ED experiments were performed at laboratory and pilot scale, which may not fully reflect industrial-scale process efficiencies, energy consumption, or mass recovery.
- The impact of feedstock particle size on reaction kinetics, morphology, and $Ca(OH)_2$ yield was not assessed, limiting optimization potential for scaling up.
- While the chemical composition and particle characteristics of the precipitated materials were characterized, other performance parameters required by standards (e.g., workability, setting behaviour) were not evaluated.
- The long-term performance, carbonation behaviour, and recyclability of ED-HLC in real-world building applications remain untested.
- Life cycle assessment was limited to a cradle-to-gate boundary, excluding operational, maintenance, and end-of-life phases.
- Secondary data for conventional lime, hemp, and benchmark insulation materials may not fully reflect regional conditions.
- The environmental assessment focused primarily on global warming potential (GWP), without including other categories such as water depletion, toxicity, or land occupation.

Future research should build upon the findings of this thesis to further optimize hemp–lime composites and the electrochemical decarbonation process for sustainable construction applications. Key areas for future investigation include:

- Develop a standardized mix design procedure for HLC production, enabling systematic optimization of hemp-to-binder ratios, particle sizes, and compaction methods for diverse applications and ensuring reproducible technical and environmental performance.

- Explore the effects of particle size reduction and increased hemp shive content on fire resistance, freeze-thaw behaviour, biological degradation, and overall durability.
- Optimize mix designs for different building envelope applications, including walls, floors, ceilings, as well as various component types such as blocks, panels, and sprayed-in or precast systems.
- Assess the optimal particle size distribution, combining coarse and fine hemp shivs to enhance compressive strength while minimizing thermal conductivity.
- Develop validated numerical models (finite element or finite volume) to simulate thermal and hygrothermal behaviour, providing insight into directional conductivity and moisture dynamics.
- Study the long-term thermal stability, moisture buffering performance, and hygrothermal cycling under realistic environmental conditions to ensure the material's reliability in building applications.
- Investigate fibre surface treatments or orientation effects, in combination with different hemp shiv sizes, to further enhance mechanical performance without compromising thermal or moisture regulation properties.
- Evaluate a broader range of densities and hemp-to-binder ratios beyond the current H:B ratios and dry density to optimize performance for diverse building requirements.
- Examine the effect of feedstock particle size on ED reaction kinetics and product characteristics, including $Ca(OH)_2$ content and particle morphology.
- Conduct a comprehensive life cycle assessment of the ED process, including upstream and downstream emissions, energy use, and environmental trade-offs beyond global warming potential.

- Scale up the ED process to pilot and industrial levels to validate laboratory-scale findings, assess process efficiencies, energy demands, and by-product handling.
- Investigate long-term availability and sustainability of alternative calcium-rich waste materials, such as chicken bones or other shellfish by-products, to expand feedstock options.
- Conduct a techno-economic analysis comparing ED lime production with conventional high-temperature lime manufacturing, including cost savings, energy reductions, and potential commercial feasibility.
- Investigate recyclability, maintenance requirements, and end-of-life performance of ED-HLC walls to ensure sustainable lifecycle management.
- Compare ED-HLC with other emerging bio-based and mineral insulation materials to assess relative advantages in terms of technical performance, environmental impact, and carbon sequestration potential.
- Integrate dynamic environmental modeling to understand the interaction of moisture, temperature, and structural changes over time, providing guidance for optimized building envelope designs.

Appendix

A. Development of a Low-Cost Method to Assess the Purity of Hemp Hurds and Hemp Bast Fibres

The main objective of this project is to identify a simple and low-cost purity test method for hemp hurds and fibres for practical adaptation by decorticators and processors. This method will assist companies and producers in sourcing hemp materials and delivering consistent products across the different manufacturing use cases. A low-cost user-friendly purity test method was developed for both hemp fibres and hurds through a flotation technique that is widely used in industries where materials can be separated through density differences and water acts as a separating layer between light and dense materials. The results were crosschecked with a handpicking method, which is a more precise method as there are no standard methods for assessing the purity of hemp hurd and bast fibre in Canada.

Figure A 1. Hemp hurd specimens used in the study.

Six samples for each test were selected from the received bast fibre and hurd specimens to have adequate representation. Four different hemp producers provided a total of 21 hemp specimens

(12 bast fibre and 9 hurd). These specimens had different sizes, purity ratios, and retting stages as shown in Figures B.1 and B.2.

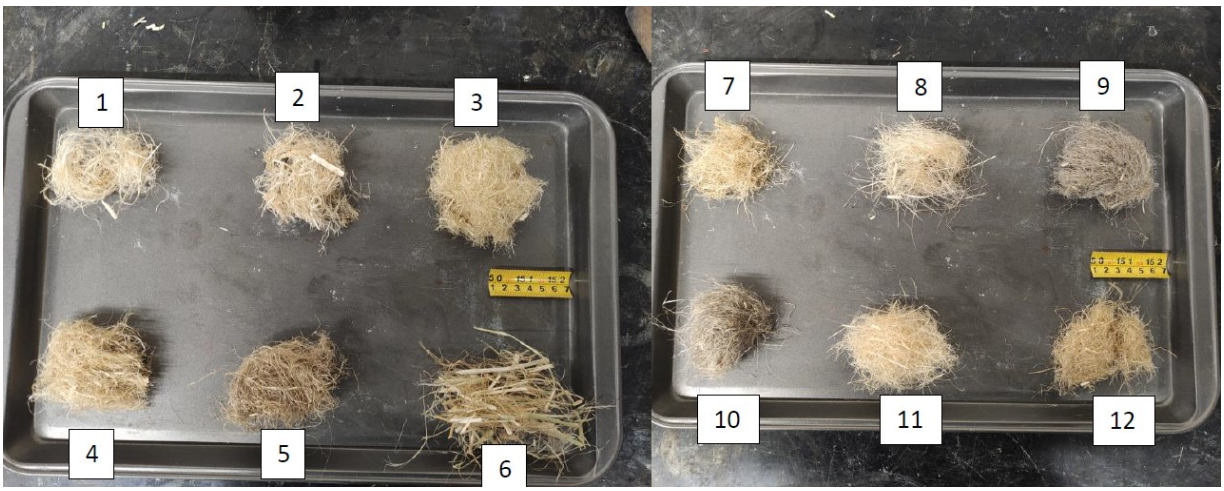

Figure A 2. Hemp fibre specimens used in the study.

Instruments used in this method were chosen to be affordable and widely available to fulfill the low-cost and user-friendly criteria. They consisted of a 4-liter plastic pail, fine mesh kitchen strainer, No. 200 sieve size, magnetic stirrer, digital balance scale (0.001 g precision), coffee grinder, and drying oven as shown in Figure B.3.

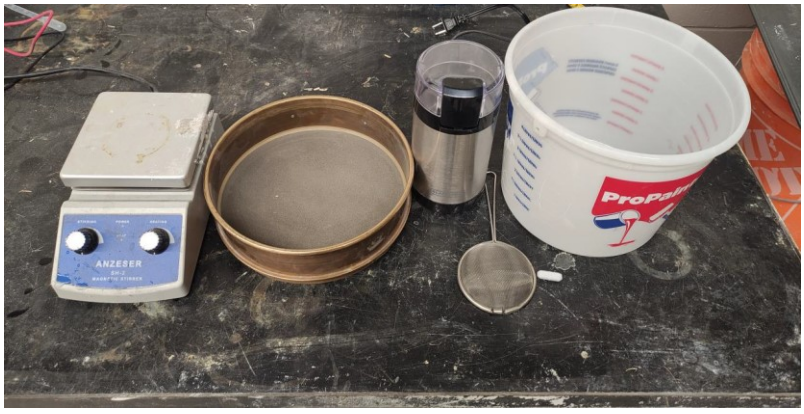

Figure A 3. Instruments and tools used in the study.

The results of the tests are summarized in Figures B.5 and B.6. A total of 126 samples were tested using both the handpicking method and the floatation method, then an average value was used to compare the results. The handpicking method was done through manual separation of bast fibre from hurd and any other impurities if existed. Then, each part is oven dried until reached a constant weight and the purity is calculated. The results show a high accuracy of the test method used to measure the purity levels in comparison with the reference method (handpicking). The results showed that this method is overestimating the purity results by less than 3% with an average of 1.83% for the hurd samples. However, the same method seems to underestimate the purity levels by less than 2% and with an average of 0.73% for the bast fibre samples. This can be explained by some fibres being trapped with the floating particles causing an increase in their mass.

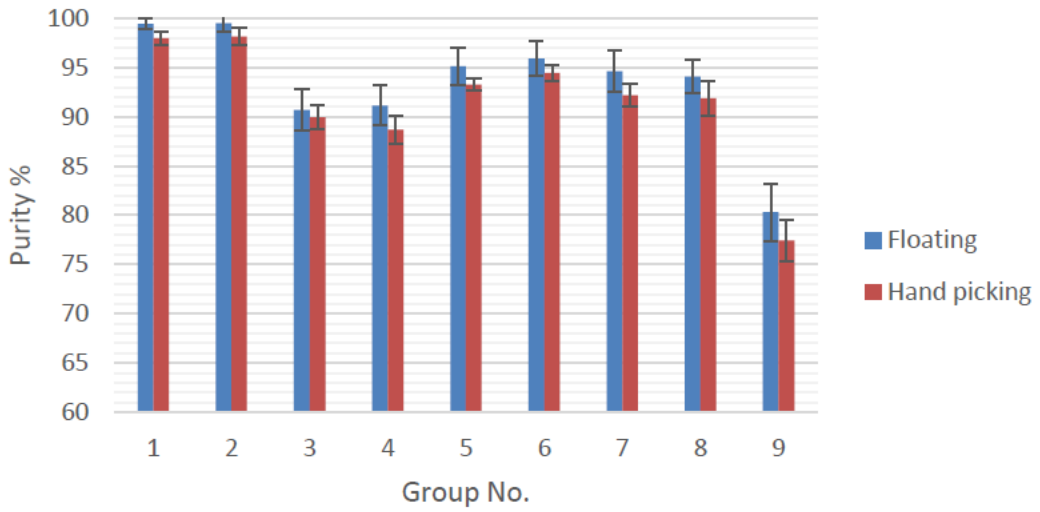

Figure A 4. Purity levels of hemp hurds floating vs handpicked method.

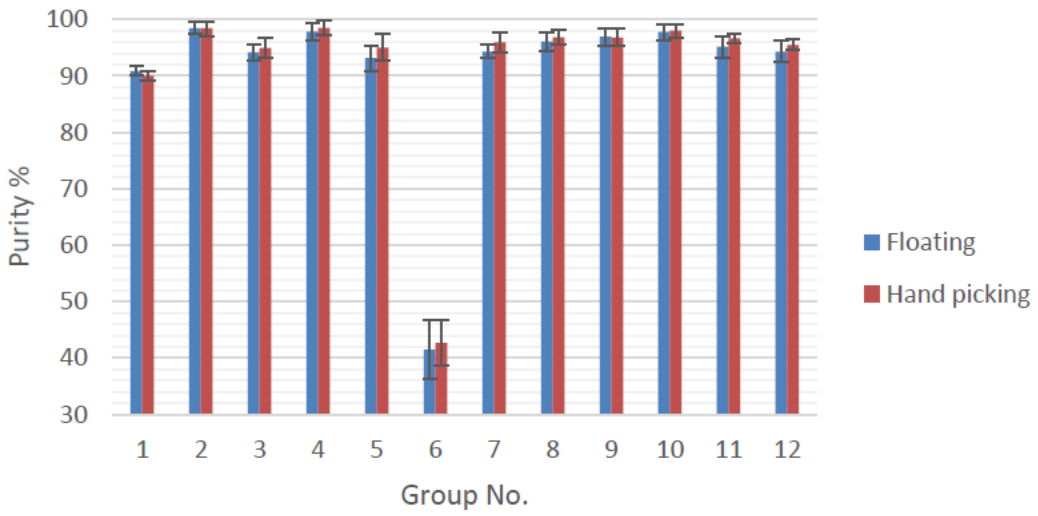

Figure A 5. Purity levels of hemp fibres floating vs handpicked method.

B. Electrochemical decarbonation of limestone

As shown in Figures C.1–C.3, the FE-SEM and EDX analyses confirmed the presence of $Ca(OH)_2$ clusters within the DMs of all samples. Distinct morphologies were observed, with compact clusters composed of fine $Ca(OH)_2$ grains identified across samples C, L1, L2, and L3. In addition, localized carbonate structures ($CaCO_3$) were detected, particularly in sample C, indicating partial carbonation of the hydroxide phase. Overall, these microstructural observations verify the coexistence of hydroxide and carbonate phases in the ED-derived materials, supporting the chemical characterization discussed in the main text.

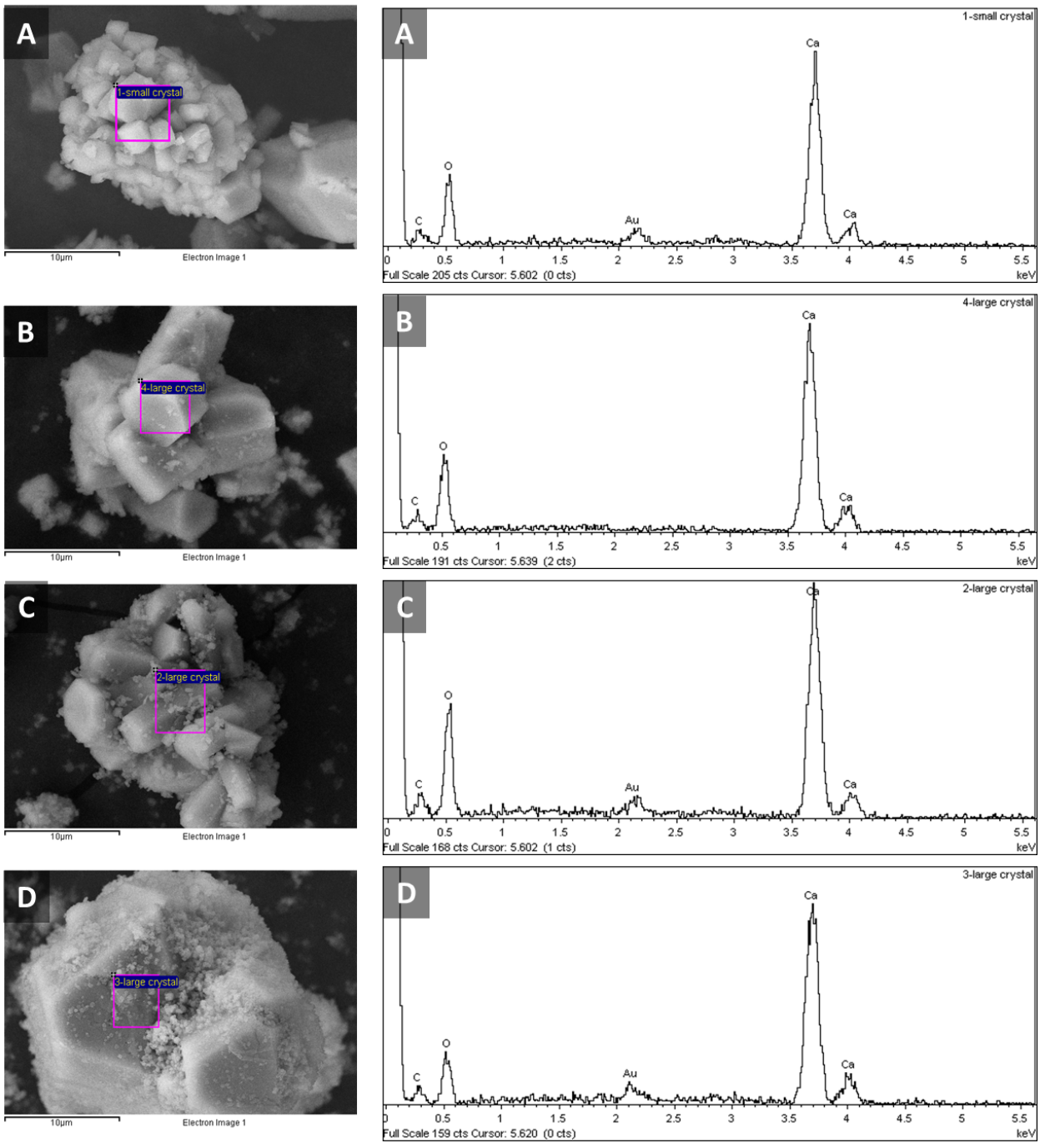

Figure B 1. EDX analysis of $Ca(OH)_2$ clusters and structures observed in DMs from samples C (A), L3 (B), L1 (C), L2 (D). The highlighted zones were the EDX analysis spots.

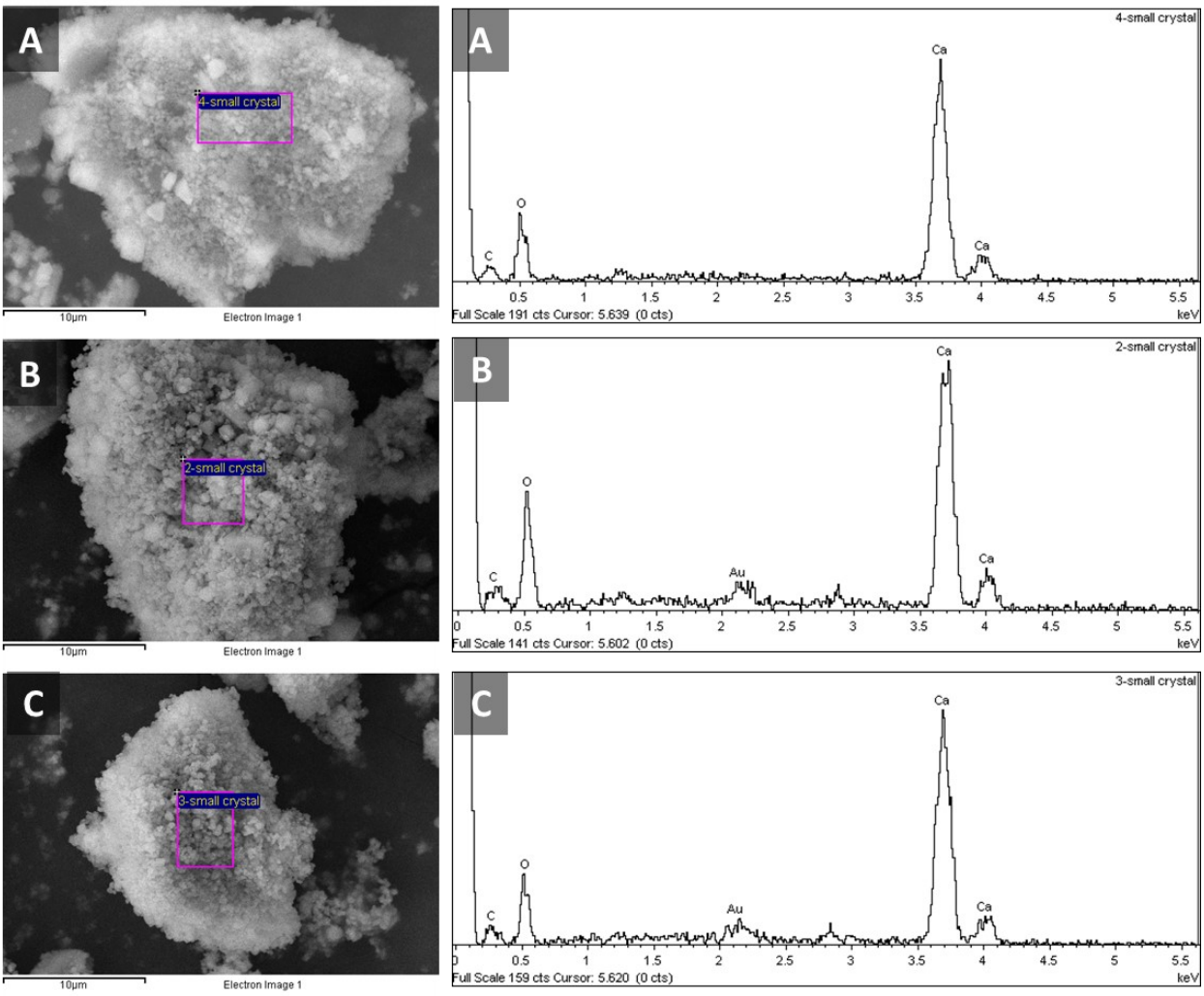

Figure B 2. Clusters comprised of small grains of $Ca(OH)_2$ were observed and chemically characterized by EDX in DMs from samples C (A), L1 (B), and L2 (C). The highlighted zones were the EDX analysis spots.

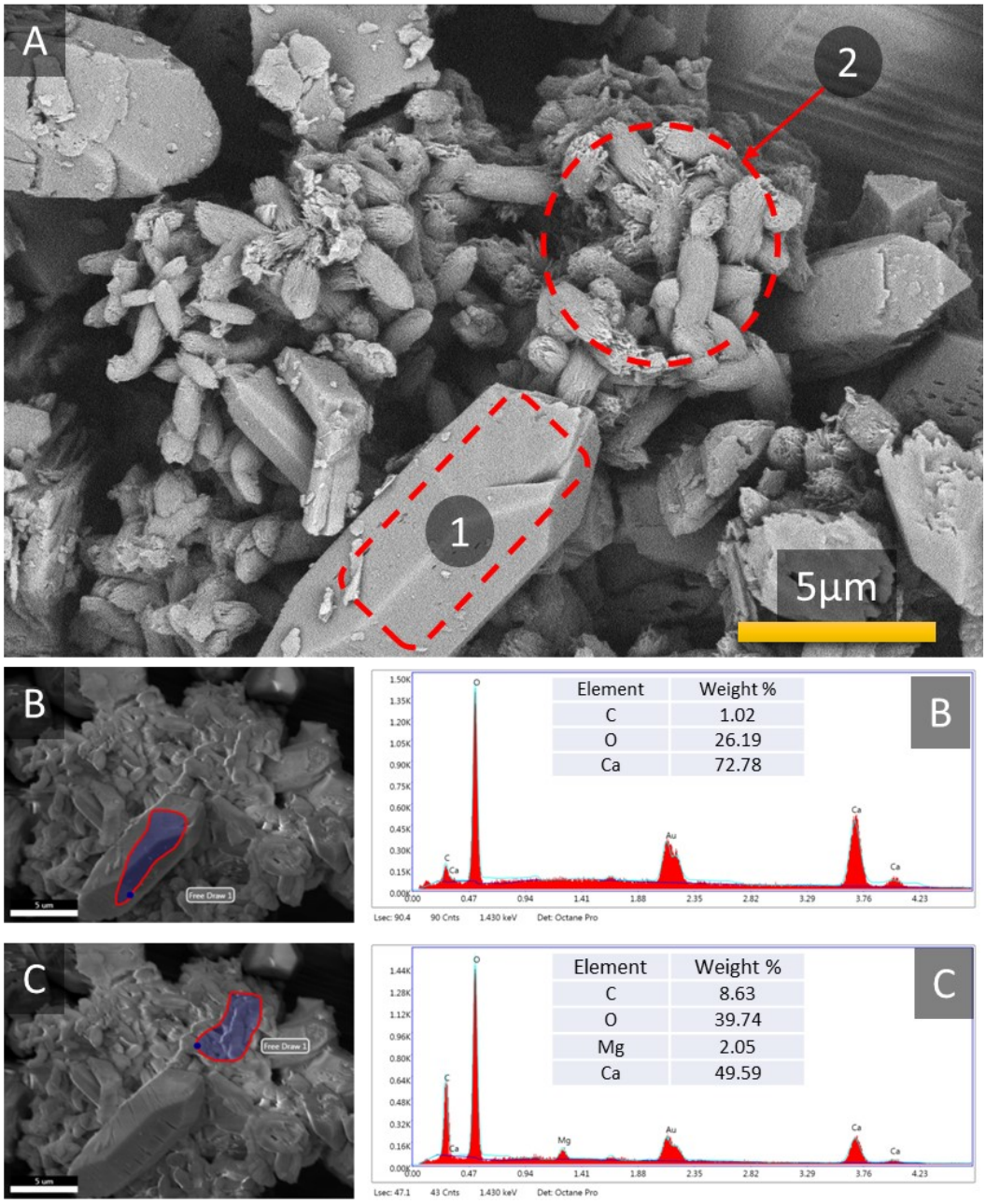

Figure B 3. FE-SEM image of a DM from sample C. There were identified Low-carbon content structures associated with $Ca(OH)_2$ (Spot 1), and a cluster of carbonate structures associated with the remanent $CaCO_3$ (Spot 2), which were chemically characterized by EDX shown in figures B and C, respectively.